

Université Libre de Bruxelles
Faculté des Sciences
Service d'Optique Nonlinéaire Théorique

Temporal Dynamics of Driven Nonlinear Optical Systems

Dissertation originale présentée par
Michel Nizette
en vue de l'obtention du grade de
Docteur en Sciences

Promoteur de thèse :
Thomas Erneux

Année académique 2002–2003

À ma mère.

Remerciements

J'ai préparé mon doctorat dans le service de Physique Théorique et Mathématique. Je souhaite tout d'abord remercier le professeur Marc Henneaux, qui dirige ce service. Au cours de mes études de licence, j'ai pu apprécier ses qualités pédagogiques immenses : je garderai de son cours de Relativité Générale le souvenir d'un exposé d'une limpidité rarement égalée.

Je tiens ensuite à remercier chaleureusement le professeur Paul Mandel pour m'avoir accueilli au sein du groupe d'Optique Nonlinéaire Théorique et pour m'avoir offert d'y préparer un doctorat. Paul est un homme de science impressionnant de par l'étendue de ses connaissances, la sûreté de son jugement, et la sagacité de son intuition physique. C'est donc pour moi un très grand honneur d'avoir pu accomplir mon travail de doctorat dans le groupe de recherche qu'il dirige d'une main si sûre. J'ai de plus une très grande reconnaissance pour les qualités d'écoute dont il a régulièrement fait preuve à mon égard, ainsi que pour l'aide précieuse qu'il m'a apportée au début de mon doctorat.

Je voudrais ensuite exprimer ma profonde gratitude envers Thomas Erneux pour avoir supervisé mon travail de thèse. Thomas a immédiatement entretenu avec moi un rapport de collaborateur à collaborateur et non de maître à apprenti. Il m'a ainsi donné une très grande liberté d'action dans l'orientation de mes recherches. Cependant, il n'a pas négligé d'émettre, en certains cas, des opinions franches sur mon travail. Le moment venu, il m'a ainsi évité de m'engager sur des voies hasardeuses, et en d'autres occasions, m'a forcé à examiner les implications de mes choix avec lucidité. La qualité de mon travail s'en est toujours trouvée améliorée, et je lui en suis extrêmement reconnaissant. Thomas m'a également poussé à de multiples reprises à collaborer avec des groupes de recherche étrangers, éveillant en moi la conscience de l'enrichissement apporté par ces échanges. Sur un plan plus technique, j'ai pu apprécier la dextérité avec laquelle Thomas manie le calcul asymptotique. J'ai suivi avec intérêt ses exposés sur certains phénomènes dynamiques subtils tels que l'effet canard. J'admire enfin son habileté à trouver d'instinct le chemin le plus court vers la solution d'un problème mathématique. Son talent en ce domaine n'est d'ailleurs qu'une manifestation particulière de son désir permanent d'exprimer les choses clairement, dans un souci de partage des connaissances efficace. C'est là un état d'esprit pour lequel j'ai le plus profond respect. Dans tout milieu professionnel — pas seulement celui de la recherche — cette attitude me paraît fructueuse, et le désir de la faire mienne ne me quittera plus.

L'interaction avec les autres membres du groupe d'Optique Nonlinéaire Théorique a été pour moi une source de stimulation intellectuelle et de progrès constants. Ils

m'ont, chacun à leur manière, fait partager leurs visions personnelles du monde de la recherche, qui m'ont été très précieuses. Didier Pieroux, dont j'ai partagé le bureau au début de ma thèse, a visiblement eu à coeur de contribuer à mon initiation au métier, ce dont je lui suis très reconnaissant. En outre, je reconnais en lui des qualités d'honnêteté intellectuelle exemplaires. Gregory Kozyreff, étudiant talentueux d'un an mon aîné, a toujours constitué pour moi un modèle vers lequel j'ai cherché à tendre. Il a traversé avant moi chaque étape du doctorat et m'a en quelque sorte balisé le chemin en me faisant profiter de son expérience. Mustapha Tlidi n'a jamais hésité un seul instant à m'apporter des conseils éclairés et à m'offrir de précieux encouragements. Les longues discussions que nous avons eues ensemble m'ont été très agréables, et ont été pour moi d'un très grand bénéfice. J'ai également apprécié la compagnie de nos collaborateurs temporaires ou extérieurs tels que Thomas Haller, Theodore Kolokolnikov, Igor Koryukin, Ba An Nguyen, Isabella Susa, Evgeni Viktorov et Andrei Vladimirov.

Je sais gré à Dominique Derozier pour m'avoir aidé à organiser mon séjour à Lille, et j'apprécie énormément l'attention dont m'ont entouré les membres du Laboratoire de Physique des Lasers, Atomes et Molécules. Mes remerciements vont en particulier à Axelle Amon, Serge Bielawski, Dominique Derozier, Nicolas Joly et Marc Lefranc pour les discussions scientifiques enrichissantes que nous avons eues. J'ai pu admirer la dextérité d'Axelle lors de notre travail en laboratoire, et la collaboration avec Marc lors de la rédaction d'un article fut l'un des moments les plus stimulants de ma thèse. Je remercie encore Axelle Amon et Jean Ringot pour les agréables soirées qu'ils m'ont offert de passer en leur compagnie, à leurs domiciles. Enfin, je suis heureux d'avoir partagé le bureau d'Andrée De Backer, dont la compagnie me fut très agréable.

Je suis très reconnaissant à Rajarshi Roy pour m'avoir accueilli dans son service de recherche à l'Université du Maryland, pour l'importante participation financière de son laboratoire à mon séjour aux États-Unis, ainsi que pour avoir veillé personnellement à ce qu'il se déroule le mieux possible. Les entretiens que j'ai eus avec lui ainsi qu'avec les autres membres du laboratoire (et je pense plus particulièrement à Parvez Guzdar et Wing-Shun Lam) ont grandement enrichi ma culture scientifique.

Mes remerciements vont également à mes collègues Athanasios Gavrielides, Fabien Rogister, Evgeni Viktorov et Sebastian Wiczorek pour les discussions intéressantes que nous avons eues. Je me réjouis du succès de mes collaborations avec Athanasios Gavrielides, Vassilios Kovanis et Tom Simpson.

J'adresse encore mes remerciements à tous les membres du Service de Physique Théorique et Mathématique et à d'autres collègues du département de Physique, en particulier Renaud Lambiotte et Christiane Schomblond, qui m'ont soutenu par leurs encouragements ou confié leurs impressions. Un grand merci aussi à Fabienne De Neyn pour son sourire et pour les nombreux services qu'elle rend quotidiennement à tous les membres du service.

Sur un plan plus privé, je souhaite remercier ici mes parents pour le soutien qu'ils m'ont apporté au cours de mes études universitaires, ainsi que pour la confiance constante qu'ils manifestent quant à ma capacité à mener à bien une thèse de doctorat. Je souhaite également exprimer mon affection pour Stéphanie et la remercier pour

l'enthousiasme qu'elle montre pour mes succès ainsi que pour la patience dont elle fait preuve et le réconfort qu'elle m'offre dans les moments de doute.

Durant la réalisation de ce travail, j'ai bénéficié d'un contrat d'emploi à charge du programme des pôles d'attraction interuniversitaires ainsi que d'une bourse de séjour à l'étranger du Commissariat Général aux Relations Internationales de la Communauté Française de Belgique. J'ai également bénéficié d'un contrat de quatre ans comme Aspirant au Fonds National de la Recherche Scientifique.

Résumé

Cette thèse est consacrée à l'étude théorique de la dynamique temporelle de certains systèmes optiques non-linéaires gouvernés par un signal externe. Le sujet est introduit et motivé dans le chapitre 1, et des perspectives de recherche future sont énoncées dans le chapitre 6.

Le chapitre 2 traite du laser à semiconducteur soumis à une perturbation optique faible. J'ai appliqué aux équations cinétiques du laser une méthode de mise à la moyenne adaptée aux oscillateurs fortement non-linéaires. Les équations ainsi obtenues constituent un bon point de départ pour une analyse plus approfondie. Deux problèmes distincts sont ainsi traités. Le premier problème est le laser à semiconducteur soumis à l'injection d'un signal optique monochromatique faible. J'ai déterminé analytiquement les régimes stationnaires, périodiques et quasipériodiques en explorant certaines limites des paramètres. Ces résultats sont discutés en regard de différents traitements analytiques partiels du problème effectués par d'autres chercheurs. Le second problème traité est le laser à semiconducteur soumis à la fois à une faible injection optique et une faible rétroaction optique. J'ai effectué une analyse de stabilité complète des régimes d'accrochage en phase des modes de cavité externe sur le signal injecté. J'ai trouvé, en particulier, une instabilité caractérisée par une période d'oscillation double du retard de la rétroaction. Cette instabilité n'apparaît pas lorsque le laser est soumis uniquement à une rétroaction.

Dans le chapitre 3, j'aborde le problème du laser à semiconducteur soumis à une injection optique plus intense. Deux questions distinctes sont étudiées, toutes deux motivées par une collaboration expérimentale. Premièrement, des expériences récentes ont identifié des régimes d'oscillations avec une période triple par rapport au régime pulsé classique caractérisé par des oscillations de relaxation entretenues. J'ai montré qu'ils correspondent à des branches de solutions isolées des équations cinétiques en appliquant à celles-ci une méthode numérique de continuation. En second lieu, j'ai étudié, dans le régime pulsé, le mécanisme de double accrochage de la phase optique et de la phase des pulsations lorsqu'une faible modulation périodique est appliquée au courant de pompage. Ce problème est traité par une méthode d'échelles multiples combinée à une méthode numérique de continuation. J'ai étudié la possibilité d'une réponse pulsée bistable du laser, et j'ai comparé ces résultats avec des mesures expérimentales.

Le chapitre 4 propose une description théorique simple d'un régime d'oscillations en rafales observé lors d'expériences récentes dans un oscillateur paramétrique optique sujet à des instabilités thermiques. J'ai montré à l'aide d'une méthode de continuation

numérique que le cycle d'oscillation s'explique par un passage lent par certains points de bifurcation. J'ai également traité le problème par une méthode d'échelles multiples, le ramenant ainsi à un cas plus simple d'oscillations périodiques décrit précédemment par d'autres chercheurs.

Dans le chapitre 5, j'étudie un modèle de système optique bistable avec une rétroaction à grand retard et soumis à un forçage externe faible. Un tel dispositif peut être décrit par une équation différentielle non-linéaire à retard. Au moyen d'une analyse à échelles multiples combinée à une méthode de développements asymptotiques composites, j'ai réduit cette équation à un système d'équations différentielles non-linéaires ordinaires. L'analyse est valable dans la limite des oscillations de faible amplitude, mais fortement anharmoniques. J'ai utilisé ces équations réduites pour montrer analytiquement l'existence d'un grand nombre d'états multistables induits par une modulation périodique et pour étudier l'influence de certains paramètres de modulation sur leur stabilité.

Contents

1	Introduction	1
2	Semiconductor laser subject to a weak optical injection and/or feedback	7
2.1	Introduction	7
2.2	The semiconductor laser rate equations	11
2.2.1	Field equation, material equation, and gain model	11
2.2.2	The free-running semiconductor laser	13
2.2.3	Dimensionless rate equations	15
2.3	Perturbed Hamiltonian problem	16
2.4	Laser subject to optical injection	19
2.4.1	Averaged equations	20
2.4.2	Low-amplitude limit	22
2.4.3	Large- α limit	25
2.5	Laser subject to optical injection and feedback	30
2.5.1	Low-amplitude averaged equations	31
2.5.2	Laser with feedback only	33
2.5.3	Laser with injection and feedback	38
2.6	Summary	45
3	Semiconductor laser subject to strong optical injection	49
3.1	Introduction	49
3.2	High-injection laser responses	51
3.3	Period-tripled limit cycles	51
3.3.1	Experimental data	51
3.3.2	Numerical bifurcation diagrams	55
3.3.3	A simplified phase equation	56
3.4	Semiconductor laser subject to optical injection and pump modulation	59
3.4.1	Normal form analysis	59
3.4.2	Bifurcation diagrams (controlling the injection rate)	61
3.4.3	Comparison of the reduced and full models	64
3.4.4	Bifurcation diagrams (controlling the master-slave detuning) . .	66
3.4.5	Experiments	66

3.5	Summary	69
3.A	Stability analysis	71
3.B	Normal form derivation	72
3.B.1	Scaling	72
3.2.2	First-order problem	72
3.2.3	Second-order problem	73
3.2.4	Third-order problem	74
4	Bursting oscillations in optical parametric oscillators	75
4.1	Introduction	75
4.2	Optical parametric oscillation mechanism	77
4.3	Optical parametric oscillator model	78
4.3.1	Single-mode OPO	78
4.3.2	Two-mode OPO	79
4.3.3	Thermal effects	81
4.4	Thermo-optical oscillations	82
4.5	Bursting oscillation experiments	84
4.6	Theory for bursting oscillations	85
4.6.1	Numerical bifurcation diagrams	85
4.6.2	Perturbative analysis	87
4.7	Summary	91
4.A	Equivalence between the degenerate and nondegenerate monomode OPO models	93
4.B	Fast oscillation averaging	94
5	Optically bistable devices with a large delay loop	97
5.1	Introduction	97
5.2	Normal form analysis	103
5.3	No-forcing case	105
5.3.1	Asymptotic states	105
5.3.2	Stability	109
5.4	Moving defect analysis	111
5.5	No-forcing case: instability growth rates	113
5.6	Modulation-locked dynamics	115
5.7	Modulation-induced multistability	117
5.8	The influence of modulation waveform	122
5.9	Summary and discussion	129
5.A	Normal form derivation	131
5.A.1	Instability conditions	131
5.A.2	Perturbation scheme	132
5.A.3	First order problem	133
5.A.4	Second order problem	133
5.A.5	Third order problem	134

5.B	Equations of the motion for the fronts	136
5.B.1	Scaling	136
5.B.2	Small corrections	137
5.B.3	Matching constraints	138
5.C	Extrema of $\mathcal{G}(z_l)$	139
5.D	Number of stable phase-locked modes	140
5.E	Stability for nonzero detuning	141
5.E.1	Sine waveform: $g = g_1$	141
5.E.2	Square waveform: $g = g_2$	142
5.E.3	Pulsed waveform: $g = g_3$	143
5.F	Stability for nonnegligible front attraction	143
5.F.1	Sine waveform: $g = g_1$	144
5.F.2	Square waveform: $g = g_2$	145
6	Perspectives	147
	Bibliography	149

Chapter 1

Introduction

Nonlinear optical phenomena do not show up in our daily life [12]. Optics studies the propagation of light and its interaction with matter. Because the light intensities that usually occur in nature are relatively low, the optical properties of materials can be considered independent of the light intensity in very good approximation. However, with the advent of the laser in 1960 [75], it became possible to create, in laboratories, conditions of illumination so intense that the optical properties depend on the intensity. The medium then reacts to illumination and alters the optical field in a nonlinear way. Matter thus makes itself the vector of the interaction of light waves that would otherwise remain unaffected by each other. Nonlinear optics is the science that deals with the nonlinear action of light upon itself through its coupling to matter.

It is generally considered that nonlinear optics begins with the first experimental observation in 1961 of second harmonic generation [35], a process by which two photons of the same frequency are converted into a single photon with a doubled frequency. In the decade that followed, many other nonlinear optical effects were identified [10]. The value of such discoveries for practical applications, notably spectroscopy, was readily acknowledged as they allowed the generation of coherent radiation at wavelengths different from those of the available lasers. In parallel to these advances, dynamical instabilities in laser systems were intriguing the scientific community [1]. Periodic or irregular spike sequences were frequently observed in laser output. Very soon, it was recognized that the fundamental nonlinear character of the interaction between the field and the active medium could play an important role in the onset of these complex temporal patterns. However, it is only in 1975 that Haken recognized the formal equivalence [52] between the semiclassical single-mode laser equations and the Lorenz model for hydrodynamic turbulence, which was then highly popular among theoreticians of deterministic chaos. The discovery of this remarkable property greatly contributed to the development of approaches of laser problems based on dynamical system theory, although the quantitative predictions of the Haken-Lorenz model were successfully compared to experimental data only a decade later [123].

One of the most important boosts of research in nonlinear optics came in the late 1970s with the advent of optical telecommunications systems using optical fibers and

semiconductor lasers [55]. Current communication networks with fiber transmission lines have a much greater information-carrying capacity than conventional coaxial-cable-based systems. Also, optical signals can be transmitted in fibers over tens of kilometers before requiring amplification. In these optical communication schemes, modulated semiconductor lasers are used for the generation of information-carrying light waves, and can also be used in repeaters, for the amplification of attenuated signals. Other important applications of semiconductor lasers include optical disks for information storage, barcode readers, and printers. Unfortunately, semiconductor lasers tend to react strongly to perturbations from the outside world. This leads to dynamical instabilities that can hamper technological progress. Therefore, it is not surprising that much research effort is devoted to the understanding and control of these instabilities. Sometimes, however, a highly pulsating laser response can be desirable for practical applications: nowadays, the use of chaotic information carriers is contemplated for secure communication schemes [122].

Another capital discovery is the observation in the mid-1970s of optical bistability in passive (*i.e.*, unexcited) media [45]. This phenomenon is defined as the hysteretic coexistence of two distinct states of light transmission of the medium. Much interest in this effect stems from potential applications to all-optical signal processing [103]. It allows the creation of devices capable of performing logical operations on optical signals, or of acting as memory elements. At present, this emerging technology is hampered by practical limitations, such as the rather large energies required for switching between transmission states, or the difficulty of coping with the heat generated in the switching process. Nevertheless, it offers exciting perspectives for optical computing. Optical bistability has also attracted much attention from the fundamental viewpoint of dynamical system theory since the prediction [57] and observation [46] in the early 1980s of what is now called the Ikeda instability. Under some conditions, delayed-feedback effects in an optically bistable system can activate a peculiar mode of spontaneous, square-wave like oscillations. This regime can evolve into chaos through a cascade of period-doubling bifurcations. The realization of a physical system exhibiting Ikeda instabilities was relatively easy in comparison to other chaotic optical systems, and allowed the first detailed investigations of “optical turbulence” with systematic confrontations between theory and experiments. Ikeda’s delayed optically bistable system is thus of great historical importance.

Nowadays, fundamental and applied research in nonlinear optics is expanding faster than ever. It has become so intense and diverse that the field has split into a manifold of subdomains with their own communities of specialized researchers.

The purpose of this thesis is to report on the dynamics of some optical systems driven by an external signal. In all cases under consideration, the system is constituted of a sample of material offering a nonlinear response to illumination, and placed inside, or bounded by, an optical resonator (*i.e.*, a set of mirrors, or other physical surfaces acting as such, arranged so as to create a closed optical path). The driving signal can be a beam of coherent light injected in the resonator through one of the (semi-transparent) mirrors, or a periodic modulation of a physical parameter, or both. The

specific problems treated have been determined mainly by timely subjects of interest to the international laser community, and by opportunities of collaboration with other research groups.

When I began my Ph. D. studies, there was a burst of research activity in semiconductor laser instabilities [61]. Semiconductor lasers are popular for a large array of applications because they are small, cheap, and reliable. The injection of a small amount of coherent light from an external source can significantly improve their spectral characteristics, but can also lead to dynamical instabilities. These instabilities are studied experimentally in laboratories, and theoretically with the help of simple nonlinear models. The mathematical tools involved are bifurcation theory, asymptotic calculus, and numerical analysis. A couple of years before I started working on lasers, detailed experimental investigations of the instability onset domains in injection parameter space became possible [108], which was boosting the interest in this problem. The research presented in this thesis began in that context, in collaboration with A. Gavrielides and V. Kovanis, from the Nonlinear Optics group at Kirtland AFB, New Mexico.

Our contribution to this topic is exposed in Chapter 2. There, we present a method of analysis of a model of a semiconductor laser subject to a weak optical perturbation from the outside world. It is an application of an averaging technique valid for strongly nonlinear oscillators. The method is then applied specifically to the problem of the semiconductor laser subject to the injection of a small amount of coherent light. At the time, the purpose of this work was to offer a unified analytical treatment of the problem in the limit of low injection. Several valuable steps towards this goal had been performed [66, 67], but all approaches had focused on particular aspects of the problem, or required quite involved algebraic manipulations. In contrast, the treatment we are presenting is of limited algebraic complexity, and leads to simple formulae for the relevant bifurcation curves in the parameter domain considered. Our results have been validated by subsequent numerical studies. Since then, the knowledge of the injected semiconductor laser instabilities has known a considerable evolution. A recent treatment of the problem based on the application of a numerical continuation method allowed the systematic investigation of higher injection levels, and has unravelled a formidable diversity of dynamical behaviors [124]. Even in the light of these new developments, it remains valuable to balance the complexity of a minute and comprehensive numerical study with the simplicity of a small number of relevant formulae, whenever possible. In its domain of application, our analysis offers a successful prediction of the essential dynamical features of the laser response, *i.e.*, the steady, periodic, or complex character of its output.

In the same chapter, we present a second application of the same averaging method, which can be thought of as a generalization of the previous problem. We tackle the case of a semiconductor laser subject both to the injection of light from a coherent source and to an optical feedback from a distant mirror. This problem found a recent motivation in the context of secure telecommunications through chaotic encryption. Semiconductor lasers with delayed optical feedback are known to generate a high-dimensional chaotic

output, which can be suitable for secure data encryption. The possibility of modulation bandwidth enhancement by optical injection has been suggested recently [118, 119]. In connection to this research domain, we find necessary to improve our understanding of even the simplest dynamical responses of such systems. We show that the interaction of weak injection and feedback can lead to a new mode of destabilization of the regime of steady emission. Specifically, we identify square-wave-like oscillations similar to the those observed in the Ikeda system.

This early work on the semiconductor laser problem led us to a collaboration with the experimentalist T. B. Simpson, from San Diego, California. An account of this joint research is the goal of Chapter 3. There, we examine specific aspects of the dynamics of a semiconductor laser subject to moderate to strong optical injection. In that parameter domain, the injected field cannot be treated as a perturbation of a nonlinear oscillator anymore, so that the approach of Chapter 2 breaks down. Other methods of investigation must be considered. Simpson recently observed the signature, in experimental spectra, of period-three subharmonic intensity oscillations in the case of an injected field perfectly tuned to the free-running laser frequency [41]. The first goal of Chapter 3 is to provide a theoretical description, on the basis of numerical and asymptotic analyses of a mathematical model, of this regime of period-tripled oscillations. The second topic presented is a theoretical study of the response of an optically injected semiconductor laser subject to a periodic modulation of the pumping current, in a regime where the injected field induces sustained intensity oscillations. Simpson's experimental investigation of this system was motivated by a desire to determine to what extent the locking of these oscillations to an external reference frequency was possible [105]. This research was performed in the prospect of realizing a tunable, spectrally pure frequency generator in the tens-of-gigahertz range with an optical carrier. Such devices could have potential useful applications in the area of telecommunications. Our approach of the problem is based on a combination of analytical and numerical methods. It allows us to identify various types of locking transitions, depending on modulation and injection parameter values. We also predict cases of bistability, which have been successfully identified experimentally.

We also had the opportunity to work with A. Amon and M. Lefranc from the University of Lille, France. We collaborated for a better understanding of a particular dynamical instability in an optical parameter oscillator (OPO). An OPO is an optical system whose operation is based on the conversion of one photon of given frequency into two photons of about half the frequency of the original photon. This process can be thought of as the reverse of second harmonic generation. The understanding and mastery of instabilities in such devices is important, because this may lead to the design of better wavelength-tunable coherent light sources. The instability considered in this thesis is characterized by periods of fast light intensity oscillations interrupted by quiescent intervals [115]. This regime of emission in bursts constitutes the topic of Chapter 4. We make use of a combination of numerical and analytical techniques in order to show that a simple phase-plane analysis of the problem is possible, leading to a simple understanding of the instability mechanism. We also compute an estimate of

the instability threshold in the limit of fast intensity oscillations.

The last topic of this thesis is presented in Chapter 5. There, we consider Ikeda instabilities in an optically bistable device. The observation of similar dynamics in semiconductor lasers motivated us to re-examine this old problem and see if anything new could be said about it. It turns out that a multiple-scale analysis combined to an approach inspired from the theory of defect motion in spatially extended systems is fruitful in new results. First, we are able to study the basic, periodic oscillatory modes farther away from instability threshold than what is possible with a linear stability analysis. In particular, we provide a complete analytical description of the continuous deformation of harmonic oscillations into square waves. We also offer new insights on the mechanisms leading to the preference of the system for highly symmetric temporal patterns. Finally, we study the effect of a periodic modulation on these patterns. We show that not only the oscillation modes existing in the free-running system can lock to the external frequency, but also that the modulation can create a large number of new coexisting attractors, with potential applications to optical information storage purposes.

Although our personal contribution in nonlinear optics is purely theoretical, we benefitted from collaborations with experimental research teams. The questions solved in this thesis all find their motivations in domains that knew, recently or in the past, an intense experimental research activity. Whenever possible, we predominantly make use of analytical methods over numerical integration. An advantage we can see to this approach is that it allows us to establish, on a sound mathematical basis, connections between different dynamical systems that might otherwise remain unnoticed, or loosely founded, in a purely numerical study. In Chapter 2, an analogy is unravelled between the Ikeda system and the semiconductor laser subject to both injection and feedback. A formal equivalence is discovered in Chapter 4 between bimode and monomode OPO operation in some relevant limit. The developments of Chapter 5 are based on the reduction of a model of a delayed-feedback system to an equation familiar from the context of spatially extended systems. These examples underline the modern idea that such comparative studies are fruitful when dealing with nonlinear phenomena.

Chapter 2

Semiconductor laser subject to a weak optical injection and/or feedback

“Physics is mathematical not because we know so much about the physical world, but because we know so little: it is only its mathematical properties that we can discover.”

—Bertrand Russell

2.1 Introduction

Semiconductor lasers meet a large array of applications due to their small size, low cost, and high reliability. They are found in everyday-life devices such as CD players or laser printers. Moreover, they are very popular as light sources in the area of optical communications. However, despite such technological successes, semiconductor lasers are quite sensitive to external perturbations. Apart from their small size, semiconductor lasers differ from other laser systems in that they are very open to the outside world. Conventional lasers let only a small fraction of the light intensity escape from the resonator, and therefore can be considered closed systems. In contrast, typical semiconductor facet reflectivities are about 30%, allowing strong exchanges with the outside world. Therefore, perturbations such as a tiny amount of light reflected from a distant surface are sufficient to destabilize the steady laser output. Such instabilities may lead to self-pulsating intensity oscillations, quasiperiodicity, or even chaos. The current trend towards all-optical signal processing in optical communication networks requires an extensive understanding of these dynamical behaviors. Until recently, complex dynamics in semiconductor laser systems was viewed as a hindrance to practical applications, and engineering efforts have been directed towards its inhibition. Nowadays, positive use of chaos in semiconductor lasers is considered for secure optical communication schemes [31, 63, 72]. For all these applications, a deep knowledge of semiconductor laser instabilities is highly desirable. Our understanding of these instabilities benefits

greatly from the study of simple mathematical models. The purpose of this chapter is to develop and present a systematic method of analysis of a simple semiconductor laser model subject to a weak optical perturbation, and to illustrate the method in cases of practical interest.

One of the most studied and best understood systems, in this context, is the single-mode semiconductor laser subject to the injection of a beam of monochromatic light. The sustained interest in this system stems for a large part from its great practical simplicity and its genericity as a nonlinear dynamical system. Moreover, optical injection locking of semiconductor lasers has led to significant advances such as single-mode oscillation under high-speed modulation, or linewidth reduction [121]. These applications required the determination of the locking domain in parameter space. Experimentally observed instabilities were understood as the result of successive bifurcations [107]. This triggered a sudden increase of interest for nonlinear analyses of the injected laser equations in various parameter domains [5, 25, 26, 39, 42, 64, 108].

Of particular interest to us in this chapter is the case of weak injection. A Hopf-saddle-node bifurcation was shown in [110] to organize the global bifurcation structure. Later, the dynamics near this point was further investigated in [67, 80, 135, 136]. Valuable insights towards a unified picture of low-injection dynamics were first obtained in [67] on the basis of averaged laser equations derived by De Jagher *et al.* [18]. The computations were quite involved, as a consequence of which there existed some doubt about the accuracy of the higher-order terms in the reduced system [66]. Nevertheless, confidence was gained in these results thanks to their successful confrontation to numerical simulations. We contributed to a significant advance and clarification of this topic by proposing a method of reduction of the laser equations with limited algebraic complexity [88]. The presentation of this method is the main goal of this chapter. We computed explicit approximate formulae for several bifurcation curves in parameter space [86, 88], which are presented here as a first application of our method. Our analytical results were validated and extended by numerical studies. Recently, a comprehensive numerical bifurcation analysis of the injected semiconductor laser model by S. Wieczorek [124] led to a mapping of the dynamics in parameter space with an unprecedented level of detail [125]. These predictions were validated against experiments with remarkable agreement [130, 131]. Experimental mapping of the injected semiconductor laser dynamics and its confrontation to theory is now an ongoing research topic [24, 106]. Wieczorek *et al.* also investigated the possibility of many interesting properties of the system [68, 126, 127, 128], including multipulse excitability [65, 129].

Another problem of great interest is the semiconductor laser subject to delayed optical feedback. Even a weak amount of light reflected from a distant mirror can destabilize steady emission, resulting in a mode of laser operation characterized by high-intensity noise and a very broad linewidth. This regime has been termed coherence collapse and has been identified as a form of chaos [121]. A large number of studies have been devoted to this type of nonlinear dynamics [79, 96, 121]. Another important dynamical behavior observed in semiconductor lasers with feedback is called low-frequency fluctuations [32]. In this regime, which occurs only if the laser is pumped near threshold, the

output intensity suddenly drops out and then recovers gradually. Such events appear at apparently random intervals. However, the investigation of low-frequency fluctuations is beyond the scope of this thesis.

Semiconductor lasers with delayed optical feedback can generate a high-dimensional chaotic signal of potential application to secure transfer of information in optical communications [63]. Recent numerical studies suggested that the modulation bandwidth in these communication systems can be enhanced by strong optical injection [118, 119]. In this context, improvement of our knowledge of a semiconductor laser subject to both injection and feedback is valuable, even in the simplest operation conditions. The study of a single-mode semiconductor laser model subject to weak injection and feedback constitutes the second application of the method of analysis presented here.

Our treatment of these problems is based on an averaging method valid for strongly nonlinear but weakly damped oscillators [11]. In Sec. 2.2, we introduce the rate equation model for a single-mode semiconductor laser. In Sec. 2.3, the model is recast into a perturbed Hamiltonian problem, which is a necessary step for the application of the averaging method. In subsequent sections, we undertake the derivation of the reduced equations and their analysis.

Two distinct practical problems are considered. The first one is the single-mode semiconductor laser subject to the injection of a small amount of monochromatic light, which is treated in Sec. 2.4. As mentioned above, this problem is well documented numerically. In contrast, analytical results remain more rare. S. Wicczorek's Ph. D. thesis [124] led to a thorough understanding of the dynamics of this laser system, which was made possible by the application of numerical continuation methods. We feel the need to complement his work with detailed analytical results, at least in the domain of low injection rate and weak injection detuning where this project can be undertaken in a unified way. There are several reasons for this. First, simple expressions for the bifurcation curves in parameter space reveal the roles of the fixed laser parameters and make scaling laws readily apparent. Our analytical results thus provide efficient guidance to further numerical simulations or physical experiments. The present analytical study finds a second motivation in a previous application of an averaging method to the injected laser equations by De Jagher *et al.* [18]. The validity of these reduced equations has been questioned because their derivation rests on the assumption of harmonic relaxation oscillations. Consequently, there existed some doubt about the accuracy of the higher-order terms in the reduced system [66]. Our analysis shows that, in the limit of a large linewidth enhancement factor α , relaxation oscillations remain nearly harmonic away from the Hopf bifurcation point. Therefore, it can be expected that De Jagher's reduced equations are rigorously valid in that limit. Indeed, we find that, asymptotically for large α , they actually match our own averaged equations.

We first propose in Sec. 2.4.1 a derivation of the injected laser averaged equations which is valid for solutions of arbitrary amplitude and arbitrary α . The derivation is motivated by the small value of the damping rate of the laser relaxation oscillations and does not require the knowledge of any bifurcation point. These averaged equations provide a good starting point for a constructive bifurcation analysis. By investigating,

in Sec. 2.4.2 and 2.4.3, two distinct limits of these equations, we obtain simple formulae for the limit point, Hopf, and quasiperiodic bifurcation curves. On the basis of these expressions, we propose a mapping of the domains of qualitatively distinct dynamics in injection parameter space. Then, we investigate the strengths and weaknesses of our analysis by checking our conclusions against the numerical bifurcation diagrams of the original laser equations. We observe good agreement for extreme values of the relaxation oscillation damping rate and the linewidth enhancement factor α . We also show that, on a more qualitative level, the main dynamical features remain well captured by the averaged equations for more realistic values of the parameters. Our formulae thus have good predictive value.

The second problem under consideration, which is treated in Sec. 2.5, is the single-mode semiconductor laser subject to both optical injection and delayed feedback from a distant mirror. First, in Sec. 2.5.1, the perturbed Hamiltonian equations are averaged in the limit of small relaxation oscillation amplitude. In Sec. 2.5.2, we then briefly review several properties of the laser subject to weak optical feedback only. There, the concept of external cavity mode is introduced and defined as one of the possible feedback-induced regimes of steady monochromatic emission. A stability analysis of such states of the laser is presented. In practice, experiments have demonstrated that the laser does not remain on a single external cavity mode for an arbitrarily long time due to noise. If the delay time is too large, then the external cavity mode frequencies can be too close to each other, preventing their successful resolution in experimental spectra. Otherwise, the coexistence of several external cavity modes can be revealed as noise-induced mode hops, provided the feedback rate is not too high and relaxation oscillations do not get excited.

It is often the case, however, that the locking of an oscillator onto an external frequency contributes to a considerable reduction of phase noise, and thus of the oscillator's spectral linewidth. We may therefore expect that the injection of a small amount of monochromatic light into the laser cavity may reveal dynamical features of the laser subject to delayed feedback whose experimental observation is more difficult otherwise. This raises a theoretical question: in addition to phase locking of the external cavity modes, to what extent does optical injection modify the dynamics of the laser subject to optical feedback? This problem is addressed in Sec. 2.5.3. There, we perform a stability analysis of the external cavity modes when they are phase-locked onto the injected field. This leads us to identify a regime of square-wave-like optical phase oscillations. This behavior results from the interplay between injection and feedback, as it has no counterpart in the laser subject to either injection or feedback only. This new kind of oscillatory instability appears if the injected field is weak enough and its frequency is close to the frequency of an antinode (*i.e.*, unstable external cavity mode).

Finally, the main results of this chapter are summarized in Sec. 2.6.

2.2 The semiconductor laser rate equations

In this section, we briefly introduce the semiconductor laser rate equations which we then study. Detailed derivations can be found in [2, 95].

2.2.1 Field equation, material equation, and gain model

Any laser system basically consists of two essential components: a medium capable of amplifying light by stimulated emission, and a resonator constantly reflecting part of the light back through the medium. In semiconductor lasers, the resonator is a Fabry-Perot-type¹ cavity where the mirrors are provided by the interfaces between the semiconductor material and air. Successive amplifications of the electromagnetic field allow a superposition of standing waves with selected frequencies to build up inside the cavity. In general, several resonant cavity modes, with various spatial configurations, can be excited simultaneously. However, if the laser operates on a single mode, then the field $\vec{\mathcal{E}}(\vec{x}, t)$ inside the cavity can be characterized by a single, slowly-varying scalar variable $\mathcal{A}(t)$ as follows:

$$\vec{\mathcal{E}}(\vec{x}, t) = \mathcal{A}(t) \vec{u}(\vec{x}) \exp(i\omega_0 t) + \text{C.C.}, \quad (2.1)$$

where C.C. denotes the complex conjugate of the preceding term. Here, ω_0 represents a reference frequency close to the laser emission frequency, and \vec{u} accounts for the spatial configuration of the field. The complex amplitude \mathcal{A} keeps track of the optical phase and may provide corrections to the lasing frequency.

In most semiconductor lasers, the time evolution of the monomode field is described by the following equation² [121]:

$$\frac{d\mathcal{A}}{dt} = \frac{1}{2}(\mathcal{G} - \gamma_p)\mathcal{A} + \eta\mathcal{A}_i(t). \quad (2.2)$$

The complex optical gain \mathcal{G} characterizes the amplifier medium. Its real part, if positive, gives the rate of amplification due to stimulated emission. Its imaginary part is related to a shift in the refraction index, and introduces a correction to the lasing frequency. The rate constant γ_p describes photon losses, mainly due to the transmission of light through the semiconductor facets: typical values are $\gamma_p \sim 10^{12} \text{ s}^{-1}$. The term $\mathcal{A}_i(t)$, when present, represents the amplitude of an external optical field injected into the cavity with a frequency close to ω_0 . η is the injection rate.

In any laser system, spontaneous emission is unavoidable. Photons resulting from this process are created with a random phase and contribute to the total electromagnetic field in stochastic increments. The importance of noise effects is discussed in [95]. However the laser model is often approximated as a purely deterministic system for

¹where light travels back and forth between two mirrors.

²Cases exist where this description is inappropriate: Eq. (2.2) results from the adiabatic elimination of interband electric polarization. If the photon lifetime in the cavity becomes comparable to the intraband scattering time, then this elimination cannot be performed.

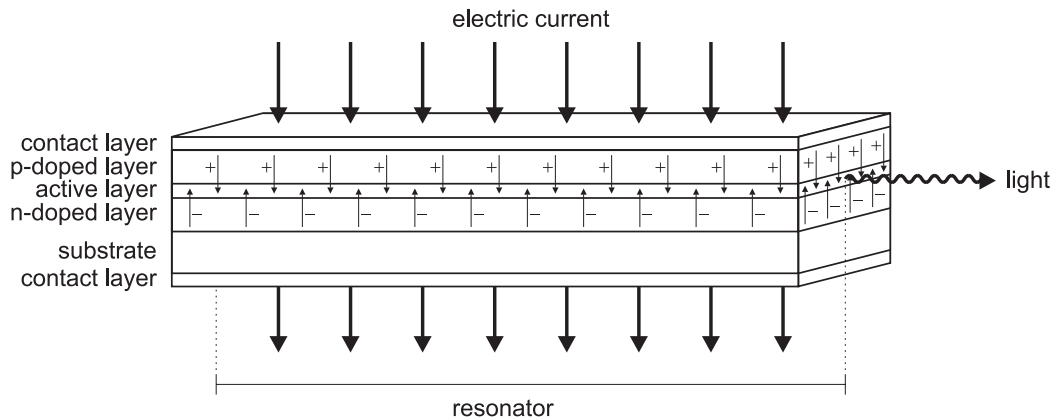


Figure 2.1: A laser diode. Electron-hole recombinations take place in the thin active layer. Electrons in the conduction band (indicated as $-$ symbols) are provided through the n-doped layer, and holes in the valence band (indicated as $+$ symbols) are provided through the p-doped layer, as a result of an applied bias current.

the sake of mathematical simplicity. This is the approach adopted here. We do not consider the case of a laser pumped near threshold, where noise effects are especially significant.

In a semiconductor, the atoms are arranged into a lattice that determines the possible quantum states of the electrons [121]. Electronic energies form continuous bands instead of discrete levels because electrons are delocalized across macroscopic distances in the lattice instead of being confined to a neighborhood of the individual atoms. Laser emission takes place as a result of transitions between two partially filled energy bands. In the ground state, the valence band is completely filled, and the conduction band is completely empty. The population inversion condition necessary for laser action is realized by constantly supplying new electrons in the conduction band and new “holes” (*i.e.*, electron lacunae) in the valence band. This is achieved by applying an electric current to a semiconductor diode consisting of a central active layer sandwiched between two doped cladding layers where charge carriers have opposite signs (see Fig. 2.1). With an appropriate bias current, electrons are conveyed through the n-doped layer and holes are conveyed through the p-doped layer towards the active layer, where electron-hole recombinations take place. The evolution in time of the number \mathcal{Z} of electron-hole pairs in the active layer can be modelled phenomenologically as follows [121]:

$$\frac{d\mathcal{Z}}{dt} = J(t) - \gamma_c \mathcal{Z} - \text{Re}(\mathcal{G}|\mathcal{A}|^2). \quad (2.3)$$

The source term $J(t)$ represents the bias current, measured as a number of electron-hole pairs per unit time. γ_c is the rate of carrier losses due to all processes other than stimulated emission (including spontaneous emission, nonradiative recombinations, and Auger processes): it is taken to be independent of \mathcal{Z} , which is justified because variations of \mathcal{Z} are usually weak. Typical values are $\gamma_c \sim 10^9 \text{ s}^{-1}$, so that $\gamma_c \ll \gamma_p$. The last

term in Eq. (2.3) describes electron-hole recombinations due to stimulated emission. The field intensity $|\mathcal{A}|^2$ is normalized in such a way as to represent the total number of photons inside the cavity³.

Obviously, the rate of stimulated emission processes increases with population inversion, so that the complex gain \mathcal{G} must depend on \mathcal{Z} . If variations of the carrier number are weak, then the gain can be approximated as a linear function of \mathcal{Z} :

$$\mathcal{G} \simeq \gamma_p + (1 + i\alpha)g \frac{\mathcal{Z} - \mathcal{Z}_0}{\mathcal{Z}_0}. \quad (2.4)$$

\mathcal{Z}_0 is defined as the number of electron-hole pairs at emission threshold, and represents the value of \mathcal{Z} such that light amplification exactly balances photon losses: for $\mathcal{Z} = \mathcal{Z}_0$, we have $\text{Re}(\mathcal{G}) = \gamma_p$. By choosing the reference frequency ω_0 to be exactly equal to the threshold emission frequency, we further have $\text{Im}(\mathcal{G}) = 0$ for $\mathcal{Z} = \mathcal{Z}_0$. The real constant g is the differential gain normalized to \mathcal{Z}_0 . It has the dimension of the inverse of a time, and its order of magnitude is comparable to γ_p . Thus, typical semiconductor lasers are characterized by two very distinct time scales, as follows:

$$\gamma_c \sim 10^9 \text{ s}^{-1} \ll \gamma_p \sim g \sim 10^{12} \text{ s}^{-1}. \quad (2.5)$$

Lasers verifying the above time scale ordering are called class B lasers. Finally, the α factor in Eq. (2.4) measures variations of the imaginary part of the gain relative to variations of the real part. This effect is very important in semiconductor lasers where α can reach values as high as 6–7. The reason for such large values is inherent to the properties of semiconductor materials. The electrons in the valence and conduction bands obey Fermi-Dirac distributions, as a result of which the electron-hole recombination energy is not fixed as in two-level systems, but obeys a probabilistic distribution that depends on the state of population inversion. The gain curve (*i.e.*, the set of values of $\text{Re}(\mathcal{G})$ as a function of the frequency of light) thus has a maximum whose location depends on the charge carrier number, and, by virtue of the Kramers-Kronig relations [134], this translates into significant variations of the refractive index as a function of \mathcal{Z} at frequency ω_0 . This effect represents the main contribution to the high value of α in semiconductors. In view of the field equation (2.2), this parameter also induces a coupling of the light intensity variations to the optical phase, so that noise-sustained relaxation oscillations (see Sec. 2.2.2) significantly contribute to the broadening of the laser linewidth. For this reason, α has been called the linewidth enhancement factor.

2.2.2 The free-running semiconductor laser

In the absence of an injected field, one has $\mathcal{A}_i(t) = 0$, and the rate equations (2.2)–(2.3) become invariant with respect to a constant phase shift of the electric field. Multiplying

³Other normalizations are possible: $|\mathcal{A}|^2$ is often taken to represent the number of photons in the thin active layer rather than in the whole cavity. In that case, the confinement factor Γ , which measures the amount of spatial overlap between the laser field and the active layer, appears explicitly either in the field equation (2.2) or in the material equation (2.3), depending on how the gain is defined.

both sides of the field equation (2.2) by \mathcal{A}^* and adding the resulting equation to its complex conjugate yields an equation for the intensity $|\mathcal{A}|^2$ that does not involve the optical phase anymore. Further assuming a constant pumping current ($J = J_{\text{dc}}$), we obtain the following rate equation model for a single-mode, dc-biased, free-running semiconductor laser:

$$\frac{d}{dt} |\mathcal{A}|^2 = g \frac{\mathcal{Z} - \mathcal{Z}_0}{\mathcal{Z}_0} |\mathcal{A}|^2, \quad (2.6a)$$

$$\frac{d\mathcal{Z}}{dt} = J_{\text{dc}} - \gamma_c \mathcal{Z} - \left[\gamma_p + g \frac{\mathcal{Z} - \mathcal{Z}_0}{\mathcal{Z}_0} \right] |\mathcal{A}|^2, \quad (2.6b)$$

where we have substituted the gain expression (2.4). This system involves only two coupled degrees of freedom as both equations are real. We immediately see that it possesses, for all values of the pumping current, a stationary solution characterized by the absence of laser emission:

$$|\mathcal{A}|_{\text{off}}^2 = 0, \quad (2.7a)$$

$$\mathcal{Z}_{\text{off}} = \frac{J_{\text{dc}}}{\gamma_c}. \quad (2.7b)$$

Also note, from the intensity equation (2.6a), that this “off” state loses stability if $\mathcal{Z} > \mathcal{Z}_0$. In view of the expression (2.7b) for \mathcal{Z}_{off} , this condition means that the pumping current J_{dc} is larger than a threshold value J_0 given by

$$J_0 \equiv \gamma_c \mathcal{Z}_0. \quad (2.8)$$

If $J_{\text{dc}} > J_0$, then the laser can sustain steady emission, and the laser equations possess a second stationary solution characterized by $|\mathcal{A}|^2 \neq 0$:

$$|\mathcal{A}|_{\text{on}}^2 = \frac{J_{\text{dc}} - J_0}{\gamma_p}, \quad (2.9a)$$

$$\mathcal{Z}_{\text{on}} = \mathcal{Z}_0. \quad (2.9b)$$

The two stationary solutions are represented in Fig. 2.2 as a function of the pumping current.

When the laser operates close enough to the steady “on” state, its dynamics is validly described by the rate equations linearized around the stationary solution (2.9). The behavior of the laser as it approaches the steady state is then characterized by the eigenvalues σ_{\pm} of the linearized system, whose computation presents no particular difficulty. We take advantage of the small value of γ_c/g : see (2.5). We also assume that the laser is pumped a few times above threshold so that $(J_{\text{dc}} - J_0)/J_0 = O(1)$. Then, the eigenvalues approximate as $\sigma_{\pm} \simeq \gamma_r \pm i\omega_r$, where

$$\gamma_r = -\frac{\gamma_c}{2} \left(1 + \frac{g}{\gamma_p} \frac{J_{\text{dc}} - J_0}{J_0} \right), \quad (2.10a)$$

$$\omega_r = \sqrt{g\gamma_c \frac{J_{\text{dc}} - J_0}{J_0}}. \quad (2.10b)$$

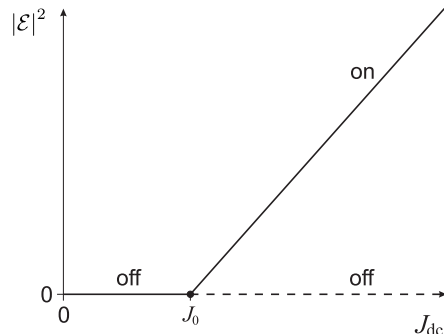


Figure 2.2: The laser on and off steady states as a function of the pumping current. Solid lines indicate stable solutions, while dashed lines represent unstable ones.

The fact that the eigenvalues possess a nonzero imaginary part and a negative real part reveals that the laser reaches the steady state through damped oscillations of the light intensity and carrier density, called relaxation oscillations. Given the orders of magnitude (2.5), one has typically $\omega_r \sim 10^{10}\text{--}10^{11}\text{ s}^{-1}$ and $\gamma_r \sim 10^9\text{ s}^{-1}$, so that the damping rate γ_r is slow in comparison to the relaxation oscillation frequency ω_r , as is typical in class B lasers. This makes such lasers weakly stable systems, which can therefore exhibit a high sensitivity to weak external perturbations. The tendency of the steady state to loose stability under such conditions is analyzed in more detail in this chapter and the next one.

The expression (2.9b) of the on-state value of the number of electron-hole pairs is independent of the bias current and is always given by \mathcal{Z}_0 . This is a consequence of having approximated the gain as a function of the charge carrier number only. A more realistic model would account for gain saturation effects [121], as a result of which the lasing condition $\text{Re}(\mathcal{G}) = \gamma_p$ requires a larger population inversion in order to support larger emission intensities. When such effects need to be taken into account, the gain expression (2.4) can be generalized as follows:

$$\mathcal{G} \simeq \gamma_p + (1 + i\alpha)g \frac{\mathcal{Z} - \mathcal{Z}_0}{\mathcal{Z}_0} + (1 + i\alpha')g' \frac{|\mathcal{A}_{\text{on}}|^2 - |\mathcal{A}|^2}{|\mathcal{A}_{\text{on}}|^2}, \quad (2.11)$$

where g' is the gain saturation coefficient, and α' describes changes of the refractive index due to intensity variations [106]. With the above redefinition of the complex gain, the expression of the on-state intensity as a function of the fixed parameters is unchanged.

2.2.3 Dimensionless rate equations

The theoretical investigation of semiconductor laser dynamics through the rate equation model is greatly simplified by its reformulation in terms of dimensionless parameters. The following choice of a new time variable s and a new complex field amplitude \mathcal{E}

given by

$$\mathcal{E} \equiv \frac{\mathcal{A}}{|\mathcal{A}|_{\text{on}}}, \quad s \equiv \omega_r t, \quad (2.12)$$

is motivated by our analysis of the free-running semiconductor laser, in Sec. 2.2.2. Furthermore, we express the time-dependent pumping current as:

$$J(t) = J_{\text{dc}} + (J_{\text{dc}} - J_0) M(s), \quad (2.13)$$

where $M(s)$ represents a modulation of the pumping current, measured relatively to the offset of its dc component above threshold. With these definitions and the gain expression (2.11), the laser rate equations (2.2)–(2.3) become:

$$\frac{d\mathcal{E}}{ds} = \frac{1}{2} [(1 + i\alpha)Z - (1 + i\alpha')\beta (|\mathcal{E}|^2 - 1)] \mathcal{E} + \mathcal{E}_i(s), \quad (2.14a)$$

$$\frac{dZ}{ds} = M(s) - [1 + \varepsilon p (Z - \beta |\mathcal{E}|^2)] (|\mathcal{E}|^2 - 1) - \varepsilon Z, \quad (2.14b)$$

where the new variables and parameters

$$\begin{aligned} Z &\equiv \frac{g}{\omega_r} \frac{\mathcal{Z} - \mathcal{Z}_0}{\mathcal{Z}_0}, & \mathcal{E}_i(s) &\equiv \frac{\eta \mathcal{A}_i(t)}{\omega_r |\mathcal{A}|_{\text{on}}}, \\ \beta &\equiv \frac{g'}{\omega_r}, & \varepsilon &\equiv \frac{2|\gamma_r|}{\omega_r}, & p &\equiv \frac{J_{\text{dc}} - J_0}{\frac{\gamma_p}{g} J_0 + J_{\text{dc}} - J_0} \end{aligned} \quad (2.15)$$

have been chosen so that Eqs. (2.14) have the simplest form. Note that $0 \leq p < 1$ if $J_{\text{dc}} \geq J_0$, with $p \simeq 0$ if the laser is pumped close to threshold, and $p \simeq 1$ if it is pumped well above threshold. Given the relation (2.5) between the time scales in a class B laser, the order of magnitude of the loss parameter ε is typically:

$$\varepsilon \sim 10^{-2} \text{ to } 10^{-1}, \quad (2.16)$$

which motivates an asymptotic analysis of the model equations in the limit of a small values of ε . The dimensionless rate equations (2.14) are the starting point of Chapters 2 and 3. The gain saturation coefficient β and the pump modulation $M(s)$ will be set to zero until Chapter 3, where we need to take such effects into account.

2.3 Perturbed Hamiltonian problem

In this chapter, we make use of the dimensionless rate equations (2.14) in order to determine the effect of a small amount of coherent light injected into the laser cavity. Specifically, we assume that the injected field $\mathcal{E}_i(s)$ is a small, $O(\varepsilon)$ quantity, and introduce:

$$\mathcal{E}_i(s) = \varepsilon e_i(s). \quad (2.17)$$

It is then advantageous to decompose the complex amplitude \mathcal{E} as

$$\mathcal{E} = \exp\left(\frac{Y}{2} + i\phi\right), \quad (2.18)$$

where ϕ is the optical phase and Y measures the light intensity on a logarithmic scale, both variables being real quantities. In terms of the definitions (2.17) and (2.18), neglecting the gain saturation term, and setting the pump modulation term $M(s)$ to zero, Eqs. (2.14) are rewritten as:

$$\frac{dY}{ds} = Z + 2\varepsilon \operatorname{Re} \left[e_i(s) \exp\left(-\frac{Y}{2} - i\phi\right) \right], \quad (2.19a)$$

$$\frac{d\phi}{ds} = \frac{1}{2}\alpha Z + \varepsilon \operatorname{Im} \left[e_i(s) \exp\left(-\frac{Y}{2} - i\phi\right) \right], \quad (2.19b)$$

$$\frac{dZ}{ds} = -(1 + \varepsilon p Z) [\exp(Y) - 1] - \varepsilon Z. \quad (2.19c)$$

Averaging techniques for strongly nonlinear oscillators have been developed for second order differential equations exhibiting nearly conservative oscillations. In order to apply these methods, we reformulate the laser rate equations in a form where a second order Hamiltonian problem appears. This reformulation is not difficult as Eqs. (2.19) are known, in the limit $\varepsilon \rightarrow 0$, to be equivalent to a second order differential equation describing the motion of a particle in a Toda potential [90]. Indeed, in that limit, they admit two first integrals, which are:

$$H \equiv \frac{1}{2} \left(\frac{dY}{ds} \right)^2 + \mathcal{V}(Y), \quad (2.20a)$$

$$\Phi \equiv \phi - \frac{1}{2}\alpha Y, \quad (2.20b)$$

where

$$\mathcal{V}(Y) \equiv \exp(Y) - (1 + Y). \quad (2.21)$$

Note that H is defined as a positive quantity, because $\mathcal{V}(Y) \geq 0$ for all Y . In the limit $\varepsilon \rightarrow 0$, the relaxation oscillations become undamped, and Eq. (2.20a) expresses the conservation of the oscillation energy. It defines closed curves in the $(Y, dY/ds)$ plane (see Fig. 2.3) : Y oscillates periodically between the two roots $Y_m(H)$ and $Y_M(H)$ of the equation $H = \mathcal{V}(Y)$. Eq. (2.20b) is a redefinition of the optical phase with the oscillatory contribution removed. Eq. (2.20a) can be solved by quadrature over a time interval of one oscillation period:

$$s - s_M = \int_{Y_M(H)}^Y \frac{dY'}{\pm \sqrt{2[H - \mathcal{V}(Y')]}}, \quad (2.22)$$

where s_M is the instant where the intensity reaches its maximum value in that period, and the symbol \pm denotes the sign of dY/ds . The relaxation oscillation frequency is

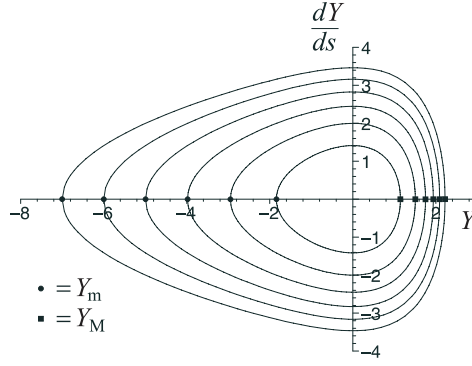


Figure 2.3: Phase plane solution of Y for fixed values of the energy H . Each curve corresponds to a different value of H going from $H = 1$ (innermost curve) to $H = 6$ (outermost curve) and changing by integer steps.

given for an arbitrary energy by

$$\Omega_r(H) \equiv \pi \left(\int_{Y_m(H)}^{Y_M(H)} \frac{dY}{\sqrt{2[H - \mathcal{V}(Y)]}} \right)^{-1}, \quad (2.23)$$

which tends towards unity for $H \rightarrow 0$, as expected in our system of units. We may therefore define the relaxation oscillation phase as:

$$\theta \equiv \Omega_r(H) \int_{Y_M(H)}^Y \frac{dY'}{\pm \sqrt{2[H - \mathcal{V}(Y')]}} \quad (2.24)$$

where the identity holds modulo 2π .

If ε is small but distinct from zero, then H , Φ , and $\theta - \Omega_r(H)s$ become functions of time. We now seek equations governing their evolution. The computation of the time derivatives of H and Φ from Eqs. (2.19) is straightforward. To leading order in ε , we obtain:

$$\begin{aligned} \frac{dH}{ds} = \varepsilon \frac{dY}{ds} & \left\{ -\{1 + p[\exp(Y) - 1]\} \frac{dY}{ds} + \text{Re} \left[\left(2 \frac{de_i}{ds}(s) - (1 + i\alpha) \frac{dY}{ds} e_i(s) \right) \right. \right. \\ & \left. \left. \exp \left(-(1 + i\alpha) \frac{Y}{2} - i\Phi \right) \right] \right\} + O(\varepsilon^2), \end{aligned} \quad (2.25a)$$

$$\frac{d\Phi}{ds} = -\varepsilon \text{Re} \left[(i + \alpha) e_i(s) \exp \left(-(1 + i\alpha) \frac{Y}{2} - i\Phi \right) \right] + O(\varepsilon^2). \quad (2.25b)$$

The computation of $d\theta/ds$ deserves more details. First, the definition (2.24) can be inverted formally to yield Y as a function of θ and H :

$$Y = y(\theta, H). \quad (2.26)$$

$y(\theta, H)$ is defined as the even, 2π -periodic function of θ such that $Y = y(\theta, H)$ solves Eq. (2.24). Substituting the above expression back into Eq. (2.24), taking the partial

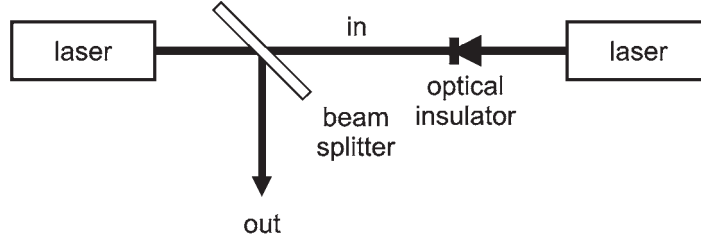


Figure 2.4: A simplified block-diagram of a semiconductor laser subject to optical injection from another laser.

derivative with respect to θ , and isolating H in the right-hand side gives:

$$H = \frac{\Omega_r(H)^2}{2} \left(\frac{\partial y}{\partial \theta}(\theta, H) \right)^2 + \mathcal{V}(y(\theta, H)), \quad (2.27)$$

from which, comparing with the definition (2.20a) of the energy, we deduce an expression of the time derivative dY/ds in terms of θ and H :

$$\frac{dY}{ds} = \Omega_r(H) \frac{\partial y}{\partial \theta}(\theta, H). \quad (2.28)$$

We now take the time derivative of Eq. (2.26), using the chain rule:

$$\frac{dY}{ds} = \frac{\partial y}{\partial \theta}(\theta, H) \frac{d\theta}{ds} + \frac{\partial y}{\partial H}(\theta, H) \frac{dH}{ds},$$

where we then substitute Eq. (2.28) and solve for $d\theta/ds$:

$$\frac{d\theta}{ds} = \Omega_r(H) - \frac{\frac{\partial y}{\partial H}(\theta, H)}{\frac{\partial y}{\partial \theta}(\theta, H)} \frac{dH}{ds}. \quad (2.29)$$

Note that, in view of the energy equation (2.25a), the second term in the right-hand side is an $O(\varepsilon)$ quantity. Eqs. (2.25) and (2.29) together provide a reformulation of the rate equations in terms of the variables H , Φ , and θ .

2.4 Laser subject to optical injection

In order to further progress in the analysis, we consider particular forms of the injected field e_i . One case of interest is the case of optical injection: a beam of monochromatic light from another laser is injected into the laser cavity. The coupling is unidirectional, so that the lasers are arranged in a master-slave configuration (see Fig. 2.4).

2.4.1 Averaged equations

In addition to the weak injection condition (2.17), we assume that the offset of the master laser frequency with respect to the slave laser frequency in free-running operation is small in comparison with the relaxation frequency. Specifically, we assume that this detuning is an $O(\varepsilon)$ quantity, which we denote $\varepsilon\delta$. The injected field is then expressed as:

$$e_i(s) = \lambda \exp(i\varepsilon\delta s), \quad (2.30)$$

and the optical phase Φ is redefined as:

$$\Phi = \Psi + \varepsilon\delta s, \quad (2.31)$$

that is, Ψ represents the phase of the slave laser with respect to the master laser. Substituting these expressions into Eqs. (2.25), and using the relations (2.26) and (2.28) yields:

$$\begin{aligned} \frac{dH}{ds} &= -\varepsilon\Omega_r(H)^2 \{ \mathcal{F}_1(\theta) + p\mathcal{F}_3(\theta) \\ &\quad + \lambda \operatorname{Re} [(1 + i\alpha)\mathcal{F}_1(\theta)\mathcal{F}_2(\theta) \exp(-i\Psi)] \} + O(\varepsilon^2), \end{aligned} \quad (2.32a)$$

$$\frac{d\Psi}{ds} = -\varepsilon \{ \delta + \lambda \operatorname{Re} [(i + \alpha)\mathcal{F}_2(\theta) \exp(-i\Psi)] \} + O(\varepsilon^2), \quad (2.32b)$$

where

$$\mathcal{F}_1(\theta) \equiv \left(\frac{\partial y}{\partial \theta}(\theta, H) \right)^2, \quad (2.33a)$$

$$\mathcal{F}_2(\theta) \equiv \exp \left[-(1 + i\alpha) \frac{y(\theta, H)}{2} \right], \quad (2.33b)$$

$$\mathcal{F}_3(\theta) \equiv \left(\frac{\partial y}{\partial \theta}(\theta, H) \right)^2 \{ \exp[y(\theta, H)] - 1 \}. \quad (2.33c)$$

In Eqs. (2.29) and (2.32), the fast time variations result from the dependence in θ exclusively. In order to obtain leading-order approximations of H , Φ and θ , we average out the fast variations in the right-hand sides by integrating over one oscillation period in θ . Note that the second term in the right-hand side of Eq. (2.29) averages to zero because it is an odd function of θ . Likewise, \mathcal{F}_3 averages to zero because it is the derivative of a periodic function of θ :

$$\begin{aligned} \mathcal{F}_3(\theta) &= \frac{\partial y}{\partial \theta}(\theta, H) \frac{\partial}{\partial \theta} \mathcal{V}(y(\theta, H)) = \frac{\partial y}{\partial \theta}(\theta, H) \frac{\partial}{\partial \theta} \left[H - \frac{\Omega_r(H)^2}{2} \left(\frac{\partial y}{\partial \theta}(\theta, H) \right)^2 \right] \\ &= -\Omega_r(H)^2 \left(\frac{\partial y}{\partial \theta}(\theta, H) \right)^2 \frac{\partial^2 y}{\partial \theta^2}(\theta, H) = \frac{\partial}{\partial \theta} \left[-\frac{\Omega_r(H)^2}{3} \left(\frac{\partial y}{\partial \theta}(\theta, H) \right)^3 \right] \end{aligned} \quad (2.34)$$

Therefore, using the same symbols for the dynamical variables as for their leading-order approximations for the sake of notation simplicity, the averaged equations read:

$$\frac{dH}{ds} = -\varepsilon \Omega_r(H)^2 \{ \mathcal{I}_1 + \lambda \operatorname{Re} [(1 + i\alpha) \mathcal{I}_{12} \exp(-i\Psi)] \} + O(\varepsilon^2), \quad (2.35a)$$

$$\frac{d\Psi}{ds} = -\varepsilon \{ \delta + \lambda \operatorname{Re} [(i + \alpha) \mathcal{I}_2 \exp(-i\Psi)] \} + O(\varepsilon^2), \quad (2.35b)$$

$$\frac{d\theta}{ds} = \Omega_r(H) + O(\varepsilon^2), \quad (2.35c)$$

where

$$\mathcal{I}_1 \equiv \frac{1}{2\pi} \oint d\theta \mathcal{F}_1(\theta), \quad \mathcal{I}_2 \equiv \frac{1}{2\pi} \oint d\theta \mathcal{F}_2(\theta), \quad \mathcal{I}_{12} \equiv \frac{1}{2\pi} \oint d\theta \mathcal{F}_1(\theta) \mathcal{F}_2(\theta). \quad (2.36)$$

Eqs. (2.35) do not depend on p anymore. Note, from Eq. (2.35c), that there is no $O(\varepsilon)$ correction to the relaxation frequency. Furthermore, Eqs. (2.35a) and (2.35b) form a closed system, while the relaxation oscillation phase θ follows passively the variations of H . This reveals the existence, under the condition of a sufficiently weak optical injection, and if the two class B laser time scales are sufficiently well separated, of a dynamical regime where the injected semiconductor laser is essentially a bidimensional system. As a consequence, in that regime, the system cannot be expected to exhibit more complex behavior than quasiperiodicity, as the light intensity cannot display more than two independent frequencies: the first one being the relaxation oscillation frequency Ω_r , and the second one being either the beat frequency between the master and slave lasers given by the time-average value of $d\Psi/ds$, in the case of a running-phase solution, or the frequency that may result from a limit cycle in the (Ψ, H) plane, in the case of a bounded-phase solution. However, the averaged-equation analysis breaks down if the optical injection is strong enough so that it cannot be treated as a perturbation of the free-running laser anymore. In particular, optically injected lasers are known to exhibit period-doubling cascades, chaotic dynamics, or even period-tripled oscillations for moderately high injection rates, as is illustrated in Chapter 3. Nevertheless, the averaged equations provide a good starting point for the analysis of the simplest phenomena associated to the perturbative regime.

Eqs. (2.35) can be solved numerically provided the functions $\Omega_r(H)$ and $y(\theta, H)$ are first sampled by discretizing and solving Eq. (2.20a) for different values of the energy H . However, in the remaining of this chapter, we aim at the analytical construction of bifurcation diagrams, a task for which the averaged equations are too unwieldy in their present form, because of the requirement of having to work with numerically sampled quantities. That difficulty may be resolved if we forgo working with equations valid for arbitrarily high values of the relaxation oscillation energy. We may then compute power series expansions of the functions $\Omega_r(H)$ and $y(\theta, H)$ for small H using a simple Poincaré-Linstedt method. Writing

$$H = \frac{1}{2} A^2, \quad (2.37)$$

we expand:

$$\Omega_r(A) = 1 + \Omega_1 A + O(A^2), \quad (2.38a)$$

$$y(\theta, A) = y_1(\theta)A + y_2(\theta)A^2 + O(A^3). \quad (2.38b)$$

Introducing $H = \frac{1}{2}A^2$, $Y = y(\theta, A)$, and $s = \theta/\Omega_r(A)$ in Eq. (2.20a) with the above expansions and collecting powers of A leads to a hierarchy of linear equations for the successive components y_1, y_2, \dots of $y(\theta, A)$:

$$\frac{1}{2} = \frac{1}{2} \left(\frac{\partial y_1}{\partial \theta}(\theta) \right)^2 + \frac{y_1(\theta)^2}{2}, \quad (2.39a)$$

$$0 = \Omega_1 \left(\frac{\partial y_1}{\partial \theta}(\theta) \right)^2 + \frac{\partial y_1}{\partial \theta}(\theta) \frac{\partial y_2}{\partial \theta}(\theta) + y_1(\theta)y_2(\theta) + \frac{y_1(\theta)^3}{6}, \quad (2.39b)$$

⋮

whose solution up to second highest order is

$$y_1(\theta) = \cos(\theta), \quad y_2(\theta) = -\frac{1}{4} + \frac{1}{12} \cos(2\theta), \quad (2.40)$$

where we had to impose the solvability condition

$$\Omega_1 = 0 \quad (2.41)$$

in order for Eq. (2.39b) to admit a periodic solution. These expressions are used in Sections 2.4.2 and 2.4.3 in order to investigate two distinct limits of the averaged equations in the case of low relaxation oscillation energy, depending on how the linewidth enhancement factor α and the energy scale with respect to each other. These two limits lead to distinct asymptotic approximations of the integrals \mathcal{I}_1 , \mathcal{I}_2 , and \mathcal{I}_{12} .

2.4.2 Low-amplitude limit

The first limit considered is the limit for small A , but α arbitrary. This limit is asymptotically valid as long as relaxation oscillations are damped or remain weak. Using the expansion (2.38), the computation of contributions to the averaged equations (2.35) up to arbitrary order in A is fairly straightforward, as it is simply a matter of evaluating the integrals \mathcal{I}_1 , \mathcal{I}_2 , and \mathcal{I}_{12} up to that order. Here, we retain only leading-order contributions in A . One has $\Omega_r(A) = 1 + o(1)$, $\mathcal{I}_1 = \mathcal{I}_{12} = \frac{1}{2}A^2 + o(A^2)$, and $\mathcal{I}_2 = 1 + o(1)$, so that the averaged equations (2.35a)–(2.35b) simplify to:

$$\frac{dA}{d\tau} = -\frac{1}{2}A \left[1 + \lambda\sqrt{\alpha^2 + 1} \sin[\Psi + \operatorname{arccot}(\alpha)] \right], \quad (2.42a)$$

$$\frac{d\Psi}{d\tau} = - \left[\delta + \lambda\sqrt{\alpha^2 + 1} \cos[\Psi - \operatorname{arccot}(\alpha)] \right], \quad (2.42b)$$

where we have set $\tau = \varepsilon s$.

The phase equation (2.42b) is the Adler equation [136], which can be solved exactly. Depending on the values of the injection parameters λ and δ , it admits two kinds of solutions. First, it may possess a pair of constant-phase solutions (one stable and one unstable), corresponding to a regime of steady emission where the frequency of the slave laser is locked onto the master laser's. Second, if the detuning δ is large enough in magnitude so that the right-hand side of Eq. (2.42b) never vanishes, then it admits a running-phase solution, corresponding to a regime where the frequency of the slave laser is merely pulled towards the master laser's, but where no locking is achieved. The boundary between the two regimes in parameter space corresponds to a limit point bifurcation, where the stable and unstable locked states collide and cease to exist beyond the locking domain. More precisely, it is a homoclinic-limit point bifurcation, as the destruction of the two steady states is accompanied by the creation of the periodic running-phase solution whose period is infinite at the bifurcation. An analytical expression for the locus of the limit points in parameter space is obtained by requiring that the phase equation (2.42b) possesses a constant solution of multiplicity two. In that case, the right-hand side of (2.42b) and its derivative with respect to Ψ must vanish simultaneously:

$$\delta = -\lambda\sqrt{\alpha^2 + 1} \cos[\Psi - \operatorname{arccot}(\alpha)], \quad (2.43)$$

$$0 = \lambda\sqrt{\alpha^2 + 1} \sin[\Psi - \operatorname{arccot}(\alpha)]. \quad (2.44)$$

Squaring and summing the two above equations, and combining the trigonometric functions, the resulting equation gives the well-known expression for the boundaries of the locking range:

$$\lambda = \lambda_{\text{LP}}(\delta) \equiv \frac{|\delta|}{\sqrt{\alpha^2 + 1}}. \quad (2.45)$$

The curve in injection parameter space corresponding to the above expression is represented in Fig. 2.5, together with all other bifurcations curves constructed in this section. Locking is achieved if $\lambda > \lambda_{\text{LP}}(\delta)$, that is, if the injected signal is intense enough, or if it is sufficiently well-tuned with the free-running laser frequency. In this case, the two stationary phase values are the roots of Eq. (2.43), modulo 2π . For $\lambda < \lambda_{\text{LP}}(\delta)$, the running-phase solution of Eq. (2.42b) is:

$$\Psi = \operatorname{arccot}(\alpha) - 2 \arctan \left[\sqrt{\frac{\delta + \lambda\sqrt{\alpha^2 + 1}}{\delta - \lambda\sqrt{\alpha^2 + 1}}} \tan \left(\frac{\sqrt{\delta^2 - \lambda^2(\alpha^2 + 1)}}{2} \tau \right) \right]. \quad (2.46)$$

In addition to its ability to induce phase-locking, the injection of a small amount of light from the master laser is also capable of destabilizing the state of steady emission, by counterbalancing the damping of relaxation oscillations. The laser response then exhibits sustained intensity oscillations. The oscillation threshold can be determined from a stability analysis of the invariant manifold characterized by $A = 0$, which can be performed very simply from the amplitude equation (2.42a). For A different from

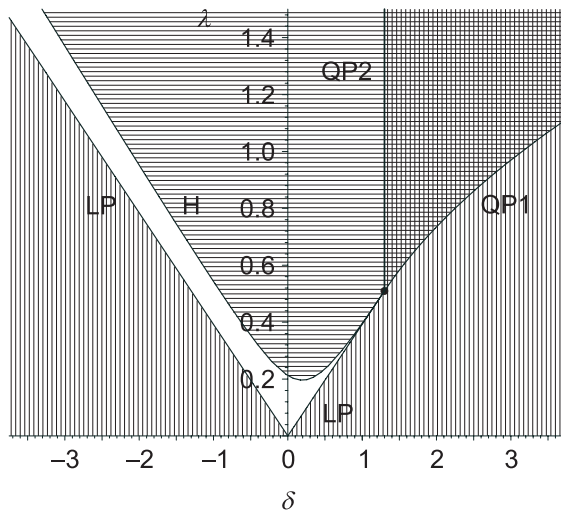


Figure 2.5: Map of the dynamics of the laser subject to weak optical injection. The limit point (LP), Hopf (H), and quasiperiodic (QP1, QP2) bifurcations are represented in injection parameter space, for $\alpha = 5$. The four curves are determined using the expressions (2.45), (2.48), (2.51), and (2.70). They all coalesce at the codimension-2 point $\delta = \delta^*$, $\lambda = \lambda^*$. The white, vertical-hatched, horizontal-hatched, and cross-hatched regions correspond, respectively, to steady phase locking, periodic running-phase dynamics, periodic sustained relaxation oscillations, and quasiperiodic dynamics.

(but arbitrarily close to) zero, it can be rewritten as:

$$\frac{d}{d\tau} \ln(A) = -\frac{1}{2} \left[1 + \lambda \sqrt{\alpha^2 + 1} \sin[\Psi + \operatorname{arccot}(\alpha)] \right], \quad (2.47)$$

therefore the $A = 0$ manifold is unstable if and only if the time-average of the right-hand side of the above equation is positive. The stability boundary is the locus of the points in parameter space where this quantity vanishes. The cases of constant and running phase must be analyzed separately. First, for constant phase, the transition to oscillatory dynamics is characterized by the appearance of only one frequency: the relaxation oscillation frequency. Therefore, the transition is a Hopf bifurcation. The stability boundary is obtained by requiring that the right-hand side of Eq. (2.47) vanishes for $\Psi = \Psi_s$, where Ψ_s solves the stationary phase equation (2.43). Eliminating the trigonometric functions between Eq. (2.47) with $\frac{d}{d\tau} \ln(A) = 0$ and Eq. (2.43) and solving for λ yields the locus of Hopf bifurcation points:

$$\lambda = \lambda_H(\delta) \equiv \frac{\sqrt{(\delta - \alpha)^2 + (\alpha\delta - 1)^2}}{\alpha^2 - 1}. \quad (2.48)$$

If $\lambda \leq \lambda_H(\delta)$, then the injected field is not strong enough to render the right-hand side of Eq. (2.47) positive, and the laser emits with a constant intensity. On the other hand, if $\lambda > \lambda_H(\delta)$, then the destabilizing effect takes place and periodic intensity oscillations

appear (see Fig. 2.5). An analysis of the expressions $\lambda_{\text{LP}}(\delta)$ and $\lambda_{\text{H}}(\delta)$ reveals that the limit point and Hopf curves are tangent at

$$\delta = \delta^* \equiv \frac{\alpha^2 + 1}{2\alpha}, \quad \lambda = \lambda^* \equiv \frac{\sqrt{\alpha^2 + 1}}{2\alpha}. \quad (2.49)$$

It turns out that only the part of the Hopf curve delimited by $\delta \leq \delta^*$ is physically relevant, as for higher values of δ , the bifurcation occurs on the unstable root of the phase equation (2.42b) rather than on the stable one, rendering the phenomenon unobservable.

The two bifurcation curves presented so far (the limit point and Hopf curves) have been obtained from a simple steady state stability analysis, and are equivalent to those presented in [121]. Now, the computation of the oscillation threshold in the running-phase case requires a stability analysis of a time-dependent solution. It is achieved by carrying out the computation and analyzing the sign of the average value of the right-hand side of Eq. (2.47), which is now time-dependent. The locus of the points in parameter space where this quantity vanishes now corresponds to a quasiperiodic, or torus bifurcation, as it is characterized by two distinct frequencies: the relaxation frequency, and the beat frequency between the master and slave lasers. The calculation involves an integration over one period, after substitution of the expression (2.46) for the running-phase solution. The variable change

$$v \equiv \tan \left(\frac{\sqrt{\delta^2 - \lambda^2(\alpha^2 + 1)}}{2} \tau \right) \quad (2.50)$$

is useful as it turns the integrand into a rational function. After calculation, it is found that the quasiperiodic bifurcation points are given by:

$$\delta \geq \delta^*, \quad \lambda = \lambda_{\text{QP1}}(\delta) \equiv \sqrt{\frac{\delta}{\alpha} - \frac{\alpha^2 + 1}{4\alpha^2}}. \quad (2.51)$$

These expressions are equivalent to those first derived in [110]. For $\lambda \leq \lambda_{\text{QP1}}(\delta)$, the injected field is not strong enough to destabilize the periodic running-phase solution (2.46). On the other hand, a higher injection rate is sufficient to induce the appearance of sustained relaxation oscillations superimposed over the running-phase dynamics, leading to quasiperiodic behavior, as it was first demonstrated in [110]. Note that the quasiperiodic bifurcation curve $\lambda = \lambda_{\text{QP1}}$ is also tangent to the limit point curve $\lambda = \lambda_{\text{LP}}$ at $\delta = \delta^*$, $\lambda = \lambda^*$ so that, in some sense, it can be interpreted as the continuation of the Hopf bifurcation curve $\lambda = \lambda_{\text{H}}$ into the region of running-phase dynamics (see Fig. 2.5).

2.4.3 Large- α limit

Eqs. (2.42) represent the small amplitude limit of our averaged evolution equations. They lead to analytical expressions of three bifurcation points, namely: the homoclinic-limit point bifurcation (2.45) above which locking occurs, the Hopf bifurcation (2.48)

from the steady locked state to sustained relaxation oscillations, and the quasiperiodic bifurcation (2.51) appearing before locking for detuning values larger than δ^* . All three bifurcation curves meet at the codimension-2 point $\delta = \delta^*$, $\lambda = \lambda^*$ and share the property of involving solutions exhibiting no or vanishingly weak relaxation oscillations. If we want to go further in the analysis and determine what happens beyond the onset of sustained relaxation oscillations at $\lambda = \lambda_H(\delta)$ or $\lambda = \lambda_{QP1}(\delta)$, then we must abandon the approximation of a linear equation in the oscillation amplitude A . Such an analysis is expected to reveal, in particular, the existence of another quasiperiodic bifurcation curve extending from the codimension-2 point into the domain of sustained relaxation oscillations, and separating the domain of periodicity from the domain of quasiperiodicity. This calls for the investigation of another limit of the averaged equations (2.35a) and (2.35b). Typical values of the linewidth enhancement factor α are 3 to 5, although values as high as 6 to 7 are sometimes observed in experiments. This motivates an analysis in the limit of large α . Specifically, we set

$$A \equiv 2\alpha^{-1}a, \quad (2.52)$$

and seek a limit of Eqs. (2.35a) and (2.35b) valid to second leading order in α^{-1} . As is demonstrated below, second leading order terms are needed because they determine the stability of the solutions. Anticipating the existence of a second quasiperiodic bifurcation curve emerging from $\delta = \delta^*$, $\lambda = \lambda^*$, we define, for convenience:

$$\bar{\delta} \equiv \frac{\delta}{2\delta^*}, \quad \bar{\lambda} \equiv \frac{\lambda}{2\lambda^*}, \quad \bar{\tau} \equiv 2\delta^*\tau. \quad (2.53)$$

In view of the expressions (2.49), one has, for large α :

$$\delta = \alpha\bar{\delta} + O(\alpha^{-1}), \quad \lambda = \lambda + O(\alpha^{-2}), \quad \tau = \alpha^{-1}\bar{\tau} + O(\alpha^{-3}). \quad (2.54)$$

Note, from the expansion (2.38b) of $y(\theta, A)$ and the definition (2.33b) of \mathcal{F}_2 , that the argument of the exponential in \mathcal{F}_2 cannot be considered small anymore in that limit. The evaluation of the integrals \mathcal{I}_{12} and \mathcal{I}_2 therefore involves Bessel functions with the scaled amplitude a as their argument, $J_n(a)$, $n = 0, 1, 2, \dots$ (see [70] or any textbook about special functions). We obtain:

$$\mathcal{I}_1 = 2\alpha^{-2}a^2 + O(\alpha^{-4}), \quad (2.55a)$$

$$\mathcal{I}_{12} = 4\alpha^{-2}a J_1(a) + \alpha^{-3}i \left[-\frac{8}{3}a^2 J_0(a) + \left(\frac{16}{3}a + \frac{4}{3}a^3 \right) J_1(a) \right] + O(\alpha^{-4}), \quad (2.55b)$$

$$\mathcal{I}_2 = J_0(a) + \alpha^{-1}i \left[\frac{1}{3}a^2 J_0(a) + \frac{4}{3}a J_1(a) \right] + O(\alpha^{-2}), \quad (2.55c)$$

where we have used the identities

$$\frac{1}{2\pi} \oint d\theta \cos(n\theta) \exp[-ia \cos(\theta)] = (-i)^n J_n(a), \quad (2.56)$$

$$J_{n-1}(a) + J_{n+1}(a) = \frac{2n}{a} J_n(a). \quad (2.57)$$

Substituting the scaling (2.54) and the expressions (2.55) for the integrals into the averaged equations (2.35) yields:

$$\frac{da}{d\bar{\tau}} = -\frac{1}{2}\alpha^{-1}a - \bar{\lambda} [J_1(a) \sin(\Psi) + \alpha^{-1}F_1(a) \cos(\Psi)] + O(\alpha^{-2}), \quad (2.58a)$$

$$\frac{d\Psi}{d\bar{\tau}} = -\bar{\delta} - \bar{\lambda} [J_0(a) \cos(\Psi) + \alpha^{-1}F_2(a) \sin(\Psi)] + O(\alpha^{-2}), \quad (2.58b)$$

where

$$F_1(a) \equiv \frac{2}{3}a J_0(a) - \frac{1}{3}(1 + a^2) J_1(a), \quad (2.59a)$$

$$F_2(a) \equiv \left(1 + \frac{1}{3}a^2\right) J_0(a) + \frac{4}{3}a J_1(a). \quad (2.59b)$$

Eqs. (2.58) can be simplified to some extent by introducing a near-identity transformation of the phase variable Ψ of the form:

$$\Psi \equiv \psi + \alpha^{-1}h(a). \quad (2.60)$$

Their structure is then conserved, but now with Ψ , $F_1(a)$, and $F_2(a)$ replaced with ψ , $f_1(a)$, and $f_2(a)$, respectively, where

$$f_1(a) \equiv F_1(a) + h(a) J_1(a), \quad (2.61a)$$

$$f_2(a) \equiv F_2(a) - h(a) J_0(a) - \frac{dh}{da}(a) J_1(a). \quad (2.61b)$$

Choosing

$$h(a) \equiv \frac{1}{3} \left(4 - 2a \frac{J_0(a)}{J_1(a)} + a^2\right) \quad (2.62)$$

and using the Bessel identities

$$\frac{d}{da} J_0(a) = -J_1(a), \quad \frac{d}{da} a J_1(a) = a J_0(a), \quad (2.63)$$

Eqs. (2.58) greatly simplify and become

$$\frac{da}{d\bar{\tau}} = -\frac{1}{2}\alpha^{-1}a - \bar{\lambda} J_1(a) [\sin(\psi) + \alpha^{-1} \cos(\psi)] + O(\alpha^{-2}), \quad (2.64a)$$

$$\frac{d\psi}{d\bar{\tau}} = -\bar{\delta} - \bar{\lambda} J_0(a) [\cos(\psi) + \alpha^{-1} \sin(\psi)] + O(\alpha^{-2}). \quad (2.64b)$$

We have verified that these equations are equivalent to Eqs. (54) derived by De Jagher *et al.* [18] in the limit of large values of the linewidth enhancement factor.

In the low amplitude limit ($a \rightarrow 0$), one has $J_0(a) \rightarrow 1$ and $J_1(a) \rightarrow \frac{1}{2}a$, and the above equations reduce to

$$\frac{da}{d\bar{\tau}} = -\frac{1}{2}a \left\{ \alpha^{-1} + \bar{\lambda} [\sin(\psi) + \alpha^{-1} \cos(\psi)] \right\} + O(\alpha^{-2}), \quad (2.65a)$$

$$\frac{d\psi}{d\bar{\tau}} = -\bar{\delta} - \bar{\lambda} [\cos(\psi) + \alpha^{-1} \sin(\psi)] + O(\alpha^{-2}). \quad (2.65b)$$

Now, observe that, in view of the scaling (2.53), these limit equations are exactly equivalent to the previously obtained small-amplitude equations (2.42), so that the $O(\alpha^{-2})$ corrections actually vanish in the low-amplitude limit. This is a remarkable fact, given that Eqs. (2.42) and Eqs. (2.65) were *a priori* expected to match up to $O(\alpha^{-1})$ only. For arbitrary amplitude a , the solutions of Eqs. (2.64) can be complicated because of the Bessel function nonlinearities. In particular, isolated branches of solutions are possible. Note that, unlike their small-amplitude limit, these equations are physically consistent for arbitrarily long times in the sense that all of their solutions are bounded. More precisely, the amplitude a and the frequency correction $|d\psi/d\bar{\tau}|$ cannot grow to infinity. Indeed, we note from Eq. (2.64a) that, whenever a reaches a value which is a zero of the Bessel function J_1 , it has to decrease, no matter the value of ψ . Since the function J_1 possesses arbitrarily large zeros, a cannot grow to infinity. Furthermore, because $|J_0(a)| \leq 1$ for all a , the absolute value of the right-hand side of Eq. (2.64b) is bounded by $|\bar{\delta}| + |\bar{\lambda}| \sqrt{1 + \alpha^{-2}}$ which means that the frequency correction $|d\psi/d\bar{\tau}|$ is bounded.

Eqs. (2.64) admit the following solutions, characterized by a stationary phase and a stationary amplitude:

$$a_S = a_0 + O(\alpha^{-2}), \quad (2.66a)$$

$$\psi_S = \arccos(\pm 1) - \alpha^{-1} \left(1 \pm \frac{a_0}{2\bar{\lambda} J_1(a_0)} \right) + O(\alpha^{-2}) \quad (2.66b)$$

where a_0 satisfies

$$\bar{\delta} \pm \bar{\lambda} J_0(a_0) = 0, \quad (2.67)$$

for corresponding values of the sign pair symbols. A solution $a_0 > 0$ always exists provided that $\bar{\lambda} > |\bar{\delta}|$, i.e., in the locking domain. From the problem (2.64) linearized about such solutions, we find two complex conjugate eigenvalues $\bar{\sigma}_{\pm}$, given by

$$\bar{\sigma}_{\pm} = \pm i\bar{\lambda} J_1(a_0) + \alpha^{-1} \left(\bar{\delta} - \frac{1}{2} \right) + O(\alpha^{-2}). \quad (2.68)$$

A bifurcation, first identified in [67] in a neighborhood of the codimension-2 bifurcation point, occurs if the real part of $\bar{\sigma}_{\pm}$ vanishes, that is, if

$$\bar{\lambda} \geq \bar{\delta}, \quad \bar{\delta} = \frac{1}{2}, \quad (2.69)$$

or, equivalently, if

$$\lambda \geq \lambda^*, \quad \delta = \delta_{\text{QP2}} \equiv \delta^*. \quad (2.70)$$

If $\delta > \delta^*$, then the amplitude a of the relaxation oscillations and the phase ψ of the laser field oscillate in time, leading to quasiperiodic variations of the light intensity (see Fig. 2.5).

We now present numerical comparisons of the solutions obtained from the large- α averaged equations (2.64) and the full laser rate equations (2.19). The results are

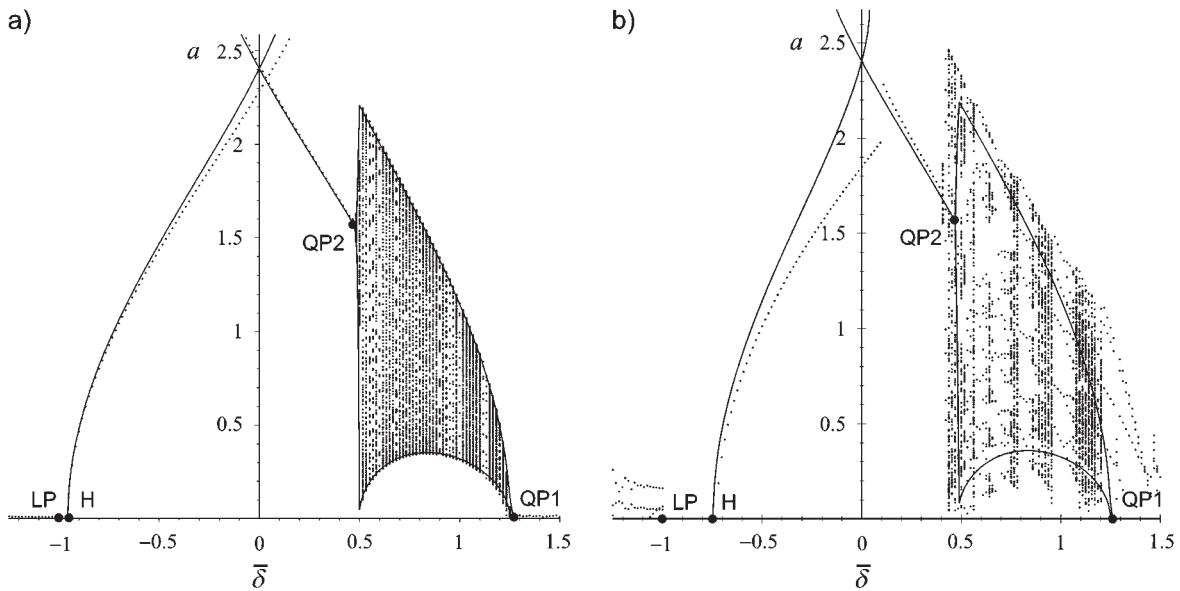


Figure 2.6: Numerical bifurcation diagrams for the laser subject to optical injection. The relaxation oscillation amplitude a is shown as a function of the detuning $\bar{\delta}$. Time series have been computed from both the full rate equations (2.19) and the large- α averaged equations (2.64). The solid lines are extrema of a computed from Eqs. (2.64). The isolated points are values of a corresponding to extrema of Y computed from Eqs. (2.19). The limit point (LP), Hopf (H), and quasiperiodic (QP1, QP2) bifurcation points are indicated.

a) The case of large α : parameter values are $\bar{\lambda} = 1$, $\alpha = 10$, $p = 0.5$, and $\varepsilon = 10^{-2}$. For both systems of equations, quasiperiodicity is observed in the interval $0.5 \lesssim \bar{\delta} \lesssim 1.25$. Note the coexistence of multiple equilibria around $\bar{\delta} = 0$.

b) The case of moderate α : parameter values are $\bar{\lambda} = 1$, $\alpha = 4$, $p = 0.5$, and $\varepsilon = 6.25 \cdot 10^{-2}$. The agreement between the rate equations and the large- α averaged equations is now qualitative. Details on how a changes with $\bar{\delta}$ are lost in the averaged equations, although the coarse dynamical features (*i.e.*, the presence, $a > 0$, or absence, $a \simeq 0$, of relaxation oscillations, as well as the steady or oscillating character of a) are well conserved.

summarized in Fig. 2.6. Fig. 2.6a illustrates the case of a high value of α and a low value of ε while Fig. 2.6b corresponds to more realistic values. In both figures, numerical time series are computed, and the amplitude a is represented as a function of the detuning $\bar{\delta}$ for a given value of the injection rate $\bar{\lambda}$. The extrema of a obtained from the large α averaged equations and the values of a at extrema of Y obtained from the full rate equations are superimposed. To this end, we need to estimate the values of a corresponding to given values of the extrema of the variable Y appearing in the rate equations (2.19). Using Eqs. (2.37) and (2.52) together with the fact that $H = \mathcal{V}(Y)$ at extrema, we find

$$a \simeq \alpha \sqrt{\frac{\mathcal{V}(Y)}{2}}. \quad (2.71)$$

We fix $\bar{\lambda} = 1$ and progressively increase the detuning $\bar{\delta}$ from negative to positive values. The observed sequence of bifurcations is in agreement with that predicted by travelling along a horizontal line above $\lambda = \lambda^*$ in Fig. 2.5. For the extreme parameter values corresponding to Fig. 2.6a, the bifurcation diagrams obtained from the reduced and full laser equations agree very well. For moderate values of α and ε (Fig. 2.6b), the agreement becomes more qualitative, as we may expect. In particular, periodic windows appear in the domain of quasiperiodicity. Such resonances may occur if the condition $\varepsilon \ll 1$ is not well realized—in other words, if the two class B laser time scales are not well separated enough. Nevertheless, the coarse dynamical features of the bifurcation diagram, and, in particular the location of the different types of dynamics (running phase, locking, sustained periodic relaxation oscillations, and complex dynamics), remain well captured by the large- α averaged equations. Note that the quasiperiodic bifurcation at $\bar{\delta} = \frac{1}{2}$ seems to remain vertical even for moderate values of α . This suggests that the quasiperiodic bifurcation is degenerate at this order of our large- α analysis and that the effect of the $O(\alpha^{-2})$ terms needs to be considered. Indeed, the codimension-2 bifurcation unfolding performed in [67], which is not restricted to large values of α , predicts the existence of a homoclinic bifurcation point slightly beyond the quasiperiodic bifurcation. The homoclinic bifurcation marks the change of the quasiperiodic oscillations from bounded-phase to running-phase dynamics, as the detuning progressively increases. However, it can be deduced from Eqs. (A3) in [67] that the quasiperiodic and homoclinic bifurcation curves get arbitrarily close to each other for large α . In both Fig. 2.6a and 2.6b, the two branches of periodic solutions are crossing at or near $\bar{\delta} = 0$. The intersection point is not a bifurcation point because each single branch of periodic solutions exhibits a different phase ψ . For higher values of the amplitude a , other (isolated) branches of periodic solutions appear near $\bar{\delta} = 0$, which are not shown in the figure.

2.5 Laser subject to optical injection and feedback

In the previous section, we studied the effect of the injection of a small amount of monochromatic light into the laser cavity. In this section, we generalize this analysis and

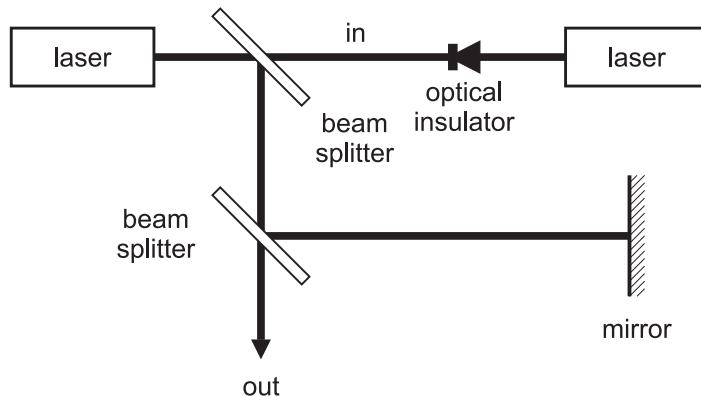


Figure 2.7: A simplified block-diagram of a semiconductor laser subject to optical injection from another laser and delayed feedback from a distant mirror.

consider the case of a semiconductor laser subject to both optical injection and optical feedback. Namely, we consider two lasers arranged in a master-slave configuration again, but now it is further assumed that part of the light emitted by the slave laser is reinjected into its cavity after reflection from a distant mirror (see Fig. 2.7).

2.5.1 Low-amplitude averaged equations

We make the assumption that the roundtrip time, that is, the time needed for the light to travel from the laser to the mirror and back into the laser, is much larger than one relaxation oscillation period. Specifically, it is assumed that the delay measured in units of time s is given by $\varepsilon^{-1}T$, where T is an $O(1)$ parameter. Taking into account both the optical injection and feedback, the injected field e_i in Eq. (2.25a) is expressed as

$$e_i(s) = \lambda \exp(i\varepsilon\delta s) + \hat{\kappa}\mathcal{F}(s - \varepsilon^{-1}T). \quad (2.72)$$

Note that the effect of multiple reflections corresponding to more than one roundtrip is neglected. The complex parameter $\hat{\kappa}$ combines, in a compact notation, the feedback strength $|\hat{\kappa}|$ and the optical phase shift $\arg(\hat{\kappa})$ of the reinjected light with respect to the field inside the cavity. The latter is sensitive to variations of the position of the distant mirror of the order of the optical wavelength. Therefore, the phase shift is most conveniently varied by moving the mirror over a few wavelengths, as such a tiny displacement does not modify the delay $\varepsilon^{-1}T$ or the feedback strength $|\hat{\kappa}|$ appreciably. With $\mathcal{F}_i(s) = \varepsilon e_i(s)$, $\lambda = 0$, and $M(s) = 0$, the rate equations (2.14) are equivalent to the well-known Lang-Kobayashi equations [69, 121].

We immediately restrict the analysis to low-amplitude relaxation oscillations and make use of the small- A expansions (2.38) with the expressions (2.40) and (2.41) for the coefficients. Then, if we define

$$\hat{\theta} \equiv \theta - \int ds \Omega_r(A), \quad (2.73)$$

we see that, because $\Omega_r(A) = 1 + O(A^2)$, one has in first approximation:

$$\widehat{\theta}(s) - \widehat{\theta}(s - \varepsilon^{-1}T) = \theta(s) - \theta(s - \varepsilon^{-1}T) - \varepsilon^{-1}T + O(\varepsilon^{-1}A^2). \quad (2.74)$$

Therefore, assuming $A^2 \ll \varepsilon$ and using the definitions (2.26) and (2.31), the injected field expression (2.72) can be rewritten in terms of A , $\widehat{\theta}$, Ψ , and θ as:

$$e_i(s) = \left\{ \lambda + \widehat{\kappa} \left[1 + \frac{1+i\alpha}{2} \operatorname{Re} \left(A(s - \varepsilon^{-1}T) \exp \left\{ i[\widehat{\theta}(s - \varepsilon^{-1}T) - \widehat{\theta} + \theta - \Theta] \right\} \right) \right] \right. \\ \left. \exp \left\{ i \left[\Psi(s - \varepsilon^{-1}T) - \delta T \right] \right\} \right\} \exp(i\varepsilon\delta s) + o(A), \quad (2.75)$$

where

$$\Theta \equiv \varepsilon^{-1}T \bmod 2\pi. \quad (2.76)$$

Note that, because we have used Eq. (2.74), the feedback term in the expression of e_i does not depend on the delayed variable $\theta(s - \varepsilon^{-1}T)$ explicitly. Now, introducing

$$\widehat{A} \equiv A \exp(i\widehat{\theta}), \quad (2.77)$$

and using the relation (2.37) between the amplitude A and the energy H , we deduce from Eq. (2.29):

$$\frac{d\widehat{A}}{ds} = \frac{1 + i \cot(\theta)}{A} \frac{dH}{ds} \exp(i\widehat{\theta}). \quad (2.78)$$

Substituting Eqs. (2.26), (2.28), (2.31), and (2.75) into the energy equation (2.25a), we evaluate dH/ds in terms of the variables A , $\widehat{\theta}$, Ψ , and θ . Eq. (2.78) then has the following structure:

$$\frac{d\widehat{A}}{ds} = \varepsilon \mathcal{K}_1 \left[A(s), A(s - \varepsilon^{-1}\tau), \widehat{\theta}(s), \widehat{\theta}(s - \varepsilon^{-1}\tau), \Psi(s), \Psi(s - \varepsilon^{-1}\tau), \theta(s) \right], \quad (2.79)$$

where \mathcal{K}_1 is a known function of its arguments. Because Eq. (2.75) does not depend on $\theta(s - \varepsilon^{-1}T)$, nor does \mathcal{K}_1 . Likewise, using Eqs. (2.26), (2.31), and (2.75), the optical phase equation (2.25b) can be written as:

$$\frac{d\Psi}{ds} = \varepsilon \mathcal{K}_2 \left[A(s), A(s - \varepsilon^{-1}\tau), \widehat{\theta}(s), \widehat{\theta}(s - \varepsilon^{-1}\tau), \Psi(s), \Psi(s - \varepsilon^{-1}\tau), \theta(s) \right], \quad (2.80)$$

where \mathcal{K}_2 is another known function of its arguments. Because A and $\widehat{\theta}$ are related to the complex amplitude \widehat{A} through Eq. (2.77), Eqs. (2.79) and (2.80) together provide a pair of equations for the complex amplitude \widehat{A} and the optical phase Ψ . Their right-hand sides are $O(\varepsilon)$ quantities whose fast variations are fully taken into account through the (undelayed) variable θ only. In order to obtain leading-order approximations of \widehat{A} and Ψ , we may average out the fast variations by integrating over one oscillation period in θ . Keeping only the leading-order contributions in the amplitude \widehat{A} , and using the

same symbols for the dynamical variables as for their leading-order approximations for the sake of notation simplicity, the averaged equations read, after a number of simplifications:

$$\frac{d\hat{A}}{d\tau} = -\frac{1}{2}\hat{A} - \frac{1}{2}\sqrt{\alpha^2 + 1} \left\{ \lambda \hat{A} \sin[\Psi + \operatorname{arccot}(\alpha)] - \kappa \left[\hat{A} - \hat{A}(\tau - T) \exp(-i\Theta) \right] \right. \\ \left. \cos[\Psi - \Psi(\tau - T) + \delta T + \vartheta + 2 \operatorname{arccot}(\alpha)] \right\}, \quad (2.81a)$$

$$\frac{d\Psi}{d\tau} = -\delta - \sqrt{\alpha^2 + 1} \left\{ \lambda \cos[\Psi - \operatorname{arccot}(\alpha)] \right. \\ \left. + \kappa \sin[\Psi - \Psi(\tau - T) + \delta T + \vartheta] \right\}, \quad (2.81b)$$

where, as before, $\tau \equiv \varepsilon s$, and where the new, real feedback parameters κ and ϑ are defined as follows:

$$\hat{\kappa} \equiv \kappa \exp \{ i [\arctan(\alpha) - \vartheta] \}.$$

The parameter ϑ represents the dephasing between the reinjected light and the field in the laser cavity. It is defined in such a way that ϑ is an increasing function of the roundtrip path length. The phase offset $\arctan(\alpha)$ has been introduced in order to simplify several expressions further on in this chapter. For $\kappa = 0$, the above equations are equivalent to the low-amplitude equations (2.42) derived in Sec. 2.4.2 in the case of monochromatic optical injection only.

2.5.2 Laser with feedback only

We first set the injection rate to zero and review a few properties of the pure feedback case. This will provide a useful background for Sec. 2.5.3. Setting $\lambda = 0$ in Eqs. (2.81) gives:

$$\frac{d\hat{A}}{d\tau} = -\frac{1}{2}\hat{A} + \frac{1}{2}\sqrt{\alpha^2 + 1}\kappa \left[\hat{A} - \hat{A}(\tau - T) \exp(-i\Theta) \right] \\ \cos[\Psi - \Psi(\tau - T) + \delta T + \vartheta + 2 \operatorname{arccot}(\alpha)], \quad (2.82a)$$

$$\frac{d\Psi}{d\tau} = -\delta - \sqrt{\alpha^2 + 1}\kappa \sin[\Psi - \Psi(\tau - T) + \delta T + \vartheta]. \quad (2.82b)$$

As there is no injected monochromatic light, the detuning δ becomes immaterial to our problem and may be fixed to any arbitrary value without loss of generality. We may exploit this freedom to our advantage in the research of pure monochromatic solutions. Indeed, a solution of the above equations with a stationary phase Ψ represents monochromatic emission with a frequency offset of δ with respect to the free-running laser frequency. Such a solution is called an external cavity mode as it corresponds to one of the oscillation modes of the electromagnetic field supported by the external resonant cavity constituted of the region of space bounded by the laser and the distant mirror. Therefore, the research of external cavity modes amounts to the determination of the values of δ that solve Eq. (2.82b) for constant Ψ :

$$0 = -\delta - \sqrt{\alpha^2 + 1}\kappa \sin(\delta T + \vartheta). \quad (2.83)$$

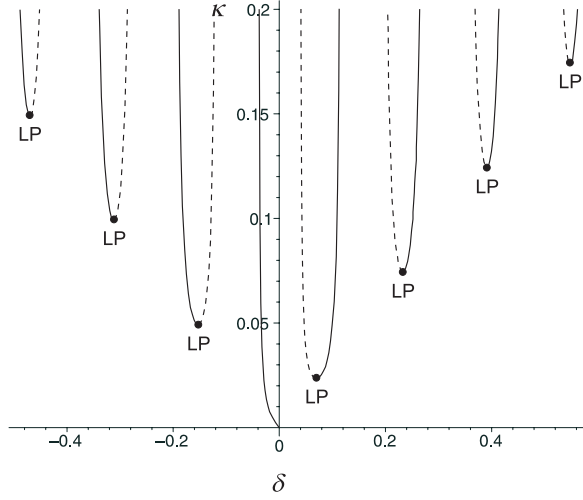


Figure 2.8: Bifurcation diagram for the laser subject to weak optical feedback. The external cavity mode frequencies (δ), as determined from Eq. (2.83) are represented as a function of the feedback rate (κ). Parameter values are $\alpha = 3$, $T = 40$, and $\vartheta = \frac{1}{2}\pi$. Solid and dashed curves correspond to modes and antimodes, respectively. Points labelled LP represent limits points, they are associated with the birth of a new mode-antimode pair.

The number of solutions of this transcendental equation grows proportionally to the feedback rate κ (see the illustration in Fig. 2.8).

The stability of external cavity modes is determined by the behavior of the solutions of Eq. (2.82b) linearized about $\Psi = 0$:

$$\frac{d\Psi}{d\tau} = -\sqrt{\alpha^2 + 1}\kappa [\Psi - \Psi(\tau - T)] \cos(\delta T + \vartheta) + O(\Psi^2). \quad (2.84)$$

The eigenvalues σ of this linear equation are obtained by seeking solutions of the form

$$\Psi = \Psi_0 \exp(\sigma\tau) \quad (2.85)$$

where Ψ_0 is a constant. Substituting this ansatz into Eq. (2.84) yields the characteristic equation from which the eigenvalues are determined. Separating the real and imaginary parts, it reads:

$$\text{Re}(\sigma) = -\sqrt{\alpha^2 + 1}\kappa \{1 - \exp[-\text{Re}(\sigma T)] \cos[\text{Im}(\sigma T)]\} \cos(\delta T + \vartheta), \quad (2.86a)$$

$$\text{Im}(\sigma) = -\sqrt{\alpha^2 + 1}\kappa \exp[-\text{Re}(\sigma T)] \sin[\text{Im}(\sigma T)] \cos(\delta T + \vartheta). \quad (2.86b)$$

In order to determine the stability of the external cavity modes, we must determine under which conditions the characteristic equation admits solutions with a positive real part. First, note that, if $\text{Re}(\sigma) > 0$, then the left-hand side of Eq. (2.86a) is positive, while the sign of the right-hand side is opposite to that of its last factor. Consequently, $\cos(\delta T + \vartheta)$ must be negative in order for such solutions to exist. Furthermore, if

$\text{Re}(\sigma) > 0$ and $-1 \leq \sqrt{\alpha^2 + 1}\kappa \cos(\delta T + \vartheta) \leq 0$, then the left-hand side of Eq. (2.86b) is greater in absolute value than its right-hand side for all values of $\text{Im}(\sigma) \neq 0$, and the left-hand side of Eq. (2.86a) is greater than its right-hand side for $\text{Im}(\sigma) = 0$. On the other hand, if

$$\sqrt{\alpha^2 + 1}\kappa T \cos(\delta T + \vartheta) < -1, \quad (2.87)$$

then Eqs. (2.86) always possesses a solution with $\text{Re}(\sigma) > 0$ and $\text{Im}(\sigma) = 0$. Therefore, an external cavity mode is unstable if the above condition holds, and is stable otherwise. Stable and unstable external cavity modes are often referred to as “modes” and “antimodes” respectively. In Fig. 2.8, modes are represented as solid curves, while antimodes are represented as dashed.

We now focus on one particular mode and determine its stability boundaries in the feedback parameter space (ϑ, κ) . Note, in view of the condition (2.87), that solutions of the stationary-phase equation (2.83) with marginal stability satisfy

$$\sqrt{\alpha^2 + 1}\kappa T \cos(\delta T + \vartheta) = -1, \quad (2.88)$$

which is just the equation obtained by differentiating Eq. (2.83) with respect to the frequency offset δ , so that marginally stable solutions are actually solutions of Eq. (2.83) with multiplicity 2. The conditions of existence of such double solutions correspond to limit points in parameter space, characterized by the simultaneous birth of one mode and one antimode. The locus of limit points is obtained by first eliminating the trigonometric functions between Eqs. (2.83) and (2.88), and then solving the resulting relation for δ and substituting its value back into Eq. (2.88). This yields, in explicit form, $\vartheta = \vartheta_{\text{LP}}^{\pm}(\kappa)$, where

$$\vartheta_{\text{LP}}^{\pm}(\kappa) \equiv \pm \left(\sqrt{(\alpha^2 + 1)\kappa^2 T^2 - 1} + \arccos \frac{-1}{\sqrt{\alpha^2 + 1}\kappa T} \right). \quad (2.89)$$

The above equation holds modulo 2π , and each distinct determination determines the stability of a different mode. The limit point curves possess cusp points at

$$\vartheta = (2n + 1)\pi, \quad n \text{ integer}, \quad (2.90a)$$

$$\kappa = \kappa_{\text{C}} \equiv \frac{1}{\sqrt{\alpha^2 + 1}T}. \quad (2.90b)$$

If the feedback level is less than its cusp point value: $\kappa \leq \kappa_{\text{C}}$, then there exists only a single mode for all values of the phase shift ϑ , which can undergo arbitrarily wide variations without destabilizing that unique solution. In that regime, the feedback induces a mere shift of the laser emission frequency, and this shift is periodic in ϑ with a period 2π . For $\kappa > \kappa_{\text{C}}$, several modes coexist for some or all values of ϑ . If the phase shift ϑ is increased or decreased sufficiently far away, the mode will eventually annihilate with an antimode at a limit point and the laser will perform a dynamical jump onto another mode. The total range of values that can be spanned by ϑ without meeting a limit point is always greater than 2π . This is illustrated in Fig. 2.9 in

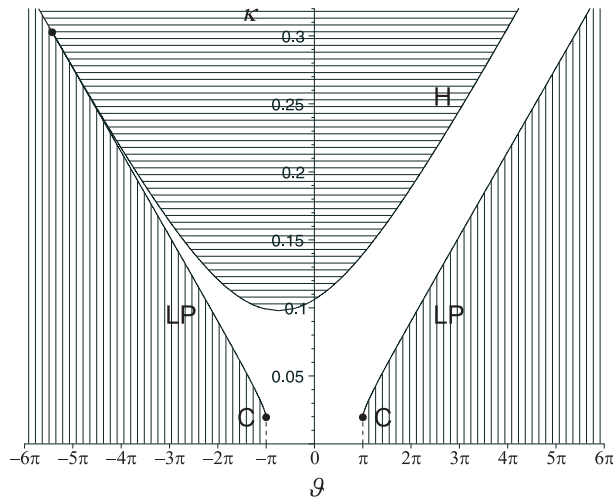


Figure 2.9: Stability boundaries of one particular external cavity mode in feedback parameter space (ϑ, κ) , for the laser subject to weak optical feedback. Parameter values are $T = 10$ and $\alpha = 5$. The stability domain (in white) is bounded by limit point curves (LP) determined from Eq. (2.89) and a Hopf bifurcations curve (H) approximated for large T using Eq. (2.98). The limit point and Hopf curves have a tangency point in the upper-left corner of the figure. In the horizontal-hatched region, the mode is unstable with respect to relaxation oscillations. Beyond the limit point curves (in the vertical-hatched region), the mode is destroyed in a mode-antimode pair annihilation and the system performs a dynamical jump onto another external cavity mode. For values of κ below the cusp points (C), the laser response is 2π -periodic in ϑ .

the form of a stability diagram in feedback parameter space. This figure presents the same information as Fig. 16 in [121], but only one mode is represented instead of a multiplicity of them, making the similarity with the pure-injection diagram (Fig. 2.5) more obvious.

We described in Sec. 2.4.2 how the injection of a sufficiently large amount of monochromatic light is able to destabilize steady emission by counterbalancing the damping of relaxation oscillations. A similar phenomenon takes place in the case of feedback, and can be analyzed from the relaxation oscillation amplitude equation (2.82a). Assuming a constant phase Ψ and an amplitude A of the form

$$\hat{A} = \hat{A}_0 \exp(\bar{\sigma}\tau) \quad (2.91)$$

where \hat{A}_0 is a constant and introducing the ansatz (2.91) into Eq. (2.82a) yields the characteristic equation from which the eigenvalues $\bar{\sigma}$ are determined. Separating the

real and imaginary parts, we find:

$$\operatorname{Re}(\bar{\sigma}) = -\frac{1}{2} + \frac{1}{2}\sqrt{\alpha^2 + 1}\kappa \{1 - \exp[-\operatorname{Re}(\bar{\sigma}T)] \cos[\operatorname{Im}(\bar{\sigma}T) + \Theta]\} \\ \cos[\delta T + \vartheta + 2 \operatorname{arccot}(\alpha)], \quad (2.92a)$$

$$\operatorname{Im}(\bar{\sigma}) = \frac{1}{2}\sqrt{\alpha^2 + 1}\kappa \exp[-\operatorname{Re}(\bar{\sigma}T)] \sin[\operatorname{Im}(\bar{\sigma}T) + \Theta] \\ \cos[\delta T + \vartheta + 2 \operatorname{arccot}(\alpha)]. \quad (2.92b)$$

The conditions of marginal stability with respect to relaxation oscillations are obtained by requiring that one of the eigenvalues be a pure imaginary number. Such conditions correspond to a Hopf bifurcation, where the external cavity mode under consideration loses stability in favor of an oscillatory state. Eqs. (2.92) then provide relations between the feedback parameters, κ and ϑ , and the relaxation oscillation frequency correction $\operatorname{Im}(\bar{\sigma})$. They can be solved for the feedback parameters, giving the locus of Hopf bifurcation points parametrically as a function of $\operatorname{Im}(\bar{\sigma})$.

In order to determine a fairly simple expression for the oscillation threshold in explicit form, we now make the assumption that the delay T is large: $T \gg 1$. Introducing the decomposition

$$\operatorname{Im}(\bar{\sigma}) \equiv T^{-1}(2\pi\bar{n} + \bar{\omega}), \quad (2.93)$$

where \bar{n} is a (possibly $O(T)$ -large) integer and $0 \leq \bar{\omega} < 2\pi$, and setting $\operatorname{Re}(\bar{\sigma}) = 0$, Eqs. (2.92) reduce to:

$$0 = -\frac{1}{2} + \frac{1}{2}\sqrt{\alpha^2 + 1}\kappa [1 - \cos(\bar{\omega} + \Theta)] \cos[\delta T + \vartheta + 2 \operatorname{arccot}(\alpha)], \quad (2.94a)$$

$$\bar{n} = \frac{1}{4\pi}\sqrt{\alpha^2 + 1}\kappa T \sin(\bar{\omega} + \Theta) \cos[\delta T + \vartheta + 2 \operatorname{arccot}(\alpha)] - \frac{\bar{\omega}}{2\pi}. \quad (2.94b)$$

Note that, because $0 \leq 1 - \cos(\bar{\omega} + \Theta) \leq 2$, a necessary and sufficient condition for Eq. (2.94a) to be solvable for $\bar{\omega}$ is

$$\sqrt{\alpha^2 + 1}\kappa \cos[\delta T + \vartheta + 2 \operatorname{arccot}(\alpha)] \geq \frac{1}{2}. \quad (2.95)$$

Eq. (2.94b) further requires that its right-hand side be an integer number. Each distinct value of \bar{n} determines a distinct Hopf bifurcation curve. There exists one value of \bar{n} such that the corresponding bifurcation curve has the smallest values of κ for given ϑ . This one corresponds to the primary instability and forms the stability boundary in parameter space. Other values of \bar{n} correspond to successive bifurcations of the same branch of solutions. Only the primary instability is observable experimentally as the system cannot remain for long on the destabilized branch. Therefore, other bifurcation points than the primary instability are of limited interest. Now, consider the least value of κ such that the constraint (2.95) holds, for given ϑ . This value is very close to the least value of κ that makes the right-hand side of Eq. (2.94b) an integer number within that constraint. Indeed, it can be found from Eq. (2.94a) that,

in a neighborhood of this point, an $O(T^{-2})$ increase in κ induces an $O(1)$ variation of $T \sin(\bar{\omega} + \Theta)$, and is therefore sufficient to bring the right-hand side of Eq. (2.94b) onto an integer value. Therefore, the least value of κ satisfying the constraint (2.95) is a close approximation of the threshold of primary instability. Specifically, the locus of primary Hopf bifurcation points is approximately determined by the condition

$$\sqrt{\alpha^2 + 1} \kappa \cos [\delta T + \vartheta + 2 \operatorname{arccot}(\alpha)] = \frac{1}{2}, \quad (2.96)$$

where δ represents the frequency of the external cavity mode under consideration. Eliminating the trigonometric functions between Eqs. (2.83) and (2.96) and solving for δ yields $\delta = \delta_{\text{H}}^{\pm}(\kappa)$, where

$$\delta_{\text{H}}^{\pm}(\kappa) \equiv \frac{\alpha \pm (\alpha^2 - 1) \sqrt{(\alpha^2 + 1) \kappa^2 - \frac{1}{4}}}{\alpha^2 + 1}. \quad (2.97)$$

Substituting this back into Eq. (2.96) gives the equation of the primary Hopf bifurcation curve in explicit form: $\vartheta = \vartheta_{\text{H}}^{\pm}(\kappa)$, where

$$\vartheta_{\text{H}}^{\pm}(\kappa) \equiv -\operatorname{sign} [\delta_{\text{H}}^{\mp}(\kappa)] \operatorname{arccos} \frac{\alpha^2 + 1 - 4\alpha \delta_{\text{H}}^{\mp}(\kappa)}{2(\alpha^2 - 1) \sqrt{\alpha^2 + 1} \kappa} - \delta_{\text{H}}^{\mp}(\kappa) T. \quad (2.98)$$

The above equation holds modulo 2π , and each distinct determination determines the stability of a different mode.

The Hopf curve and the limit point curve constructed above are illustrated in Fig. 2.9 for one particular mode. Note the similarity between this diagram and the map of the dynamics for the case of pure monochromatic injection represented in Fig. 2.5. Both diagrams display, in white, a region corresponding to a regime of monochromatic steady emission with a frequency that varies quasistatically with the control parameters. This region is bounded by a limit point curve and a Hopf bifurcation curve possessing a tangency point and has roughly the same shape in both diagrams.

2.5.3 Laser with injection and feedback

In Sec. 2.5.2, we described how a weak feedback of the emitted light from a distant mirror into the laser cavity creates a multiplicity of possible emission frequencies corresponding to external cavity modes. In Sec. 2.4 we described how a small amount of injected monochromatic light may induce phase-locking of the laser output frequency. As a natural extension of both analyses, we now investigate how optical injection may induce phase-locking of the external cavity modes generated by optical feedback. To this end, we make use of Eqs. (2.81) with $\lambda \neq 0$ and $\kappa \neq 0$. As in the case of pure injection, the phase-locked states are obtained as constant solutions $\Psi = \Psi_s$ of the phase equation (2.81b):

$$0 = -\delta - \sqrt{\alpha^2 + 1} \{ \lambda \cos [\Psi_s - \operatorname{arccot}(\alpha)] + \kappa \sin (\delta T + \vartheta) \}, \quad (2.99)$$

and their stability is determined from Eq. (2.81b) linearized about the stationary phase. Seeking solutions of the linearized equation of the form $\Psi - \Psi_s \propto \exp(\sigma\tau)$ then gives the characteristic equation:

$$\begin{aligned} \operatorname{Re}(\sigma) &= \sqrt{\alpha^2 + 1} \{ \lambda \sin[\Psi_s - \operatorname{arccot}(\alpha)] \\ &\quad - \kappa [1 - \exp(-\operatorname{Re}(\sigma T)) \cos(\operatorname{Im}(\sigma T))] \cos(\delta T + \vartheta) \}, \end{aligned} \quad (2.100a)$$

$$\operatorname{Im}(\sigma) = -\kappa \sqrt{\alpha^2 + 1} \exp(-\operatorname{Re}(\sigma T)) \sin(\operatorname{Im}(\sigma T)) \cos(\delta T + \vartheta), \quad (2.100b)$$

where we have separated the real and imaginary parts again. Note that stationary-phase solutions such that $\sin[\Psi_s - \operatorname{arccot}(\alpha)] > 0$ are always unstable, because in that case the characteristic equation (2.100) always possesses a solution with $\operatorname{Re}(\sigma) > 0$ and $\operatorname{Im}(\sigma) = 0$ (this is a consequence of the continuity of Eq. (2.100a) in $\operatorname{Re}(\sigma)$, given that its right-hand side is positive for $\operatorname{Re}(\sigma) = 0$ and tends towards a constant for large $\operatorname{Re}(\sigma)$). Therefore, from now on, we restrict our stability analysis to phase-locked solutions such that

$$\sin[\Psi_s - \operatorname{arccot}(\alpha)] \leq 0. \quad (2.101)$$

As in the case of pure optical injection, the boundaries of the locking domain are obtained as the locus of limit points in parameter space. Limit points are determined by requiring that the stationary-phase equation (2.99) possesses a solution with multiplicity 2, so that Ψ_s must also solve the equation obtained by differentiating Eq. (2.99) with respect to Ψ_s . This gives:

$$\sin[\Psi_s - \operatorname{arccot}(\alpha)] = 0. \quad (2.102)$$

This is just the condition of existence of a solution of the characteristic equation (2.100) with $\operatorname{Re}(\sigma) = \operatorname{Im}(\sigma) = 0$, and it forms the boundary of the domain defined by Eq. (2.101). Therefore, phase locking is associated with the creation of a pair of stationary-phase solutions, one of which satisfies Eq. (2.101) and the other of which belongs to the kind of always-unstable solutions mentioned earlier. Note that the pair of stationary-phase solutions created this way is not to be mistaken for a new mode-antimode pair—in fact, as we shall see below, both modes and antimodes undergo this kind of splitting into two stationary-phase solutions in the transition from running-phase to phase-locked dynamics.

The condition (2.102) can be equivalently written as $\cos[\Psi_s - \operatorname{arccot}(\alpha)] = \pm 1$. Substituting this into Eq. (2.99) and solving for λ gives the limit point curve, $\lambda = \lambda_{\text{LP}}(\delta, \kappa, \vartheta)$, where

$$\lambda_{\text{LP}}(\delta, \kappa, \vartheta) \equiv \left| \frac{\delta}{\sqrt{\alpha^2 + 1}} + \kappa \sin(\delta T + \vartheta) \right|. \quad (2.103)$$

Note that, in absence of feedback ($\kappa = 0$), the above expression reduces, as expected, to the limit point expression (2.45) computed in the case of injection only. For weak feedback ($\kappa \neq 0$ but small), the locking domain is roughly similar in shape to the case of no feedback, but its boundaries now have “ripples” as a consequence of the sine

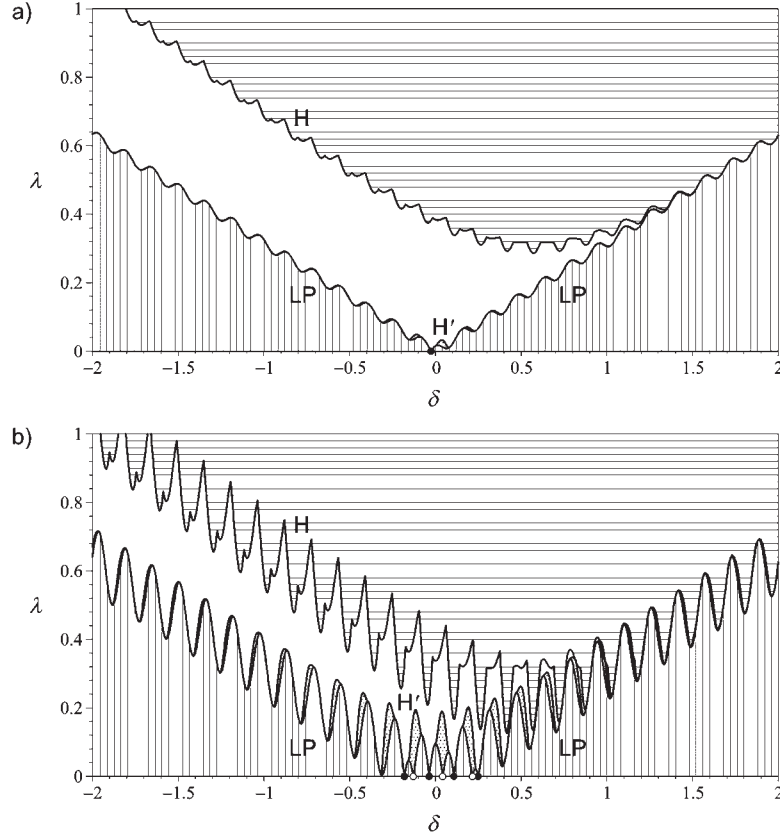


Figure 2.10: Locking domain in injection parameter space and its stability, for the laser subject to weak optical injection and feedback. Figs. 2.10a and 2.10b correspond to two different values of the feedback level κ . Other parameters are fixed to $\alpha = 3$, $T = 40$, and $\vartheta = \frac{1}{2}\pi$. In both figures, the locus of bifurcation points are represented as solid curves. The curve labelled LP is the limit point curve obtained from Eq. (2.103). The curve labelled H indicates a Hopf bifurcation to sustained relaxation oscillations and is obtained from Eq. (2.108). The curves labelled H' indicate Hopf bifurcations to period- $2T$ oscillations and are obtained from Eqs. (2.110a) and (2.112). Vertical-hatched, horizontal-hatched, and dotted areas represent, respectively, the region outside the locking domain, the region of instability with respect to relaxation oscillations, and the region of instability with respect to period- $2T$ oscillations. The circles at $\lambda = 0$ indicate resonances between the injected field from the master laser and feedback-induced external cavity modes: filled and hollow circles correspond to modes and antimodes respectively.

a) A very weak feedback level value: $\kappa = 0.015$. The locking domain and the Hopf bifurcation curve to sustained relaxation oscillations have similar shapes as in the case of no feedback, but with the addition of ripples induced by the small amount of feedback.

b) A stronger feedback level value: $\kappa = 0.095$. The ripples are larger than in Fig. 2.10a. The shape of the locking domain presents resonances tongues at those values of the master laser frequency corresponding to external cavity mode frequencies.

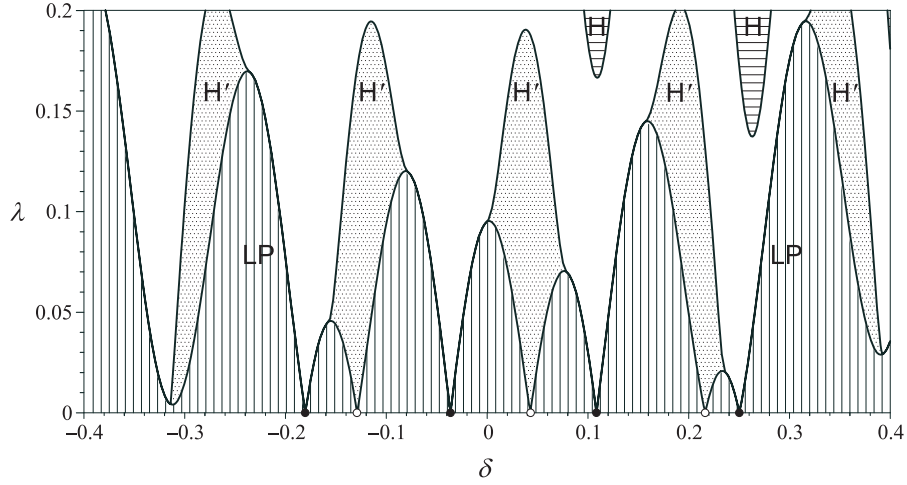


Figure 2.11: A detail of Fig. 2.10b: the resonances between the injected field from the master laser and the feedback-induced external cavity modes. The various curves, symbols, and areas in this figure have the same meanings as in Fig. 2.10. Note that the regions of antimode phase-locking (dotted resonance tongues) are unstable with respect to period- $2T$ oscillations, while the regions of mode phase-locking (blank resonance tongues) are stable.

term in the expression (2.103) (see the illustration in Fig. 2.10a). The ripples grow as a function of the feedback level in such a way that $\lambda_{LP}(\delta, \kappa, \vartheta)$ may vanish for several values of the frequency offset δ of the injected field for strong enough feedback, as shown in Fig. 2.10b. See also Fig. 2.11, which is a close-up on the zeros of $\lambda_{LP}(\delta, \kappa, \vartheta)$ in Fig. 2.10b. Now, observe from the expression (2.103) that $\lambda_{LP}(\delta, \kappa, \vartheta)$ possesses exactly the same roots as Eq. (2.83), which gives the values of the frequencies of the external cavity modes in the case of pure feedback. Therefore, each of these roots correspond to resonances between the injected field and an external cavity mode. From Fig. 2.11, we see that, in a close neighborhood of each resonance, phase-locking of the corresponding mode takes place for a range of values of δ which is centered on the resonance and grows roughly proportionally to the injection rate λ . If the injection is strong enough, the locking ranges merge together into a single locking interval whose width is of the same order of magnitude as the whole external cavity spectrum, or larger. Furthermore, note from Fig. 2.10b that, in addition to a finite number of roots, the limit point curve $\lambda = \lambda_{LP}(\delta, \kappa, \vartheta)$ possesses an infinite number of minima with $\lambda \neq 0$. These minima can be identified as resonances with complex roots of Eq. (2.83). If the feedback level is increased beyond the point where a pair of complex conjugate roots becomes real, giving birth to a new mode-antimode pair, then the corresponding minimum of the limit point curve splits into a pair of resonances with the newly-born external cavity modes. This phenomenon can be observed by comparing the number and the nature of the minima between Figs. 2.10a and 2.10b. The existence of such resonances with the complex roots implies that, for a fixed value of the injection rate λ and for fixed

values of the feedback parameters κ and ϑ , the number of disjoint frequency intervals where phase locking occurs can be larger than the number of external cavity modes in absence of optical injection, for the same values of the feedback parameters. To observe this, count, for example, the number of crossings of the horizontal line at $\lambda = 0.01$ with the locking domain in Fig. 2.11 and notice that this number is larger than the number of modes and antimodes.

The analysis of the characteristic equation (2.100) is not complete yet at this point, as there remains to investigate the conditions of oscillatory instability corresponding to eigenvalues σ with a nonvanishing imaginary part. Such an oscillatory instability would be of a different nature from the relaxation oscillation instability that we have met in various forms in the previous sections, as it would be associated to the phase equation (2.81b) rather than to the amplitude equation (2.81a). Therefore, before proceeding to an analysis of instabilities of this sort, we first discuss the more familiar relaxation oscillation instability. Assuming a stationary phase, $\Psi = \Psi_s$, and seeking solutions of the amplitude equation (2.81a) of the form $\hat{A} = \hat{A}_0 \exp(\bar{\sigma}\tau)$, we obtain the characteristic equation associated with relaxation oscillations. The locus of Hopf bifurcation points is obtained by requiring the existence of pure imaginary eigenvalues: $\text{Re}(\bar{\sigma}) = 0$. The characteristic equation then becomes:

$$0 = -\frac{1}{2} - \frac{1}{2}\sqrt{\alpha^2 + 1} \{ \lambda \sin[\Psi_s + \text{arccot}(\alpha)] - \kappa [1 - \cos[\text{Im}(\bar{\sigma}T) + \Theta]] \cos[\delta T + \vartheta + 2 \text{arccot}(\alpha)] \}, \quad (2.104a)$$

$$\text{Im} \bar{\sigma} = \frac{1}{2}\sqrt{\alpha^2 + 1} \kappa \sin[\text{Im}(\bar{\sigma}T) + \Theta] \cos[\delta T + \vartheta + 2 \text{arccot}(\alpha)]. \quad (2.104b)$$

Because $0 \leq 1 - \cos[\text{Im}(\bar{\sigma}T) + \Theta] \leq 2$, from Eq. (2.104a), one must have

$$0 \leq \frac{(\alpha^2 + 1)^{-\frac{1}{2}} + \lambda \sin[\Psi_s + \text{arccot}(\alpha)]}{\kappa \cos[\delta T + \vartheta + 2 \text{arccot}(\alpha)]} \leq 2 \quad (2.105)$$

in order for Eqs. (2.104) to admit a solution. By an argument analogous to that of Sec. 2.5.2, it can be shown that, for sufficiently large T , the least value of λ satisfying the conditions (2.105) for δ , κ , and ϑ fixed is an approximation of the value of the injection rate at the primary Hopf bifurcation accurate to within $O(T^{-2})$ errors. This threshold value satisfies either

$$\lambda \sin[\Psi_s + \text{arccot}(\alpha)] = L_1 \equiv -(\alpha^2 + 1)^{-\frac{1}{2}} \quad (2.106)$$

or

$$\lambda \sin[\Psi_s + \text{arccot}(\alpha)] = L_2(\delta, \kappa, \vartheta) \equiv -(\alpha^2 + 1)^{-\frac{1}{2}} + 2\kappa \cos[\delta T + \vartheta + 2 \text{arccot}(\alpha)], \quad (2.107)$$

depending on which one gives the lowest value of λ . Eliminating the trigonometric functions of Ψ_s between the stationary phase equation (2.99) and either of the above

conditions gives the primary Hopf bifurcation curve, $\lambda = \lambda_{\text{H}}(\delta, \kappa, \vartheta)$, where

$$\lambda_{\text{H}}(\delta, \kappa, \vartheta) \equiv \min_{n=1,2} \left\{ \lambda_{\text{LP}}(\delta, \kappa, \vartheta)^2 + \left[\frac{\alpha^2 + 1}{\alpha^2 - 1} L_n(\delta, \kappa, \vartheta) + \frac{2\alpha}{\alpha^2 - 1} \left(\frac{\delta}{\sqrt{\alpha^2 + 1}} + \kappa \sin(\delta T + \vartheta) \right) \right]^2 \right\}^{\frac{1}{2}}. \quad (2.108)$$

Thus, sustained relaxation oscillations take place if the injection rate is higher than $\lambda_{\text{H}}(\delta, \kappa, \vartheta)$. See the illustrations in Fig. 2.10, and observe that optical feedback induces the appearance of ripples on the Hopf bifurcation curve that roughly follow the ripples of the limit point curve.

So far in the discussion of the interaction between optical injection and external cavity modes, we treated modes and antimodes equivalently. Indeed, their role is symmetric with respect to phase locking and relaxation oscillation instabilities. However, there must exist a mechanism that breaks this symmetry and accounts for the instability of the antimodes. This mechanism is another sequence of Hopf bifurcations, but this time associated with the phase equation (2.81b) rather than with the amplitude equation (2.81a). It can be determined from the characteristic equation (2.100) that govern phase instabilities. Seeking solutions with $\text{Re}(\sigma) = 0$ but $\text{Im}(\sigma) \neq 0$, the characteristic equation reduces to:

$$0 = \sqrt{\alpha^2 + 1} \{ \lambda \sin[\Psi_s - \text{arccot}(\alpha)] - \kappa [1 - \cos[\text{Im}(\sigma T)]] \cos(\delta T + \vartheta) \}, \quad (2.109a)$$

$$\text{Im}(\sigma) = -\kappa \sqrt{\alpha^2 + 1} \sin[\text{Im}(\sigma T)] \cos(\delta T + \vartheta). \quad (2.109b)$$

Because $0 \leq 1 - \cos[\text{Im}(\sigma T)] \leq 2$, and within the restriction (2.101), Eq. (2.109a) can be solved for $\text{Im}(\sigma)$ only if

$$\cos(\delta T + \vartheta) \leq 0, \quad (2.110a)$$

$$\lambda \leq \frac{2\kappa \cos(\delta T + \vartheta)}{\sin[\Psi_s - \text{arccot}(\alpha)]}. \quad (2.110b)$$

We see from Eq. (2.110b) that, in contrast to the instabilities related to relaxation oscillations, this kind of oscillatory instability takes place below a critical value of the optical injection, rather than above. Now, remember that Eq. (2.87) distinguishes antimodes from stable modes in the absence of injection, and observe that if Eq. (2.87) is satisfied, then Eqs. (2.110) are also satisfied for $\lambda = 0$. This means that the Hopf bifurcation mechanism described here correctly accounts for the instability of the phase-locked antimodes at sufficiently low injection.

Again, if T is sufficiently large, the boundary of the domain delimited by Eqs. (2.110) in parameter space is a close approximation of the locus of primary Hopf bifurcation points, which are therefore given by Eq. (2.110a) and

$$\lambda = \frac{2\kappa \cos(\delta T + \vartheta)}{\sin[\Psi_s - \text{arccot}(\alpha)]}. \quad (2.111)$$

Eliminating the trigonometric functions of $\Psi_s - \text{arccot}(\alpha)$ between Eqs. (2.99) and (2.111) yields the primary Hopf bifurcation curve, $\lambda = \lambda_{\text{H}'}(\delta, \kappa, \vartheta)$, where

$$\lambda_{\text{H}'}(\delta, \kappa, \vartheta) \equiv \sqrt{\lambda_{\text{LP}}(\delta, \kappa, \vartheta)^2 + 4\kappa^2 \cos^2(\delta T + \vartheta)}. \quad (2.112)$$

The portions of this curve delimited by the condition (2.110a) are represented in Figs. 2.10 and 2.11. Observe from Fig. 2.11 that, as expected, the phase-locked dynamics is unstable close to the antimode resonances, while it is stable close to the mode resonances.

In order to determine the primary instability oscillation frequency, we now introduce the decompositions

$$\lambda = \lambda_0 + T^{-2}\lambda_2 + o(T^{-2}), \quad \text{Im}(\sigma) = \text{Im}(\sigma_0) + T^{-1}\text{Im}(\sigma_1) + o(T^{-1}) \quad (2.113)$$

into Eqs. (2.109), where λ_0 is given exactly by Eq. (2.111). λ_2 is chosen to be the largest possible value such that the characteristic equation (2.109) admits a solution. λ_2 represents a small correction to the location of the primary Hopf bifurcation. Solving for $\text{Im}(\sigma_0)$ then gives $\text{Im}(\sigma_0) = \pm\pi T^{-1}$, so that the oscillation period, $2\pi/\text{Im}(\sigma)$, is close to twice the delay. Fig. 2.12 illustrates the stable period- $2T$ dynamics that can be observed for $\lambda < \lambda_{\text{H}'}(\delta, \kappa, \vartheta)$. The detuning value δ is chosen so that the master laser frequency is resonant with an antimode. Fig. 2.12a displays a numerical time series for the optical phase Ψ computed from the phase equation (2.81b). Fig. 2.12b also represents the time dependence of the phase Ψ , but computed directly from the full rate equations (2.19). The agreement between the approximate and exact solutions is excellent: both time series are visually undistinguishable in Fig. 2.12. The existence of square-wave oscillation modes such as that represented in this figure is a generic dynamical feature of scalar nonlinear delay-differential equations with a large delay, beyond a supercritical Hopf bifurcation point. Such square-wave dynamics is also observed, for example, in time series of the well-known Ikeda equation [56, 57], which provides an idealized model for an optically bistable device with a delayed feedback line. The whole Chapter 5 is devoted to the study of square-wave dynamics close to the oscillation threshold and of how it is affected by a weak modulation signal. Although the emphasis is put on delayed optically bistable systems, the analysis presented there is applicable to the phase equation (2.81b) derived in the present chapter.

In the limit of a large delay, the study of the stability of period- $2T$ solutions can be simplified, as the phase equation (2.81b) reduces to a discrete-time map for T large. Indeed, square-wave solutions are characterized by an alternance of plateaus whose length is approximately equal to the delay, and connected by thin transition layers. Away from the sharp transitions, one has $d\Psi/d\tau \ll 1$, so that the plateau structure of these solutions is correctly described by neglecting the left-hand side of Eq. (2.81b). This yields:

$$0 = -\delta - \sqrt{\alpha^2 + 1} \{ \lambda \cos[\Psi - \text{arccot}(\alpha)] + \kappa \sin[\Psi - \Psi(\tau - T) + \delta T + \vartheta] \}, \quad (2.114)$$

which gives the possible plateau values of the optical phase $\Psi(\tau)$ implicitly in terms of its plateau value one delay time earlier $\Psi(\tau - T)$. The bifurcations of period- $2T$

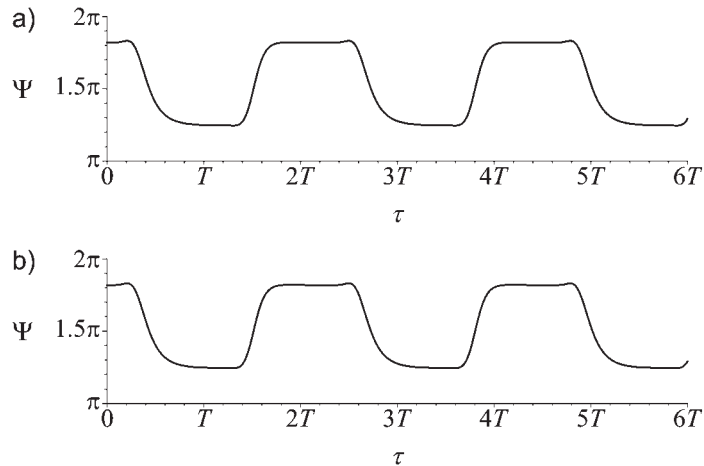


Figure 2.12: Periodic square-wave dynamics of the laser subject to both optical injection and feedback. Parameter values are $\alpha = 3$, $T = 40$, $\kappa = 0.095$, $\vartheta = \frac{1}{2}\pi$, and $\lambda = 0.12$. The detuning value, $\delta = 0.0428$, is chosen so that exact resonance is achieved between the injected field from the master laser and an antimode.

a) Numerical solution of the phase equation (2.81b): optical phase Ψ as a function of time, in units of the delay. The solution shape is a smoothed square wave with a period approximately equal to twice the delay.

b) Time series of the optical phase Ψ computed from the full laser rate equations (2.19), in the same conditions as for Fig. 2.13a, and with $\varepsilon = 6.25 \cdot 10^{-2}$. The agreement between Figs. 2.12a and 2.12b is excellent: the exact and approximate solutions are visually undistinguishable.

solutions can be determined by solving the discrete-time map numerically. A bifurcation diagram is represented in Fig. 2.13. There again, the detuning δ is chosen to be resonant with an antimode. The optical injection rate λ is selected as a control parameter. We see that, as λ is decreased below the primary Hopf bifurcation point $\lambda = \lambda_{H'}(\delta, \kappa, \vartheta)$, the phase-locked state loses stability in favor of a branch of stable period- $2T$ solutions. Stable period- $2T$ dynamics cannot be observed for arbitrarily low values of the injection rate, however, because the period- $2T$ branch presents a limit point. The branch of unstable period- $2T$ solutions emerging at the limit point is also represented, and extends arbitrarily far in the direction of increasing λ .

2.6 Summary

In this chapter, advanced averaging techniques valid for strongly nonlinear but weakly damped oscillators have been used for a laser problem exhibiting multiple instabilities under the effect of a small optical perturbation. The laser rate equations were reduced to a pair of averaged equations governing the time evolution of the optical phase and the relaxation oscillation amplitude. The averaged equations are a good starting point

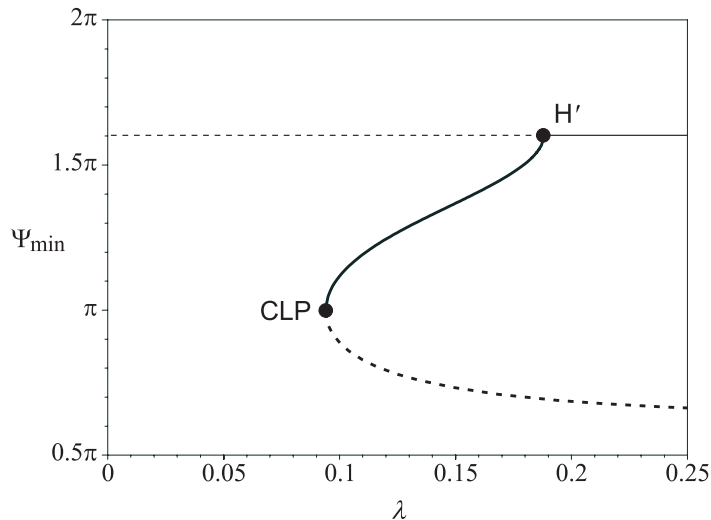


Figure 2.13: Bifurcation diagram for the laser subject to both optical injection and feedback. Parameter values are $\alpha = 3$, $T = 40$, $\kappa = 0.095$, and $\vartheta = \frac{1}{2}\pi$. The detuning value, $\delta = 0.0428$, is chosen so that exact resonance is achieved between the injected field from the master laser and an antimode. The thin straight line represents a stationary phase solution of Eq. (2.114) (the phase-locked antimode) as a function of the optical injection rate λ . The thick curve represents minima of period- $2T$ square-wave solutions of Eq. (2.114). Stable and unstable solutions are represented as solid and dashed lines, respectively. As the optical injection rate is decreased, the phase-locked state is destabilized at the period- $2T$ oscillation threshold (H'). There, a stable branch of periodic square wave solutions emerges and develops, until it is destroyed in a cycle limit point (CLP), where the stable periodic solution collapses onto an unstable one.

for analysis because sustained laser relaxation oscillations now correspond to steady state solutions of these equations. Compared to previous applications of an averaging method, the algebraic manipulations are limited. Two problems were treated specifically: the semiconductor laser subject to optical injection, and the semiconductor laser subject to both optical injection and feedback.

For the first problem, it was possible to obtain averaged equations valid for arbitrary values of the relaxation oscillation amplitude. This has an important consequence from a dynamical point of view. If the two relevant time scales of the problem (*i.e.*, the relaxation oscillation frequency and damping rate) are sufficiently well separated, and if the optical injection rate and detuning are sufficiently weak (in the sense that they scale as the ratio of these two time scales), then the laser rate equations remain an essentially bidimensional system for arbitrary values of the oscillation amplitude. Under these conditions, the system cannot display more complex dynamics than periodicity in the relaxation oscillation amplitude, which means quasiperiodicity in the light intensity. Departure from these ideal conditions may, of course, result in higher complexity, as extensively illustrated in recent numerical studies [80, 125].

Although the averaged equations valid for arbitrary amplitude represent an important tool for our understanding of the laser dynamics, a complete study remains a difficult project because explicit analytical expressions of these equations are unavailable. Therefore, in order to have an analytically tractable problem, we considered the case of harmonic relaxation oscillations, which leads to two distinct asymptotic limits. The first one is the case of vanishingly weak oscillations, where we restricted the analysis to leading-order contributions in the oscillation amplitude. The role of the higher order nonlinear terms has not been investigated. Recent studies [67, 136] have emphasized the effects of some of these terms. The determination of the higher order terms is relatively straightforward from the general formulation of the averaged equations. The second limit considered is the case of large α , where the oscillations remain harmonic away from Hopf bifurcation points. The detailed investigation of these two limits led to the analytical construction of a complete mapping of the different dynamical regimes observable in the parameter domain considered. The validity of the analytical predictions is discussed by comparing numerical bifurcation diagrams obtained from the averaged equations and from the original rate equations. We conclude that the averaged equations capture the main dynamical features of the original laser equations for realistic values of α .

The second problem treated is the semiconductor laser subject to both optical injection and feedback. Using small-amplitude averaged equations, we studied the phase-locking of feedback-induced external cavity modes onto the injected field. A complete stability analysis of the locked state of the laser has been performed. In addition to the limit point bifurcations that constitute the boundary of the locking domain and the Hopf bifurcation to sustained relaxation oscillations, we found a third kind of periodic instability, leading to square-wave like modulations of the optical phase with a period equal to twice the feedback delay. This new kind of instability has no counterpart in the cases of either pure injection or pure feedback, and results from the interplay between these two perturbations. It takes place near resonances between the injected field and antimode frequencies, and constitutes the mechanism that is responsible for the instability of antimodes as the optical injection rate goes to zero. Periodic solutions have been computed numerically from both the averaged phase equation and the original rate equations, and the agreement is excellent. We also identified a limit point bifurcation of the branch of square-wave solutions. Its existence implies that square-wave dynamics cannot take place for arbitrarily weak optical injection.

Chapter 3

Semiconductor laser subject to strong optical injection

“Allow me to express now, once and for all, my deep respect for the work of the experimenter and for his fight to wring significant facts from an inflexible Nature, who says so distinctly ‘No’ and so indistinctly ‘Yes’ to our theories.”

—Hermann Weyl

3.1 Introduction

In Chapter 2, we examined the effect of a weak optical perturbation on a semiconductor laser. In particular, we considered, in Sec. 2.4, the case of optical injection from a second laser, and determined analytically the boundaries of different domains in injection parameter space corresponding to different kinds of dynamical responses of the laser. The analysis was based on the assumption of weak injection rate and detuning, and we found bifurcations to periodic and quasiperiodic oscillations. It is known, however, that more complex time-periodic regimes progressively appear as the injection level is further increased, and that a chaotic output is even possible. In the present chapter, we again consider the optically injected semiconductor laser, but this time we do not assume that the injection parameters are small. A typical bifurcation diagram is shown in Sec. 3.2, and several modes of laser operation are identified in different parameter domains. We then focus on two distinct dynamical regimes, characterized by two distinct orders of magnitude of the injection rate. Both works have been done in collaboration with the research groups of A. Gavrielides and T. B. Simpson.

Despite its great practical simplicity, the injected semiconductor laser is a dynamical system of tremendous richness. A whole Ph. D. thesis has been devoted to its study recently [124], and yet it would seem that the discovery of new dynamical behaviors is never to come to an end. The first goal of this chapter is to report and explain the existence of a regime of period-three subharmonic oscillations in the case of perfect tuning between the master and slave lasers [41]. Previously, period-tripled oscillations

have been found for periodically modulated lasers. They have been determined numerically and analytically for class B lasers [14, 81]. Experiments using a parametrically modulated CO₂ laser have shown low-amplitude period-tripled oscillations appearing close to a period doubling bifurcation [94]. These regimes are not exceptional for modulated class B lasers because the laser rate equations are equivalent to the equations of a nearly conservative oscillator. Provided the damping rate of the laser relaxation oscillations is sufficiently small, a low-amplitude periodic modulation of a parameter may sustain a large number of periodic states [49]. Period-tripled oscillations have also been observed numerically and experimentally in optically injected semiconductor lasers in cases of significant master-slave detuning [23, 126, 131]. In particular, in [126, 131], this behavior was clearly associated to a resonance tongue for negative detuning. Here, period-tripled dynamics is reported for the first time in the perfectly tuned case. The phenomenon is presented and discussed in Sec. 3.3. An account of its experimental observation by Simpson is given in Sec. 3.3.1. It is then explained theoretically in Sec. 3.3.2 by the means of numerical bifurcation analysis of the laser rate equations. Finally, the existence of period-tripled solutions in a simplified equation is examined in Sec. 3.3.3.

The second problem considered in this chapter is the optically injected semiconductor laser operating in a regime of large-amplitude intensity oscillations, and subject to a weak harmonic modulation of the pumping current. Experiments have demonstrated that limit-cycle oscillations can be phase-locked to the modulation signal, if the two frequencies are sufficiently close to each other [105]. Because the optical frequency is also locked to the injected field, we thus have a state where the laser is doubly locked to the cw optical injection and a current modulation. The output power then exhibits a deep, high quality microwave oscillation. Such devices can be promising for a number of applications in the area of optical communications or optical control of antennas, where a spectrally pure oscillator with frequencies in the tens of GHz that can easily interface with optical systems is required [105]. In Sec. 3.4, we model such a double-locking experiment using the laser rate equations (2.14), which are then analyzed by combined analytical and numerical bifurcation techniques. Our approach [87, 89] differs from a previous analysis based on large values of the linewidth enhancement factor, where only periodic solutions were constructed [40]. Here, in contrast, we are able to investigate both periodic (double-locked) dynamics and quasiperiodic (running-phase) dynamics. In Sec. 3.4.1, we derive an equation governing the amplitude of the intensity oscillations using the method of multiple scales. The injection rate is then taken as a control parameter, and numerical bifurcation diagrams for the amplitude equation are then constructed and analyzed in Sec. 3.4.2. They are validated by comparing our results with the solutions of the full rate equations in Sec. 3.4.3. In Sec. 3.4.4, we present another set of bifurcation diagrams of the amplitude equation where the master-slave detuning is chosen as a control parameter. We show that this leads to cases of bistability. Finally, our theoretical diagrams are compared with experimental diagrams by Simpson in Sec. 3.4.5, which leads to the confirmation of the existence of small domains of bistability.

The main results presented in this chapter are summarized in Sec. 3.5.

3.2 High-injection laser responses

The theoretical treatment of the two problems presented in this chapter is based on the rate equations (2.14). The injected signal from the master laser is modelled as $\mathcal{E}_i = \Lambda \exp(i\Delta s)$, where Λ and Δ represent the injection rate and detuning, respectively. In the approach of Chapter 2, these quantities were assumed $O(\varepsilon)$ small and were written as $\Lambda \equiv \varepsilon\lambda$, $\Delta \equiv \varepsilon\delta$. Here, in contrast, Λ and Δ are assumed $O(1)$ quantities. We also redefine the electric field envelope as $\mathcal{E} = E \exp(i\Delta s)$, so that frequency offsets are now measured with respect to the master laser frequency. Written in terms of the injection parameters Λ and Δ and the new field variable E , the rate equations are given by:

$$\frac{dE}{ds} = \frac{1}{2} [(1 + i\alpha)Z - (1 + i\alpha')\beta (|E|^2 - 1)] E - i\Delta E + \Lambda, \quad (3.1a)$$

$$\frac{dZ}{ds} = M(s) - [1 + \varepsilon p (Z - \beta |E|^2)] (|E|^2 - 1) - \varepsilon Z. \quad (3.1b)$$

A numerically computed bifurcation diagram of the above equations is represented in Fig. 3.1. There, the injection rate Λ is taken as a control parameter, and the master laser is assumed to be perfectly tuned to the slave laser ($\Delta = 0$). The pump modulation term $M(s)$ is set to zero. Several bifurcation features deserve to be pointed out. First, we recover, at $\Lambda \simeq 0.05$, the Hopf bifurcation to sustained relaxation oscillations from the perturbative analysis of Chapter 2. Second, a period-doubling cascade to chaos takes place within a small range of values of Λ , with an accumulation point near $\Lambda \simeq 0.2$. Chaos persists up to $\Lambda \simeq 0.5$, after which we observe an inverse period-doubling sequence leading back to periodic dynamics. Third, we note that this stable oscillatory state is maintained over a wide range of injection rate values ($0.5 \lesssim \Lambda \lesssim 2.4$, with a period-doubled “bubble” within $0.8 \lesssim \Lambda \lesssim 1$). Finally, the laser output becomes again steady as $\Lambda \gtrsim 2.4$. The two problems treated in this chapter correspond to distinct parameter domains. Period-tripled dynamics has been found for moderate injection, alongside the period-doubling route to chaos. Simpson’s double-locking experiment was performed with a higher injection level, in the region of large oscillations bounded by the higher Hopf bifurcation point ($\Lambda \lesssim 2.4$ in Fig. 3.1).

3.3 Period-tripled limit cycles

3.3.1 Experimental data

We first give a brief description of the experiment by T. B. Simpson leading to the observation of period-three limit cycles (full details are given in [41]). The experimental apparatus is shown in Fig. 3.2. Two current- and temperature-stabilized, dc-biased

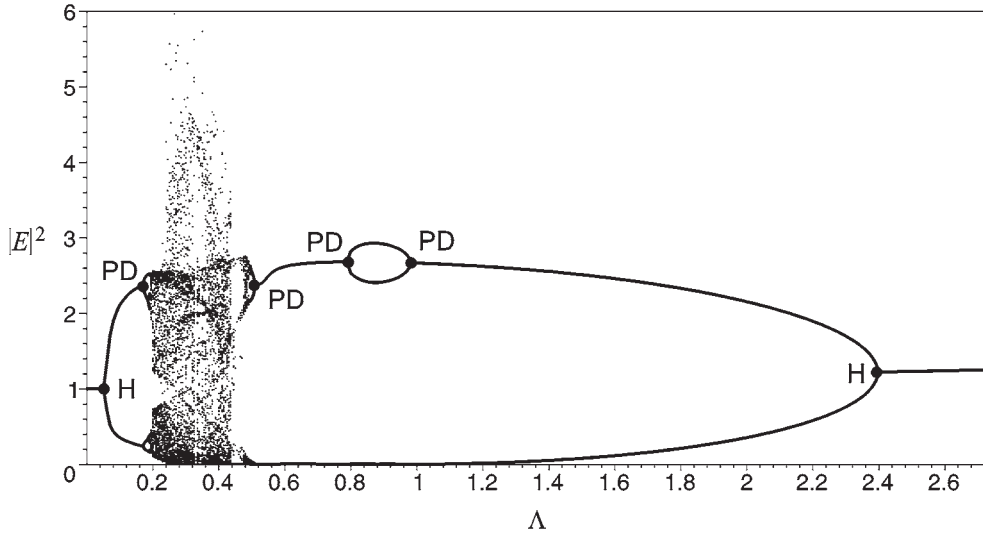


Figure 3.1: Numerical bifurcation diagrams for the laser subject to optical injection, computed from the full laser rate equations (3.5). The extrema of the intensity are shown as a function of the injection rate Λ . The symbols H and PD indicate Hopf and period doubling bifurcations, respectively. Parameter values are $\alpha = 3.2$, $\alpha' = 3.2$, $\beta = 0.011$, $\varepsilon = 0.1557$, $p = 0.4898$, and $\Delta = 0$ (no detuning). We recover, at $\Lambda \simeq 0.05$, the Hopf bifurcation point from the low-injection analysis of Chapter 2. Note the period-doubling cascade leading to chaos for moderate injection, and the large domain of regular intensity oscillations that terminates at a second Hopf bifurcation point for high injection.

semiconductor lasers are in a master-slave configuration. Part of the emitted light of the master laser is injected into the slave laser after having passed through an optical isolator to block reflections of radiation back into the master laser. The amplitude of the injected signal can be adjusted by a variable attenuator, and the offset of the injected frequency relative to the free-running frequency of the slave laser can be readily shifted by varying the injection current to the master laser. The output of a third, tunable laser is passed through an acousto-optic modulator where part of the beam is deflected and shifted in frequency by 80 MHz. The deflected beam can be attenuated and injected into the slave laser as a weak optical probe (more on this below).

The undeflected beam is used as a local oscillator at the photodetector for coherent detection of the emitted optical field from the slave laser. The output from the slave laser is mixed with this part of the output from the tunable laser and monitored by a fast photodiode followed by a broadband amplifier and a microwave spectrum analyzer. This combination is used to make heterodyne measurements and generate the spectra presented here. The microwave spectrum analyzer is set to monitor the component of the detected signal at 80 MHz, and the tunable laser frequency is scanned about the output frequency of the slave laser. In the absence of the probe input to the slave laser, and when the resolution of the spectrum analyzer is fairly broad (3 MHz), the

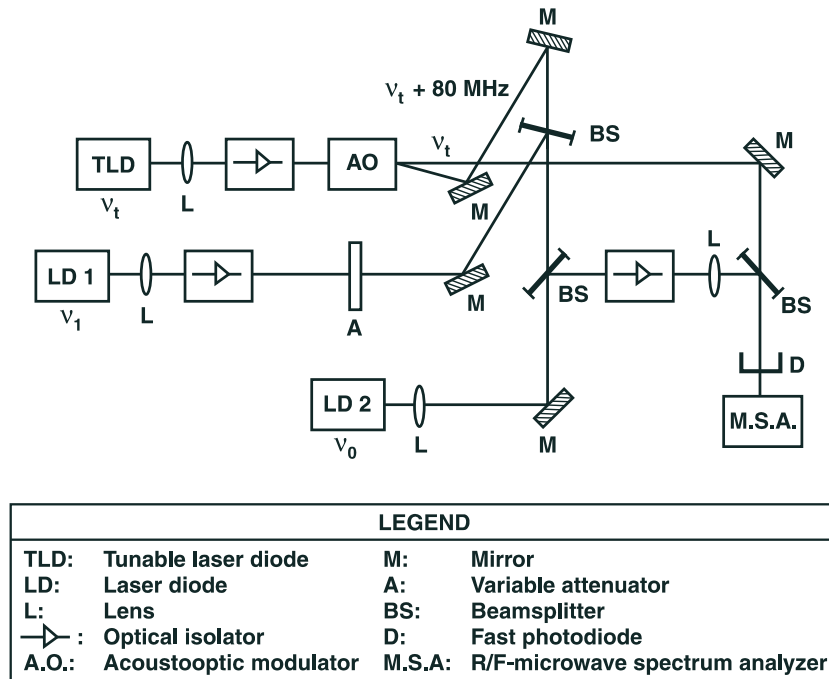


Figure 3.2: The experimental apparatus used by T. B. Simpson for the detection of period-tripled limit cycles in optically injected semiconductor lasers (figure created by T. B. Simpson, reproduced from [41]).

photodetector measures the beat between the slave and tunable laser at 80 MHz. The optical spectrum of the slave laser is then generated as the tunable laser is scanned in frequency. Because of the 80 MHz mixing frequency, spectral features narrower than approximately 160 MHz are lost, due to the double measurement of features at offsets of both ± 80 MHz.

When the probe beam is injected into the slave laser and the resolution bandwidth of the spectrum analyzer is narrowed to 100 kHz or less, the regeneratively amplified probe signal becomes the strongest component at 80 MHz, and the spectrum analyzer records this spectrum as the tunable laser is scanned in frequency.

The optical spectrum of the free-running slave laser consists of a single strong optical mode and several weak side modes, all more than 30db below the oscillating mode. Thus the laser is essentially operating on a single longitudinal mode. Examination of the optical and regenerative amplification spectra reveals the average dynamics of the slave laser and it is easily apparent whether the laser is operating with steady state output, or in a periodic, oscillating state. The frequency of oscillation is also readily determined from the frequency separation of spectral features. Fig. 3.3 shows a progression of spectra for the optical output and regenerative amplification signal as a function of injection rate. The spectra are taken with the master laser perfectly tuned to the free-running slave laser frequency.

In the absence of optical injection (Fig. 3.3a), the optical spectrum of the free-

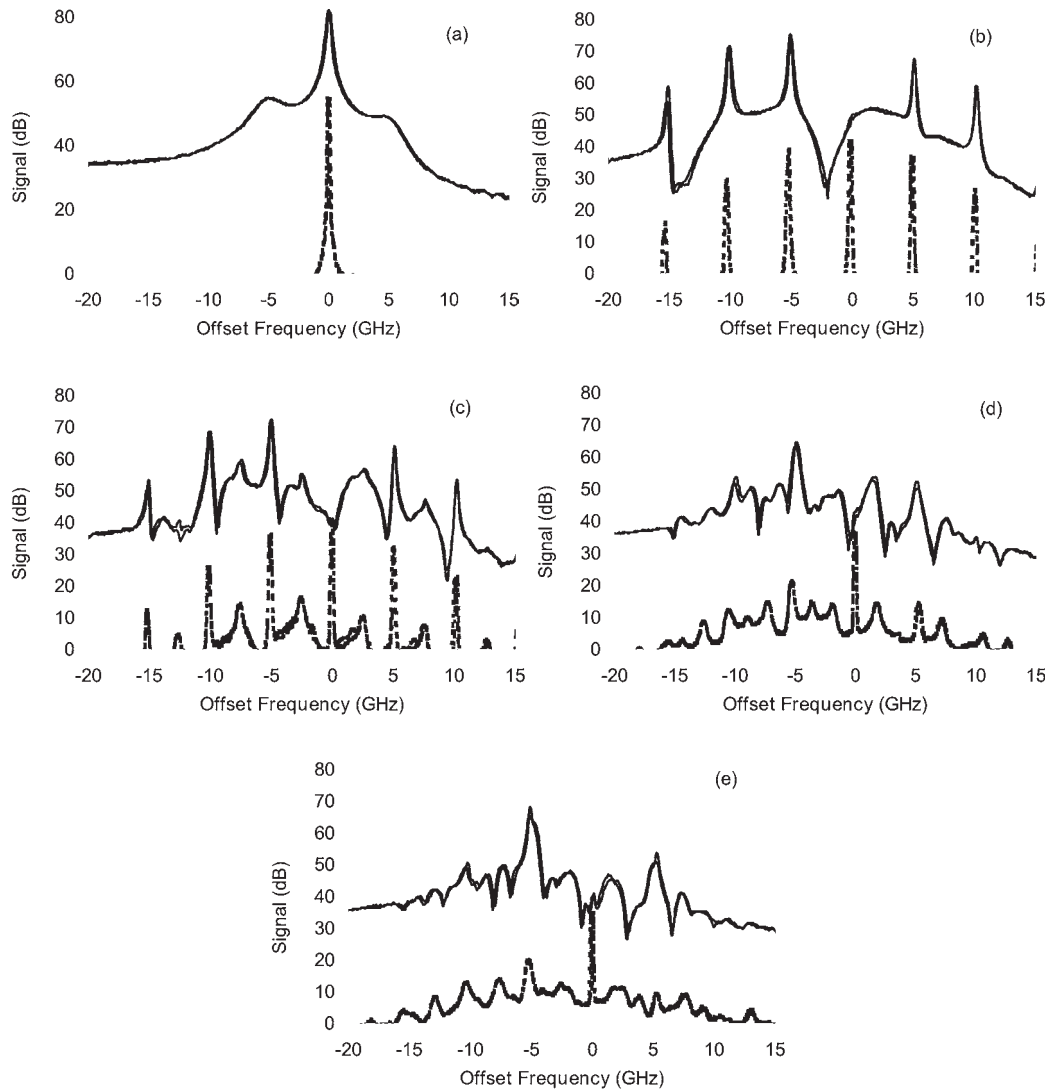


Figure 3.3: Experimental optical spectra for the semiconductor laser subject to optical injection, by T. B. Simpson (figure created by T. B. Simpson, reproduced from [41]). The master laser is perfectly tuned to the free-running frequency of the slave laser. Lower dashed curve: spectra of the slave laser output. Upper solid curve: spectra of the regenerative amplification of a weak optical probe. Frequency is relative to the free-running optical frequency and signal level is relative to noise background.

- (a) Free-running operation.
- (b) Limit cycle spectra at $5\times$ and $4\times$ the Hopf bifurcation level of injection for the optical and regenerative amplification spectra, respectively.
- (c) Period-two spectra at $9\times$ and $11\times$.
- (d) Period-tripled spectra at $15\times$ and $14\times$.
- (e) Chaotic spectra at $17\times$ and $16\times$.

running laser consists of a single narrow feature indicating that the laser is operating in the steady state. The regenerative amplification spectrum shows broad, weak, asymmetric¹ sidebands about the central peak with maxima offset by the relaxation resonance frequency. Injecting a sufficiently strong optical signal causes relaxation oscillations to become undamped. The optical spectrum now consists of a series of peaks offset by approximately the relaxation resonance frequency, as shown in Fig. 3.3b. The presence of many peaks indicates the anharmonicity of the laser output oscillations: in terms of the theoretical considerations presented in Chapter 2, this means that a large number of terms are significant in the power series expansion (2.38b) of the laser intensity. The regenerative amplification spectra shows a similar set of peaks, with the notable exception of a peak at the injection frequency, superimposed on a broad, structured background feature. At higher injection levels (Fig. 3.3c), new spectral components appear at frequencies half way between the resonance frequency lines. The appearance of these features indicates that a period doubling bifurcation has occurred. Increasing the injection level still further causes the features in the spectra to shift out of a period-two progression (Fig. 3.3d): frequencies at 1/3 and 2/3 of the fundamental frequency are now present, most clearly in the optical spectrum, suggesting that the attractor is a period-tripled limit cycle. The discrete spectral features are superimposed on a broad background feature. Finally, in Fig. 3.3e, the spectra display various broadened resonance peaks and a strong, structured background signal that is consistent with chaotic dynamics.

3.3.2 Numerical bifurcation diagrams

We now show how the existence of period-tripled limit cycles can be explained from the rate equation model (3.1). We set the pump modulation term $M(s)$ to zero, and choose the following values for the fixed parameters: $\Delta = 0$, $\varepsilon = 0.1557$, $\alpha = 3.2$, $\alpha' = 3.2$, $\beta = 0.1384$, and $p = 0.4898$. All parameters have been evaluated from the experiments. Note that the gain saturation coefficient β has been given a nonzero value. Fig. 3.4 shows a reproduction of a bifurcation diagram computed numerically by A. Gavrielides and V. Kovanis, where the injection rate Λ is taken as the control parameter. Two distinct branches of solutions are clearly identified. A first branch starts from a Hopf bifurcation point and undergoes a cascade of period doubling bifurcations to chaos; the second branch appears to be isolated and corresponds to a period-tripled regime that may itself exhibit period-doubling bifurcations. Note that the period-tripled branch overlaps with the region of chaos. Furthermore, it appears after the first period-doubled regime, in agreement with the experiments.

This bifurcation diagram is based on long-time integration of the laser equations, which only follows stable solutions. In order to demonstrate that the branch of period-tripled solutions is indeed isolated, we use AUTO, a numerical continuation software that follows branches of solutions regardless of their stability properties [21]. Fig. 3.5

¹The asymmetry is due to the fact that the carrier density modulation induced by the probe laser causes changes in the refractive index, as well as the gain, of the semiconductor medium [71].

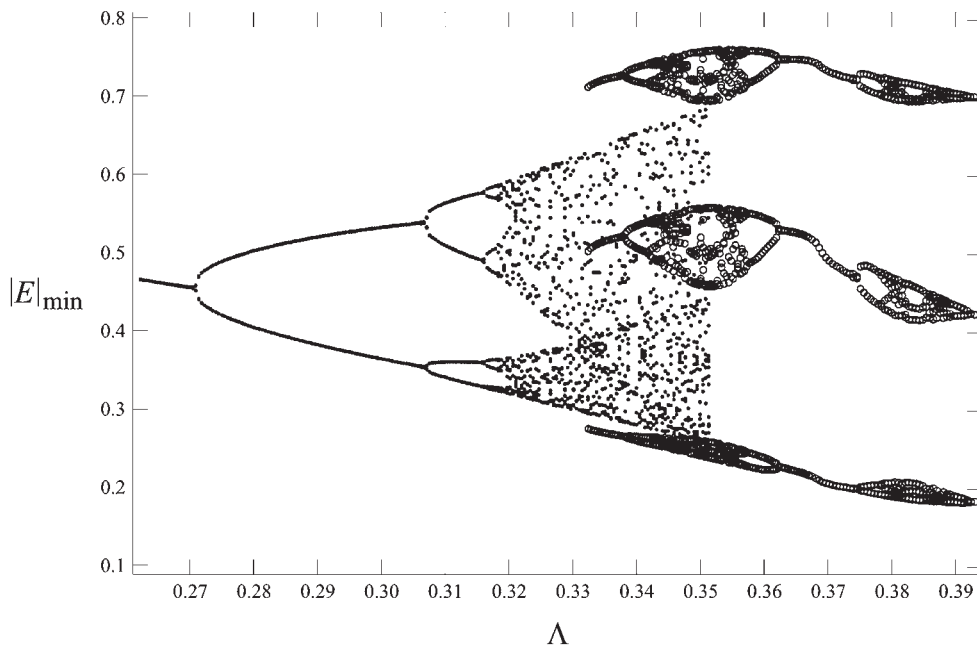


Figure 3.4: Numerical bifurcation diagram of the laser rate equations (3.1) by A. Gavrielides and V. Kovanis (reproduced from [41] and edited). The local minima of the electric field are shown as a function of the optical injection rate, for zero detuning ($\Delta = 0$). Parameter values are $\varepsilon = 0.1557$, $\alpha = 3.2$, $\alpha' = 3.2$, $\beta = 0.1385$, and $p = 0.4898$. The figure clearly shows two distinct branches of periodic solutions. First, the primary branch emerging at the Hopf bifurcation point (at $\Lambda \simeq 0.27 \cdot 10^{-3}$) is undergoing a series of period doubling bifurcations leading to a chaotic state as $\Lambda \gtrsim 0.32 \cdot 10^{-3}$. Second, an isolated branch of period-tripled solutions (represented as circles) appears suddenly at $\Lambda \simeq 0.33 \cdot 10^{-3}$. This branch of period-tripled regimes may itself exhibit several period doubling bifurcations.

represents the bifurcation diagram of the stable and unstable period-tripled solutions. The diagram clearly shows that the domain of period-tripled regime is bounded at either side by a limit point, where a stable and an unstable period-tripled limit cycle collapse.

3.3.3 A simplified phase equation

We now investigate a simplified form of the laser rate equations (3.1) derived in the asymptotic limit α large. This will unravel an interesting similarity between period-tripled limit cycles in the injected semiconductor laser and the dynamics of an oscillator driven by an external, subharmonic modulation. Specifically, we neglect the effect of gain saturation ($\beta = 0$) and introduce the scaled dynamical variables and injection rate

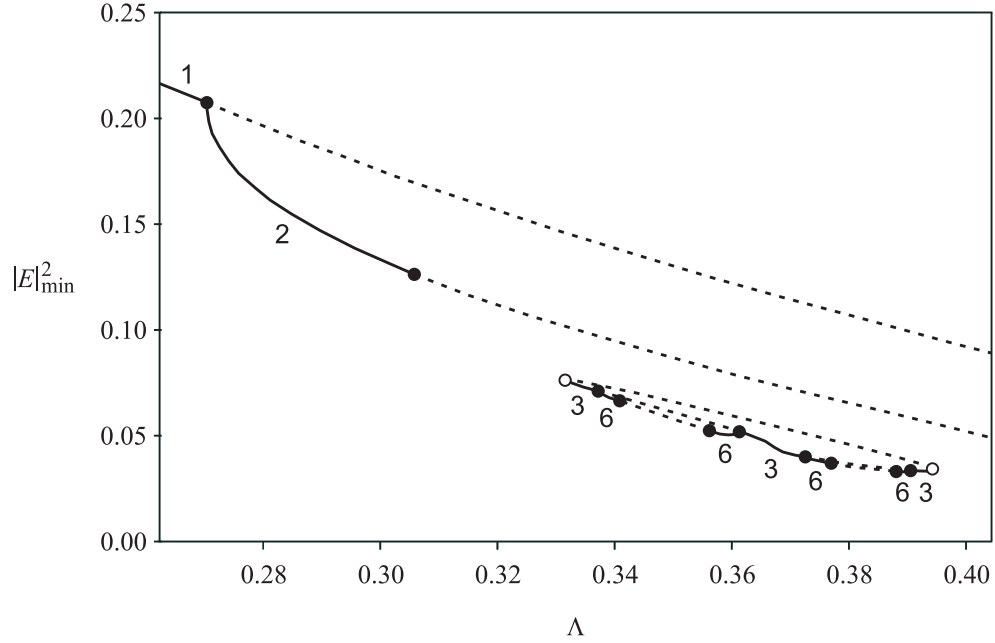


Figure 3.5: Numerical bifurcation diagram of the laser rate equations (3.1) computed with AUTO. The global minima of the light intensity are represented as a function of the optical injection rate, for zero detuning. Both stable solutions (solid curves) and unstable solutions (dashed curves) are shown. Full and hollow circles indicate period-doubling bifurcations and limit points, respectively. The digits superimposed over the diagram indicate the solution periodicity (1: fundamental, 2: period-doubled, 3: period-tripled, 6: period-sextupled). Parameter values are the same as in Fig. 3.4. The diagram shows that the branch of period-tripled solutions is an isola.

as follows:

$$E = \exp\left(\frac{1}{2}\alpha^{-1}\bar{Y} + i\Psi\right), \quad Z = \alpha^{-1}\bar{Z}, \quad \Lambda = \alpha^{-1}\bar{\Lambda}. \quad (3.2)$$

Substituting these definitions into the rate equations (3.1) with $\beta = 0$ and $M(s) = 0$ leads to the following problem for \bar{Y} , Ψ , and \bar{Z} :

$$\frac{1}{2} \frac{d\bar{Y}}{ds} = \frac{1}{2}\bar{Z} + \bar{\Lambda} \cos(\Psi) + O(\alpha^{-1}), \quad (3.3a)$$

$$\frac{d\Psi}{ds} = \frac{1}{2}\bar{Z} - \Delta + O(\alpha^{-1}), \quad (3.3b)$$

$$\frac{d\bar{Z}}{ds} = -\bar{Y} - \varepsilon\bar{Z} + O(\alpha^{-1}). \quad (3.3c)$$

By eliminating \bar{Y} and \bar{Z} , Eqs. (3.3) are equivalent to a third order differential equation for Ψ given by

$$\frac{d^3\Psi}{ds^3} + \varepsilon \frac{d^2\Psi}{ds^2} + \frac{d\Psi}{ds} + \Delta + \bar{\Lambda} \cos(\Psi) = O(\alpha^{-1}). \quad (3.4)$$

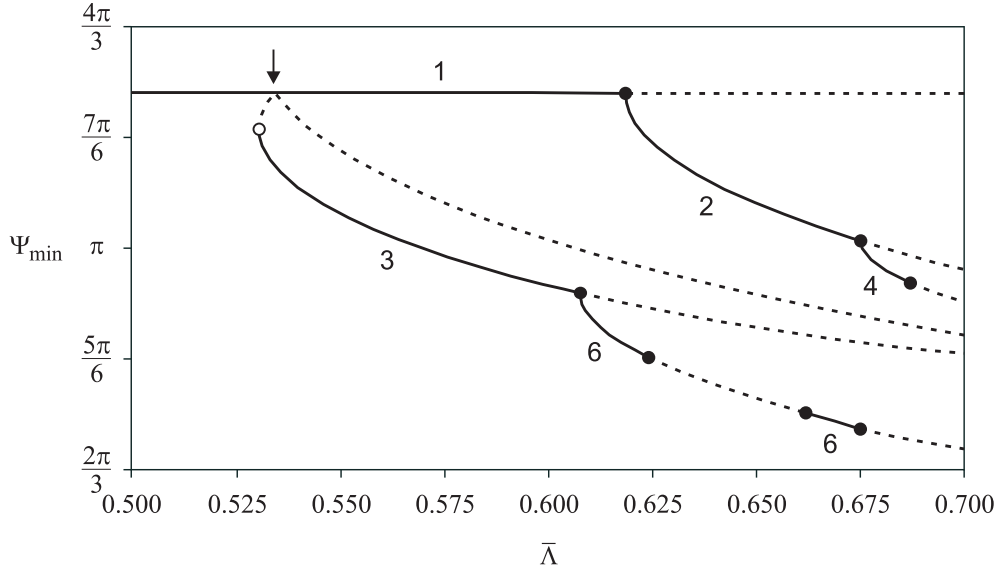


Figure 3.6: Numerical bifurcation diagram of the phase equation (3.4) computed with AUTO. The global minima of the optical phase are represented as a function of the optical injection rate, for zero detuning ($\Delta = 0$) and a very small value of the damping rate ($\varepsilon = 10^{-4}$). Stable solutions are represented as solid curves, and unstable ones are represented as dashed curves. Full and hollow circles indicate period-doubling bifurcations and limit points, respectively. The digits superimposed over the diagram indicate the solution periodicity in the same way as in Fig. 3.5. The diagram suggests that, as $\varepsilon \rightarrow 0$, the period-tripled branch connects to the fundamental one at a degenerate bifurcation point (indicated by the arrow).

Note that this equation bears some similarity to the Adler equation that we have encountered in Chapter 2, but with higher-order derivative terms accounting for a higher dimensionality of the state space. This higher complexity of the dynamics results from the fact that the injection parameters are not assumed small anymore.

The main advantage of Eq. (3.4) over the full rate equations is the fact that it depends only on two fixed parameters (ε and Δ), and only one in the perfectly tuned case $\Delta = 0$. It has been useful in earlier studies: analytical bifurcation diagrams have been constructed from this equation [26, 42], and periodic solutions were also explored experimentally in an electronic circuit implementation in which the characteristics of period-tripled solutions were clearly seen [111]. The analysis of period-tripled dynamics in this simplified equation (3.4) still requires a numerical analysis, but it leads to an interesting observation in the limit where the relaxation oscillation damping rate ε goes to zero. Fig. 3.6 shows a bifurcation diagram of the simplified equation (3.4) for $\Delta = 0$, and for a very small value of ε . The figure suggests that the unstable branch of period-tripled solutions connects to the primary branch at a degenerate bifurcation point as $\varepsilon \rightarrow 0$. This diagram is strikingly similar to the diagram of an oscillator near a Hopf bifurcation point and driven by a small-amplitude modulation with a frequency

equal to one third of the Hopf frequency (see Fig. 2 in [102]).

Differences between the bifurcation diagram of the rate equations (3.1) and the simplified equation (3.4) are quantitative. In Fig. 3.6 again, stable and unstable branches of period-tripled solutions emerge from a limit point, but this time, it is located before the first period doubling bifurcation of the primary branch (of fundamental period), in contrast to Fig. 3.5. We also note in Fig. 3.5 that the branch of period-tripled solutions is a real isola bounded by two limit points while only the left limit point was found in the case of Eq. (3.4).

Finally, we were unable to find any period-tripled solution of the full rate equations (3.1) for $\beta = 0$, $\Delta = 0$, and realistic values of the other parameters. This may explain why no such dynamics was reported in [124], where gain saturation effects have been systematically neglected. On the other hand, the simplified phase equation (3.4) has been derived for $\beta = 0$, and yet it successfully predicts period-tripled limit cycles. Their existence thus seems to require either a very large value of the linewidth enhancement factor (so that the approximations leading to the reduced equation are well justified) or a nonvanishing value of the gain saturation coefficient.

3.4 Semiconductor laser subject to optical injection and pump modulation

In Chapter 2, we gave a detailed analysis of the locking properties of a semiconductor laser subject to the injection of a weak optical signal. In Sec. 3.3, we then studied a particular aspect of the complex dynamics taking place when the injected field becomes moderately strong. Namely, we showed the existence of regimes of period-tripled intensity oscillations embedded in the domain where the primary branch of periodic oscillations undergoes a cascade of period-doubling bifurcations leading to chaos. We now consider the domain between the highest period-doubling point (at $\Lambda \simeq 1$ in Fig. 3.1) and the higher Hopf bifurcation point (at $\Lambda \simeq 2.4$) where the laser intensity exhibits regular periodic oscillations. Of particular physical and engineering interest is the effect of a weak sinusoidal modulation of the bias current, and, in particular, of how this can induce phase-locking of the intensity oscillations. The experiment that we are modelling here is thus a semiconductor laser subject to both optical injection and pump modulation (see the simplified block diagram in Fig. 3.7).

3.4.1 Normal form analysis

Our approach consists in a multiple-scale analysis of the laser rate equations (3.1) in a neighborhood of the higher Hopf bifurcation point, in the limit of a weak detuning Δ . For simplicity, we set the relaxation oscillation damping rate ε and the gain saturation

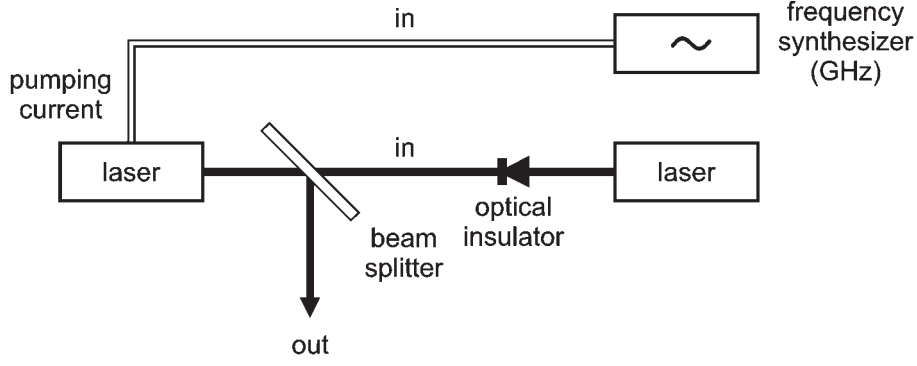


Figure 3.7: A simplified block-diagram of a semiconductor laser subject to both optical injection from another laser and modulation of the pumping current.

coefficient β to zero. Eqs. (3.1) then reduce to

$$\frac{dE}{ds} = \frac{1}{2}(1 + i\alpha)ZE - i\Delta E + \Lambda, \quad (3.5a)$$

$$\frac{dZ}{ds} = M(s) - (|E|^2 - 1). \quad (3.5b)$$

Our first goal is the research of analytical expressions for the critical value $\tilde{\Lambda}$ of the injection rate and the corresponding oscillation frequency $\tilde{\Omega}$ as functions of the only remaining fixed parameter, α . They are obtained from a stability analysis of the above equations, which is carried out in Appendix 3.A. We find:

$$\tilde{\Lambda} = \sqrt{\frac{\alpha^2 - 1}{2}}, \quad \tilde{\Omega} = \sqrt{\frac{\alpha^2 + 1}{2}}. \quad (3.6)$$

We further assume that the weak modulation term $M(s)$ is harmonic and nearly resonant with the intrinsic oscillation frequency:

$$M(s) \equiv m \cos(\Omega s), \quad (3.7)$$

where $|\Omega - \tilde{\Omega}| \ll \tilde{\Omega}$ and $0 < m \ll 1$. Under the conditions that the detuning is weak ($|\Delta| \ll \tilde{\Omega}$) and the injection rate is close to its critical value ($\Lambda - \tilde{\Lambda} \ll \tilde{\Lambda}$), we perform a multiple scale analysis of Eqs. (3.5). Full calculation details are given in Appendix 3.B. We find that leading-order approximation of the light intensity is given by

$$|E|^2 = 1 + \hat{A} \exp(i\Omega s) + \hat{A}^* \exp(-i\Omega s) + O\left(|\hat{A}|^2\right), \quad (3.8)$$

where the complex amplitude \hat{A} varies slowly in time according to the equation:

$$iC_\Omega \frac{1}{\tilde{\Omega}} \frac{d\hat{A}}{ds} = m + \hat{A} \left(C_\Omega \frac{\Omega - \tilde{\Omega}}{\tilde{\Omega}} + C_\Lambda \frac{\Lambda - \tilde{\Lambda}}{\tilde{\Lambda}} + C_\Delta \frac{\Delta}{\tilde{\Omega}} + C_3 |\hat{A}|^2 \right). \quad (3.9)$$

The oscillations are harmonic in first approximation. The new, complex variable \widehat{A} combines the oscillation amplitude as its modulus and the phase between the intensity oscillations and the modulation signal as its argument. A value of $\arg(\widehat{A})$ that is constant in time means that phase locking to the reference frequency is achieved. The amplitude equation (3.9) resembles the normal form of a Hopf bifurcation, but with an additional term accounting for the nearly resonant modulation. The derivation of such an equation is well documented for simple oscillator problems [62, 102]. For problems like our laser equations (3.5), the perturbation analysis is algebraically longer but the asymptotic method is technically the same. The complex coefficients C_Ω , C_Λ , C_Δ , and C_3 appearing in Eq. (3.9) depend only on the linewidth enhancement factor α and are given at the end of Appendix 3.B.

3.4.2 Bifurcation diagrams (controlling the injection rate)

Steady-state solutions of the amplitude equation (3.9) correspond to phase-locked limit cycles of the original laser equations. In that regime, the optical phase of the emitted light is locked to the injected field, whereas the phase of the intensity oscillations is locked to the periodic modulation of the pumping current. Besides such double-locked states, the amplitude equation may admit periodic solutions, meaning that the phase between the intensity oscillations and the pump modulation varies slowly in time. The corresponding solutions of the rate equations are quasiperiodic, as they are characterized by two distinct frequencies: the pump modulation frequency Ω , and the beat frequency between the modulation and the intrinsic oscillation frequency. Therefore, our multiple scale analysis reduces the study of both locked (periodic) and non-locked (quasiperiodic) intensity oscillations to the simpler task that consists in finding constant and periodic solutions of the amplitude equation. In this section, we determine bifurcation diagrams for both kinds of solutions using the numerical continuation software AUTO [21]. This allows the determination of both stable and unstable branches of solutions, and, therefore, contributes to a better understanding of the laser bifurcation possibilities.

We first present, in Fig. 3.8, a series of bifurcation diagrams where the injection rate Λ is taken as a control parameter, all other parameters being fixed. The detuning Δ is set to zero, and the value of the modulation frequency Ω is chosen so that resonance between the modulation signal and the intrinsic oscillation frequency occurs for a value of Λ slightly below the Hopf bifurcation point $\widetilde{\Lambda}$. Each diagram in Fig. 3.8 corresponds to a different value of the modulation index m . Fig. 3.8a depicts the trivial case of no modulation ($m = 0$). As the injection rate is decreased below the Hopf bifurcation point, the basic steady state solution $\widehat{A} = 0$ transfers its stability to a stable limit cycle, as expected: this diagram matches Fig. 3.1 close to the higher Hopf bifurcation point. Fig. 3.8b corresponds to a nonzero but very small modulation index. There, the steady state solution $\widehat{A} = 0$ is replaced by a branch of weak, $O(m)$ modulations of the intensity. The Hopf bifurcation point now becomes a quasiperiodic bifurcation as a consequence of the presence of the new frequency Ω in the system, and the branch of limit cycles

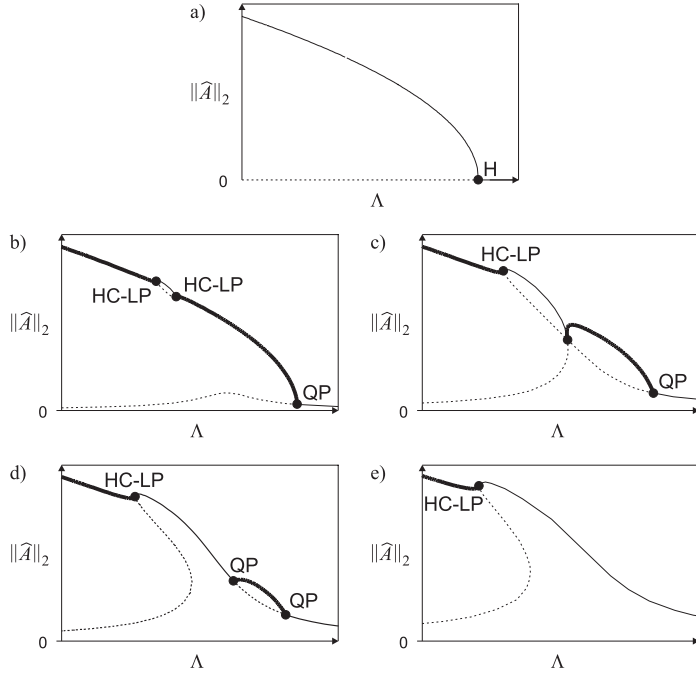


Figure 3.8: Numerical bifurcation diagrams for the laser subject to optical injection and pump modulation, computed from the amplitude equation (3.9). The L_2 -norm of the amplitude \hat{A} is represented as a function of the optical injection rate Λ (with an arbitrary offset) for several values of the modulation index m . Units are arbitrary. Fixed parameter values are $\alpha = 5$ and $\Delta = 0$. The modulation frequency is chosen to be slightly larger than the limit cycle frequency at the Hopf bifurcation. Thin curves represent periodic solutions. Thick curves represent non-locked, quasiperiodic dynamics. Solid and dashed curves represent stable and unstable solutions respectively. The meaning of the bifurcation labels is as follows: H = Hopf bifurcation, QP = quasiperiodic bifurcation, HC-LP = homoclinic-limit point bifurcation between a pair of limit cycles and a torus attractor.

a) $m = 0$: no modulation. The steady state ($\hat{A} = 0$) loses stability in favor of limit-cycle oscillations at the Hopf bifurcation point.

b) $0 < m < m_1$: very weak modulation. The steady state has become weakly modulated, and the limit-cycle oscillations have become quasiperiodic. A small locking range, bounded by two homoclinic-limit point bifurcations, is observed.

c) $m = m_1$: this is a critical value of the modulation index where two branches of periodic solutions connect.

d) $m_1 < m < m_2$. The rightmost homoclinic-limit point bifurcation is now replaced with a second quasiperiodic bifurcation. Also, the formerly disconnected branches of periodic solutions have merged.

e) $m > m_2$: strong modulation. The two quasiperiodic bifurcation points have collapsed. The locking range and the region of where spontaneous oscillations are not excited have now merged into one stable, continuous branch of limit cycles.

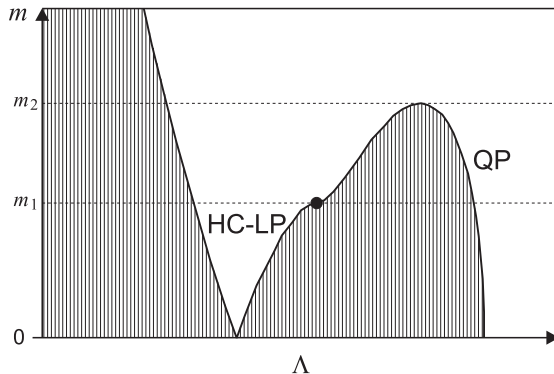


Figure 3.9: Numerical map of the possible responses of the laser subject to optical injection and pump modulation, computed from the amplitude equation (3.9). The dynamics is mapped in the m vs. Λ plane. Units are arbitrary. Fixed parameter values are identical as in Fig. 3.8, and the meaning of the bifurcation labels is the same. White and vertical-hatched regions mean phase-locked and quasiperiodic dynamics, respectively. The two threshold values of m relevant to Fig. 3.8 are indicated.

is now a branch of quasiperiodic oscillations, except in an $O(m)$ neighborhood of the resonance between the modulation frequency and the intrinsic oscillation frequency, where we observe a “bubble” of limit cycles locked to the modulation signal. The locking domain is bounded at either side by an homoclinic-limit point bifurcation: as the injection rate approaches the resonance, the beat frequency goes to zero, and the destruction of the non-locked attractor is accompanied by the birth of a pair of locked limit cycles. This is the same mechanism as Adler’s mechanism for steady state locking, but transposed to the case of periodic solutions.

There exists a critical value m_1 of the modulation index such that the bubble of locked limit cycles is connecting the branch of weakly modulated intensity, as shown in Fig. 3.8c. Almost simultaneously, the rightmost homoclinic-limit point bifurcation turns into a second quasiperiodic bifurcation, as seen in Fig. 3.8d. We also note that, for m slightly larger than m_1 , the two connected branches of limit cycles unfold and form an S-shaped curve, but there is no bistability involved, as only the upper part of the S curve is stable. Increasing m further, we see that the two quasiperiodic bifurcation points are coming closer to each other until they eventually collide and disappear at a second critical value m_2 of the modulation index. Consequently, for a large enough modulation index, quasiperiodic bifurcations are no more possible (see Fig. 3.8e): the branch of weakly modulated intensity and the branch of large-amplitude phase-locked limit cycles have merged into a single branch of periodic solutions where the oscillation amplitude grows continuously as the injection rate is decreased. The leftmost homoclinic-limit point bifurcation exists for all realistic values of m , and therefore the locking domain is always bounded to the left.

Fig. 3.9 summarizes the different responses of the laser in the m vs. Λ parameter space. Each diagram of Fig. 3.8 corresponds to the sweeping across a horizontal

line in Fig. 3.9 from right to left. We distinguished three distinct locking scenarios depending on the value of the modulation index. For small m (Fig. 3.8b, Fig. 3.9 for $m < m_1$), intensity oscillations lock through a homoclinic-limit point bifurcation as Λ decreases, which is characterized by one of the frequencies going to zero. For intermediate values of m (Fig. 3.8d, Fig. 3.9 for $m_1 < m < m_2$), locking occurs through a quasiperiodic bifurcation, where the depth of the slow oscillation amplitude variations becomes vanishingly small. Finally, for large values of m (Fig. 3.8e, Fig. 3.9 for $m > m_2$), no abrupt locking transition takes place: instead, the weakly modulated solution deforms continuously into a large-amplitude locked limit cycle. In all cases, the leftmost boundary of the locking domain remains a homoclinic-limit point bifurcation.

3.4.3 Comparison of the reduced and full models

We now compare the bifurcation diagrams obtained in the previous subsection by solving the amplitude equation (3.9) and bifurcation diagrams obtained by solving the full rate equations (3.1). To this end, we use AUTO again to determine branches of limit cycle solutions. Note, however, that AUTO is unable to follow branches of quasiperiodic solutions, and therefore only partial diagrams are obtained. In order to compare both sets of diagrams, we need a way to evaluate the amplitude $|\hat{A}|$ from the rate equations variables. To this end, we use the relation

$$\sqrt{\frac{\|E\|_2^2 - |\langle E \rangle|^2}{\|E\|_2^2}} = |\hat{A}| + O\left(|\hat{A}|^2\right), \quad (3.10)$$

where $\|E\|_2^2$ is defined as the squared L_2 -norm of the electric field and $\langle E \rangle$ denotes the time average of the electric field envelope over a modulation period. The above relation can be proven from the identity $\|E\|_2^2 - |\langle E \rangle|^2 = \|E - \langle E \rangle\|_2^2$ and the expressions for the $O(1)$ and $O(\hat{A})$ contributions to the electric field given in Appendices 3.A and 3.B. Therefore, we use the left-hand side of Eq. (3.10) as an estimation for the amplitude $|\hat{A}|$. This quantity has a simple physical meaning in terms of optical spectra: its square represents the ratio of the field power in the sideband modes to the total field power.

In the bifurcation diagrams shown in Fig. 3.10, the following values of the fixed parameters have been chosen: $\alpha = 5$, $\beta = 0$, $\varepsilon = 0.1704$, $p = \frac{1}{3}$, $\Delta = 0$, and $\Omega = 3.336$. This choice is equivalent to the parameter values considered by A. Gavrielides *et al.* in [40] in order to model previous experiments by T. B. Simpson [105]. Note that, for these parameter values, the amplitude $|\hat{A}|$ is not quite small in Fig. 3.10. Therefore, the asymptotic diagrams of Fig. 3.8 are in very satisfactory agreement with the exact ones, given that the derivation of the reduced model rests upon a small-amplitude limit.

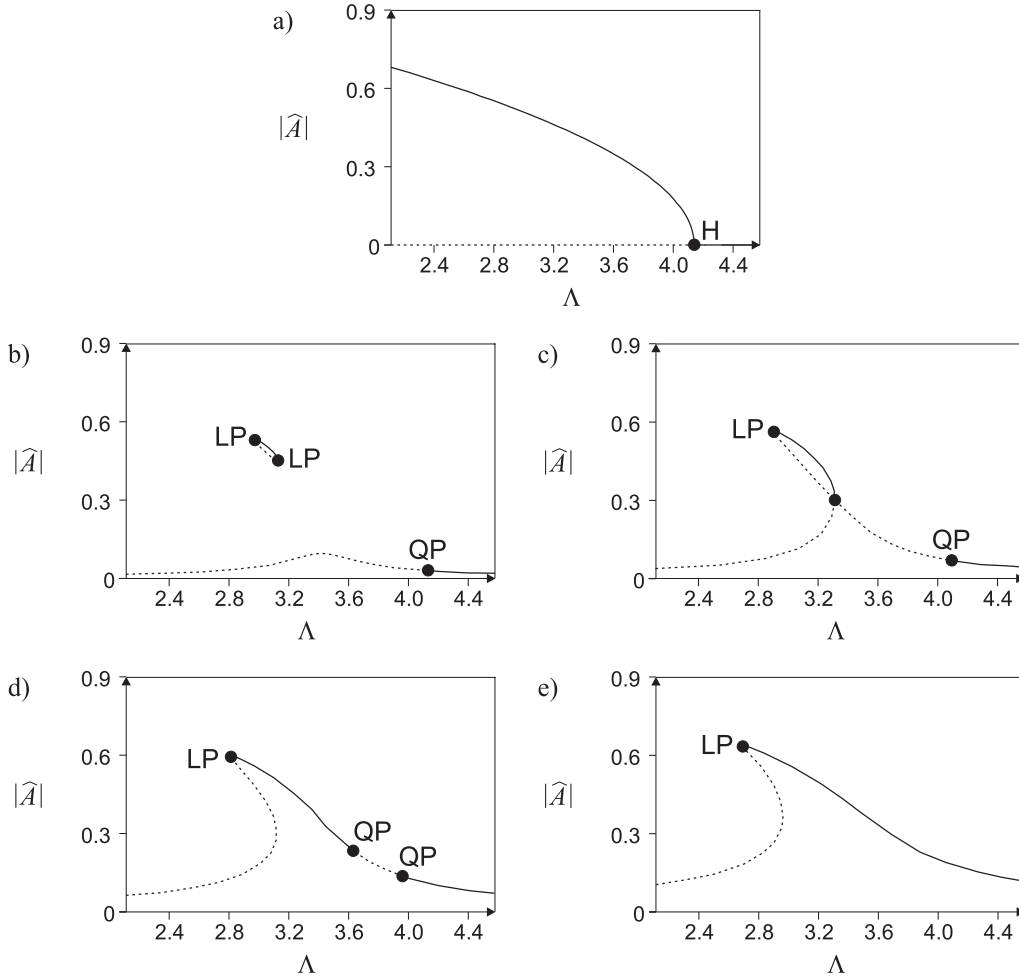


Figure 3.10: Numerical bifurcation diagrams for the laser subject to optical injection and pump modulation, computed from the rate equations (3.1). The amplitude $|\hat{A}|$, estimated from Eq. (3.10), is represented as a function of the optical injection rate Λ for several values of the modulation index m . Fixed parameter values are $\alpha = 5$, $\beta = 0$, $\varepsilon = 0.1704$, $p = \frac{1}{3}$, $\Delta = 0$, and $\Omega = 3.336$. Only the branches of periodic solutions are represented. Solid and dashed curves represent stable and unstable solutions respectively. The meaning of the bifurcation labels is as follows: H = Hopf bifurcation, QP = quasiperiodic bifurcation, LP = limit point bifurcation of a pair of limit cycles. a) $m = 0$: no modulation. b) $0 < m < m_1$: very weak modulation. c) $m = m_1$. d) $m_1 < m < m_2$. e) $m > m_2$: strong modulation.

3.4.4 Bifurcation diagrams (controlling the master-slave detuning)

We now present a set of bifurcation diagrams of the amplitude equation (3.9) where the detuning Δ instead of the injection rate is chosen as a control parameter. Each diagram in Fig. 3.11 corresponds to progressively larger values of the modulation index m and illustrates a typical double-locking experiment, where the control parameter is quasistatically swept across the locking range, all other parameters being fixed. We now note the possibility of bistable responses. Bistability means that two stable solutions may coexist for a range of values of Δ (see Fig. 3.11b–e). Note that a bistable output does not exist for arbitrarily small values of the modulation index m . Moreover, two kinds of bistability may be distinguished. First, from Fig. 3.11d–e, we observe the coexistence of two distinct branches of phase-locked solutions. Second, Fig. 3.11b–c also shows a small region of bistability between a locked state and a quasiperiodic state.

An alternative description of the dynamics is shown in Fig. 3.12. In this figure, we represent the regions of qualitatively different regimes in the m vs. Δ parameter space. Both kinds of bistability domains correspond to the two roughly triangular shapes in the upper right corner of the figure. We have found that their size tends to expand for larger values of the linewidth enhancement factor α . We contrast this diagram with the map of the dynamics in the m vs. Λ parameter space (Fig. 3.9). We noted no domain of bistability for realistic values of m , which suggests that only experiments with the detuning as the sweeping parameter may lead to the observation of bistability.

3.4.5 Experiments

The theory predicts that a bistable output is possible if we sweep back and forth the optical detuning and if the modulation amplitude surpasses a threshold. This prediction has been confirmed by a set of experiments performed by T. B. Simpson. We now give a brief description of the experiments and compare the experimental figures with the theoretical bifurcation diagrams.

The experimental configuration used to study the bistability characteristics has been described in detail in [105]. Both the master and the slave lasers are under separate temperature and current control. The master laser output is passed through a variable attenuator, optical isolator, and beamsplitter before injection into the slave. Temperature and current control is used to bring the optical frequencies of the two lasers into near resonance. The attenuator adjusts the amplitude of the optical injection. The slave laser is operated at a bias of approximately five times the threshold value, and a microwave modulation current from a frequency synthesizer is added to the bias. After being split off at the beamsplitter, the output from the slave laser is passed through additional optical isolators and detected by a fast photodiode. The photodiode signal is amplified and split with one arm going to a microwave spectrum analyzer and the other being mixed with the signal from the microwave frequency synthesizer. The low-frequency component of the output voltage from the mixer is detected with a digitizing

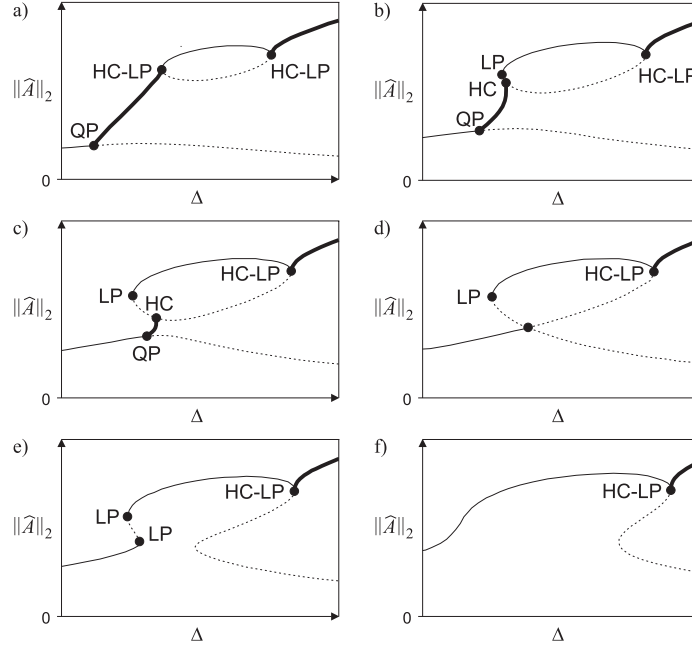


Figure 3.11: Numerical bifurcation diagrams for the laser subject to optical injection and pump modulation, computed from the amplitude equation (3.9). The L_2 -norm of the amplitude \hat{A} is represented as a function of the optical detuning Δ (with an arbitrary offset) for several values of the modulation index m . Units are arbitrary. Fixed parameter values are $\alpha = 5$ and $\Lambda = 0$. The modulation frequency is chosen to be slightly larger than the limit cycle frequency at the Hopf bifurcation. The meaning of the various curves and bifurcation labels is the same as in Fig. 3.8; in addition, the labels LP and HC denote, respectively, limit points of periodic solutions, and homoclinic bifurcations of a torus attractor.

a) $0 < m < m_1$: very weak modulation. The locking domain is bounded by two homoclinic-limit point bifurcations.

b) $m_1 < m < m_2$: The leftmost homoclinic-limit point bifurcation is now split into a cycle limit point and a homoclinic bifurcation of a torus. This results in the existence of a small domain of bistability between locked and non-locked dynamics.

c) $m_2 < m < m_3$: The quasiperiodic bifurcation point now has moved to the right of the limit point. As a consequence, there is an additional region of bistability between low-amplitude and high-amplitude limit-cycle oscillations.

d) $m = m_3$: critical value of the modulation index where two branches of periodic solutions connect. Almost simultaneously, the leftmost quasiperiodic branch has shrunk into one point, and therefore, only the domain of bistability between two limit cycles is observable.

e) $m_3 < m < m_4$. The branch of periodic solution has unfolded into a bistable S-shaped curve.

f) $m > m_4$: strong modulation. The two limit points have collapsed, so that there is no bistability anymore.

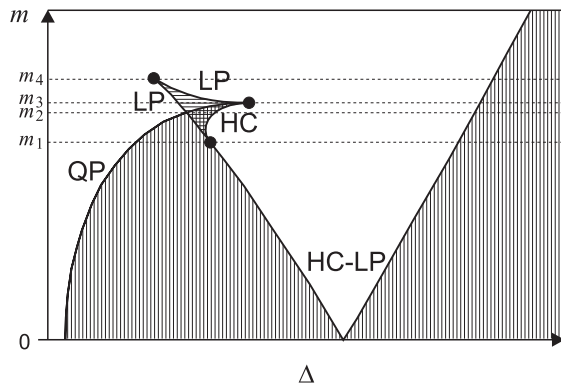


Figure 3.12: Numerical map of the possible responses of the laser subject to optical injection and pump modulation, computed from the amplitude equation (3.9). The dynamics is mapped in the m vs. Δ plane. Units are arbitrary. Fixed parameter values are identical as in Fig. 3.11, and the meaning of the bifurcation labels is the same. The four threshold values of m relevant to Fig. 3.11 are indicated. The meaning of the different regions is as follows: white: phase-locked dynamics. Vertical-hatched: quasiperiodicity. Horizontal-hatched: bistability between two phase-locked states. Cross-hatched: bistability between locked and quasiperiodic dynamics.

oscilloscope and tracks the phase offset when the two input signals are frequency-locked, while it varies rapidly when they are not. Tuned to the frequency of the synthesizer, the microwave spectrum analyzer is used to measure the power at the reference frequency.

The master and slave lasers are biased so that optical injection causes the slave laser to operate near the Hopf bifurcation. The injected optical power is on the order of 1 % of the free-running output from the slave laser and the master laser is slightly detuned to an offset of a few GHz below the free-running optical frequency of the slave. The dc bias to the master laser is slowly varied. While this produces a small change in the amplitude of the injection signal, the primary effect is to vary the optical frequency of the master laser at a rate of approximately -2.8 GHz/mA. Thus, a positive variation of the bias current corresponds to a negative variation of the detuning parameter Δ . Both the mixer output and the power at the reference frequency are recorded as functions of the master laser bias, and the resulting diagrams can be compared to the bifurcation diagrams of Fig. 3.11.

Fig. 3.13 shows measurements at two different powers of the modulation signal. The modulation frequency was fixed at 7.63 GHz. For weak modulation currents (Fig. 3.13a), two locking domains are observed. First, a region of periodic oscillations corresponding to the small amplitude modulation of the stable steady state above the Hopf point appears for master laser currents above approximately 170.3 mA. Second, a region of locked oscillations was centered about 169 mA. Both these regions show relatively weak fluctuations in the power at the modulation frequency and the latter also shows a relatively strong locked power. Outside these two regions, quasiperiodic oscillations are observed as indicated by the strong fluctuations of the mixer signal and the optical

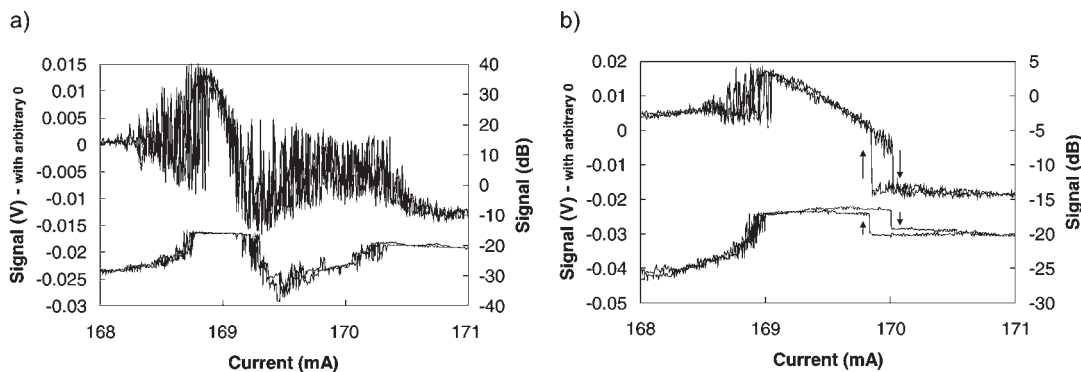


Figure 3.13: Experimental diagrams from double-locking experiments by T. B. Simpson (reproduced from [89]). Output voltage from the microwave mixer (top curves, left axis), and power at the modulation frequency (bottom curves, right axis).

a) Weak current modulation.

b) Stronger current modulation: note the presence of a hysteresis curve indicated by the arrows.

power. The experiment clearly illustrates the bifurcation diagram of Fig. 3.13a (but with a reversal of the horizontal axis). When the modulation power is increased by 7 dB, the stronger modulation currents cause the two regions to merge, as shown in Figure 3.13b. The smoothly varying mixer voltage, and a relatively strong locked power, indicate the region of locked periodic dynamics between approximately 169–170 mA. Note the region of bistability at the edge of this locked region as the laser makes the transition to limit cycle dynamics due to modulation of the stably locked laser. The arrows give the direction of the sweep and the transition. The experiment illustrates the bifurcation diagram of Fig. 3.11e. No bistability is observed for modulation powers 2 dB below those used for the data in Figure 3.11b.

3.5 Summary

In this chapter, we have analyzed a number of possible responses of a semiconductor laser subject to moderate to strong optical injection. First, in Sec. 3.3, we focused on a particular aspect of the dynamics in the domain of moderate injection where the laser exhibits complex dynamics. Specifically, we discussed the existence of isolas of period-tripled limit cycles alongside the period-doubling route to chaos. This problem has been motivated by a set of experiments by T. B. Simpson where optical spectra clearly bears the signature of period-tripled dynamics. Our theoretical analysis was based on the rate equation model and considered the case of perfect tuning between the master and slave laser frequencies. The presence of period-tripled features in the experiments was explained from numerical bifurcation diagrams exhibiting isolas of period-tripled limit cycles. Furthermore, a reduced equation for the optical phase

was derived. The phase equation also exhibited period-tripled dynamics, with the particularity that the period-tripled branch connects the branch of fundamental period at a degenerate bifurcation point if the damping rate of the laser relaxation oscillations tends to zero. This establishes a remarkable analogy with the case of a nonlinear oscillator driven by a modulation with a frequency equal to one third of the oscillator's intrinsic frequency.

Then, in Sec. 3.4, we considered higher values of the injection rate and investigated the domain where the laser exhibits strong, regular intensity oscillations. In particular, we investigated the laser response to a weak modulation of the laser bias current that is nearly resonant with the intrinsic oscillation frequency. Again, this problem finds its motivation in double-locking experiments by T. B. Simpson, who sought to determine the conditions of simultaneous locking of the optical and intensity oscillation frequencies, respectively, to the master laser and pump modulation frequencies. Our theoretical analysis consisted in the derivation of an equation governing the slow variations of the oscillation amplitude in the vicinity of the higher Hopf bifurcation point. The advantage is that the research of quasiperiodic (*i.e.*, non-locked) solutions of the rate equations is reduced to the research of periodic solutions of the amplitude equation. Using the numerical continuation package AUTO (which can only follow periodic solutions), we could produce full bifurcation diagrams, including branches of non-locked solutions.

The laser exhibiting limit-cycle oscillations and subject to a weak modulation may lock to the reference frequency, if it is close enough to the intrinsic frequency. Otherwise, it may sustain quasiperiodic oscillations with two frequencies, namely, the modulation frequency and the beat frequency between the modulation and limit-cycle oscillations. This is the typical response of an oscillator driven by a small amplitude and near resonant modulation. The effect of the nonlinearity is to bend the amplitude curve, allowing multivalued regions. If stable low- and high-amplitude solutions may coexist, we have a case of bistability that we may observe by sweeping back and forth the control parameter. Transitions between low and high amplitude regimes then occur through jumps that can be identified experimentally. However, we found that the domain of bistability is relatively small and requires that the modulation amplitude be sufficiently large and that the linewidth enhancement factor be not too small. These conditions guided T.B. Simpson's experiments shown in Fig. 3.13b, clearly displaying a hysteresis curve.

Appendices to Chapter 3

3.A Stability analysis

Here, we perform a stability analysis of the steady states of Eqs. (3.5) in the absence of pump modulation ($M(s) = 0$) and for a vanishing detuning ($\Delta = 0$). There are two distinct steady states, given by

$$Z = Z_s^\pm \equiv \frac{\pm 2\Lambda}{\sqrt{\alpha^2 + 1}}, \quad E = E_s^\pm \equiv \mp \frac{1 - i\alpha}{\sqrt{\alpha^2 + 1}}. \quad (3.11)$$

Stability is determined by linearizing the equations about the steady states and seeking solutions of the form $Z = Z_s^\pm + \zeta \exp(\sigma s)$, $E = E_s^\pm + \epsilon \exp(\sigma s)$, for small ζ and ϵ . This yields, in matrix form, the following problem for ζ and ϵ :

$$\begin{bmatrix} \frac{1}{2}(1 + i\alpha)Z_s^\pm - \sigma & 0 & \frac{1}{2}(1 + i\alpha)E_s^\pm \\ 0 & \frac{1}{2}(1 - i\alpha)Z_s^\pm - \sigma & \frac{1}{2}(1 - i\alpha)(E_s^\pm)^* \\ -(E_s^\pm)^* & -E_s^\pm & -\sigma \end{bmatrix} \begin{bmatrix} \epsilon \\ \epsilon^* \\ \zeta \end{bmatrix} = \mathbf{0}. \quad (3.12)$$

Nontrivial solutions exist if and only if the determinant of the above square matrix vanishes, which gives the characteristic equation:

$$-\sigma^3 + Z_s^\pm \sigma^2 - \left[\frac{1}{4}(\alpha^2 + 1)(Z_s^\pm)^2 + 1 \right] \sigma + \frac{1}{2}(\alpha^2 + 1)Z_s^\pm = 0, \quad (3.13)$$

where we have used the fact that $|E_s^\pm|^2 = 1$. Note that, for $Z = Z_s^+$, the term independent of σ in the above equation is always positive. Because this term is equal to the product of all three roots of the characteristic equation, this means that there always exists a real, positive value of the eigenvalue σ , so that the solution $Z = Z_s^+$, $E = E_s^+$ is always unstable. Therefore, from now on, we restrict the analysis to the other steady state: $Z = Z_s^-$, $E = E_s^-$. This solution remains stable as long as all roots of the characteristic equation have a negative real part, and the critical values of the optical injection rate Λ where it loses stability are determined by requiring that $\text{Re}(\sigma) = 0$. Substituting $\sigma = i\tilde{\Omega}$ into Eq. (3.13) and separating the real and imaginary parts yields:

$$-Z_s^- \tilde{\Omega}^2 + \frac{1}{2}(\alpha^2 + 1)Z_s^- = 0, \quad (3.14a)$$

$$\tilde{\Omega}^3 - \left[\frac{1}{4}(\alpha^2 + 1)(Z_s^-)^2 + 1 \right] \tilde{\Omega} = 0. \quad (3.14b)$$

In view of the expression (3.11) for Z_s^- , the critical value $\tilde{\Lambda}$ of the injection rate and the Hopf bifurcation frequency $\tilde{\Omega}$ can be determined from the conditions (3.14). They are given by Eqs. (3.6). These values correspond to the higher Hopf bifurcation point, which is observable in Fig. 3.1 (for nonzero values of the damping rate ε and the gain saturation coefficient β).

3.B Normal form derivation

3.B.1 Scaling

In this appendix, we reduce the laser rate equations (3.5) to the amplitude equation (3.9) using a multiple-scale method. The calculations are quite involved, and it proves advantageous to make use of a symbolic calculation software such as MAPLE. We assume that the modulation index m defined in Eq. (3.7) is small and define an order parameter μ as follows:

$$m \equiv \mu^3. \quad (3.15)$$

We then introduce the scaled parameters

$$\frac{\Lambda - \tilde{\Lambda}}{\tilde{\Lambda}} \equiv \mu^2 \Lambda_2, \quad \frac{\Omega - \tilde{\Omega}}{\tilde{\Omega}} \equiv \mu^2 \Omega_2, \quad \frac{\Delta}{\tilde{\Omega}} \equiv \mu^2 \Delta_2, \quad (3.16)$$

and the perturbative expansions

$$E \equiv E_s^- + \mu E_1 + \mu^2 E_2 + \mu^3 E_3 + \dots, \quad (3.17a)$$

$$Z \equiv Z_s^- + \mu Z_1 + \mu^2 Z_2 + \mu^3 Z_3 + \dots, \quad (3.17b)$$

$$\frac{d}{ds} \equiv \tilde{\Omega} (1 + \mu^2 \Omega_2) \left(\frac{\partial}{\partial \theta_0} + \mu^2 \frac{\partial}{\partial \theta_2} + \dots \right). \quad (3.17c)$$

In the choice of the above definitions, we have anticipated the fact that the sought amplitude equation will closely resemble the normal form of a Hopf bifurcation, which allows an *a priori* guess of the correct scaling laws. The factor $\tilde{\Omega} (1 + \mu^2 \Omega_2)$ in Eq. (3.17c) has been introduced so that the pump modulation is 2π -periodic in the variable θ_0 , as a consequence of which Eq. (3.7) is rewritten as

$$M(\theta_0) = m \cos(\theta_0). \quad (3.18)$$

Substituting Eqs. (3.15), (3.16), (3.17), and (3.18) into Eqs. (3.5) and equating to zero the coefficients of each power of μ leads to a hierarchy of linear problems for the unknown variables $E_1, Z_1, E_2, Z_2, \dots$. We analyze each problem sequentially.

3.2.2 First-order problem

The $O(\mu^1)$ problem is equivalent to the system (3.5) linearized about the steady-state solution. Its most general solution, after exponentially decaying transients have died

out, is given by

$$\begin{bmatrix} E_1 \\ E_1^* \\ Z_1 \end{bmatrix} = \begin{bmatrix} \epsilon_1(\alpha) \\ \epsilon_1(-\alpha) \\ \zeta_1(\alpha) \end{bmatrix} \exp(i\theta_0) + \begin{bmatrix} \epsilon_1(-\alpha)^* \\ \epsilon_1(\alpha)^* \\ \zeta_1(\alpha)^* \end{bmatrix} \exp(-i\theta_0), \quad (3.19)$$

where star (*) denotes complex conjugation, and the functions ϵ_1 and ζ_1 are defined as

$$\epsilon_1(\alpha) \equiv \frac{i(1-i\alpha)(1-i\alpha+i\sqrt{\alpha^2-1})}{2\alpha\sqrt{\alpha^2+1}} \widehat{A}_1(\theta_2), \quad (3.20a)$$

$$\zeta_1(\alpha) \equiv \frac{\sqrt{2}i}{\sqrt{\alpha^2+1}} \widehat{A}_1(\theta_2). \quad (3.20b)$$

The amplitude \widehat{A}_1 is undetermined at this stage and varies on the large time scale θ_2 . It is normalized so that the expression (3.8) of the light intensity holds with $\widehat{A} \equiv m\widehat{A}_1$.

3.2.3 Second-order problem

A particular solution to the $O(\mu^2)$ problem is

$$\begin{bmatrix} E_2 \\ E_2^* \\ Z_2 \end{bmatrix} = \begin{bmatrix} \epsilon_2(\alpha) \\ \epsilon_2(-\alpha) \\ \zeta_2(\alpha) \end{bmatrix} \exp(2i\theta_0) + \begin{bmatrix} \epsilon_2'(\alpha) \\ \epsilon_2'(\alpha)^* \\ \zeta_2'(\alpha) \end{bmatrix} + \begin{bmatrix} \epsilon_2(-\alpha)^* \\ \epsilon_2(\alpha)^* \\ \zeta_2(\alpha)^* \end{bmatrix} \exp(-2i\theta_0), \quad (3.21)$$

where the functions ϵ_2 , ϵ_2' , ζ_2 , and ζ_2' are defined as

$$\epsilon_2(\alpha) \equiv -\frac{(1-i\alpha)(2-i\sqrt{\alpha^2-1})(1+i\sqrt{\alpha^2-1})}{12\alpha^4(\alpha^2+3)\sqrt{\alpha^2+1}} \left[-6i\alpha^3 - \alpha^2 - 2i\alpha - 1 + i\sqrt{\alpha^2-1}(6\alpha^2 - 2i\alpha - 1) \right] \widehat{A}_1^2, \quad (3.22a)$$

$$\epsilon_2'(\alpha) \equiv -\frac{i(1-i\alpha)}{\sqrt{\alpha^2+1}\sqrt{\alpha^2-1}} \Delta_2 + \frac{i(1-i\alpha)(2+i\alpha)}{2\alpha\sqrt{\alpha^2+1}} \left| \widehat{A}_1 \right|^2, \quad (3.22b)$$

$$\zeta_2(\alpha) \equiv \frac{-i(1+i\sqrt{\alpha^2-1})[3\alpha^4 - 18\alpha^2 - 1 + i\sqrt{\alpha^2-1}(13\alpha^2 - 1)]}{6\sqrt{2}\alpha^4(\alpha^2+3)\sqrt{\alpha^2+1}} \widehat{A}_1^2, \quad (3.22c)$$

$$\zeta_2'(\alpha) \equiv -\frac{\sqrt{2}(-\alpha\Delta_2 + \sqrt{\alpha^2-1}\Lambda_2)}{\sqrt{\alpha^2+1}} - \frac{\sqrt{\alpha^2-1}}{\sqrt{2}\sqrt{\alpha^2+1}} \left| \widehat{A}_1 \right|^2. \quad (3.22d)$$

3.2.4 Third-order problem

Writing the $O(\mu^3)$ problem as

$$\frac{\partial E_3}{\partial \theta_0} - \frac{1}{2}(1+i\alpha)(Z_s^- E_3 + E_s^- Z_3) = R_1(\theta_0), \quad (3.23a)$$

$$\frac{\partial E_3^*}{\partial \theta_0} - \frac{1}{2}(1-i\alpha)(Z_s^- E_3^* + (E_s^-)^* Z_3) = R_2(\theta_0), \quad (3.23b)$$

$$\frac{\partial Z_3}{\partial \theta_0} + ((E_s^-)^* E_3 + E_s^- E_3^*) = R_3(\theta_0), \quad (3.23c)$$

it turns out that the right-hand sides R_1 , R_2 , R_3 are known functions of θ_0 that contain terms proportional to the periodic solutions of the corresponding homogeneous problem. This implies that a solvability condition needs to be satisfied. Solving the adjoint problem to (3.12), we find that it can be formulated as

$$\int_0^{2\pi} d\theta_0 \begin{bmatrix} u(\alpha) & u(-\alpha) & 1 \end{bmatrix} \begin{bmatrix} R_1(\theta_0) \\ R_2(\theta_0) \\ R_3(\theta_0) \end{bmatrix} \exp(-i\theta_0) = 0, \quad (3.24)$$

where the function $u(\alpha)$ is defined as

$$u(\alpha) \equiv -\frac{1-i\alpha+i\sqrt{\alpha^2-1}}{\sqrt{2}\alpha}. \quad (3.25)$$

Evaluating the solvability condition (3.24) yields a differential equation for the complex amplitude \widehat{A}_1 :

$$iC_\Omega \frac{\partial \widehat{A}_1}{\partial \theta_2} = 1 + \widehat{A}_1 \left(C_\Omega \Omega_2 + C_\Lambda \Lambda_2 + C_\Delta \Delta_2 + C_3 \left| \widehat{A}_1 \right|^2 \right), \quad (3.26)$$

where

$$C_\Omega \equiv \frac{2(1+i\sqrt{\alpha^2-1})(\alpha^2+1-2i\sqrt{\alpha^2-1})}{\alpha^2}, \quad (3.27a)$$

$$C_\Lambda \equiv -\frac{2(1+i\sqrt{\alpha^2-1})(\alpha^2-1)}{\alpha^2}, \quad (3.27b)$$

$$C_\Delta \equiv \frac{2i(1+i\sqrt{\alpha^2-1})}{\alpha}, \quad (3.27c)$$

$$C_3 \equiv \frac{(1+i\sqrt{\alpha^2-1})^2(2-i\sqrt{\alpha^2-1})[3\alpha^4-7+i\sqrt{\alpha^2-1}(3\alpha^2+9)]}{3\alpha^4(\alpha^2+3)}. \quad (3.27d)$$

The final form (3.9) of the amplitude equation is obtained by introducing $\widehat{A} \equiv m\widehat{A}_1$ and substituting the original time variable and control parameters back into Eq. (3.26).

Chapter 4

Bursting oscillations in optical parametric oscillators

“One of the principal objects of theoretical research in my department of knowledge is to find the point of view from which the subject appears in its greatest simplicity.”

—Josiah Willard Gibbs

4.1 Introduction

Ever since their appearance in 1965, optical parametric oscillators (OPOs) have been regarded as very promising sources of coherent radiation because of their great wavelength tunability [47]. Technological difficulties have long remained a challenge to practical applications, until in the 1980s their common use, in spectroscopy for example, was made possible by successive enhancements of the properties of the lasers and crystals required for their operation [112]. The energy necessary to the amplification mechanism in an OPO is provided by a pump laser emitting either in pulse mode or continuously. Pulsed OPOs are more easily tuned and less subject to instabilities, as a consequence of which they are now developed in the industry and commercialized. Continuous-wave OPOs have known a renewal of interest in the last decade for their ability to generate squeezed states of light [132], which was used for high-resolution spectroscopy measurements [99], and advances are ongoing at a rapid pace [22].

As many practical lasers, OPOs exhibit a variety of dynamical instabilities. Complex temporal or spatiotemporal dynamical regimes can result from the nonlinearity at the origin of the amplification mechanism and have motivated numerous theoretical works [73, 117, 120]. Periodic and chaotic behavior has been predicted to occur in continuous-wave OPOs. However, self-pulsing regimes in experimental systems have been reported only recently [100, 112, 113, 114, 115]. The experimentally observed instabilities were not well understood in the light of existing theories, which therefore proved insufficient. In particular, instabilities observed in an OPO at frequencies of a few kHz have been traced back to slow variations of the crystal temperature which were

not taken into account in existing theories. A thermo-optical OPO model was then devised and successfully confronted to experiments [112, 113, 114]. Observations of fast oscillations at frequencies in the MHz range have also been reported [100, 112, 115] and a mechanism based on the interaction of two interacting transverse cavity modes [104] has been proposed [112, 115]. This interpretation has been recently confirmed by experiments monitoring simultaneously the spatial structure of the output beam and its total intensity. When multimode and thermal effects are combined, these fast oscillations appear in bursts separated by periods of no activity. The objective of this chapter is to propose a simple description of these bursting oscillations.

Such bursting cycles can be compared to the activity of some biological systems. Neurons as well as many other cell types like to communicate by brief bursts of oscillations separated by quiescent periods [48]. Although specific models describing these bursting oscillations can be complicated, they are generally based on the assumption that the phenomenon is caused by a slow variable modulating a rapid oscillatory system. Phase-plane studies where the response of a fast variable is studied as a function of the slow variable have been particularly useful to explain the periodic switching between oscillatory and steady responses. Bursting oscillatory outputs have been recently investigated for a CO₂ laser subject to feedback [82] and for two coupled CO₂ lasers [116]; however they are too complex to be described in terms of a simple two-variable phase plane. In this chapter, we show that such a simple analysis is possible for continuous-wave, triply resonant OPOs subject to thermal effects.

Our analysis unveils a surprising property of our OPO system. The regime where two cavity modes with well separated optical wavelengths jointly oscillate is in first approximation equivalent to a non-detuned monomode oscillation. This indicates that, contrary to naive intuition, two-mode operation does not necessarily rely on the near coincidence of two cavity resonances. Thus, these new regimes cannot be neglected when studying frequency selection in OPOs, especially at the high pump powers currently available.

This chapter is organized as follows. Sec. 4.2 to 4.4 are introductory. In Sec. 4.2, we briefly explain the basics of parametric amplification and the optical implementation of this mechanism as an OPO. In Sec. 4.3, we introduce the thermo-optical OPO models considered in this chapter and previously used in [112]. Special attention is paid to the justification of the use of degenerate models where the so-called “signal” and “idler” fields are subsumed as a single variable. In Sec. 4.4, we describe the thermo-optical instability mechanism in the simple case of monomode OPO operation.

In Sec. 4.5 and 4.6, we come to bursting dynamics, which is the main topic of this chapter. In Sec. 4.5, we describe recent experimental reports on these bursting oscillations by A. Amon and M. Lefranc in Lille. Their setup is a triply-resonant type-II continuously-pumped OPO using a KTP¹ crystal. The bursting cycle is then explained in Sec. 4.6.1 by studying the bifurcation properties of a two-mode OPO model. We note that the bursting oscillations are the result of a slow passage through a subcritical Hopf bifurcation followed by a fast jump to rapid oscillations, and then

¹Potassium Titanyl Phosphate

back to a quiescent state after reaching a limit point. In Sec. 4.6.2, we then proceed to a perturbative analysis of the problem, leading to a reduction of the two-mode equations to an effective monomode model. Finally, our results are summarized in Sec. 4.7.

4.2 Optical parametric oscillation mechanism

Parametric resonance is a general mechanism by which a system can be destabilized if one of its parameters varies periodically [112]. In many cases, this effect manifests itself as the amplification of an oscillatory phenomenon by an external forcing at twice its intrinsic frequency. An optical parametric oscillator is an optical implementation of this mechanism. It is constituted of an optical resonator pumped by a coherent source of light and containing a sample of $\chi^{(2)}$ material, *i.e.*, a nonlinear medium whose polarization in response to electromagnetic solicitations is asymmetric with respect to a reversal of the orientation of the electric field. Such a situation is possible if the structure of the material is not centrosymmetric [134]. A $\chi^{(2)}$ medium is characterized by an order-two nonlinearity, which means that the expansion of the polarization as a power series of the electric field contains an order-two contribution. Two photon-conversion processes, known as second-harmonic generation and parametric down-conversion, can take place due to the order-two nonlinearity. Second-harmonic generation is the emission of an electromagnetic field with frequency 2ω when a field with frequency ω propagates in the medium, due to the presence of a term proportional to $\exp(2i\omega t)$ in the expression of the polarization. In quantum terms, this corresponds to the conversion of two photons with frequency ω into one photon with frequency 2ω . Parametric down-conversion is the amplification of two fields, called “signal” and “idler”, in presence of a third one, called “pump”, which is providing energy. The elementary interaction is the conversion of one pump photon into one signal photon and one idler photon. Energy conservation requires that the pump frequency ω_p , the signal frequency ω_s , and the idler frequency ω_i be related as: $\omega_p = \omega_s + \omega_i$. The case of degenerate parametric down-conversion, where signal and idler photons are undistinguished and $\omega_s = \omega_i = \omega_p/2$, can be viewed as the reverse process to second-harmonic generation.

In an OPO, the pump field is provided by a laser operating either in pulse mode [47] or continuously [109]. Signal and idler field emission starts up from the amplification of a quantum fluctuation in the $\chi^{(2)}$ medium. Parametric gain is weak, especially under continuous pumping, so that many round-trips are necessary for the fields to build up inside the resonator. Eventually, the amplification mechanism comes to saturation and an equilibrium is reached where the gain is exactly balanced by the losses due to the escape of light from the resonator. Depending on the experimental setup, the pump, signal, and idler fields can be more or less resonant in the cavity. In this work, we are exclusively concerned with the case of a continuously pumped, triply resonant OPO (*i.e.*, where all three fields are in good resonance with the cavity): see a schematic illustration in Fig. 4.1. The experimental setup used in Lille is a type-II triply resonant OPO, which means that the signal and idler fields correspond to distinct polarization states of light.

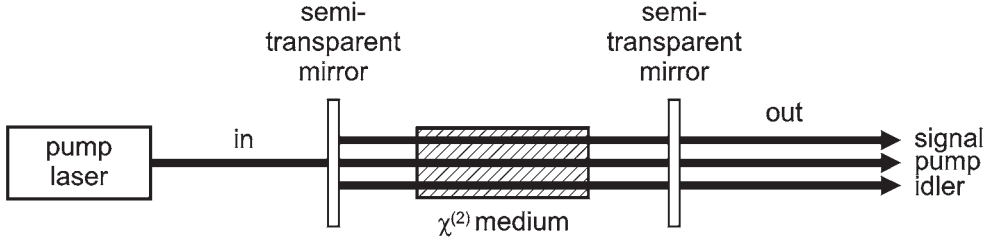


Figure 4.1: A simplified block diagram of a triply-resonant optical parametric oscillator.

4.3 Optical parametric oscillator model

4.3.1 Single-mode OPO

If the pump, signal, and idler fields all oscillate on a single mode of the resonant cavity, and if the signal and idler frequencies are close to half the pump frequency, then the electric field $\vec{\mathcal{E}}(\vec{x}, t)$ inside the cavity can be written as

$$\begin{aligned} \vec{\mathcal{E}}(\vec{x}, t) = & \left[A_p(t) \vec{u}_p(\vec{x}) \exp(i\omega_p t) + A_s(t) \vec{u}_s(\vec{x}) \exp\left(\frac{i\omega_p t}{2}\right) \right. \\ & \left. + A_i(t) \vec{u}_i(\vec{x}) \exp\left(\frac{i\omega_p t}{2}\right) \right] + \text{C.C.}, \end{aligned} \quad (4.1)$$

where C.C. denotes the complex conjugate of the preceding term; A_p , A_s , and A_i are the slowly-varying complex amplitudes of the pump, signal, and idler fields, respectively; and \vec{u}_p , \vec{u}_s , and \vec{u}_i account for the spatial structure of the corresponding cavity modes. The coupled evolution of the amplitudes A_p , A_s , and A_i is governed by the following equations [73]:

$$\frac{dA_p}{dt} = \gamma [(-1 - i\sigma_p)A_p - \chi A_s A_i + 1], \quad (4.2a)$$

$$\frac{dA_s}{dt} = (-1 - i\sigma_s)A_s + \chi A_p A_i^*, \quad (4.2b)$$

$$\frac{dA_i}{dt} = (-1 - i\sigma_i)A_i + \chi A_p A_s^*. \quad (4.2c)$$

In these equations, time is measured in units of the signal and idler photon loss rates, assumed identical. The pump amplitude A_p is normalized to the amount of injected light from the pump laser², described by the last term in Eq. (4.2a). γ represents the pump photon loss rate. χ introduces the coupling between the three fields. Its value is determined by the amount of spatial overlap between the three modes \vec{u}_p , \vec{u}_s , and \vec{u}_i [104], and can be assumed real and positive by choosing an appropriate definition

²Another common field normalization choice, used in [112], is to work in the system of units where $\chi = 1$.

of the phases of the three fields. σ_p , σ_s , and σ_i represent the cavity detunings for the pump, signal, and idler fields. The detunings are defined by:

$$\gamma\sigma_p \equiv \omega_p^* - \omega_p, \quad \sigma_s \equiv \omega_s^* - \frac{\omega_p}{2}, \quad \sigma_i \equiv \omega_i^* - \frac{\omega_p}{2}, \quad (4.3)$$

where ω_p^* , ω_s^* , and ω_i^* denote the resonance frequencies for the pump, signal, and idler cavity modes.

In the degenerate case where the signal and idler fields correspond to the same cavity mode, the monomode OPO model (4.2) reduces to

$$\frac{dA_p}{dt} = \gamma [(-1 - i\sigma_p)A_p - \chi A^2 + 1], \quad (4.4a)$$

$$\frac{dA}{dt} = (-1 - i\sigma)A + \chi A_p A^*, \quad (4.4b)$$

where $\sigma \equiv \sigma_s = \sigma_i$ and $A \equiv A_s = A_i$. It is important to realize that the degenerate case cannot actually happen in a type-II OPO, because the signal and idler fields have different polarization states, and thus cannot correspond to the same cavity mode. Therefore, it would seem, at first sight, that a proper account of the Lille experiments requires the nondegenerate model (4.2). However, we show in Appendix 4.A that, if one is only interested in the possible asymptotic behaviors (that is, the states reached after transients have died out), then there is a formal equivalence between the nondegenerate and degenerate models. More precisely, no matter what initial condition is chosen, after a sufficient amount of time elapses, the nondegenerate system (4.2) eventually reaches a state where the signal and idler amplitudes can be expressed as

$$A_s(t) = A(t) \exp \left[i \frac{\sigma_i - \sigma_s}{2} (t - t_0) \right], \quad (4.5a)$$

$$A_i(t) = A(t) \exp \left[-i \frac{\sigma_i - \sigma_s}{2} (t - t_0) \right], \quad (4.5b)$$

where the new amplitude A evolves in interaction with the pump field according to Eqs. (4.4), with σ being defined as

$$\sigma \equiv \frac{\sigma_s + \sigma_i}{2}. \quad (4.6)$$

This equivalence property legitimates the use of the degenerate model for the theoretical description of the Lille experiments. When working with the degenerate model, we shall always refer to the variable A as the ‘‘signal’’ amplitude, even though it actually describes both the signal and idler fields.

4.3.2 Two-mode OPO

Bursting phenomena in OPOs have been identified as resulting from multimode operation [104]. The theoretical description of bursting dynamics therefore requires an

extension of the model (4.2) taking two signal and idler modes into account:

$$\begin{aligned} \frac{dA_p}{dt} &= \gamma [(-1 - i\sigma_p)A_p - \chi_{11}A_{s,1}A_{i,1} - \chi_{12}A_{s,1}A_{i,2} \\ &\quad - \chi_{21}A_{s,2}A_{i,1} - \chi_{22}A_{s,2}A_{i,2} + 1], \end{aligned} \quad (4.7a)$$

$$\frac{dA_{s,1}}{dt} = (-1 - i\sigma_{s,1})A_{s,1} + \chi_{11}A_pA_{i,1}^* + \chi_{12}A_pA_{i,2}^*, \quad (4.7b)$$

$$\frac{dA_{i,1}}{dt} = (-1 - i\sigma_{i,1})A_{i,1} + \chi_{11}A_pA_{s,1}^* + \chi_{21}A_pA_{s,2}^*, \quad (4.7c)$$

$$\frac{dA_{s,2}}{dt} = (-1 - i\sigma_{s,2})A_{s,2} + \chi_{21}A_pA_{i,1}^* + \chi_{22}A_pA_{i,2}^*, \quad (4.7d)$$

$$\frac{dA_{i,2}}{dt} = (-1 - i\sigma_{i,2})A_{i,2} + \chi_{12}A_pA_{s,1}^* + \chi_{22}A_pA_{s,2}^*. \quad (4.7e)$$

In order to simplify the above equations somewhat, it would be convenient if, by analogy to the single-mode case, we could find a formal equivalence with a degenerate model. Unfortunately, the multimode equations do not appear to have such a property. Therefore, we shall restrict our analysis to a particular case defined by

$$\chi_{12} = \chi_{21}, \quad (4.8a)$$

$$\sigma_{s,1} - \sigma_{s,2} = \sigma_{i,1} - \sigma_{i,2}. \quad (4.8b)$$

The relation between the detunings means that the spectral distance between the two signal mode resonances is assumed equal to the spectral distance between the two idler mode resonances. The system (4.7) then admits particular solutions of the form

$$A_{s,j} = A_j \exp \left[i \frac{\sigma_{i,j} - \sigma_{s,j}}{2} (t - t_0) \right], \quad (4.9a)$$

$$A_{i,j} = A_j \exp \left[-i \frac{\sigma_{i,j} - \sigma_{s,j}}{2} (t - t_0) \right], \quad (4.9b)$$

for $j = 1, 2$. The evolution of the new variables A_j is governed by the following reduced system:

$$\frac{dA_p}{dt} = \gamma [(-1 - i\sigma_p)A_p - \chi_1A_1^2 - \chi_2A_2^2 - 2\chi_{12}A_1A_2 + 1], \quad (4.10a)$$

$$\frac{dA_1}{dt} = (-1 - i\sigma_1)A_1 + \chi_1A_pA_1^* + \chi_{12}A_pA_2^*, \quad (4.10b)$$

$$\frac{dA_2}{dt} = (-1 - i\sigma_2)A_2 + \chi_2A_pA_2^* + \chi_{12}A_pA_1^*, \quad (4.10c)$$

where

$$\chi_j \equiv \chi_{jj}, \quad (4.11a)$$

$$\sigma_j \equiv \frac{\sigma_{s,j} + \sigma_{c,j}}{2}. \quad (4.11b)$$

Under the restrictions (4.8), and limiting the discussion to particular solutions of the multimode equations of the form (4.9), a description of bursting phenomena can be proposed in terms of the so-called two-mode degenerate OPO model (4.10). Similarly to the monomode case, we shall refer to the variables A_1 and A_2 as the “signal” amplitudes.

4.3.3 Thermal effects

The experiments reported in [112] support the important assumption that the optical length of the crystal is slowly changing due to thermal variations. We may thus relate the optical length L of the cavity to the crystal temperature θ as follows:

$$\frac{L}{L_0} = 1 + \lambda\theta, \quad (4.12)$$

where L_0 is the optical length of the cavity at room temperature, defined as $\theta = 0$, and where λ is the cavity’s effective thermal expansion coefficient. This induces a dependence of any cavity resonance frequency ω^* on the temperature:

$$\frac{\omega^*}{\omega_0^*} = \frac{L_0}{L} = \frac{1}{1 + \lambda\theta} \simeq 1 - \lambda\theta, \quad (4.13)$$

where ω_0^* is the value of ω^* at room temperature, and where the approximation used above is valid as long as optical length variations remain weak. Therefore, the various pump, signal, and idler detunings can be expressed as

$$\gamma\sigma_p = \gamma\Delta_p - \omega_{p,0}^*\lambda\theta, \quad (4.14a)$$

$$\sigma_{s,j} = \Delta_{s,j} - \omega_{s,j,0}^*\lambda\theta \simeq \Delta_{s,j} - \frac{1}{2}\omega_{p,0}^*\lambda\theta, \quad (4.14b)$$

$$\sigma_{i,j} = \Delta_{i,j} - \omega_{i,j,0}^*\lambda\theta \simeq \Delta_{i,j} - \frac{1}{2}\omega_{p,0}^*\lambda\theta, \quad (4.14c)$$

where Δ_p , $\Delta_{s,j}$, and $\Delta_{i,j}$ are the detunings at room temperature, and where all signal and idler resonances have been approximated as half the pump resonance.

From now on, we are only concerned with the degenerate OPO models (4.4) and (4.10). In view of Eqs. (4.14), and noting that we have the freedom to measure temperature in units such that $\frac{1}{2}\omega_{p,0}^*\lambda = 1$, the various detunings appearing in the degenerate models are related to the temperature as:

$$\sigma_p = \Delta_p - 2\gamma^{-1}\theta, \quad \sigma = \Delta - \theta, \quad \sigma_j = \Delta_j - \theta. \quad (4.15)$$

In order to close the thermo-optical OPO models, there remains to write an equation describing the time evolution of the temperature. The main source of temperature fluctuations is the heating of the crystal due to the residual absorption of the signal fields. This effect can be modelled as follows:

$$\frac{d\theta}{dt} = \varepsilon [-\theta + \alpha I_p + \beta I], \quad (4.16)$$

where $\varepsilon \ll 1$ is the relaxation rate towards room temperature, and α and β are the normalized absorption coefficients of the crystal at the wavelength of the pump and of the signal, respectively. I_p is the pump field intensity:

$$I_p \equiv |A_p|^2, \quad (4.17)$$

and I is the signal intensity. For the degenerate monomode model, it is given by

$$I \equiv |A|^2. \quad (4.18)$$

For the degenerate two-mode model, the total signal intensity is the sum of the intensities in each mode:

$$I \equiv |A_1|^2 + |A_2|^2. \quad (4.19)$$

4.4 Thermo-optical oscillations

Past experiments have demonstrated that slow, spontaneous oscillations of the field intensities in a continuous-wave OPO arise as a result of temperature fluctuations in the $\chi^{(2)}$ medium [112]. In this preliminary section, the generic thermo-optical instability mechanism is briefly presented and described in the light of the simple, degenerate monomode OPO model (4.4) coupled to the temperature evolution equation (4.16). The understanding of this mechanism in the simplest case is a necessary prerequisite to the main topic of this chapter, which is the analysis of the more complex instabilities characterized by intermittent bursts of fast intensity oscillations.

Let us first consider an idealized situation where the crystal temperature θ is a constant and controllable parameter, and let us describe the response of the OPO as a function of θ . The steady states of the monomode OPO equations can be computed analytically and are presented in Fig. 4.2a in the form of a bifurcation diagram. The possible values of the signal intensity I are represented as functions of the temperature, taken as a control parameter. Two branches of solutions can be observed. The horizontal branch characterized by $I = 0$ is the off state, where no signal emission does take place. The off state always exists, but it is not always stable, and its domain of instability roughly coincides with the domain of existence of another branch of solutions. This second branch corresponds to steady signal emission as it is characterized by constant but nonzero values of the signal intensity I : this is the on state. The shape of the on-state branch is strongly dependent on fixed parameters. As a consequence of our particular choice of parameter values in Fig. 4.2a, there are two regions of bistability between the on and off states. However the on-state branch is always bounded, and located in a temperature interval where the resonance frequency of the signal cavity mode does not differ too much from $\omega_p/2$.

The existence of bistability domains induces the possibility of hysteresis cycles if the temperature θ is slowly varied. As we shall now see, the presence of a hysteresis path around the high-temperature end of the on-state branch is responsible for a spontaneous, periodic switching between the on and off states, if the OPO equations

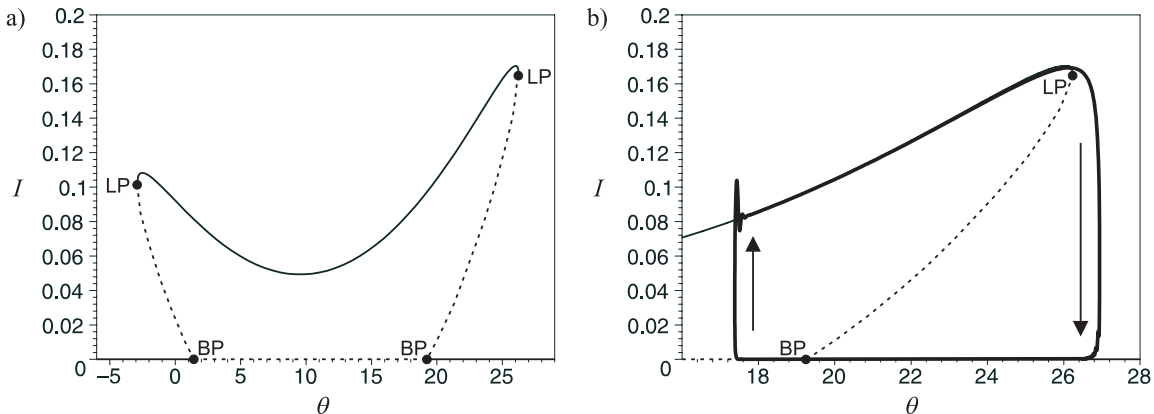


Figure 4.2: Bifurcation diagram of the degenerate monomode OPO equations (4.4). The signal intensity I is represented as a function of the temperature θ . Frame b is a close-up on the right part of Frame a. In addition, Frame b shows a representation in the (θ, I) plane of a thermo-optical oscillation cycle obtained by direct integration of the OPO equations (4.4) coupled to the temperature equation (4.16). Fixed parameter values are $\chi = 17.5$, $\Delta_p = 1.5$, $\Delta = 12.5$, $\gamma = 10$, $\varepsilon = 10^{-2}$, $\alpha = 0$, and $\beta = 5 \cdot 10^2$. Stable and unstable solutions are represented as solid and dashed curves respectively. Bifurcation points are denoted as follows: BP = branch point, LP = limit point. The horizontal branch $I = 0$ is the off state. The closed branch with nonzero intensity is a branch of steady emission (on state). Thermo-optical oscillations correspond to the periodic switching between the on and off states.

are now coupled to the temperature evolution equation (4.16). Fig. 4.2b is a close-up on the bistability domain to the right of Fig. 4.2a. A representation of a limit-cycle solution of the coupled field-temperature equations in the (θ, I) plane is superimposed on this diagram. It has been assumed that the signal field is more efficient in heating the crystal than the pump field, so that $\alpha < \beta$ (for the sake of simplicity, we have set $\alpha = 0$). The thermo-optical oscillation cycle described by this solution closely follows the hysteresis path. The oscillation mechanism can be described as follows: when the OPO operates in the on state, conversion of photons of the signal field into heat takes place in the crystal, inducing a slow increase of the crystal temperature, up to the limit point where the system has to jump off the upper branch. It then settles onto the off state and, because there is no signal emission anymore, the crystal slowly cools down, until the off state loses stability through a branch point. Note that leaving the unstable branch past the bifurcation requires a significant amount of time, which is roughly proportional to the time the system has previously spent on the stable part of the off-state branch. Consequently, the temperature value where it jumps back onto the on state does not coincide with the bifurcation point. This delayed-bifurcation phenomenon is a well-known, generic feature of systems where a parameter slowly varies in time [9, 78].

Fig. 4.3 shows the pump and signal intensities as a function of time. Signal os-

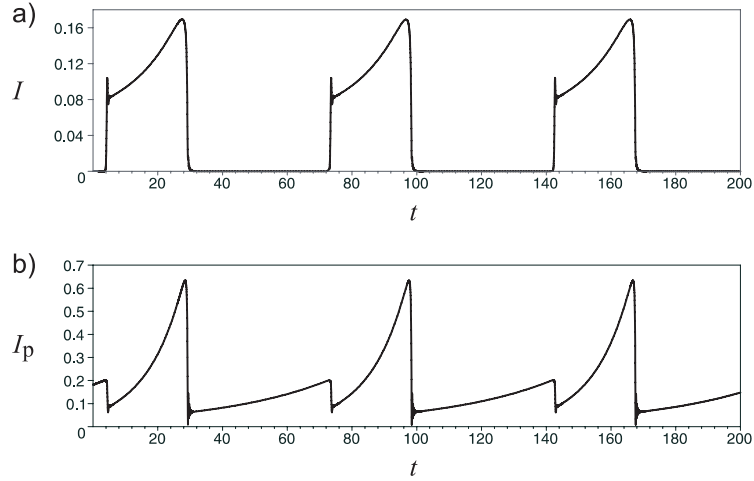


Figure 4.3: Thermo-optical oscillations in an OPO, computed by direct integration Eqs. (4.4) and (4.16). Parameter values are the same as in Fig. 4.2. a) signal intensity as a function of time, b) pump intensity as a function of time.

oscillations are readily identified as a periodic switching between the on and off states. Between the fast transitions, the intensities evolve slowly as a result of the heating or cooling of the crystal.

4.5 Bursting oscillation experiments

In this section, we describe recent experimental measurements of bursting oscillations in a type-II triply resonant OPO. The experimental setup used by A. Amon and M. Lefranc in Lille consists of a 15-mm-long KTP crystal enclosed in a 47-mm-long cavity delimited by two spherical mirrors with a radius of curvature of 50 mm. The cavity is resonant at 532 nm, the wavelength of the pump laser (Coherent Verdi, with a maximum power of 5 W), and highly resonant at the first subharmonic at 1064 nm, near which two infrared fields (signal and idler) are generated in the crystal. At these two wavelengths, the cavity finesse estimated from mirror reflectivities and crystal absorption coefficients are of 50 and 540, respectively. When observing the regimes described below, threshold for parametric oscillation was reached at pump powers of the order of 30 mW, and the pump power injected in the cavity was at its maximum value (*i.e.*, about a hundred times the threshold power).

Different regimes are obtained as the cavity length is scanned with a piezoelectric transducer over one wavelength of the infrared field: no parametric emission, stable parametric emission, and thermo-optical instabilities, as well as fast oscillations with frequencies from a few MHz [115] to hundreds of MHz. While fast oscillations do not appear for every cavity geometry, they have been observed in a large number of different configurations at high pump power and, in particular, for widely different cavity lengths.

In most situations, fast oscillations interact with the slow thermal oscillations, giving rise to bursting oscillations. A large variety of bursting regimes can be observed, both with respect to waveform and to oscillation frequency. Three examples recorded under the operating conditions described above are presented here. Fig. 4.4a shows a regime where the slow dynamics alternates between two branches, with fast oscillations appearing on the upper branch through a supercritical Hopf bifurcation and stopping suddenly to return to the lower branch. The low and high frequencies are around 8 kHz and 3 MHz, respectively. In Fig. 4.4b, fast oscillations at 1 MHz are periodically switched on and off, with a characteristic frequency in the 15–20 kHz range. Finally, the waveform in Fig. 4.4c features fast oscillations that start with a nonzero amplitude and occupy the entire time interval where signal intensity is above zero. The parabolic envelope at the end of the burst is suggestive of a limit-point bifurcation. While the low frequency is comparable to that of regimes in Figs. 4.4a and 4.4b, the high frequency, at 130 MHz, is much larger than in the two other examples.

Clearly, reproducing such a variety of bursting regimes with a theoretical model is a challenging task. In the remaining of this chapter, we focus on the bursting mode of the type of Fig. 4.4c. This regime bears some similarity with the simple, periodic thermal oscillations presented in Sec. 4.4, in the sense that the envelope of the fast signal oscillations in Fig. 4.4c seems to undergo a periodic sequence of bifurcations analogous to the intensity oscillation cycle in Fig. 4.2b. The reason for such a similarity will be made clear in Sec. 4.6 on the basis of a perturbative analysis of the two-mode degenerate OPO model (4.10) taking advantage of the very high frequency observed.

4.6 Theory for bursting oscillations

4.6.1 Numerical bifurcation diagrams

The theoretical description of bursting oscillations requires a multimode approach. Fig. 4.5a shows a bifurcation diagram of the degenerate two-mode equations (4.10), where the temperature θ is treated as a static parameter. It has been constructed numerically with the numerical continuation software AUTO [21]. The signal intensity I is represented as a function of θ . The closed branches to the left and to the right of the figure correspond to mixed-mode steady emission. However, there is a third closed branch in the middle of the figure which corresponds to fast time-periodic oscillations. Fig. 4.5b is a close-up on the branch of periodic solutions: it emerges from the off state at a first Hopf bifurcation at $\theta \simeq 22.5$, reaches a limit point at $\theta \simeq 26.5$, and then reconnects the off state at a second (subcritical) Hopf bifurcation at $\theta \simeq 25.7$. The presence of a limit point induces the existence of a domain of bistability between the off state and the oscillatory state. Treating now the temperature as time-dependent and governed by Eq. (4.16), we have numerically computed a solution that corresponds to a bursting cycle. Its phase-plane representation is superimposed over the static bifurcation diagram in Fig. 4.5b. The corresponding intensity-*vs.*-time diagrams are shown in Fig. 4.6. Because temperature variations are slow, the complete bursting cycle

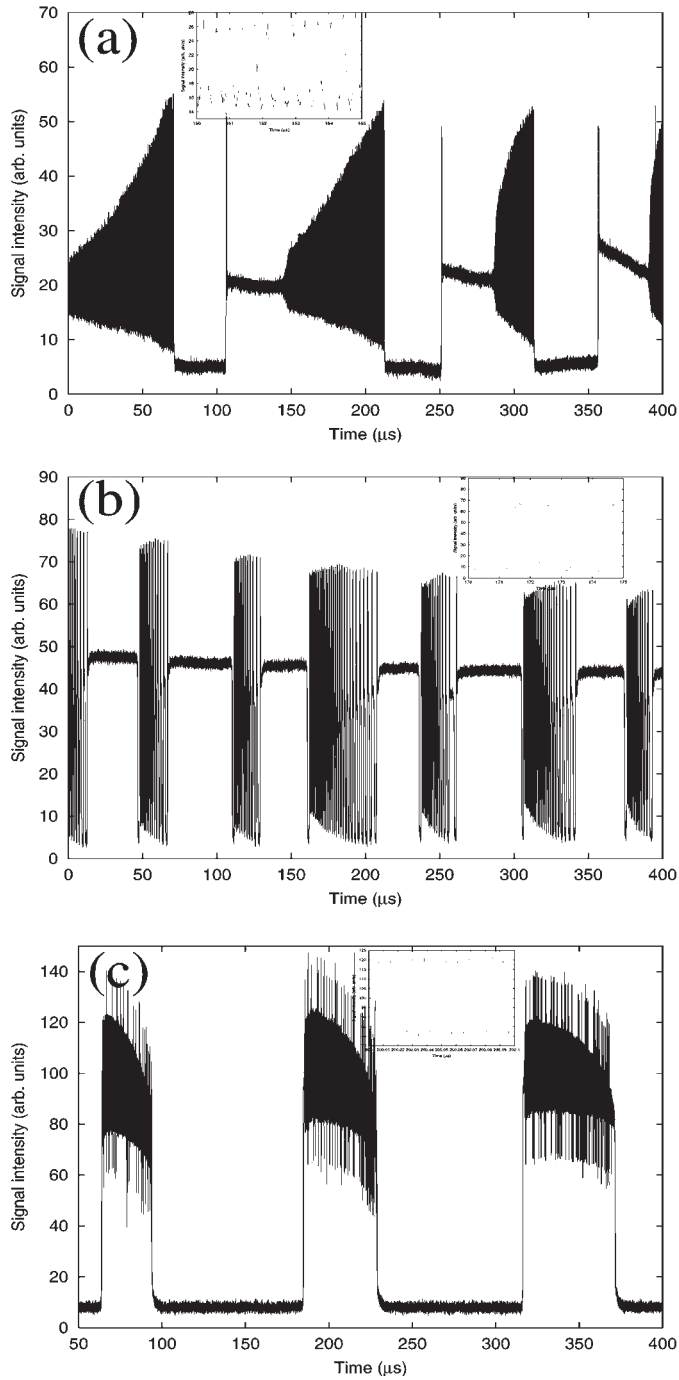


Figure 4.4: Signal intensity versus time for three different bursting regimes observed in the OPO instability experiments at Lille. In each plot, the inset shows the fast oscillations for time intervals (a) of $5 \mu\text{s}$ around $150 \mu\text{s}$; (b) of $5 \mu\text{s}$ around $170 \mu\text{s}$; (c) of 100 ns around $200 \mu\text{s}$.

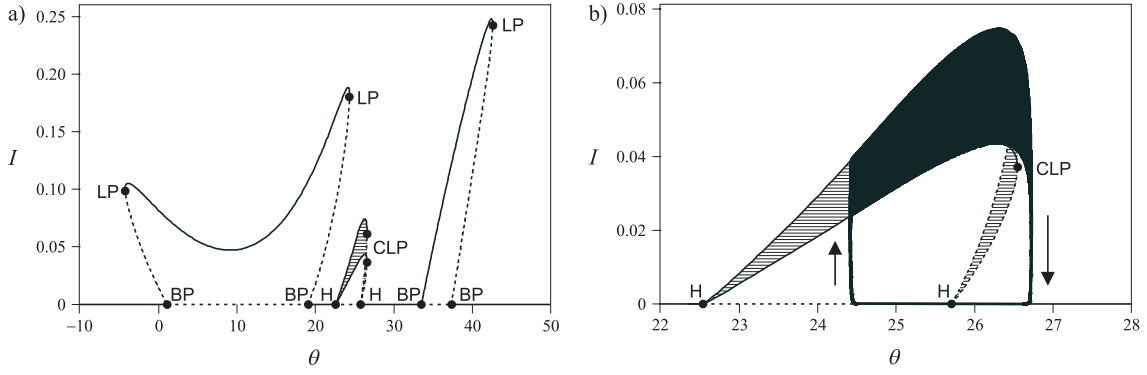


Figure 4.5: Bifurcation diagram of the degenerate two-mode OPO equations (4.10). The intensity I is represented as a function of the temperature θ (for periodic solutions, minima and maxima are represented as curves, and intermediate values are represented as a hatched region). Frame b is a close-up on the branch of periodic solutions in Frame a. In addition, Frame b shows a representation in the (θ, I) plane of a bursting cycle obtained by direct integration of the OPO equations (4.10) coupled to the temperature equation (4.16). Fixed parameter values are $\chi_1 = 17.5$, $\chi_2 = 12.25$, $\chi_{12} = 7$, $\Delta_p = 1.5$, $\Delta_1 = 12.5$, $\Delta_2 = 35.5$, $\gamma = 10$, $\varepsilon = 10^{-3}$, $\alpha = 0$, and $\beta = 1.225 \cdot 10^3$. Stable and unstable solutions are represented as solid and dashed curves respectively. Bifurcation points are denoted as follows: BP = steady state branch point, LP = steady state limit point, H = Hopf bifurcation, CLP = cycle limit point. The horizontal branch $I = 0$ is the off state. The closed branches to the left and to the right of Frame a are branches of steady emission (on states). The middle closed branch is a branch of fast periodic intensity oscillations. The bursting cycle corresponds to the periodic switching between the off state and the oscillatory state.

can be understood as a slow motion of the system state along the branches of equilibria and limit cycles. We see from Fig. 4.5b that the system is periodically switching between the off-state branch and the stable branch of rapid oscillations. After passing through the subcritical Hopf bifurcation, the system jumps to the upper state with a delay. This bursting scenario has been called subcritical elliptic bursting of Bautin type in [60].

This phase-plane analysis shows that the bursting oscillations can be understood as a periodic switching between two branches of solutions of the two-mode field equations (4.10), just like periodic thermal oscillations could be described as a periodic switching between the on and off states in the monomode OPO model. This analogy and the simplicity of these equations encourages further analytical studies.

4.6.2 Perturbative analysis

We now make the assumption of a large spectral distance between the mode-1 and mode-2 resonances. Introducing

$$\sigma_b \equiv \sigma_2 - \sigma_1, \quad (4.20)$$

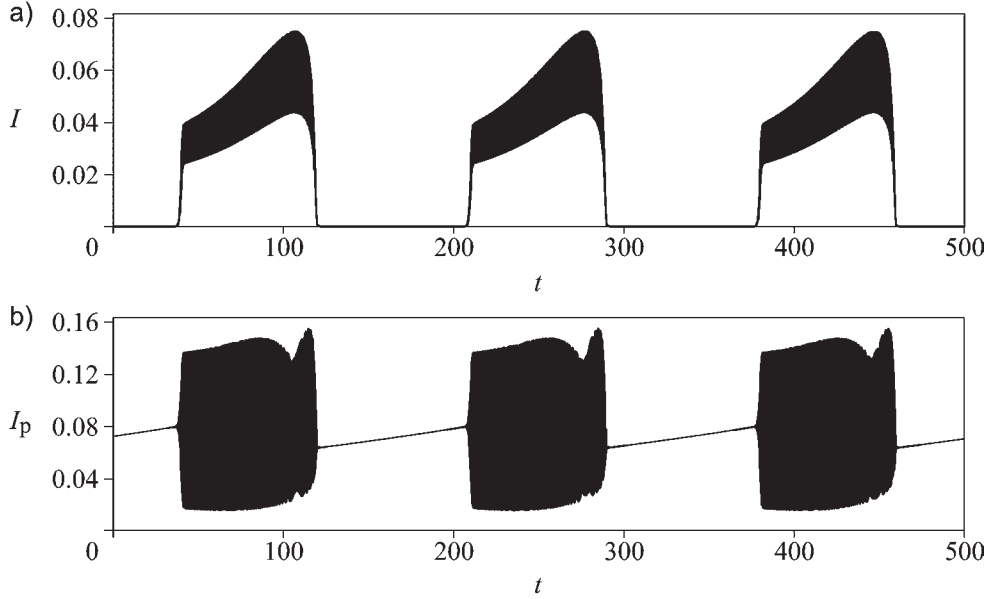


Figure 4.6: Bursting oscillations in an OPO, computed by direct integration Eqs. (4.10) and (4.16). Parameter values are the same as in Fig. 4.5. a) signal intensity as a function of time, b) pump intensity as a function of time.

this limit can be expressed as:

$$|\sigma_b| \gg 1. \quad (4.21)$$

The reason for the ‘b’ subscript is that σ_b will appear as the frequency of the fast intensity oscillations in the bursting cycle. We further assume that the arithmetic mean of the mode-1 and mode-2 detunings,

$$\sigma \equiv \frac{\sigma_1 + \sigma_2}{2}, \quad (4.22)$$

and the pump detuning σ_p are $O(1)$ quantities, for only this case leads to bursting oscillations under the condition (4.21). By substituting

$$\sigma_1 = \sigma - \frac{1}{2}\sigma_b, \quad \sigma_2 = \sigma_s + \frac{1}{2}\sigma \quad (4.23)$$

into Eqs. (4.10b) and (4.10c), we then note that their right-hand sides are dominated by the terms proportional to σ_b , so that

$$A_1 \propto \exp\left(\frac{i\sigma_b t}{2}\right), \quad A_2 \propto \exp\left(-\frac{i\sigma_b t}{2}\right), \quad (4.24)$$

showing that the amplitudes A_1 and A_2 are rapidly oscillating functions of t . This suggests to average the OPO evolution equations with respect to these fast oscillations. The averaging is described in detail in Appendix 4.B and uses a two-time perturbation

analysis. In first approximation, Eqs. (4.10) reduce to:

$$\frac{da_p}{dt} = \gamma [(-1 - i\sigma_p)a_p - \chi_{12}a_1a_2 + 1], \quad (4.25a)$$

$$\frac{da_1}{dt} = (-1 - i\sigma_1)a_1 + \chi_{12}a_p a_2^*, \quad (4.25b)$$

$$\frac{da_2}{dt} = (-1 - i\sigma_2)a_2 + \chi_{12}a_p a_1^*, \quad (4.25c)$$

where

$$A_p = a_p + O(\sigma_b^{-1}), \quad A_1 = \frac{a_1}{\sqrt{2}} + O(\sigma_b^{-1}), \quad A_2 = \frac{a_2}{\sqrt{2}} + O(\sigma_b^{-1}). \quad (4.26)$$

Eqs. (4.25) are formally identical to the nondegenerate monomode OPO model (4.2). Now, remember from Sec. 4.3.1 that, in the long-time limit, the nondegenerate monomode model is reducible without loss of generality to the degenerate monomode model with the help of a variable change. The same exact method applies here, as a consequence of which we find that the averaged multimode equations (4.25) can be further reduced to:

$$\frac{da_p}{dt} = \gamma [(-1 - i\sigma_p)a_p - \chi_{12}a^2 + 1], \quad (4.27a)$$

$$\frac{da}{dt} = (-1 - i\sigma)a + \chi_{12}a_p a^*, \quad (4.27b)$$

where the new variable a is related to the signal amplitudes as:

$$a_1 = a \exp \left[\frac{i\sigma_b(t - t_0)}{2} \right], \quad (4.28a)$$

$$a_2 = a \exp \left[\frac{-i\sigma_b(t - t_0)}{2} \right]. \quad (4.28b)$$

Substituting the above relations into the expressions (4.47) computed in Appendix 4.B for the signal and pump intensities, we obtain:

$$I_p = |a_p|^2 - \gamma I_b + O(\sigma_b^{-2}), \quad (4.29a)$$

$$I = |a|^2 + I_b + O(\sigma_b^{-2}), \quad (4.29b)$$

where

$$I_b \equiv \sigma_b^{-1} \text{Im} [(\chi_1 a_p^* a^2 + \chi_2 a_p (a^*)^2) \exp [i\sigma_b(t - t_0)]] \quad (4.30)$$

is a fast oscillatory contribution to the intensities.

We thus found that, in the limit of a large separation of the mode-1 and mode-2 resonances, the degenerate two-mode OPO equations (4.10) used in Sec. 4.6.1 to simulate a bursting experiment ultimately reduce to the system (4.27), which is formally equivalent to the degenerate monomode OPO equations used in Sec. 4.4 to describe the

simple, periodic thermo-optical oscillations. This complements, with a sound theoretical basis, the observation in Sec. 4.5 that the envelope of the fast intensity oscillations in the case of bursting dynamics seems to undergo the same qualitative sequence of bifurcations as the signal intensity in the case of slow periodic oscillations. These two physically distinct situations are distinguished by the absence (in the case of slow oscillations) or presence (in the case of bursting) of a fast oscillatory contribution to the intensities, as is readily observed by comparing the expressions (4.17), (4.18), and (4.29).

An important consequence of the asymptotic equivalence between the two-mode and monomode models is that the whole bulk of existing knowledge about the monomode equations can be immediately extended to the context of the fast oscillatory dynamics described here. In particular, the condition of fast oscillations for large σ_b can be deduced from the condition of signal emission in the monomode model [73]:

$$(1 + \sigma_p^2)(1 + \sigma^2) < \chi_{12}^2. \quad (4.31)$$

A remarkable property of this condition is that it does not depend on the difference σ_b between the two resonance frequencies. This indicates that contrary to naive intuition the two resonance curves need not overlap for the two modes to interact. This was illustrated in the numerical bifurcation diagram of Fig. 4.5a, carried out for $\sigma_b = 23$ in units of the resonance half-width. Thus, bimode regimes featuring fast oscillations are expected to be much more common than if near coincidence of the resonances were required. This is consistent with the experiments where such oscillations have been observed relatively easily in a number of different configurations [115].

Under the assumption of a large separation of the two resonances, we could treat the self-couplings of the amplitudes A_1 and A_2 with a perturbative approach. The structure of the averaged equations (4.25) implies that, in first approximation, the two modes behave effectively as a signal-idler pair: both modes independently oscillate close to their respective resonances, with a constraint over the sum of the two oscillation frequencies expressed by Eqs. (4.28). This fact can be understood from the expressions (4.9) of the four nondegenerate signal and idler amplitudes associated to the “degenerate” mode amplitudes A_1 and A_2 . In the limit $\sigma_b \gg 1$, the signal-idler couplings become only weakly efficient for the pairs $(A_{s,1}, A_{i,1})$ and $(A_{s,2}, A_{i,2})$ due to the large spectral separation of the resonances involved. The four fields then arrange themselves into two pairs of signal and idler fields $(A_{s,1}, A_{i,2})$ and $(A_{s,2}, A_{i,1})$ that nearly “ignore” each other, but are subsumed as a single amplitude pair (A_1, A_2) in the degenerate description. Our perturbative calculation can be envisioned as a way of taking advantage of the weak efficiency of the coupling between these two signal-idler pairs in order to compute the oscillatory contributions to the intensities as corrections to the leading-order expressions.

4.7 Summary

We proposed a simple theoretical description of a case of bursting oscillations observed experimentally by A. Amon and M. Lefranc in Lille for an OPO system subject to thermal effects. First, these oscillations have been simulated numerically using previously derived equations for an OPO operating on two transverse modes. With the help of the numerical continuation software `AUTO` we showed that a simple phase-plane analysis explains the bursting cycle. Furthermore, by taking advantage of the very high oscillation frequencies observed, we performed a perturbative analysis of the model, which was reduced, in two steps, to a pair of equations that are formally equivalent to a degenerate monomode OPO model. This equivalence was exploited to obtain an estimate of the condition of fast intensity oscillations. One of the two reduction steps consisted in showing that the nondegenerate monomode OPO model is reducible without loss of generality to the degenerate one in the long-time limit.

Appendices to Chapter 4

4.A Equivalence between the degenerate and non-degenerate monomode OPO models

The monomode nondegenerate OPO equations (4.2) can be simplified if they are rewritten in terms of a new complex amplitude A , defined as

$$A(t) \equiv \sqrt{A_s(t)A_i(t)}. \quad (4.32)$$

Because A_s and A_i are complex quantities, there are two possible determinations of the above definition; however, which one is chosen does not matter. After substitution of Eq. (4.32), the pump equation (4.2a) becomes identical to the monomode degenerate pump equation (4.4a). We now seek an evolution equation for A . First, from the field equations (4.2b) and (4.2c), we note that

$$\begin{aligned} & \frac{d}{dt} (|A_s|^2 - |A_i|^2) \\ = & 2 \operatorname{Re} \left(A_s^* \frac{dA_s}{dt} - A_i^* \frac{dA_i}{dt} \right) \\ = & 2 \operatorname{Re} (A_s^* [(-1 - i\sigma_s)A_s + \chi A_p A_i^*] - A_i^* [(-1 - i\sigma_i)A_i + \chi A_p A_s^*]) \\ = & -2 (|A_s|^2 - |A_i|^2), \end{aligned} \quad (4.33)$$

from which we deduce that $|A_s|^2 - |A_i|^2 \rightarrow 0$ after a sufficient amount of time elapses. If we are only interested in long-time asymptotics, we may therefore assume that $|A_s| = |A_i|$, so that the two amplitudes differ only by a (possibly time-dependent) phase factor, $\exp[i\phi(t)]$. In view of the definition (4.32) of A , this fact can be expressed as follows:

$$A_s(t) = A(t) \exp\left(\frac{i\phi(t)}{2}\right), \quad (4.34a)$$

$$A_i(t) = A(t) \exp\left(-\frac{i\phi(t)}{2}\right), \quad (4.34b)$$

which can be viewed as a variable change from (A_s, A_i) to (A, ϕ) . Carrying out this variable change in the field equations (4.2b) and (4.2c) leads to a pair of coupled

equations for A and ϕ :

$$\frac{dA}{dt} + \frac{1}{2}iA\frac{d\phi}{dt} = (-1 - i\sigma_s)A + \chi A_p A^*, \quad (4.35a)$$

$$\frac{dA}{dt} - \frac{1}{2}iA\frac{d\phi}{dt} = (-1 - i\sigma_i)A + \chi A_p A^*. \quad (4.35b)$$

By performing linear combinations of these two equations, we find:

$$\frac{dA}{dt} = \left(-1 - i\frac{\sigma_s + \sigma_i}{2}\right)A + \chi A_p A^*, \quad (4.36a)$$

$$\frac{d\phi}{dt} = \sigma_i - \sigma_s. \quad (4.36b)$$

Eq. (4.36a) is the required equation for A and is identical to Eq. (4.4b), which is the monomode degenerate signal equation. The phase ϕ is solved from Eq. (4.36b):

$$\phi(t) = (\sigma_i - \sigma_s)(t - t_0). \quad (4.37)$$

Substituting this solution into the relations (4.34) yields Eqs. (4.5).

4.B Fast oscillation averaging

In this appendix, we average the two-mode degenerate OPO equations (4.10) in the limit of large σ_b , and taking the pump detuning σ_p and the mean signal detuning σ to be $O(1)$ quantities. We expand solutions of the system (4.10) as power series of the small parameter σ_b^{-1} :

$$A_p = A_p^0(\vartheta, \tau) + \sigma_b^{-1}A_p^1(\vartheta, \tau) + O(\sigma_b^{-2}), \quad (4.38a)$$

$$A_1 = A_1^0(\vartheta, \tau) + \sigma_b^{-1}A_1^1(\vartheta, \tau) + O(\sigma_b^{-2}), \quad (4.38b)$$

$$A_2 = A_1^0(\vartheta, \tau) + \sigma_b^{-1}A_1^1(\vartheta, \tau) + O(\sigma_b^{-2}), \quad (4.38c)$$

where we have introduced

$$\vartheta \equiv \sigma_b t, \quad \tau \equiv t \quad (4.39)$$

as fast and slow time variables, respectively. The assumption of two independent time variables implies the derivation rule

$$\frac{d}{dt} = \sigma_b \frac{\partial}{\partial \vartheta} + \frac{\partial}{\partial \tau}. \quad (4.40)$$

Inserting the expansions (4.38) and (4.40) and the expressions (4.23) for the signal detunings σ_1 and σ_2 into the OPO equations (4.10), and then equating to zero the coefficient of each power of σ_b leads to a sequence of problems for the unknown coefficients in Eqs. (4.38). The leading-order problem is $O(\sigma_b)$ and given by

$$\frac{\partial A_p^0}{\partial \vartheta} = 0, \quad \frac{\partial A_1^0}{\partial \vartheta} = \frac{1}{2}iA_1^0, \quad \frac{\partial A_2^0}{\partial \vartheta} = -\frac{1}{2}iA_2^0, \quad (4.41)$$

whose solution is of the form

$$A_p^0 = B_p(\tau), \quad A_1^0 = B_1(\tau) \exp\left(\frac{i\vartheta}{2}\right), \quad A_2^0 = B_2(\tau) \exp\left(-\frac{i\vartheta}{2}\right), \quad (4.42)$$

where $B_p(\tau)$, $B_1(\tau)$, and $B_2(\tau)$ are so-far-undetermined functions of τ . The next problem is $O(1)$ and is given by

$$\frac{\partial A_p^1}{\partial \vartheta} = -\frac{dB_p}{d\tau} + \gamma [(-1 - i\sigma_p)B_p - 2\chi_{12}B_1B_2 + 1 - \chi_1B_1^2 \exp(i\vartheta) - \chi_2B_2^2 \exp(-i\vartheta)], \quad (4.43a)$$

$$\begin{aligned} \frac{\partial B_1^1}{\partial \vartheta} - \frac{1}{2}iB_1^1 &= \left(-\frac{dB_1}{d\tau} + (-1 - i\sigma)B_1 + \chi_{12}B_pB_2^*\right) \exp\left(\frac{i\vartheta}{2}\right) \\ &+ \chi_1B_pB_1^* \exp\left(-\frac{i\vartheta}{2}\right), \end{aligned} \quad (4.43b)$$

$$\begin{aligned} \frac{\partial B_2^1}{\partial \vartheta} + \frac{1}{2}iB_2^1 &= \left(-\frac{dB_2}{d\tau} + (-1 - i\sigma)B_2 + \chi_{12}B_pB_1^*\right) \exp\left(-\frac{i\vartheta}{2}\right) \\ &+ \chi_2B_pB_2^* \exp\left(\frac{i\vartheta}{2}\right). \end{aligned} \quad (4.43c)$$

Solvability with respect to the fast time variable requires the conditions

$$\frac{dB_p}{d\tau} = \gamma [(-1 - i\sigma_p)B_p - 2\chi_{12}B_1B_2 + 1], \quad (4.44a)$$

$$\frac{dB_1}{d\tau} = (-1 - i\sigma)B_1 + \chi_{12}B_pB_2^*, \quad (4.44b)$$

$$\frac{dB_2}{d\tau} = (-1 - i\sigma)B_2 + \chi_{12}B_pB_1^*. \quad (4.44c)$$

Using Eqs. (4.39) and (4.42), and introducing

$$a_p \equiv A_p^0, \quad a_1 \equiv \sqrt{2}A_1^0, \quad a_2 \equiv \sqrt{2}A_2^0, \quad (4.45)$$

we can rewrite these conditions in the form (4.25), which is formally equivalent to the nondegenerate monomode OPO model (4.2). Expressed in terms of the variables (4.45), we seek a particular solution of Eqs. (4.43). It is not necessary to compute the most general solution because the additional terms therein can be cancelled with a near-identity transformation of the $O(1)$ amplitudes. We thus have:

$$A_p^1 = \frac{1}{2}\gamma [i\chi_1a_1^2 - i\chi_2a_2^2], \quad (4.46a)$$

$$A_1^1 = \frac{1}{\sqrt{2}}i\chi_1a_p a_1^*, \quad (4.46b)$$

$$A_2^1 = -\frac{1}{\sqrt{2}}i\chi_2a_p a_2^*. \quad (4.46c)$$

Therefore, using the $O(1)$ and $O(\sigma_b^{-1})$ solutions, the pump and signal intensities are given by

$$I_p = |a_p|^2 - \gamma I_b + O(\sigma_b^{-2}), \quad (4.47a)$$

$$I_s = \frac{|a_1|^2 + |a_2|^2}{2} + I_b + O(\sigma_b^{-2}), \quad (4.47b)$$

where

$$I_b \equiv \sigma_b^{-1} \text{Im} [a_p^* (\chi_1 a_1^2 - \chi_2 a_2^2)]. \quad (4.48)$$

Chapter 5

Optically bistable devices with a large delay loop

“Mathematics is the art of giving the same name to different things.”
—Henri Poincaré

5.1 Introduction

Nonlinear delayed-feedback systems are known to manifest very complex behavior. In 1979, Ikeda predicted the existence of chaos in an optically bistable device as a result of a delay-induced instability [56, 57]. It was then observed in a hybrid electro-optical system with computer-generated delay [46] and later in an all-optical system [84]. From then on, the study of the various oscillation modes along the route to chaos has attracted much attention from both the theoretical and experimental viewpoints. For delay times much larger than the relaxation time of the bistable medium, square-wave-like oscillations with a period of roughly twice the delay time (period-2 oscillations) were observed to emerge from a steady state, and to undergo a truncated Feigenbaum cascade of successive period doubling bifurcations as the feedback level is increased [54]. The truncation was shown to be a consequence of noise [19]. Furthermore, isolas of higher-harmonic square-wave states were discovered alongside the period-doubling route to chaos of the fundamental mode [54, 58]. Allowed oscillation frequencies were identified as odd multiples of the fundamental frequency. Each harmonic was observed to undergo its own sequence of period doublings, resulting in a large number of stable oscillatory states [20]. Their phase-locking to external modulation signals was predicted theoretically [37] and demonstrated experimentally [36].

It was then realized that such multistable output could be used to encode information in high-capacity memory devices [59]. Experiments showed that an electro-optical hybrid bistable system with a fiber delay loop could indeed sustain a large number of oscillatory states, and demonstrated the efficiency of two methods for the selection of oscillation mode known as seeded bifurcation switch [3] and chaotic search [4]. However, the experiments also produced evidence that such systems were very sensitive to

spurious resonances [3], or nonlinearities [20]. Therefore, discrepancies between theory and experiments occurred, and were difficult to interpret. Especially disturbing was the fact that a large number of harmonics predicted by numerical studies were not observed in physical implementations, although they could be recovered by subjecting the system to a periodic modulation with the same frequency as the missing harmonics [3]. This raised the need for a rigorous stability analysis of all the bifurcating modes.

Analytical stability results are difficult to establish, because mathematical models of delayed-feedback systems usually consist in delay-differential equations, whose mathematical understanding is much more challenging than the study of systems with a local evolution in time. Simple models of a delayed optically bistable device often consist in a scalar nonlinear singularly perturbed delay-differential equation of the form:

$$\varepsilon \frac{dx(S)}{dS} = F(x(S), x(S-1), \Lambda), \quad (5.1)$$

where the scalar variable x characterizes the state of the bistable medium and determines the output intensity, S represents time in units of the delay, ε denotes the ratio of the relaxation time to the delay time (a small quantity if the delay is large), and Λ represents a control parameter, such as the amount of light injected in the optical resonator. F is a nonlinear function of its arguments and depends on the delayed variable, $x(S-1)$. More specifically, an idealized model is provided by the well-known Ikeda equation [56, 57], where the nonlinear function F assumes the form:

$$F(x(S), x(S-1), \Lambda) = -x(S) + \Lambda [1 + 2B \cos(x(S-1) - A)]. \quad (5.2)$$

This model has been formulated in order to provide a simple description of a delayed optically bistable device implemented as a saturable absorber inside a ring cavity (see Fig. 5.1). A is a detuning parameter of the cavity, and B , Λ , x , and F are proportional, respectively, to the feedback level, the injected power, the average refractive index shift in the bistable material, and the output intensity.

Strictly speaking, the Ikeda model is valid only in the case of purely dispersive bistability¹, and if $B \ll 1$, that is, if the amount of light fed back in the cavity is small. It has proven to be of limited validity for the description of an all-optical bistable system, and more accurate models have been proposed [13, 53]. Nevertheless, there exists a class of electro-optical hybrid bistable systems for which the Ikeda equation provides a reasonably good description [3]. Stable oscillation regimes observed in these physical experiments are correctly reproduced by the Ikeda equation: see, for example, the fundamental period-2 square-wave oscillation regime (Fig. 5.2a) and its third harmonic (Fig. 5.2b); the fundamental period-4 solution (5.2c) and two period-4 “isomers” of the third harmonic (Figs. 5.2d, 5.2e). This contributes to the interest in the Ikeda equation, and motivates the analysis of the generic scalar equation (5.1) undertaken in this chapter. Delayed equations of this kind also arise in other domains of research, for example in ecology [51] and physiology [74].

¹where variations of the refractive index dominate variations of the absorption in the nonlinear medium.

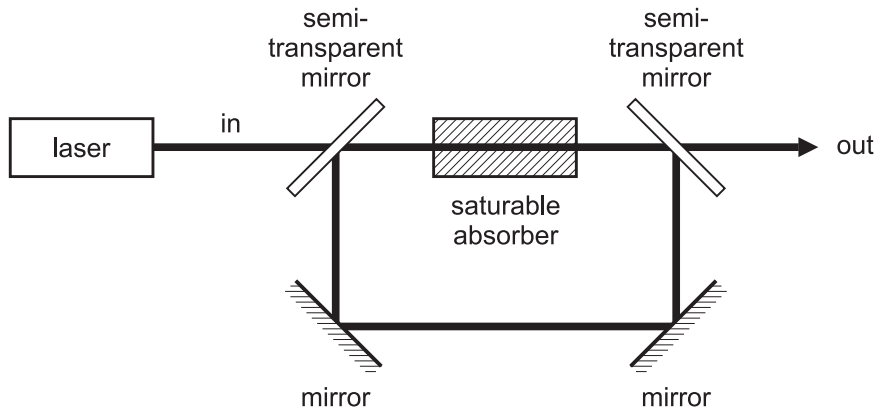


Figure 5.1: Optical bistability is a phenomenon by which a cavity filled with a nonlinear medium and driven by a source of coherent light exhibits two distinct states of optical transmission. This simplified block-diagram represents a bistable device with delayed feedback, implemented as a saturable absorber inside a ring cavity.

For small ε , the difference equation

$$F(x(S), x(S-1), \Lambda) = 0 \quad (5.3)$$

obtained by setting $\varepsilon = 0$ in Eq. (5.1) is often used as a simplified model. Its resolution reduces to an iterative computation of the value of a solution at a given instant from its value one delay time earlier. A numerical analysis of the difference equation successfully reproduces the Feigenbaum cascade of period doublings and the chaos domain beyond the Feigenbaum accumulation point (see Fig. 5.3). However, such a rough simplification may alter the stability properties of the system, because it fails to account for the very large time scales generated by the small but finite left-hand side of Eq. (5.1) [50]. As a result, the difference equation is unable to provide an explanation for the observed differences in the stability properties of the successive odd harmonic solutions [58]. A question that has received much interest is then of exactly how faithful the description provided by such a simplified model is to the dynamics of the delay-differential equation (5.1).

Much progress has been accomplished over the past decades in our analytical understanding of Eq. (5.1) and how it relates to the limit form (5.3). The existence of periodic solutions and the asymptotic structure of their transition layers in the square-wave limit are extensively studied in [17, 76]. From the viewpoint of bifurcation theory, the period-2 oscillation threshold has been found to unfold, for small but finite ε , into a sequence of Hopf bifurcations corresponding to the emergence of successive odd harmonics of the fundamental oscillation mode [85]. Each mode was found to be unstable in the vicinity of its respective onset threshold, except the fundamental one. The continuous deformation of the fundamental mode from sine waves into square waves away from the bifurcation point has been related to an increase of the number of unstable roots in the characteristic equation arising from the linear stability analysis of the steady state [38]. Domain boundaries of steady, periodic, and subharmonic

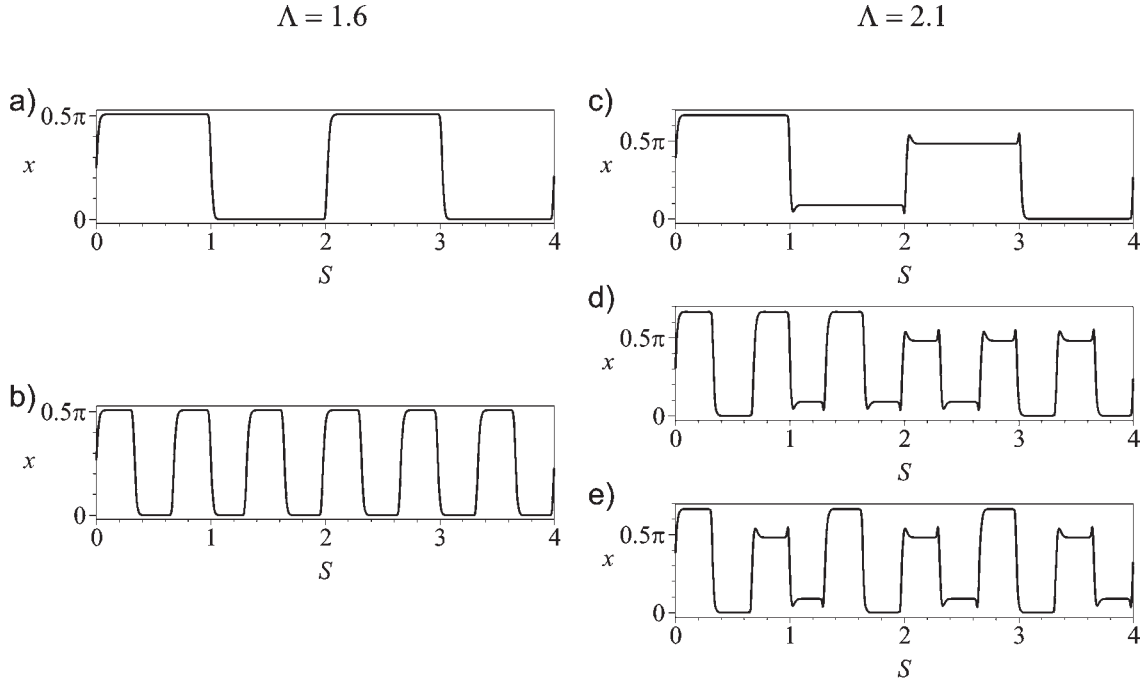


Figure 5.2: Numerically computed periodic solutions of the Ikeda equation (Eq. (5.1) with (5.2)). Parameter values are $A = -\frac{1}{2}\pi$, $B = 0.5$, and $\varepsilon = 10^{-2}$.

- a) The fundamental period-2 solution for $\Lambda = 1.6$, which lies beyond the primary periodic instability.
- b) The third harmonic for $\Lambda = 1.6$.
- c) The fundamental period-4 solution for $\Lambda = 2.1$, which lies beyond the period doubling transition to period-4 dynamics.
- d, e) Two period-4 “isomers” of the third harmonic for $\Lambda = 2.1$. They are distinguished by the arrangement of plateau values, as described in [20].

periodic dynamics in the map equation (5.3), and their unfolding for finite ε , were thoroughly analyzed [77, 85]. Despite these achievements, however, stability results taking properly the finiteness of ε into account remain rare, especially in presence of external perturbations. The mechanisms that determine the stability properties of the higher-harmonic solutions still lack a good analytical understanding beyond the linear theory.

Other physical systems known to manifest multistability and to display memory properties include models of neuronal recurrent feedback loops [33], electronic circuits [34], multimode lasers [91], and spatially extended nonlinear optical systems such as globally coupled lasers [92]. Otsuka and Ikeda showed that coupled nonlinear elements distributed in an optical ring cavity could cooperate to create a stable memory function, even though each individual element had no such ability in isolation [93]. In

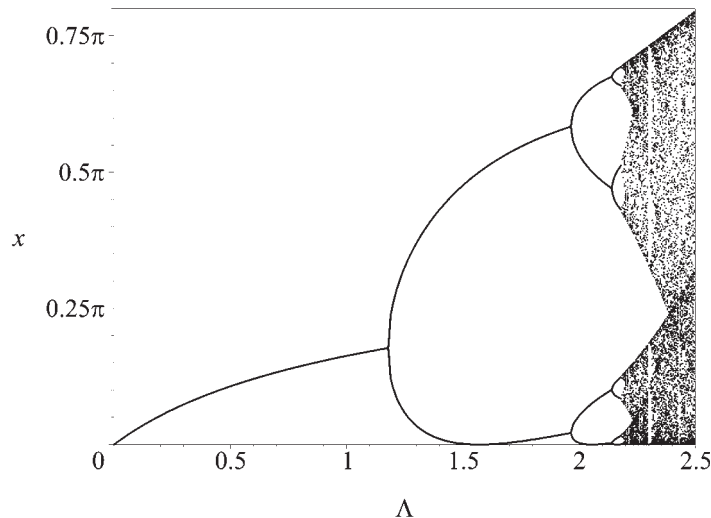


Figure 5.3: Numerically computed bifurcation diagram for the Ikeda map (Eq. (5.3) with (5.2)). Parameter values are $A = -\frac{1}{2}\pi$, $B = 0.5$, and $\varepsilon = 10^{-2}$. For each value of the feedback rate Λ , up to 128 successive values of x have been computed by iteration. They are represented as continuous curves up to the period-16 threshold, and as a set of discrete points beyond. The Feigenbaum accumulation point lies approximately at $\Lambda = 2.18$.

such unidimensional spatial arrangements, information is stored in the form of highly complex periodic configurations embedded within spatial chaos. Their role as memory carriers is comparable to the large-period oscillation modes observed along the route to temporal chaos in delayed-feedback systems.

Both classes of dynamical systems indeed exhibit strong similarities in many respects. Time series from delayed-feedback systems with a sufficiently large delay tend to display two widely separated time scales. A two-dimensional data representation reflecting this structure has revealed striking analogies with spatiotemporal dynamics [6]. The relevance of such a representation has motivated the work of Giacomelli and Politi in [43, 44], where a generic mathematical model for a delayed-feedback system, provided as a set of nonlinear delay-differential equations, is reduced to a partial differential equation using the method of multiple scales. It was pointed out that the identification of such analogies between different classes of dynamical systems should be encouraged as it could result in extensions of the field of application of existing analysis procedures. In this chapter, we propose to pursue this line of research with the aim of reducing the stability analysis of square-wave-like solutions of Eq. (5.1) to a simple, analytically tractable problem, even in presence of a weak additive forcing. Taking into account such an external perturbation is motivated by the important role played by periodic modulations in the stabilization of oscillation modes [3, 37, 36]. Its effect is introduced through the term $G(S)$, as follows:

$$\varepsilon \frac{dx(S)}{dS} = F(x(S), x(S-1), \Lambda) + G(S). \quad (5.4)$$

The first goal of this chapter is the reduction of the above equation to a mathematically simpler system. We proceed in two steps. First, we compute a normal form for Eq. (5.4) in the vicinity of the period-2 instability. An adapted multiple scale method is used that correctly takes into account the infinite-dimensional character of this equation and the presence of a source term. The normal form is a partial differential equation where the small parameter ε does not appear anymore, and where the effect of the delay appears only as a boundary condition. In this new formulation, the problem appears to be isomorphic to a spatially-extended system displaying domain-wall solutions, and this analogy is then exploited in the second reduction step. A mathematical technique based on the principle of matched asymptotic expansions, and inspired from a methodology suitable for the analysis of the motion of defect-like structures in spatially extended systems [97], is used to reduce the normal form to a set of ordinary equations involving only a finite number of degrees of freedom.

The restriction of our analysis to the vicinity of the period-2 instability constitutes a limitation of its scope to weakly nonlinear dynamics. Nevertheless, our results go beyond the linear theory: we are able, in that regime, to provide a thorough analytical understanding of the stability of the square wave solution and its harmonics, taking both the finiteness of ε and the presence of external forcing into account. We also identify in a precise way the mechanism responsible for the selection of such highly symmetric oscillation modes. This is contrasted with the dynamics of the map equation (5.3), whose square-wave solutions have much more arbitrariness in the time-distribution of plateau lengths and transition instants. Moreover, on the basis of the present analysis, we show that a suitably chosen periodic modulation may create and stabilize a large number of new oscillation modes, resulting in a kind of multistability different from that predicted in [59]. Such multistable dynamics could meet potential interest in information storage applications. The presentation of these new solutions constitutes the second goal of this chapter.

It is a known fact that a weak periodic forcing may fundamentally modify the nature of a nonlinear dynamical system, in that it may result in the creation of new attractors [16, 15]. The adjective “new,” in this sense, means that they cannot be identified to any of the asymptotic states, either attractor or repeller, that may exist in the autonomous system. Our reduced, finite-dimensional system is sufficiently simple mathematically to allow the analytical investigation of such a fundamental alteration of the dynamical properties of our delayed-feedback system. Our finding is that a weak periodic modulation resonant with one of the odd harmonic oscillation modes may induce the coexistence of a large number of new stable oscillatory states, even in the weakly nonlinear regime where our reduced model is relevant. The new attractors resemble the odd harmonic square-wave oscillations of the autonomous system, but with some of the fast transitions from one plateau value to another removed. No sequence of successive period doublings is involved in the phenomenon, as all new modes are strictly period-2. Such irregular oscillation patterns are reminiscent of the extremely long-lived transients described in [50]. The effect of the modulation is actually to turn a subset of them into genuine attractors, enabling them to act as persistent information

carriers.

This chapter is organized as follows. In Sec. 5.2, we proceed to the reduction of Eq. (5.4) to a normal form. We then perform, in Sec. 5.3, a thorough analysis of the case where the forcing is absent ($G(S) = 0$). Using various methods applicable to partial differential equations, we offer a complete analytical description of the emergence of odd harmonic oscillation modes from successive Hopf bifurcation points and of their continuous deformation from sine waves to square waves. We determine their stability over the whole domain of validity of our normal form analysis. In Sec. 5.4, we further reduce the partial differential equation to a set of ordinary differential equations. The stability of square-wave solutions in the absence of forcing is re-examined quantitatively in Sec. 5.5: we compute estimates of the temporal growth rates of small fluctuations around unstable solutions. In Sec. 5.6, we set the background for the treatment of the forced problem ($G(S) \neq 0$): we specialize the reduced equations for the description of oscillatory states phase-locked to a periodic modulation. In Sec. 5.7, we discuss the phenomenon of modulation-induced multistability, paying particular attention to its potential value in the context of information storage applications. In Sec. 5.8, we analyze the influence of several modulation characteristics such as frequency, detuning, and waveform on the stability of the phase-locked oscillation modes. Finally, our results are summarized and discussed in Sec. 5.9.

5.2 Normal form analysis

Our first goal is the derivation of a normal form for Eq. (5.4) in the vicinity of a period-2 oscillatory instability of a steady state, and in the case of a weak external forcing ($G(S) \ll 1$). To this end, we apply the principles of multiple-scale analysis. Here we only state and comment the final result; the detailed calculation is relegated to Appendix 5.A. In the absence of forcing, the normal form matches that of Giacomelli and Politi [43, 44]. As previously found by these authors, it is obtained as a solvability condition to order 3 in the perturbative analysis. It is a partial differential equation that does not involve a time delay anymore, but that depends explicitly on two time variables acting on different time scales. The existence of two time scales behaving as though they were independent variables is a remarkable fact that has helped unravelling analogies between delayed and spatially extended systems [43], and that is observable experimentally [6].

In our case, the normal form is a real Ginzburg-Landau equation with a source term:

$$\frac{\partial u}{\partial t} = \frac{\partial^2 u}{\partial s^2} + 2u(\lambda \pm u^2) + \mathcal{A}g(s, t), \quad (5.5)$$

and the solutions $u(s, t)$ are further constrained by an antiperiodic boundary condition:

$$u(s, t) = -u(s - 1, t), \quad (5.6)$$

which comes up as the solvability condition to order 1. This constraint is a consequence of the marginal stability of the steady state of the difference equation (5.3) at the

instability threshold, and results in the selection of period-2 dynamics. The symbol \pm in Eq. (5.5) assumes the value $+$ or $-$ depending on whether the bifurcating branch of periodic solutions is subcritical or supercritical, respectively. The reason for Eq. (5.5) to be real and not complex as in [43, 44] is that we restricted our analysis to a scalar delay-differential equation, which turns out to admit a real normal form. The independent variables s and t represent two distinct time scales: $s \simeq S$ is comparable to the delay, while t is a much longer time scale. $u(s, t)$, λ , and $g(s, t)$ are scaled representations of the dynamical variable $x(S)$, the control parameter Λ , and the forcing term $G(S)$, respectively. Because variations of x are small, they contribute linearly to the field intensity, and thus u can be thought of as a modulation of the output power. The precise relationships between the scaled quantities and their unscaled counterparts are listed at the end of Appendix 5.A, in Eqs. (5.105). Note that the normal form involves a combined description of the forcing term $g(s, t)$ on the two time scales s and t .

The symbol \mathcal{A} denotes a linear operator that appears naturally in the course of the derivation of the normal form. It acts on the forcing term $g(s, t)$ as follows:

$$\mathcal{A}g(s, t) \equiv \lim_{N \rightarrow \infty} \frac{1}{2N} \sum_{j=-N}^{N-1} (-1)^j g(s - j, t), \quad (5.7)$$

so that $\mathcal{A}g(s, t)$ is an antiperiodic function of s : $\mathcal{A}g(s, t) = -\mathcal{A}g(s - 1, t)$, by definition of \mathcal{A} . This is necessary for the problem (5.5)–(5.6) to be well-posed. The action of the operator \mathcal{A} on the forcing term is more transparent if expressed in the frequency domain. For $g(s, t) = \widehat{g}(t) \exp i\omega s$, Eq. (5.7) reduces to:

$$\mathcal{A}\widehat{g}(t) \exp i\omega s = \widehat{\mathcal{A}}(\omega) \widehat{g}(t) \exp i\omega s, \quad (5.8)$$

where $\widehat{\mathcal{A}}(\omega) = 1$ if ω is an odd integer multiple of π , and $\widehat{\mathcal{A}}(\omega) = 0$ otherwise. The linear operator $\mathcal{A}(s, t)$ thus simply filters out, on the short time scale s , all frequencies that are not odd harmonics of the fundamental frequency of the oscillatory instability. This means that only such resonant components of the forcing signal have a significant effect on the system, in the domain of validity of our analysis. However, the fact that the operator \mathcal{A} does not act on the long time scale t means that this filtering is not infinitely narrow, because it is always possible to model a very weak detuning from this perfect resonance condition on the t time scale, by introducing a phase drift in the forcing signal that depends on t only.

Although formally derived for the scaling $\Lambda - \Lambda_0 = O(\varepsilon^2)$, where Λ_0 is the period-2 instability threshold of Eq. (5.3), the normal form should be valid as long as $|\Lambda - \Lambda_0| \ll 1$, or equivalently, $|\lambda| \ll \varepsilon^{-2}$. In the domain characterized by $1 \ll \lambda \ll \varepsilon^{-2}$, it reduces to the second-order ordinary differential equation obtained in [17]. Throughout this chapter, we are only concerned with the case of a supercritical bifurcation, corresponding to the sign $-$ in Eq. (5.5):

$$\frac{\partial u}{\partial t} = \frac{\partial^2 u}{\partial s^2} + 2u(\lambda - u^2) + \mathcal{A}g(s, t), \quad (5.9a)$$

$$u(s, t) = -u(s - 1, t). \quad (5.9b)$$

5.3 No-forcing case

In this section, we focus on the problem (5.9) in the case where the forcing is absent ($g(s, t) = 0$):

$$\frac{\partial u}{\partial t} = \frac{\partial^2 u}{\partial s^2} + 2u(\lambda - u^2), \quad (5.10a)$$

$$u(s, t) = -u(s - 1, t). \quad (5.10b)$$

we completely solve the problem of the determination of the asymptotic states (*i.e.*, the possible long-time behaviors) and determine their stability. We compare the results with previous studies of the delay-differential equation (5.1) in the absence of forcing. This provides a way of testing the validity of our normal form while reviewing and complementing current understanding of the dynamics of the delay-differential equation (5.1) at the onset of period-2 oscillations.

Eq. (5.10a) subject to various types of boundary conditions, such as Dirichlet or Neumann conditions, that arise naturally in the context of spatially extended systems, has been extensively studied (see [133] and references therein). The analytical study of asymptotic states of such systems and their stability properties rests to a large extent upon comparison methods, Lyapunov functionals, and bifurcation theory [28]. In our case, the boundary condition (5.10b) is unusual, but nevertheless most of the aforementioned techniques remain applicable to our problem.

5.3.1 Asymptotic states

The following analysis follows closely an argument in [29], in which the author discusses the asymptotic states of Eq. (5.10a) over an infinite domain ($-\infty < s < \infty$). In order to determine the long-time behavior of solutions of the antiperiodic problem (5.10), we introduce the Lyapunov functional

$$L(t) \equiv \frac{1}{2} \int_0^1 \left[\left(\frac{\partial u}{\partial s} \right)^2 + (u^2 - \lambda)^2 \right] ds \quad (5.11)$$

and compute its time derivative:

$$\begin{aligned} \frac{dL}{dt} &= \int_0^1 \left[\frac{\partial u}{\partial s} \frac{\partial^2 u}{\partial s \partial t} + 2u(u^2 - \lambda) \frac{\partial u}{\partial t} \right] ds \\ &= - \int_0^1 \left[\frac{\partial^2 u}{\partial s^2} \frac{\partial u}{\partial t} + 2u(\lambda - u^2) \frac{\partial u}{\partial t} \right] ds \\ &= - \int_0^1 \left[\frac{\partial^2 u}{\partial s^2} + 2u(\lambda - u^2) \right]^2 ds = - \int_0^1 \left(\frac{\partial u}{\partial t} \right)^2 ds. \end{aligned} \quad (5.12)$$

The passage from the first to the second line involves an integration by parts of the first term under the integral sign. The boundary terms cancel each other because of the

antiperiodicity condition (5.10b). In the two last steps, we used Eq. (5.10a) to perform substitutions. Now, in view of Eqs. (5.11) and (5.12), L is a positive function of t that is strictly decreasing unless $\frac{\partial u}{\partial t} = 0$. Therefore, it must tend towards a constant for $t \rightarrow \infty$. By an argument analogous to that of Lemma 6 in [29], which essentially ensures that L and u evolve smoothly enough, one deduces therefrom that $\frac{dL}{dt} \rightarrow 0$ and thus, from Eq. (5.12),

$$\frac{\partial^2 u}{\partial s^2} + 2u(\lambda - u^2) \rightarrow 0 \quad (5.13)$$

uniformly in s for $t \rightarrow \infty$. This, in turn, implies that any solution u of the problem (5.10) tends towards a solution that ceases to depend on t after a sufficiently long time. Consequently, any asymptotic state is a solution of the t -independent problem

$$\frac{\partial^2 u}{\partial s^2} + 2u(\lambda - u^2) = 0, \quad (5.14a)$$

$$u(s, t) = -u(s - 1, t). \quad (5.14b)$$

The t -independent problem (5.14) is exactly soluble. First, note that the trivial solution $u = 0$ exists for any value of λ . Next, by multiplying both sides of Eq. (5.14a) by $\frac{\partial u}{\partial s}$ and integrating, we get a first order differential equation that is soluble by quadrature. The most general nontrivial solution satisfying the boundary condition (5.14b) is expressible in terms of elliptic functions (see [70] or any textbook about special functions):

$$u = u_m(s - \phi; k) \equiv 2mk \operatorname{K}(k) \operatorname{sn}(2\operatorname{K}(k)m(s - \phi); k). \quad (5.15)$$

Here m is an odd integer index that numbers nontrivial solutions, ϕ is a real integration constant that accounts for time translation invariance, and k is another integration constant ranging from 0 to 1. $\operatorname{K}(k)$ denotes the complete elliptic integral of the first kind, and the above expression also involves Jacobi's elliptic sn function. The constants k and m are related to the control parameter λ as follows:

$$\lambda = \lambda_m(k) \equiv 2(1 + k^2)\operatorname{K}(k)^2 m^2. \quad (5.16)$$

For a fixed value of the index m , Eqs. (5.15) and (5.16) provide parametric expressions of the solution for any value of λ . Each value of m corresponds to a different branch of solutions bifurcating from the trivial solution $u = 0$ at a critical value of λ given by

$$\lambda = \lambda_m^C \equiv \lambda_m(0) = \frac{1}{2}\pi^2 m^2. \quad (5.17)$$

The different branches are represented on a bifurcation diagram in Fig. 5.4 (ignore the indications of stability for now). The existence of an infinite sequence of Hopf bifurcation points beyond the first threshold of periodic instability is known to be a consequence of the finiteness of the small parameter ε [85], which is therefore correctly captured in our normal form analysis. This multiplicity of bifurcation points has no counterpart in the difference equation (5.3) obtained by setting $\varepsilon = 0$ in Eq. (5.1).

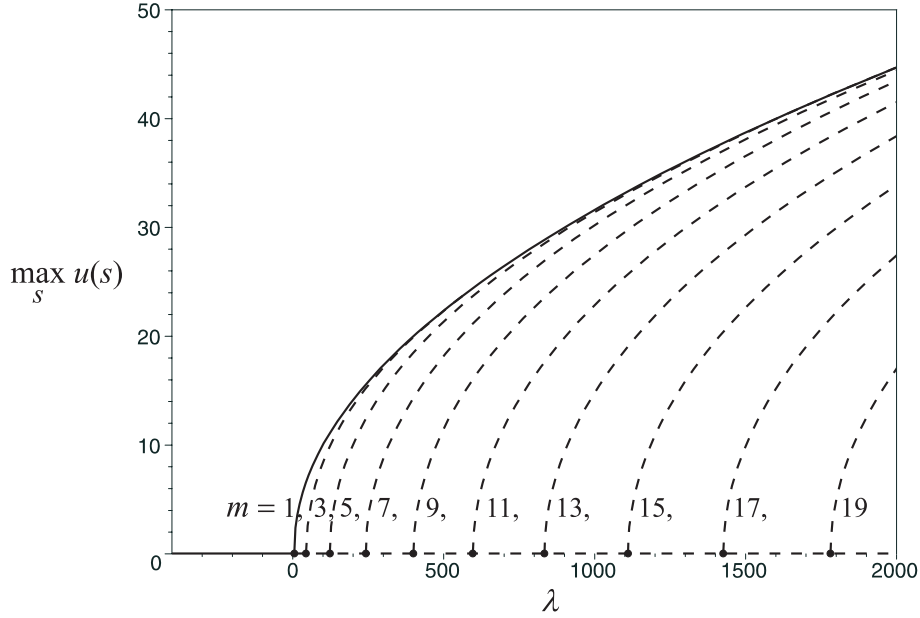


Figure 5.4: Bifurcation diagram for Eqs. (5.10). The trivial solution $u = 0$ and the maximum values of the periodic solutions $u = u_m(s; k)$ are shown as a function of λ . Solid and dashed curves represent stable and unstable solutions, respectively. The steady state $u = 0$ is destabilized at $\lambda = \frac{1}{2}\pi^2$, and the fundamental oscillatory state $u = u_1$ becomes the new attractor. The other harmonics, $u = u_m$ for $m \neq 1$, are unstable for all λ within the limits of validity of the normal form (5.10).

The constant k parameterizes the possible solution shapes, which are given in terms of Jacobi's elliptic function $\text{sn}(x; k)$. This function deforms continuously from sine waves for $k = 0$ (the bifurcation point) to square waves for $k \rightarrow 1$, which corresponds to the limit of large λ . This is consistent with previous studies of the delay-differential equation (5.1) [38]. The function $\text{sn}(x; k)$ is periodic in x with period $4K(k)$. Therefore, the solutions $u_m(s; k)$ are periodic with period $2/m$, and oscillate at frequencies that are odd multiples of the fundamental frequency characteristic of the period-2 instability, again in accordance with previous knowledge [58]. The shapes of the first few harmonics are shown for different values of λ in Fig. 5.5.

Note, finally, that in the limit $k \simeq 1$, we have

$$\lambda \simeq \left[\ln \left(\frac{1-k}{8} \right) \right]^2 m^2, \quad (5.18)$$

and the periodic oscillation modes admit the piecewise approximations

$$u_m(s) \simeq (-1)^l U(s - lm^{-1}), \quad \left(l - \frac{1}{2} \right) m^{-1} \lesssim s \lesssim \left(l + \frac{1}{2} \right) m^{-1}, \quad l \text{ integer}, \quad (5.19)$$

where the transition layer shape U is the well-known heteroclinic solution of Eq. (5.14a)

$$\lambda = \frac{1}{2}(2\pi)^2, \quad \frac{1}{2}(4\pi)^2, \quad \frac{1}{2}(6\pi)^2, \quad \frac{1}{2}(8\pi)^2, \quad \frac{1}{2}(10\pi)^2, \quad \frac{1}{2}(12\pi)^2$$

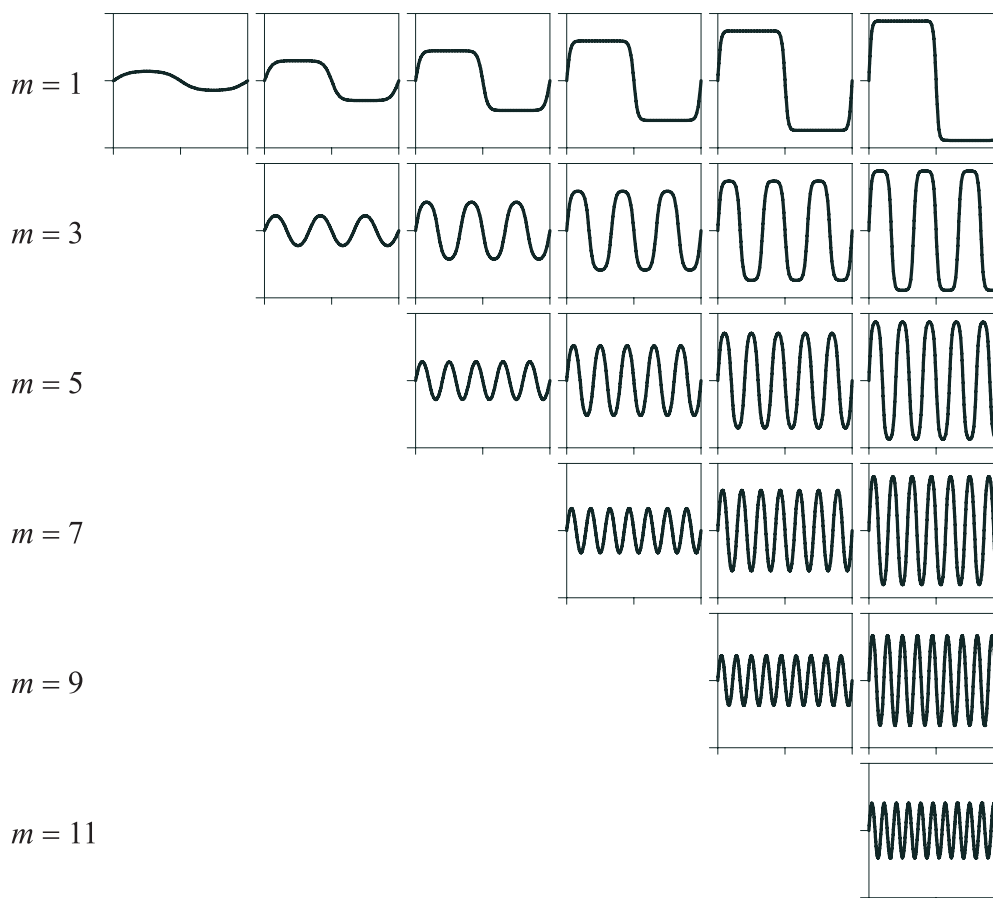


Figure 5.5: Shapes of the first harmonics $u = u_m$, $m \leq 11$, for several values of λ . The small frames are graphs of $u = u_m(s; k)$ as a function of s . The horizontal coordinate (s) ranges from 0 to 2, and the vertical coordinate (u) ranges from -30 to 30 . As λ increases, new harmonics appear and deform continuously from sine waves to square waves.

over the infinite domain $-\infty < s < \infty$ [17]:

$$U(s) \equiv \lambda^{\frac{1}{2}} \tanh\left(\lambda^{\frac{1}{2}} s\right). \quad (5.20)$$

Eq. (5.19) expresses the modes u_m as smoothed square waves, that is, as alternations of plateaus connected by transition layers of finite thickness. This is the expected behavior away from the bifurcation points $\lambda = \lambda_m^C$, for small ε [76]. Eq. (5.18) combined with the condition that $1 - k$ be a small quantity gives the range of validity of this layered approximation in terms of the control parameter λ and the harmonic number m :

$$\exp \rho \gg 1, \quad \rho \equiv m^{-1} \lambda^{\frac{1}{2}}. \quad (5.21)$$

The ratio ρ measures how large the plateau width m^{-1} is in comparison to the transition layer width $\lambda^{-1/2}$. The validity criterion (5.21) does not require λ itself to be very large, only that ρ be the logarithm of a large quantity, which is a much weaker constraint. Indeed, the harmonic u_3 for $\lambda = \frac{1}{2}(12\pi^2)$, which is represented in Fig. 5.5, provides an example of a case where the layered approximation is very accurately realized although the transition layers are not thin: the relative error between the approximation (5.19) and the exact expression (5.15) is no larger than $1.11 \cdot 10^{-3}$.

5.3.2 Stability

Comparison methods provide powerful tools for the analysis of the stability of t -independent solutions of scalar parabolic equations such as (5.10a) with various kinds of boundary conditions [8, 27, 28]. However, the application of such methods to our specific problem is not immediate because the antiperiodic condition (5.10b) invalidates the maximum principle for the parabolic equation (5.10a). Nevertheless, the reader familiar with comparison methods will be interested to see how this limitation can be worked around. Therefore, we sketch briefly the principle of the adaptation of the method to our problem, after which we present a simpler argument from bifurcation theory leading to the same conclusions. We establish that the only stable asymptotic states of the problem (5.10) are the trivial solution $u = 0$ for $\lambda \leq \lambda_1^C$, and the fundamental mode $u = u_1$ for $\lambda > \lambda_1^C$.

The adapted comparison method involves an auxiliary problem for Eq. (5.10a):

$$\frac{\partial u}{\partial t} = \frac{\partial^2 u}{\partial s^2} + 2u(\lambda - u^2), \quad (5.22a)$$

$$u(0, t) = 0 = u(1, t), \quad (5.22b)$$

$$u(s, t) = u(1 - s, t). \quad (5.22c)$$

Eq. (5.22b) is a pair of Dirichlet boundary conditions, and Eq. (5.22c) is an additional symmetry requirement. Given an initial condition $u(s, 0)$ compatible with these constraints, the determination of the solution of Eqs. (5.22) forms a well-posed problem for which the maximum principle holds. As a straightforward application of the comparison method presented in [27] and in Section 4.3 of [28], the harmonics $u = u_m(s; k)$

for $m \neq 1$ and the trivial solution $u = 0$ for $\lambda > \lambda_1^C$ are found to be unstable as solutions of the auxiliary problem (5.22). In order to prove that they are also unstable as solutions of the original antiperiodic problem (5.10), it is then sufficient to show that any solution of the auxiliary problem, extended antiperiodically, is also a solution of the original problem. This ensures that transient solutions moving away from the unstable solutions are preserved from the auxiliary problem to the original one. The proof presents no difficulty: it consists to acknowledge that any bounded solution of the Ginzburg-Landau equation (5.22a) defined for $-\infty < s < \infty$ and whose values at $t = 0$ are compatible with all three conditions (5.10b), (5.22b), and (5.22c) is the unique solution of both problems (5.10) and (5.22) with the given initial values. This establishes the instability of all asymptotic states of the antiperiodic problem except for the fundamental mode $u = u_1$ for $\lambda > \lambda_1^C$, and the trivial solution $u = 0$ for $\lambda \leq \lambda_1^C$. Now, these two solution branches must be stable, because, for all values of λ , there must exist at least one stable asymptotic state, and they are the unique candidates not ruled out as per the preceding discussion.

A simpler argument from bifurcation theory leads to the same conclusion. Since, as found in Sec. 5.3.1, all asymptotic states are t -independent, any bifurcation in the system must involve exclusively t -independent solutions. Now, there exists no t -independent solution other than the trivial one and the oscillatory modes u_m emerging from it at $\lambda = \lambda_m^C$, so that there cannot exist any bifurcation other than the periodic instabilities of the trivial solution at $\lambda = \lambda_m^C$. Therefore, the stability properties of each mode are conserved everywhere along its branch, so that their determination only requires an analysis in a neighborhood of the trivial solution. To this end, we linearize Eq. (5.10a) about $u = 0$ and seek fundamental solutions of the form

$$u(s, t) \propto \exp(i\pi m s + \sigma t), \quad (5.23)$$

where m is an odd integer so as to satisfy the antiperiodicity condition. This yields the dispersion relation

$$\sigma = 2\lambda - \pi^2 m^2. \quad (5.24)$$

The trivial solution is unstable if there exist values of m for which the fluctuation growth rate σ is positive, and stable if σ is negative for all m . It is thus stable for $\lambda < \lambda_1^C$ and unstable for $\lambda > \lambda_1^C$. From the parametric expressions (5.15) and (5.16) we know that the bifurcation at $\lambda = \lambda_1^C$ is supercritical, which means that the fundamental mode u_1 is stable and, by the above argument, remains stable for all $\lambda > \lambda_1^C$. On the other hand, the trivial solution is unstable on either side of any subsequent bifurcation point $\lambda = \lambda_m^C$ for $m \neq 1$, which implies that the bifurcating solutions u_m for $m \neq 1$ are unstable as well, and remain unstable for all $\lambda > \lambda_m^C$.

These stability results are illustrated in Fig. 5.4, where stable solution branches are represented as solid curves and unstable ones are represented as dashed. We showed that, within the limits of validity of the normal form (5.10), the only stable periodic solution beyond the oscillation threshold is the fundamental mode u_1 . Note that this result goes beyond the conclusions that can be drawn from an analysis of the difference

equation (5.3). Indeed, the difference equation does not take into account the long time scale t generated by the small but nonvanishing left-hand side of Eq. (5.1), and therefore cannot describe the slow transients that determine the stability properties.

Our conclusion of a unique stable asymptotic state if the system is close to the onset of period-2 oscillations must be contrasted with numerical studies of Eq. (5.1), which demonstrated that the odd harmonics can be successively stabilized by increasing the control parameter sufficiently far away from the oscillation threshold [58]. Our analysis revealed that, in the absence of external perturbations, this stabilization phenomenon lies beyond the scope of a normal form analysis, and therefore cannot arise if the nonlinearity in Eq. (5.1) is not strong enough. Nevertheless, it will become obvious from Sec. 5.7 that, beyond the immediate vicinity of the bifurcation points $\lambda = \lambda_m^C$, the system becomes extremely sensitive to external perturbations, even at the level of description provided by the normal form. A weak external forcing can indeed strongly modify the dynamics, and in particular, the stability properties of the system, even when it is operating in the weakly nonlinear regime.

5.4 Moving defect analysis

We now apply a second level of reduction to the description of the dynamics of the delay-differential equation (5.4). In the absence of forcing, recall from Sec. 5.3.1 that, beyond its onset threshold, any oscillatory asymptotic state of the system very quickly satisfies a layered approximation, that is, admits a piecewise description as a set of adjacent transition layers. Up to sign inversions, the profile of each consecutive layer is described by the same function $U(s)$, which is a heteroclinic solution of Eq. (5.14a). It is then natural to assume an analogous layered description of the solutions of the externally forced problem (5.9):

$$u \simeq (-1)^l U(s - s_l), \quad \frac{s_{l-1} + s_l}{2} \lesssim s \lesssim \frac{s_l + s_{l+1}}{2}, \quad l \text{ integer}, \quad (5.25)$$

but this time the quantities s_l denoting, on the short time scale, the instants of occurrence of the transitions, are not assumed equidistant (see the illustration in Fig. 5.6). Therefore, the validity criterion (5.21) of the layered approximation has to be generalized as follows:

$$\exp \rho \gg 1, \quad \rho \equiv \lambda^{\frac{1}{2}} \min_{l \text{ integer}} (s_l - s_{l-1}), \quad (5.26)$$

where $\min (s_l - s_{l-1})$ represents the shortest distance between two successive fronts. In view of Eq. (5.20), the width of a transition layer is proportional to $\lambda^{-1/2}$. The parameter ρ can therefore be interpreted as a measure of the shortest front separation relative to the front width. In the absence of forcing, we found in the previous Sec. 5.3.1 that $s_l - s_{l-1} = m^{-1}$ for all l , so that Eq. (5.26) matches the criterion (5.21). By analogy with spatially-extended systems, in the remaining of this chapter, the quantities s_l are simply referred to as the fronts positions (where, in the present context, these

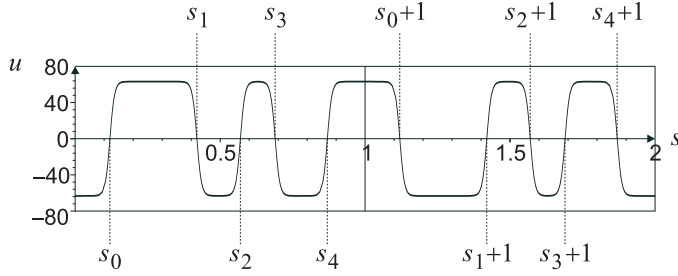


Figure 5.6: A generic multiple-front solution as defined in Eq. (5.25), for $\lambda = 4 \cdot 10^3$ (this value remains generic within the limits of validity of the normal form analysis as long as it is small compared to ε^{-2}). The coordinates s_0 to s_4 and $s_0 + 1$ to $s_4 + 1$ are instants of transition between plateau values, also referred to as the “fronts positions” throughout this chapter.

“positions” actually mean instants in time), and a solution of the type (5.25) is called a multiple-front solution.

We further assume that the forcing is weak in the following sense:

$$g(s, t) \ll \lambda^{\frac{3}{2}}. \quad (5.27)$$

In the absence of forcing, the transition layer profile $U(s - s_l)$ is known to be a stable solution of Eq. (5.10a), in the sense that any weak deformation will die out after a sufficiently long time, only resulting in a small shift of the front position s_l [30]. Therefore, it is expected that the dominant effect of the forcing term upon the solution (5.25) is simply a slow drift of the fronts, without a significant permanent deformation of the transition layer. Consequently, we assume that the fronts positions s_l are not constant, but depend on the slow time variable t , and that all dynamical features of interest are captured in this description.

Our goal is then to obtain a set of ordinary differential equations governing the motion of the fronts positions s_l as a function of t . The strategy is based on an argument involving the matching of piecewise asymptotic expansions of the solution of the system (5.9) between adjacent transition layers. The required equations of the motion are provided by the matching conditions. This analysis presents analogies to matched asymptotic expansion methods applied in other research domains concerned with spatially extended systems [98, 97, 101]. The complete derivation of the equations of the motion is presented in Appendix 5.B. Here we only give the results:

$$\frac{ds_l}{dt} = -\frac{\partial}{\partial s_l} [\mathcal{V}(s_l - s_{l-1}) + \mathcal{V}(s_{l+1} - s_l)] - (-1)^l \int_{-\infty}^{\infty} ds \mathcal{W}(s - s_l) \mathcal{A}g(s, t), \quad l \text{ integer}, \quad (5.28)$$

where the “potential” function $\mathcal{V}(s)$ and the “window” function $\mathcal{W}(s)$ appear naturally

in the course of the derivation of Eqs. (5.28). They are given by:

$$\mathcal{V}(s) \equiv -12 \exp\left(-2\lambda^{\frac{1}{2}}s\right), \quad (5.29)$$

$$\mathcal{W}(s) \equiv \frac{3}{4}\lambda^{-\frac{1}{2}} \operatorname{sech}^2\left(\lambda^{\frac{1}{2}}s\right). \quad (5.30)$$

Eqs. (5.28) must be supplemented with the following conditions:

$$s_l(t) = s_{l-m}(t) + 1, \quad l \text{ integer}, \quad (5.31)$$

for some odd integer m . These constraints ensure that the multiple-front ansatz (5.25) satisfies the antiperiodicity condition (5.9b). They restrict the number of independent unknown variables in Eq. (5.28) to a finite number m .

The first term in the right-hand side of Eq. (5.28) describes a short range (*i.e.*, exponentially decaying with distance) interaction accounting for a tendency of the fronts to attract each other, in a way analogous to the defect interaction described in [101]. The second term introduces the effect of the forcing. The window function $\mathcal{W}(s)$ weights the values of the forcing term $\mathcal{A}g(s, t)$ in such a way that it is only effective in neighborhoods of the fronts. Note that the description of the front interaction through the potential (5.29) breaks down if two fronts s_l and s_{l+1} get so close to each other that $\mathcal{V}(s_{l+1} - s_l)$ becomes $O(1)$, invalidating the assumed layered approximation. In that case, the ‘‘colliding’’ variables s_l and s_{l+1} diverge in a finite time t_∞ :

$$s_{l+1} - s_l \sim \frac{1}{2}\lambda^{-\frac{1}{2}} \ln[-(t - t_\infty)]. \quad (5.32)$$

The solution breakdown is actually a manifestation of a front pair annihilation in the multiple-front solution (5.25), a phenomenon that is known to occur in the partial differential equation (5.9a) when two fronts get sufficiently close to each other [83].

5.5 No-forcing case: instability growth rates

As a quick check of the validity of the equations of the motion, we re-examine the case where the forcing term $g(s, t)$ is absent. It is instructive to compare the results of Sec. 5.3 with the conclusions that can be drawn at the level of the equations of the motion. If $g(s, t) = 0$, Eqs. (5.28) and (5.31) reduce to:

$$\frac{ds_l}{dt} = -\frac{\partial}{\partial s_l} [\mathcal{V}(s_l - s_{l-1}) + \mathcal{V}(s_{l+1} - s_l)], \quad (5.33a)$$

$$s_l(t) = s_{l-m}(t) + 1. \quad (5.33b)$$

It is clear, from Eq. (5.33a), that any solution $\{s_l, l \text{ integer}\}$ that does not diverge must tend towards a t -independent state after a sufficiently long time. Such states are obtained by setting the left-hand side to zero in Eq. (5.33a), and are characterized

by equidistant fronts. we thus recover faithfully the $2/m$ -periodic asymptotic states of Sec. 5.3.1, in their square-wave limit.

In [58], Ikeda *et al.* pointed out that a large number of asymptotic states of the difference equation (5.3) do not have a counterpart in the singularly perturbed delay-differential equation (5.1), no matter how small ε is. Specifically, the difference equation (5.3) admits piecewise constant solutions where the length of the plateaus can be arbitrary over a delay time interval, provided that Eq. (5.3) is satisfied pointwise from one interval to the next one. On the other hand, the presence of the derivative term in the delay-differential equation (5.1) results in a smoothening of the solutions, and Ikeda *et al* invoked this argument to suggest why only the $2/m$ -periodic harmonics, presenting a high degree of regularity, survive from the difference equation (5.3) to the delay-differential equation (5.1). Now, see how transparent this selection mechanism is, expressed in terms of front interactions: it can be observed from Eq. (5.33a) that the $2/m$ -periodic harmonics are the only solutions for which the attractions exerted on each front by its two immediate neighbors exactly compensate each other, and are therefore the only possible equilibria.

We found in Sec. 5.3.2 that all harmonics were unstable for $m \neq 1$. The motion equations (5.33) are sufficiently simple to allow the computation of estimates of the temporal fluctuation growth rates. To this end, we linearize Eqs. (5.33) around the m^{th} harmonic by substituting the ansatz:

$$s_l = m^{-1}l + a_l \exp \sigma t, \quad (5.34)$$

where $a_l \ll 1$, and keeping only $O(a_l)$ terms. This yields:

$$\sigma a_l = 48\lambda (2a_l - a_{l-1} - a_{l+1}) \exp -2m^{-1}\lambda^{\frac{1}{2}}, \quad (5.35a)$$

$$a_l = a_{l-m}. \quad (5.35b)$$

Eq. (5.35a) is a second order linear recurrence relation for the fluctuation amplitudes a_l , and the condition (5.35b) further imposes that the sequence (a_l) be m -periodic. Therefore, the possible values of the fluctuation growth rate σ are obtained by requiring that Eq. (5.35) possesses nontrivial m -periodic solutions. Rewriting Eq. (5.35a) as an equivalent first order matrix recurrence relation:

$$\begin{bmatrix} a_{l+1} \\ b_{l+1} \end{bmatrix} = \begin{bmatrix} 2 - \frac{1}{48}\lambda^{-1}\sigma \exp 2m^{-1}\lambda^{\frac{1}{2}} & -1 \\ 1 & 0 \end{bmatrix} \begin{bmatrix} a_l \\ b_l \end{bmatrix}, \quad (5.36)$$

it becomes obvious that such a nontrivial m -periodic solution exists if and only if the square matrix in the above equation possesses an eigenvalue that is a complex m^{th} root of unity. Solving this condition provides the possible values of σ :

$$\sigma = 192\lambda \left(\exp -2m^{-1}\lambda^{\frac{1}{2}} \right) \sin^2 (\pi m^{-1}n) \quad (5.37)$$

where n is any integer number between 0 and $m - 1$. The value $\sigma = 0$, corresponding to $n = 0$, is always authorized, and merely reflects the time translation invariance of

the system. This is the only possibility for $m = 1$, again confirming the stability of the fundamental oscillatory solution. For $m \neq 1$, the other fluctuation growth rates are positive and bounded from above by:

$$\sigma < 192\lambda \exp -2m^{-1}\lambda^{\frac{1}{2}}. \quad (5.38)$$

Note how this bound tends exponentially fast towards zero as the ratio $\rho = m^{-1}\lambda^{1/2}$ between the front separation distance and the transition layer width increases. This illustrates the fact that, although the harmonics for $m \neq 1$ are all unstable, the fluctuation growth becomes extremely slow as the control parameter λ leaves the immediate neighborhood of the bifurcation point, resulting in extremely slow transients. Such transients are so slow, in fact, that they are sometimes qualified metastable solutions [50]. The extreme smallness of the values of σ also means that the oscillatory states are very sensitive to even a tiny external perturbation, which may therefore result in strong modifications of the dynamics.

5.6 Modulation-locked dynamics

Using the equations of the motion (5.28), we may now proceed to the analytical study of an externally-forced problem. In this section, we specialize Eqs. (5.28) to the case where $g(s, t)$ describes a periodic modulation, and undergo the research of solutions that are phase-locked onto the modulation signal. A question immediately arises: how should a time-periodic forcing be modelled on the two distinct time scales s and t ? We shall assume that the modulation period is of the order of magnitude of the delay time or shorter. Therefore, as a first constraint, $g(s, t)$ must be periodic in the faster time variable s :

$$g(s, t) = g(s - P, t). \quad (5.39)$$

Consequently, it admits a Fourier series representation:

$$g(s, t) \equiv \sum_{q=-\infty}^{\infty} \widehat{g}_q(t) \exp iq\Omega s, \quad \Omega = \frac{2\pi}{P}. \quad (5.40)$$

The exponentials in the above expansion are eigenfunctions of the operator \mathcal{A} with eigenvalue 1 if $q\Omega$ is an odd multiple of π , and 0 otherwise. Therefore, the values of Ω such that $\mathcal{A}g(s, t)$ does not vanish identically form a discrete set. The modulation frequency must be chosen among this set in order for the forcing term to have any effect in Eqs. (5.28). We shall assume that Ω itself is an odd multiple of π :

$$\Omega = M\pi, \quad M \text{ odd integer}, \quad (5.41)$$

so that the modulation is in 1–1 resonance with the natural M^{th} harmonic square-wave oscillation mode of the system.

We must now specify the behavior of $g(s, t)$ on the long time scale t . For fixed t , the function $s \mapsto g(s, t)$ defines the instantaneous shape of the modulation waveform.

We impose that this shape does not vary on the longer time scale t , although a uniform translation in s at an arbitrary rate ν is authorized:

$$g(s, t) = g(s + \nu t, 0). \quad (5.42)$$

The rate ν defines how fast the modulation phase drifts as measured by a clock synchronized with natural oscillations of the system. Therefore, it accounts for a weak detuning of the modulation frequency with respect to the ideal resonance condition expressed by Eq. (5.41). More precisely, ν is proportional to the difference between the modulation frequency and the closest natural oscillation frequency.

Eq. (5.42) suggests a redefinition of the faster time variable comoving with the modulation signal:

$$z \equiv s + \nu t, \quad z_l \equiv s_l + \nu t, \quad (5.43)$$

in terms of which the periodicity conditions (5.42) and (5.39) read respectively:

$$g(s, t) = g(z, 0) \equiv g(z), \quad (5.44)$$

$$g(z) = g(z - P) = g(z - 2M^{-1}). \quad (5.45)$$

Unless explicitly mentioned otherwise, we shall impose, for the remaining of this chapter, some additional symmetry constraints on the modulation waveform, in order to make the algebra simpler. Specifically, we assume that $g(z)$ is an odd and antiperiodic function of z :

$$g(-z) = -g(z), \quad (5.46)$$

$$g(z) = -g(z - M^{-1}), \quad (5.47)$$

and that $g(z)$ possesses exactly two extrema per modulation period (an extremal plateau counting as a single extremum). An immediate consequence of the antiperiodicity of $g(z)$ is that $\mathcal{A}g(z) = g(z)$, allowing the dropping of the symbol \mathcal{A} in Eqs. (5.28). The other constraints further imply that $g(z)$ vanishes at integer multiples of M^{-1} , and changes sign exactly twice per modulation period. For this reason, integer multiples of M^{-1} are subsequently referred to as “the zeros” of $g(z)$, even though it might actually vanish over intervals of nonzero measure centered on these points. Moreover, $g(z)$ is invariant with respect to time reversal about its extrema, which are located at odd integer multiples of $\frac{1}{2}M^{-1}$. Finally, an important property that will be invoked repeatedly is that the integral

$$\mathcal{G}(z_l) \equiv \int_{-\infty}^{\infty} dz \mathcal{W}(z - z_l) g(z) \quad (5.48)$$

possesses the same symmetry and the same distribution of zeros and extrema as $g(z_l)$. The only non-obvious part of this statement is the assertion about the extrema, which is justified in Appendix 5.C.

In terms of comoving variables, Eqs. (5.28) read:

$$\frac{dz_l}{dt} = \nu - \frac{\partial}{\partial z_l} [\mathcal{V}(z_l - z_{l-1}) + \mathcal{V}(z_{l+1} - z_l)] - (-1)^l \mathcal{G}(z_l). \quad (5.49)$$

They form an autonomous system of ordinary differential equations.

Solutions that do not depend on t represent periodic oscillation modes that are phase-locked onto the modulation signal. Expressing Eq. (5.25) in terms of comoving time variables provides explicit forms of such phase-locked oscillation patterns:

$$u \simeq (-1)^l U(z - z_l), \quad \frac{z_{l-1} + z_l}{2} \lesssim z \lesssim \frac{z_l + z_{l+1}}{2}. \quad (5.50)$$

The characterization of phase-locked dynamics therefore amounts to the determination of t -independent solutions of Eqs. (5.49) and their linear stability analysis, which are carried out subsequently. To this end, we introduce the ansatz:

$$z_l(t) = z_l^{\text{eq}} + a_l \exp \sigma t + O(a_l^2), \quad (5.51)$$

where the constants z_l^{eq} represent the equilibrium positions of the fronts. The second term in the right-hand side accounts for small deviations from equilibrium with growth rate σ . The equilibrium front positions z_l^{eq} are obtained by setting the t -derivative to zero in Eqs. (5.49):

$$\nu = \frac{\partial}{\partial z_l} [\mathcal{V}(z_l - z_{l-1}) + \mathcal{V}(z_{l+1} - z_l)] + (-1)^l \mathcal{G}(z_l), \quad (5.52)$$

where, as in the remaining of this chapter, the ‘eq’ superscripts are dropped for the sake of readability. These equations determine the equilibrium front positions z_l as a function of the detuning ν and the modulation waveform $g(z)$.

The substitution of the ansatz (5.51) into Eqs. (5.49) and their linearization about equilibrium yields:

$$\sigma a_l = -(a_l - a_{l-1}) \frac{\partial^2}{\partial z_l^2} \mathcal{V}(z_l - z_{l-1}) - (a_l - a_{l+1}) \frac{\partial^2}{\partial z_l^2} \mathcal{V}(z_{l+1} - z_l) - (-1)^l a_l \frac{d}{dz_l} \mathcal{G}(z_l), \quad (5.53)$$

These linear equations determine the deviation amplitudes a_l and govern the stability of the phase-locked solutions. A given oscillation mode is stable if and only if there does not exist any value of the fluctuation growth rate σ with a positive real part such that Eqs. (5.53) admit nontrivial solutions.

5.7 Modulation-induced multistability

We now proceed to a qualitative analysis of phase-locked dynamics under a number of simplifying assumptions which are successively relaxed in Sec. 5.8:

1. We consider the case of a perfectly tuned modulation signal, that is, we set the detuning ν to zero.
2. the interaction terms (*i.e.*, the terms involving derivatives of \mathcal{V}) are treated as negligible with respect to the modulation terms in Eqs. (5.52) and (5.53). The

validity of this approximation is guaranteed if the shortest distance between any two consecutive fronts is sufficiently large with respect to the width of a transition layer, a condition that may be expressed as

$$\rho \gg 1. \quad (5.54)$$

Note that this is a stronger constraint than the validity criterion (5.26) of the equations of the motion.

3. the modulation period is assumed large with respect to the width of a transition layer:

$$M^{-1} \gg \lambda^{-\frac{1}{2}}. \quad (5.55)$$

Under Hypothesis 2, the fronts can be treated as decoupled from each other. This case is rather trivial mathematically; nevertheless the investigation of the possible solutions and their stability properties in that simple limit leads to a good understanding of the basic mechanism by which multistability results from a periodic modulation, which justifies a fairly detailed discussion of this case. Under hypotheses 1–3, Eqs. (5.52) and (5.53) reduce to

$$\mathcal{G}(z_l) = 0, \quad (5.56)$$

$$\sigma = -(-1)^l \frac{d}{dz_l} \mathcal{G}(z_l). \quad (5.57)$$

We see from the first equation that the fronts are constrained to occupy positions that correspond to zeros of the modulation waveform. If $n_l = n_{l-1} + 1$ for all l , then all such positions are occupied. This particular configuration describes the pure M^{th} harmonic square wave oscillation mode phase-locked onto the modulation signal (see Fig. 5.7a). However, all possible positions need not be occupied in order to achieve dynamical equilibrium. Therefore, unlike in the case of no forcing, all plateaus in the oscillation pattern (5.50) need not have the same length, although the length of any plateau must be an integer multiple of half the modulation period. Over each time interval between consecutive zeros of the modulation waveform, the solution may independently assume one of its two possible plateau values, before it begins to repeat itself antiperiodically after a finite number M of half modulation periods. Assuming that we dispose of a clock with a defined time origin in order to distinguish between solutions that are identical up to time translations, this makes a total of 2^M distinct oscillation modes.

A “bitfield” representation of phase-locked oscillation patterns may be introduced as follows: let I be an M -dimensional vector of boolean values: $I = (I_0, I_1, \dots, I_{M-1})$, where $I_j = 0$ or 1 for all j . Then, there exists a one-to-one correspondence between possible values of the bitfield I and phase-locked solutions. This correspondence is established by defining the value of the bit I_j to be 0 if the solution reaches its lower plateau value for $jM^{-1} < z < (j+1)M^{-1}$, and 1 if it reaches its higher plateau value in that interval. This construction is illustrated in Figs. 5.7 and 5.8. The applicability

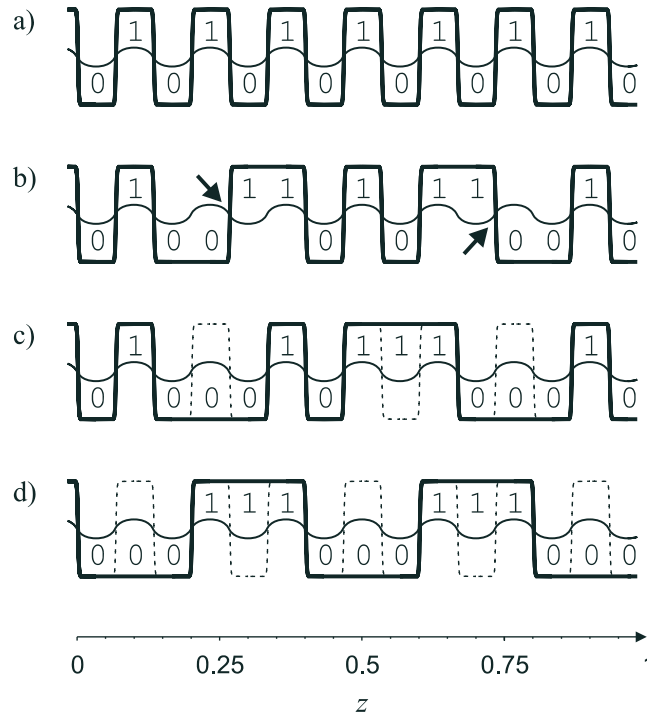


Figure 5.7: Several phase-locked oscillation modes for $M = 15$, that is, for a modulation frequency resonant with the 15th harmonic. Thin smooth curves represent the modulation waveform. Thick curves represent phase-locked oscillation patterns. Ordinate units are arbitrary. Numbers superimposed over the diagrams indicate the bitfield representations of the solutions.

- a) The stabilized pure 15th harmonic. Its bitfield representation is an alternance of 0's and 1's.
- b) An unstable mode. Arrows indicate unstable fronts, characterized by the fact that the slope of the oscillation pattern and the slope of the modulation waveform have opposite signs.
- c) A lacunar harmonic (*i.e.*, a harmonic with missing front pairs). Lacunae are represented as thin dashed curves. Lacunar harmonics are stable because the slopes of the oscillation pattern and the modulation waveform have the same sign at every front.
- d) The pure 5th harmonic is a particular lacunar 15th harmonic and can therefore be stabilized by a modulation frequency at the 15th resonance.

of phase-locked modes to information storage is conveniently discussed in terms of such a bitfield representation.

We must now determine which modes are dynamically stable, for only stable modes can be observed experimentally. Eqs. (5.57) determine the stability of each front individually: a front is stable if and only if σ is negative for the corresponding value of l . The fact that each value of σ is associated to a single front is, of course, specific to the case where the fronts are decoupled. Stable oscillation modes are those which only contain stable fronts. Remember that the slopes of $\mathcal{G}(z_l)$ and $g(z_l)$ have the same sign everywhere. Therefore, From Eqs. (5.50), we see that a solution is stable if and only if the slope of the oscillation pattern and the slope of the modulation waveform have the same direction in the vicinity of all fronts (see Fig. 5.7). The pure M^{th} harmonic oscillation mode, where all possible front positions are occupied, is a stable solution if it oscillates in phase with the modulation signal (Fig. 5.7a). This contrasts with the case of no forcing where, in the limits of validity of the equations of the motion (5.28), all square-wave oscillation modes are unstable except the fundamental mode. Note also that all stable modes may be constructed from the stabilized pure harmonic by removing as many pairs of adjacent fronts as necessary (Figs. 5.7c, 5.7d, and 5.8); or, equivalently, by flipping a finite number of isolated bits in its bitfield representation. (We define an *isolated bit* as a bit of one kind surrounded by two bits of the other kind, provided the bitfield representation I is extended antiperiodically as follows: $I_j \equiv \text{not } I_{j-M}$ for all integer j .) For this reason, the stable phase-locked oscillation modes identified in this section are subsequently referred to as lacunar harmonics.

There are much more unstable modes than stable modes. In Appendix 5.D, we compute that, for given M (*i.e.*, given modulation frequency), the number N_M of stable modes is

$$N_M = \lfloor \Phi^M \rfloor, \quad \Phi \equiv \frac{1 + \sqrt{5}}{2} \simeq 1.618, \quad (5.58)$$

where the operator $\lfloor \]$ denotes the largest integer less than or equal to its argument. For large M , this is a small number in comparison to the total number of modes, 2^M . This puts important restrictions upon information storage applications, since any encoding scheme of practical value is restricted to make use of stable modes only. This implies that only a fraction of the available bits can be used to store information, and that the values of the remaining bits must be imposed so as to fulfill the stability constraints. For given M , there is a theoretical limit to the number of information-carrying bits, which is equal to the number of digits needed to write the binary representation of N_M . This limit is given approximately by $M \log_2 \Phi$. This means that any encoding scheme is bound to waste, as a minimum, a fraction of $1 - \log_2 \Phi \simeq 31\%$ of the total number of available bits in order to fulfill the stability constraints.

As an example of a very simple information encoding scheme compliant with the stability constraints, it is possible to store an arbitrary $\frac{1}{2}(M - 1)$ -bits-long string of boolean values, $J = \left(J_0, J_1, \dots, J_{\frac{1}{2}(M-3)} \right)$, as a lacunar harmonic, by interlacing it with

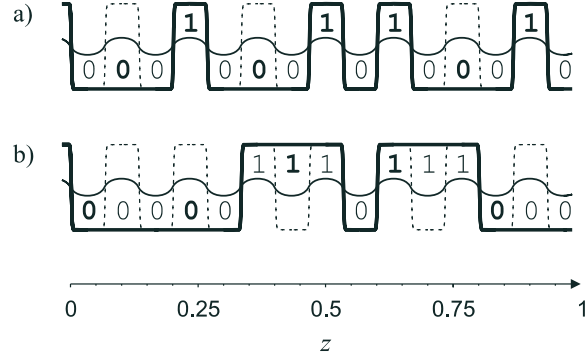


Figure 5.8: Two stable information encoding schemes, for $M = 15$. Thin solid curves represent the modulation waveform. Thick solid curves are information-carrying lacunar harmonics. Thin dashed curves represent lacunae. Ordinate units are arbitrary. Numbers superimposed over the diagrams indicate the bitfield representations of the solutions.

a) Any arbitrary sequence of bits of length $\frac{1}{2}(M - 1)$, here the binary string **0101101** (boldface digits), can be stored in a stable way as a lacunar harmonic, by interlacing it with a sequence of zeros (normal face digits), as prescribed in Eqs. (5.59).

b) If M is an odd multiple of 3, then any arbitrary sequence of bits of length $\frac{1}{3}M$, here the binary string **00110**, can be stored in a stable way using every third bit (boldface digits) of a lacunar harmonic, by defining the other bits (normal face digits) as prescribed in Eq. (5.60). This scheme presents the particularity that any meaningful configuration possesses the same number of fronts per delay time, and therefore switching between configurations with different informational content never involves the creation or the destruction of a front pair.

a sequence of zeros as follows:

$$I_{2j} = 0 \quad \text{for} \quad 0 \leq j \leq \frac{1}{2}(M - 1), \quad j \text{ integer}, \quad (5.59a)$$

$$I_{2j+1} = J_j \quad \text{for} \quad 0 \leq j \leq \frac{1}{2}(M - 3), \quad j \text{ integer}. \quad (5.59b)$$

The M -dimensional bitfield $I = (I_0, I_1, \dots, I_{M-1})$ that results from this construction always corresponds to a stable mode. This encoding scheme is illustrated in Fig. 5.8a. Although not optimal (only 50% of the bits carry information), it may be sufficiently simple to be of practical interest.

If M is an odd multiple of 3, then another stable encoding scheme consists to store an $\frac{1}{3}M$ -bits-long string of boolean values, $K = (K_0, K_1, \dots, K_{\frac{1}{3}M-1})$, in the following way:

$$I_{3j} = I_{3j+1} = K_j, \quad I_{3j+2} = (\text{not})^j 0, \quad \text{for} \quad 0 \leq j \leq \frac{1}{3}M - 1, \quad j \text{ integer}, \quad (5.60)$$

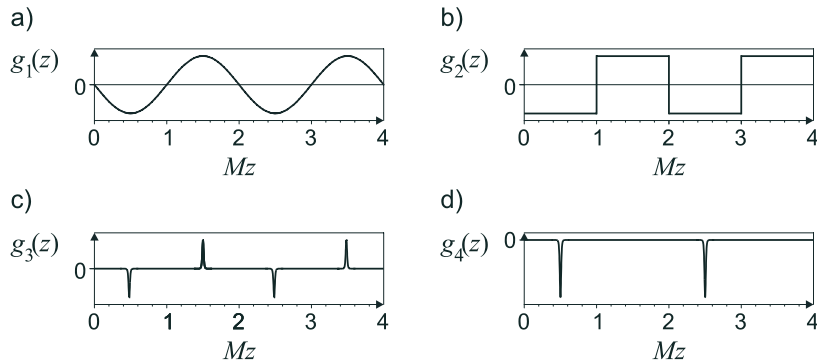


Figure 5.9: Four particular modulation waveforms. Ordinate units are arbitrary. a) g_1 : a sine waveform. b) g_2 : a square waveform. c) g_3 : an antiperiodic pulse train. d) g_4 : another kind of pulse train having the same effect as g_3 . This is because $\mathcal{A}g_4 = \mathcal{A}g_3$, so that the equations of the motion (5.28) cannot discern between these two signals.

where $(\text{not})^j 0$ assumes the value 0 or 1 depending on the parity of j . This encoding scheme, which is illustrated in Fig. 5.8b, uses only $\frac{1}{3}$ of the available bits to store information. However, it presents the particularity that all oscillation patterns constructed in this fashion possess the same number of fronts over one delay time. Therefore, switching from one state that is meaningful in this encoding scheme to another never involves the creation or the destruction of a front pair, only the displacement of one or several fronts. Such a displacement may be induced by temporarily superposing an adequately chosen driving signal over the modulation, in such a way as to “hide” some of the zeros of the modulation waveform. The amplitude of the switching signal therefore needs not be much larger than that of the modulation, which may constitute a practical advantage (at the expense of switching time) if the injection of intense signals in the system is difficult.

5.8 The influence of modulation waveform

The above discussion of phase-locked dynamics is only qualitative. We demonstrated the phenomenon of modulation-induced multistability for a class of resonant periodic modulation signals with high symmetry, but we did not address the question of how phase-locking and stabilization performances depend on the characteristics of the modulation, such as detuning ν , frequency Ω , and waveform. A good measure of the stabilization efficiency is given by the magnitude of the fluctuation growth rate σ . The more negative σ is, the faster fluctuations are damped out, and so the less sensitive the system is to noisy perturbations. In view of Eq. (5.57), we may therefore anticipate that modulation waveforms with stiff slopes (such as square waves) provide better stabilization than smooth modulation waveforms (such as sine waves), as long as detuning and front interaction effects are negligible. In this section, we compare the stabilization efficiencies of the three different modulation waveforms represented in Fig. 5.9a–c: a

sine wave g_1 , a square wave g_2 , and an antiperiodic pulse train g_3 . Such modulation signals are modelled by the following expressions:

$$g_1(z) \equiv -\gamma \sin(\pi Mz), \quad (5.61a)$$

$$g_2(z) \equiv -\gamma(-1)^q, \quad M^{-1}q < z < M^{-1}(q+1), \quad q \text{ integer}, \quad (5.61b)$$

$$g_3(z) \equiv -\gamma \sum_{q=-\infty}^{\infty} (-1)^q \delta\left(z - \left[q + \frac{1}{2}\right] M^{-1}\right), \quad (5.61c)$$

where γ is the modulation amplitude. Each individual pulse in the modulation signal g_3 is idealized as infinitely narrow and modelled as a Dirac distribution, denoted by δ . All three waveforms satisfy the geometrical constraints imposed at the in Sec 5.6.

We first relax hypothesis 1 so as to analyze the effect of detuning. Our goal is to obtain closed-form relations between our measure of stabilization efficiency, σ , and the detuning ν , for the three modulation waveforms g_1 to g_3 . By hypothesis 2, Eqs. (5.52) and (5.53) reduce to

$$\nu = (-1)^l \mathcal{G}(z_l), \quad (5.62)$$

$$\sigma = -(-1)^l \frac{d}{dz_l} \mathcal{G}(z_l). \quad (5.63)$$

An immediate consequence of Eq. (5.62) is that the possible values of the detuning such that a phase-locked solution exists are bounded:

$$|\nu| \leq |\nu^C| \equiv \max_z \mathcal{G}(z). \quad (5.64)$$

The above relation therefore defines the locking range of the detuning for a given modulation signal. It is proportional to the modulation amplitude. For a given detuning value and a specific modulation waveform, Eq. (5.62) gives the equilibrium front positions. An analysis of the signs of the right-hand sides of Eqs. (5.62) and (5.63) reveals that stable and unstable fronts tend to shift opposite ways under the effect of detuning. The locking range boundaries $|\nu| = |\nu^C|$ correspond to limit points where phase-locked solutions collide by pairs, and cease to exist for stronger detunings. This route towards non-locked dynamics is illustrated in Fig. 5.10 in the case of a sine modulation.

Once the equilibrium front positions z_l are determined from Eq. (5.62), the possible values of σ can be computed from Eq. (5.63). Therefore, Eqs. (5.62)–(5.63) together provide closed relations between the instability growth rate σ and the detuning ν . Detailed calculations are given in Appendix 5.E for all three modulation waveforms, g_1 to g_3 . The results are represented in Fig. 5.11. For the sine and square modulations, stability is optimal for perfect tuning, and becomes arbitrarily precarious near the locking boundaries. In the case of the pulsed modulation waveform, we see in contrast that σ approaches zero if the modulation signal is perfectly tuned. Therefore, the pulsed waveform g_3 cannot provide efficient stabilization unless some amount of detuning is introduced. Note furthermore that this conclusion can be extended to the fourth

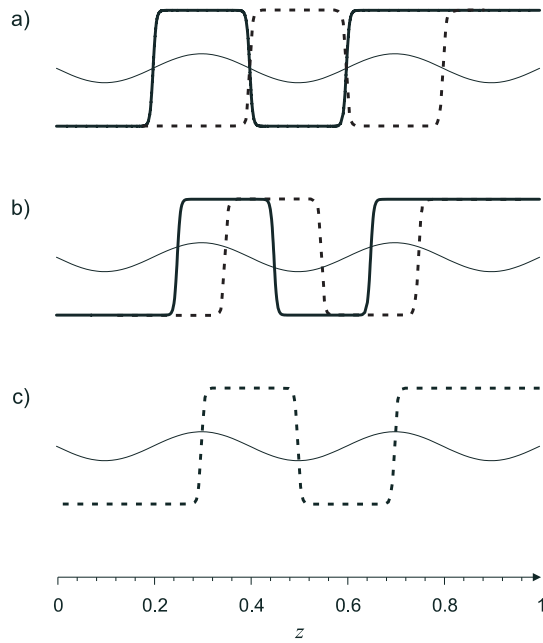


Figure 5.10: The effect of detuning upon phase-locked solutions. The three diagrams represent a stable solution (thick solid curve) and an unstable solution (thick dashed curve) supported by a sine modulation waveform (thin curve) resonant with the 5th harmonic ($M = 5$). Ordinate units are arbitrary.

- a) The perfectly tuned case: $\nu = 0$. Fronts are located at zeros of the modulation signal.
- b) Positive detuning: $\nu = 0.707 |\nu^C|$. Stable fronts are retarded, and unstable fronts are advanced in time.
- c) Positive detuning at the limit of the locking range: $\nu = |\nu^C|$. The stable and unstable solutions collide in a limit point bifurcation.

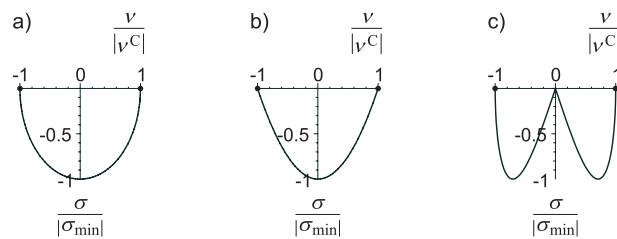


Figure 5.11: Fluctuation growth rate about phase-locked solutions as a function of the detuning, for three different modulation signals: a) sine waveform, b) square waveform, c) pulsed waveform. The domain of stable locking is bounded by limit points at $\nu = \pm |\nu^C|$. In the case of the pulsed waveform, stability becomes arbitrarily weak as the detuning approaches zero.

waveform represented in Fig. 5.9, which essentially differs from g_3 by the absence of the upwards pulse:

$$g_4(z) \equiv -2\gamma \sum_{q=-\infty}^{\infty} \delta \left(z - \left[2q + \frac{1}{2} \right] M^{-1} \right). \quad (5.65)$$

This is because $\mathcal{A}g_4 = g_3 = \mathcal{A}g_3$, so that both modulation signals have the same effect on the dynamics, and are interchangeable in the full equations of the motion (5.28).

We now assume a zero detuning again, and relax hypotheses 2 and 3 in Sec. 5.7, in order to investigate how the stability of phase-locked modes is threatened by the tendency of the fronts to attract each other, if the distance between consecutive fronts is not large anymore. This is an important consideration for information encoding applications, since one usually wants to store as many bits of information as possible in a delay line of given length. We shall only treat the cases of the sine waveform g_1 and the square waveform g_2 . Having assumed perfect tuning, we do not consider the pulsed waveform g_3 here, because the degenerate stability properties of the supported solutions at $\nu = 0$ make the analysis trivial and physically uninteresting.

If we define a *strongly isolated bit* to be a phase-locked solution whose bitfield representation contains a bit of one kind surrounded by long sequences of bits of the other kind, then it is clear that strongly isolated bits are the most difficult solutions to stabilize. Indeed, in this configuration, the attraction exerted by the fronts at the boundaries of the isolated bit upon each other is maximal, their separation being the shortest possible. Furthermore, there is no other nearby front on either side of the bit to compensate the attraction. We therefore particularize Eqs. (5.52) and (5.53) to the case of a strongly isolated bit, since this provides the thoroughest test of stabilization efficiency for a given modulation signal. If z_1 and z_2 denote fronts that form such a bit's boundaries, this amounts to take the limits

$$\mathcal{V}(z_1 - z_0) \rightarrow 0, \quad \mathcal{V}(z_3 - z_2) \rightarrow 0. \quad (5.66)$$

Assuming zero detuning, writing Eqs. (5.52) for $l = 1$ and $l = 2$ then gives:

$$0 = \frac{\partial}{\partial z_1} \mathcal{V}(z_2 - z_1) - \mathcal{G}(z_1) \quad (5.67a)$$

$$0 = \frac{\partial}{\partial z_2} \mathcal{V}(z_2 - z_1) + \mathcal{G}(z_2). \quad (5.67b)$$

Summing the two above equations, the terms in \mathcal{V} cancel each other, leaving

$$\mathcal{G}(z_1) = \mathcal{G}(z_2). \quad (5.68)$$

In Sec. 5.7, we found that, in absence of interactions, the front separation for a stable isolated bit is given by M^{-1} . we expect this value to be reduced as a consequence of front attraction, and therefore seek solutions of Eqs. (5.67) such that

$$0 < Z \equiv z_2 - z_1 \leq M^{-1}. \quad (5.69)$$

In the limits of this constraint, $z_2 + z_1$ must be an odd multiple of M^{-1} for Eq. (5.68) to be satisfied. With the help of a possible redefinition of the time origin compatible with the assumed symmetry properties of the modulation waveform, we may choose

$$z_2 + z_1 = M^{-1} \quad (5.70)$$

without loss of generality. Eq. (5.67a) then yields:

$$\frac{d}{dZ}\mathcal{V}(Z) = -\mathcal{G}\left(\frac{1}{2}[M^{-1} - Z]\right). \quad (5.71)$$

This relation determines the equilibrium values of the front separation Z as a function of M , which is proportional to the modulation frequency. The calculation details are given in Appendix 5.F for both the sine and square waveforms.

In the analytical expressions of $g_1(z)$ and $g_2(z)$, the time origin is chosen in such a way that $Z = M^{-1}$ is a stable solution in the limit $M^{-1} \gg \lambda^{-1/2}$, as per the stability criterion given in Sec. 5.7. For both waveforms, there exists two solutions in the range (5.69) up to a critical value of $M = M^C$. The larger solution $Z = Z^+$ tends towards M^{-1} in the limit $M^{-1} \gg \lambda^{-1/2}$, and therefore corresponds to the stable strongly isolated bit configuration. The lesser solution $Z = Z^-$ is an unstable equilibrium point where the stabilizing effect of the modulation exactly compensates the front attraction: if the fronts get closer than a distance Z^- apart, then they will collide and annihilate. At $M = M^C$, we have $Z^+ = Z^-$. This critical value defines the maximum modulation frequency such that a particular modulation waveform with a fixed amplitude can support stable strongly isolated bit solutions. Beyond this point, the solution pair is destroyed through a limit point bifurcation. This is illustrated in Fig. 5.12 for the sine waveform.

Possible values of the instability growth rate σ for a given equilibrium are obtained by writing Eqs. (5.53) for $l = 1$ and $l = 2$, in the limit (5.66):

$$\sigma a_1 = -(a_1 - a_2) \frac{d^2}{dZ^2} \mathcal{V}(Z) + a_1 \left. \frac{d}{dz} \mathcal{G}(z) \right|_{z=z_1}, \quad (5.72a)$$

$$\sigma a_2 = -(a_2 - a_1) \frac{d^2}{dZ^2} \mathcal{V}(Z) - a_2 \left. \frac{d}{dz} \mathcal{G}(z) \right|_{z=z_2}. \quad (5.72b)$$

From Eq. (5.70), we deduce that the values of $\left. \frac{d}{dz} \mathcal{G}(z) \right|_{z=z_1}$ and $z = z_2$ are opposite. Therefore, decoupled equations are obtained by taking the sum and the difference of Eqs. (5.72a) and (5.72b):

$$\sigma(a_1 + a_2) = (a_1 + a_2) \left. \frac{d}{dz} \mathcal{G}(z) \right|_{z=z_1}, \quad (5.73a)$$

$$\sigma(a_1 - a_2) = (a_1 - a_2) \left[-2 \frac{d^2}{dZ^2} \mathcal{V}(Z) + \left. \frac{d}{dz} \mathcal{G}(z) \right|_{z=z_1} \right]. \quad (5.73b)$$

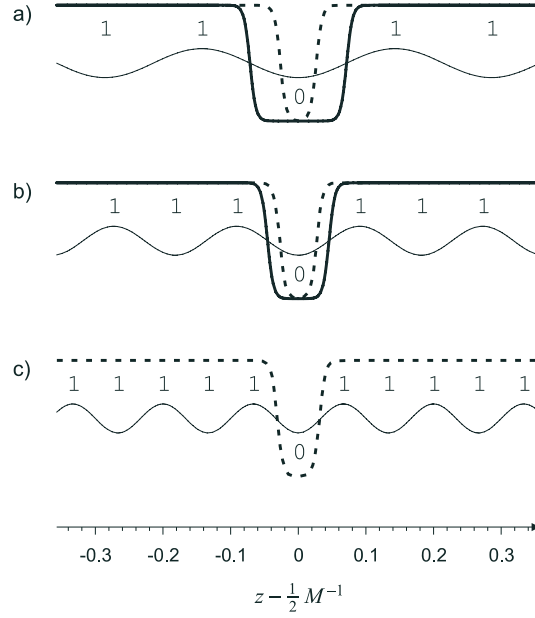


Figure 5.12: The effect of front attraction upon phase-locked solutions. The three diagrams represent a stable strongly isolated bit solution (thick solid curve) and the unstable solution with the shortest front separation (thick dashed curve) supported by a sine modulation waveform (thin curve). Ordinate units are arbitrary. Numbers superimposed over the diagrams indicate the stable solution's bitfield representation. Parameter values are: $\lambda = 1.322 \cdot 10^4$, $\lambda^{-3/2}\gamma = 10^{-4}$. These values have been chosen so that $M^C = 15$.

- a) $M = 5$. The distance between the stable solution's fronts is fairly large, and the front attraction is negligible.
- b) $M = 11$. The stable and unstable solutions are closer to each other.
- c) $M = M^C = 15$. The stable and unstable solutions collide in a limit point bifurcation. The stable strongly isolated bit solution ceases to exist beyond this point.

There are two possible values of σ , given respectively by the coefficients of $a_1 + a_2$ and $a_1 - a_2$ in the right-hand sides of the above equations. We are only interested in the larger (*i.e.*, less negative) one, which alone determines stability. It is given by Eq. (5.73b) since the second derivative of \mathcal{V} is always negative. Using Eq. (5.70), it is expressed in terms of the front separation Z as

$$\sigma = -2 \frac{d^2}{dZ^2} \mathcal{V}(Z) - 2 \frac{d}{dZ} \mathcal{G} \left(\frac{1}{2} [M^{-1} - Z] \right). \quad (5.74)$$

Eqs. (5.71) and (5.74) together provide closed relations between the instability growth rate σ and the modulation frequency $\Omega = M\pi$. Detailed calculations are given in Appendix 5.F for the sine waveform g_1 and the square waveform g_2 . The results are shown in Fig. 5.13. For the sine waveform, we see that σ reaches a minimum at an

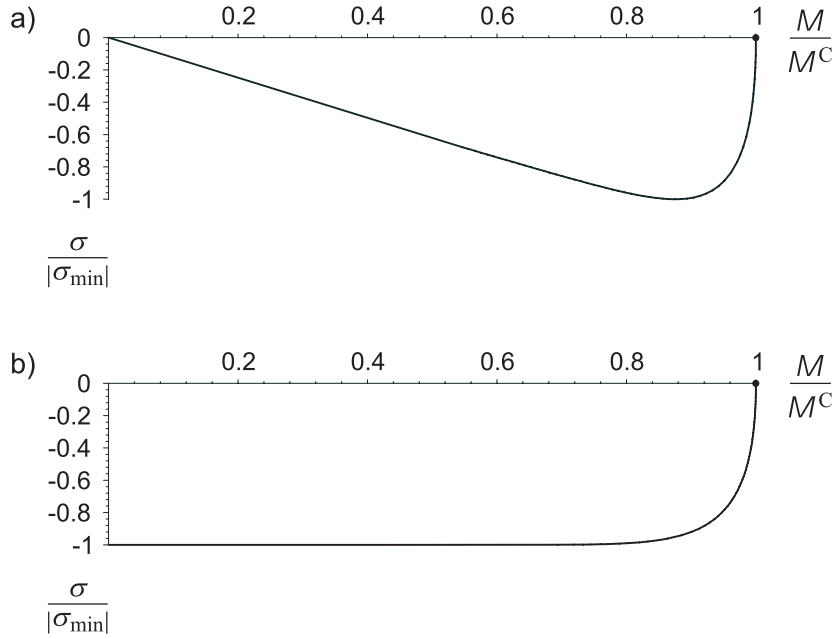


Figure 5.13: Fluctuation growth rate about phase-locked solutions as a function of the resonance number M (which is proportional to the modulation frequency), for two different modulation signals: a) sine waveform, b) square waveform. In both cases, the domain of stable locking has an upper bound at $M = M^C$. Away from $M = M^C$, stability is uniform for the square waveform, whereas it weakens at low modulation frequencies for the sine waveform.

optimal value of $M = M^*$ slightly less than M^C , and then quickly rises towards 0 as M approaches M^C . Modulation frequencies offering maximal stabilization performances are characterized by values of M close to M^* . In contrast, no such optimal modulation frequency exists in the case of the square waveform: the stabilization is equally good for all values of M up to a neighborhood of M^C . This difference in behavior between sine and square wave modulation signals admits a simple physical explanation. In absence of strong front attraction, remember from Sec. 5.7 that σ is proportional in magnitude to the slope of the modulation waveform in the vicinity of the fronts, as shown by formula (5.57). Indeed, it is intuitively clear that stability is determined by the variations in the forcing conditions experienced by the fronts as they move away from their equilibrium positions, so that faster variations of the modulation signal induce stronger stability or instability. Now, the slope of a sine function is proportional to its frequency, which explains why the stabilization effect is better for larger values of M , until this effect is counterbalanced by front attraction. In contrast, the slope of a square wave is independent of its frequency: it is idealized as exactly vertical in our model expression (5.61b). In information storage applications where one usually wants to encode as many bits of information as possible in a delay line of given length, there is advantage to work in a neighborhood of $M = M^C$ anyway, so that the choice of a sine

or a square modulation signal should be indifferent. However, in an experiment where a large spectrum of modulation frequencies is to be studied, a square wave modulation may be a better choice since it should provide uniformly good stabilization efficiency over all frequencies as long as the front interactions remain weak.

5.9 Summary and discussion

Combining the methods of multiple scales and matched asymptotic expansions, we reduced, in two steps, a scalar nonlinear delay-differential equation with a forcing term to a set of ordinary differential equations with a finite number of degrees of freedom. First, assuming a large delay and a weak forcing, we derived a normal form for the delay-differential equation in the vicinity of a period-2 oscillatory instability of a steady state. The normal form is a partial differential equation involving two distinct time scales explicitly, as previously found by Giacomelli and Politi in the absence of forcing [43]. In our case, the forcing appears in the form of a source term resonant with natural frequencies of the system. Away from an immediate neighborhood of the instability threshold, if the bifurcation is supercritical, the partial differential equation admits solutions constituted of an alternation of plateaus connected by thin transition layers. By analogy with methods used to study the dynamics of defects in spatially extended systems [97], we regarded the transition layers as slowly moving fronts in interaction. We obtained a set of ordinary differential equations governing their motion, taking into account the effects of both the attraction between first-neighbor fronts and the external forcing.

The simplest problem that could be analyzed with our simplified equations is the case where the forcing term is absent. Then, the problem of the determination of the asymptotic states of the system and their stability turned out to be solvable analytically. We mentioned, consistently with known results, the emergence, at successive Hopf bifurcation points, of periodic solutions whose frequencies are odd multiples of a fundamental frequency. We provided a complete analytical description of the continuous deformation of the periodic solutions from sine waves to square waves as the control parameter is increased away from the bifurcation points. The fact that the delay-differential equation admits only such highly symmetric states for large but finite delay contrasts with the behavior of the difference equation obtained in the limit of infinite delay ($\varepsilon = 0$), which authorizes solutions constituted of a sequence of plateaus of arbitrary length over a time interval of one delay. This found a very simple explanation, complementary to Ikeda *et al.*'s [58], in terms of front dynamics: the highly symmetric harmonics are the only possible equilibrium configurations of the equations of the motion, where the attraction exerted on each front by its two nearest neighbors exactly compensate each other. The difference equation does not take front interaction into account, and therefore does not provide such a selection mechanism. We found, however, that the fundamental periodic solution is the only stable one, all other harmonics remaining unstable for any value of the control parameter, in the limits of validity of our equations. The successive stabilization of higher harmonics observed by

Ikeda *et al.* [58] therefore appears to lie beyond the scope of a normal form analysis. Nevertheless, quantitative estimates of the growth rates of the fluctuations around an unstable periodic solution showed that the instability becomes extremely weak away from the bifurcation points. Therefore, even a very weak external forcing is expected to have a significant effect, and may strongly alter the stability of the solutions.

It was suggested recently that metastable states of the system (*i.e.*, long-lived multiple-front transients) might be used to encode information [50]. Such a mechanism is different from that proposed by Ikeda and Matsumoto in [59] since it does not involve a period doubling sequence. However, the finite lifetime of such states limits their applicability to short-term memory devices. Here, we made use of the equations of the motion of the fronts to study the effect of a periodic modulation. We showed that a large number of multiple-front solutions can be simultaneously stabilized by a periodic modulation at a suitably chosen frequency, making their lifetime infinite. We have termed the coexisting attractors “lacunar harmonics” because they take the form of higher-harmonic square-wave oscillations with missing front pairs.

We suggested that lacunar harmonics could be used for information storage applications, similarly to Ikeda’s period-doubled multistable oscillation modes [59]. Both approaches may provide complementary advantages. In theory, Ikeda’s period-doubling-based approach may provide ultrahigh memory capacity, because the number of bits of information that can be stored in a delay line doubles with each period-doubling bifurcation. In practice, however, the level of noise reduction needed for existence of high-period oscillation modes can be quite challenging [19]. On the other hand, our lacunar harmonic mechanism operates in the weakly nonlinear regime, at moderate distance of the primary instability threshold. The storage capacity cannot be made larger than the order of the harmonic, in contrast to the multiple-period-doubling scenario. However, the use of lacunar harmonics may offer the convenience of low sensitivity to noise, because their identification in experiments should not require the precise thresholding capabilities needed for the resolution of possible plateau values in the period-doubling-based approach. Moreover, our theoretical study is ultimately based on a normal form analysis, which pleads for the universality of the phenomenon.

In Sec. 5.8, we analyzed the effect of a weak detuning between the modulation frequency and the ideal resonance frequency, and then we analyzed how the stability of phase-locked dynamics depends on the modulation frequency. This required the taking into account of the attraction exerted by adjacent fronts of the oscillation pattern on each other. We found that pulsed modulation waveforms cannot offer efficient stabilization unless some amount of detuning is introduced. Sine modulation waveforms were shown to induce stronger stability with higher modulation frequency, up to the point where front attraction becomes significant and quickly degrades the stabilization performances. In contrast, square modulation waveforms displayed uniform stabilization efficiency over the whole frequency domain where front attraction is negligible.

Appendices to Chapter 5

5.A Normal form derivation

Throughout this appendix, it is assumed that the nonlinear function F and the forcing term G behave regularly enough for all subsequently introduced quantities to be well-defined. Consider a branch of steady state solutions $x = x_S(\Lambda)$ of the difference equation (5.3) parameterized by a continuum of values of the control parameter Λ . Assume that this branch loses stability at the threshold value $\Lambda = \Lambda_0$, where a continuum of period-2 oscillatory solutions emerges, and denote by $x = x_0 \equiv x_S(\Lambda_0)$ the value of the marginally stable steady state at $\Lambda = \Lambda_0$. If ε and the forcing term $G(S)$ are sufficiently small, then the delay-differential equation (5.4) admits weakly modulated, nearly constant solutions close to the steady states $x_S(\Lambda)$ of the difference equation (5.3). We further assume that these nearly constant solutions are stable wherever the solutions $x_S(\Lambda)$ are stable as solutions of the difference equation (5.3); that is, we assume that they are subject to no instability other than the delay-induced one at $\Lambda = \Lambda_0$. We seek a set of equations governing the dynamics of the solutions $x(S)$ of the delay-differential equation (5.4) close to the instability threshold $\Lambda = \Lambda_0$, and under the effect the weak forcing term $G(S)$.

5.A.1 Instability conditions

$x = x_0$ being a steady state of Eq. (5.3) at $\Lambda = \Lambda_0$, we have:

$$F(x_0, x_0, \Lambda_0) = 0. \quad (5.75)$$

Furthermore, the linearization of Eq. (5.3) around $x(S) = x_0$ at $\Lambda = \Lambda_0$ yields:

$$\left. \frac{\partial F(X, x_0, \Lambda_0)}{\partial X} \right|_{X=x_0} [x(S) - x_0] + \left. \frac{\partial F(x_0, Y, \Lambda_0)}{\partial Y} \right|_{Y=x_0} [x(S-1) - x_0] = 0. \quad (5.76)$$

At the period-2 instability threshold, the steady state is marginally stable with respect to period-2 oscillations, so that the above equation must reduce to

$$x(S) - x_0 = -[x(S-1) - x_0]. \quad (5.77)$$

This requires:

$$\left. \frac{\partial F(X, x_0, \Lambda_0)}{\partial X} \right|_{X=x_0} = \left. \frac{\partial F(x_0, Y, \Lambda_0)}{\partial Y} \right|_{Y=x_0} < 0. \quad (5.78)$$

We introduce the following notations for convenience:

$$F_{jkl} \equiv \left. \frac{\partial^{j+k+l} F(X, Y, Z)}{\partial X^j \partial Y^k \partial Z^l} \right|_{X=x_0, Y=x_0, Z=\Lambda_0}, \quad (5.79)$$

for nonnegative integers j , k , and l . In terms of these notations, the conditions (5.75) and (5.78) read:

$$F_{000} = 0, \quad (5.80)$$

$$F_{100} = F_{010} < 0. \quad (5.81)$$

5.A.2 Perturbation scheme

In order to perform a multiple-scale analysis, we now introduce a multiple-time-scale expansion of time-derivative and time-delay operators, alongside perturbative expansions of the dynamical variables. First, as a provision for its further multiple-scale expansion, we express the delayed variable $x(S-1)$ in terms of a delay operator D acting on $x(S)$, as

$$x(S-1) \equiv Dx(S) = \left(\exp -\frac{d}{dS} \right) x(S). \quad (5.82)$$

We next introduce the expansions:

$$x \equiv x_0 + \varepsilon x_1 + \varepsilon^2 x_2 + \varepsilon^3 x_3 + O(\varepsilon^4), \quad (5.83)$$

$$\frac{d}{dS} \equiv \frac{2}{p} \frac{\partial}{\partial S_0} + \varepsilon \frac{\partial}{\partial S_1} + \varepsilon^2 \frac{\partial}{\partial S_2} + O(\varepsilon^3), \quad (5.84)$$

$$p \equiv 2(1 + \varepsilon p_1) + O(\varepsilon^3). \quad (5.85)$$

The parameter p in Eq. (5.84) fixes the ratio of the fast time variable S_0 with respect to the original time variable S . Through the unspecified parameter p_1 in Eq. (5.85), we reserve, for convenience, the possibility of fixing, later on in the analysis, an arbitrary $O(\varepsilon)$ correction to the S_0 time scale without loss of generality. Eq. (5.85) will turn out to provide a perturbative expansion of the delay-induced oscillation period, which, for small but nonvanishing ε , is known to differ slightly from twice the delay time [76]. In terms of the time derivative expansion (5.84), and in view of the last equality in (5.82), the delay operator expands as:

$$D = \left\{ 1 + \varepsilon \left(p_1 \frac{\partial}{\partial S_0} - \frac{\partial}{\partial S_1} \right) + \varepsilon^2 \left[\frac{1}{2} \left(p_1 \frac{\partial}{\partial S_0} - \frac{\partial}{\partial S_1} \right)^2 - p_1^2 \frac{\partial}{\partial S_0} - \frac{\partial}{\partial S_2} \right] \right\} D_0 + O(\varepsilon^3), \quad (5.86)$$

where $D_0 \equiv \exp -\frac{\partial}{\partial S_0}$ is a delay operator for the fast time variable S_0 . Theory predicts that the amplitude of period-2 solutions of Eq. (5.3) scales as $(\Lambda - \Lambda_0)^{1/2}$ near the instability threshold. Furthermore, from Giacomelli and Politi's analysis [43], we expect

the normal form to be obtained as an $O(\varepsilon^3)$ solvability condition, which motivates the scaling $G(S) = O(\varepsilon^3)$. We therefore introduce the scaled quantities:

$$\Lambda \equiv \Lambda_0 + \varepsilon^2 \Lambda_2, \quad (5.87)$$

$$G(S) \equiv \varepsilon^3 G_3(S_0, S_1, S_2). \quad (5.88)$$

5.A.3 First order problem

Using the above expansions and collecting terms of equal powers of ε in Eq. (5.4), a hierarchy of problems is obtained. The zeroth-order problem is identically satisfied as per the condition (5.80). The first-order problem is:

$$F_{100}x_1 = -F_{010}D_0x_1, \quad (5.89)$$

which, by Eq. (5.81), reduces to the marginal stability condition

$$x_1 = -D_0x_1. \quad (5.90)$$

This relation requires x_1 to change sign, its absolute value remaining unchanged, each time S_0 increases by unity; that is, x_1 must be an antiperiodic function of S_0 with period 2. This implies, in particular, that any odd power of x_1 is antiperiodic (with period 2) and that any even power of x_1 is a periodic function of S_0 (with period 1).

5.A.4 Second order problem

The second order problem is:

$$x_2 + D_0x_2 = F_{100}^{-1} \left[\frac{\partial x_1}{\partial S_0} - \frac{1}{2} (F_{200} - 2F_{110} + F_{020}) x_1^2 - F_{001} \Lambda_2 \right] + p_1 \frac{\partial x_1}{\partial S_0} - \frac{\partial x_1}{\partial S_1}. \quad (5.91)$$

It assumes the form an inhomogeneous linear recurrence relation for x_2 . We now compute its second iterate, making use of the antiperiodicity condition (5.90). All period-1 terms cancel out of the right-hand side, leaving only antiperiodic terms:

$$x_2 - (D_0)^2 x_2 = 2 \left(F_{100}^{-1} \frac{\partial x_1}{\partial S_0} + p_1 \frac{\partial x_1}{\partial S_0} - \frac{\partial x_1}{\partial S_1} \right). \quad (5.92)$$

This is an inhomogeneous linear recurrence relation with a time step equal to the period of the right-hand side. Therefore, the right-hand side must vanish, or else the solution x_2 would be an unbounded function of S_0 , invalidating the perturbative expansion (5.83) by a finite time. This provides a solvability condition:

$$F_{100}^{-1} \frac{\partial x_1}{\partial S_0} + p_1 \frac{\partial x_1}{\partial S_0} - \frac{\partial x_1}{\partial S_1} = 0. \quad (5.93)$$

The constant p_1 may be fixed arbitrarily without loss of generality. The above equation motivates the choice $p_1 = -F_{100}^{-1}$, by which it reduces to

$$\frac{\partial x_1}{\partial S_1} = 0, \quad (5.94)$$

with the simple meaning that the first order solution x_1 does not depend on the time variable S_1 . The recurrence relation (5.91) then becomes:

$$x_2 + D_0 x_2 = -F_{100}^{-1} \left[\frac{1}{2} (F_{200} - 2F_{110} + F_{020}) x_1^2 + F_{001} \Lambda_2 \right], \quad (5.95)$$

whose most general solution is

$$x_2 \equiv x'_2 - \frac{1}{2} F_{100}^{-1} \left[\frac{1}{2} (F_{200} - 2F_{110} + F_{020}) x_1^2 + F_{001} \Lambda_2 \right], \quad (5.96)$$

where x'_2 is an arbitrary function satisfying an antiperiodicity condition:

$$x'_2 = -D_0 x'_2. \quad (5.97)$$

5.A.5 Third order problem

The third order problem is an inhomogeneous linear recurrence relation for x_3 :

$$\begin{aligned} x_3 + D_0 x_3 &= -\frac{\partial x_1}{\partial S_2} + \frac{1}{2} F_{100}^{-2} \frac{\partial^2 x_1}{\partial S_0^2} + k_1 \Lambda_2 x_1 + k_3 x_1^3 - \frac{\partial x'_2}{\partial S_1} \\ &\quad - F_{100}^{-1} G_3(S_0, S_1, S_2) + H(S_0, S_1, S_2), \end{aligned} \quad (5.98)$$

where $H(S_0, S_1, S_2)$ represents terms that are independent of x_3 and periodic in S_0 with period 1, and

$$k_1 \equiv F_{100}^{-1} \left[F_{011} - F_{101} + \frac{1}{2} F_{100}^{-1} F_{001} (F_{200} - F_{020}) \right], \quad (5.99a)$$

$$k_3 \equiv F_{100}^{-1} \left[\frac{1}{2} (F_{210} - F_{120}) + \frac{1}{6} (F_{030} - F_{300}) + \frac{1}{4} F_{100}^{-1} (F_{200} - F_{020}) (F_{200} - 2F_{110} + F_{020}) \right]. \quad (5.99b)$$

The coefficients k_1 and k_3 are assumed nonzero. The $(2N)^{\text{th}}$ iterate of the relation (5.98) may be written as:

$$\begin{aligned} &\frac{(-1)^N}{2N} \left[(D_0)^{-N} x_3 - (D_0)^N x_3 \right] \\ &= -\frac{\partial x_1}{\partial S_2} + \frac{1}{2} F_{100}^{-2} \frac{\partial^2 x_1}{\partial S_0^2} + k_1 \Lambda_2 x_1 + k_3 x_1^3 - \frac{\partial x'_2}{\partial S_1} - F_{100}^{-1} \frac{1}{2N} \sum_{j=-N}^{N-1} (-D_0)^j G_3(S_0, S_1, S_2). \end{aligned} \quad (5.100)$$

In order for the perturbative analysis to remain valid over all times, we require x_3 to be bounded as $s \rightarrow \pm\infty$. Then the left-hand side of the above equation vanishes for $N \rightarrow \infty$. This yields a solvability condition:

$$\begin{aligned} \frac{\partial x'_2}{\partial S_1} &= -\frac{\partial x_1}{\partial S_2} + \frac{1}{2}F_{100}^{-2} \frac{\partial^2 x_1}{\partial S_0^2} + k_1 \Lambda_2 x_1 + k_3 x_1^3 \\ &\quad - F_{100}^{-1} \lim_{N \rightarrow \infty} \frac{1}{2N} \sum_{j=-N}^{N-1} (-D_0)^j G_3(S_0, S_1, S_2), \end{aligned} \quad (5.101)$$

where the last term is, by construction, an antiperiodic function of S_0 . Eq. (5.101) is a differential equation for x'_2 that is solvable by quadrature. Now, for x'_2 to remain a bounded quantity for all S_1 , it is necessary that the right-hand side of Eq. (5.101) average to zero over all S_1 , which provides a secondary solvability condition:

$$\begin{aligned} \frac{\partial x_1}{\partial S_2} &= \frac{1}{2}F_{100}^{-2} \frac{\partial^2 x_1}{\partial S_0^2} + k_1 \Lambda_2 x_1 + k_3 x_1^3 \\ &\quad - F_{100}^{-1} \lim_{R \rightarrow \infty} \lim_{N \rightarrow \infty} \frac{1}{2R} \frac{1}{2N} \sum_{j=-N}^{N-1} (-D_0)^j \int_{-R}^R dS_1 G_3(S_0, S_1, S_2). \end{aligned} \quad (5.102)$$

Eq. (5.102) is a closed equation in x_1 which provides the required normal form. Note that the effect of the integral operator in the last term is to average out any dependence of the forcing term on the intermediate time scale S_1 . Therefore, we may forget about the formal dependence of the forcing term G_3 on S_1 and replace Eq. (5.88) with

$$G(S) \equiv \varepsilon^3 G_3(S_0, S_2). \quad (5.103)$$

Eq. (5.102) then reduces to

$$\frac{\partial x_1}{\partial S_2} = \frac{1}{2}F_{100}^{-2} \frac{\partial^2 x_1}{\partial S_0^2} + k_1 \Lambda_2 x_1 + k_3 x_1^3 - F_{100}^{-1} \lim_{N \rightarrow \infty} \frac{1}{2N} \sum_{j=-N}^{N-1} (-D_0)^j G_3(S_0, S_2). \quad (5.104)$$

Eqs. (5.5) and (5.6) are equivalent to Eqs. (5.104) and (5.90) with the final scaling:

$$u \equiv -F_{100} |k_3|^{\frac{1}{2}} x_1 \equiv -\varepsilon^{-1} F_{100} |k_3|^{\frac{1}{2}} [x - x_0 + O(\varepsilon^2)], \quad (5.105a)$$

$$s \equiv S_0 \equiv \frac{2}{p} S, \quad (5.105b)$$

$$t \equiv \frac{1}{2} F_{100}^{-2} S_2 \equiv \frac{1}{2} \varepsilon^2 F_{100}^{-2} S, \quad (5.105c)$$

$$\lambda \equiv F_{100}^2 k_1 \Lambda_2 \equiv \varepsilon^{-2} F_{100}^2 k_1 (\Lambda - \Lambda_0), \quad (5.105d)$$

$$g(s, t) \equiv 2F_{100}^2 |k_3|^{\frac{1}{2}} G_3(S_0, S_2) \equiv 2\varepsilon^{-3} F_{100}^2 |k_3|^{\frac{1}{2}} G(S), \quad (5.105e)$$

where the constants k_1 and k_3 are given in (5.99), the derivative notations F_{ijk} are defined in (5.79), and

$$p \equiv 2(1 - \varepsilon F_{100}^{-1}) + O(\varepsilon^3). \quad (5.106)$$

For $g(s, t) = 0$, periodic solutions of the delay-differential equation (5.1) close to the oscillatory instability threshold are found in Sec. 5.3 to correspond to solutions of the normal form (5.104) that do not vary on the S_2 time scale and are periodic in S_0 with period 2. Therefore, Eq. (5.106) expresses the period of delay-induced oscillations in the original time scale S .

5.B Equations of the motion for the fronts

We seek a closed set of differential equations governing the slow dynamics of the fronts $s_l(t)$, in the framework of the layered approximation as defined by the relations (5.25) and (5.26), and with the additional forcing weakness assumption (5.27).

5.B.1 Scaling

We express Eq. (5.27) in terms of a formal order parameter ϵ as follows:

$$g(s, t) \equiv \epsilon g'(s, t). \quad (5.107)$$

Using the layered approximation, we expand the solution u in a neighborhood of the transition layer centered on $s = s_l$ as:

$$u \equiv (-1)^l [U(s - s_l) + \epsilon v_l(s - s_l)] + O(\epsilon^2), \quad (5.108)$$

where the dominant-order expression comes from Eq. (5.25), and the small corrections v_l are unknown at this stage. This expansion should be valid up to a neighborhood of the adjacent fronts at $s = s_{l\pm 1}$. We then expand the slow time derivative operator as:

$$\frac{\partial}{\partial t} \equiv \frac{\partial}{\partial t_0} + \epsilon \frac{\partial}{\partial t_1} + O(\epsilon^2). \quad (5.109)$$

Substituting the above expansions, Eq. (5.9a), truncated to dominant order, reads:

$$\frac{\partial s_l}{\partial t_0} = 0. \quad (5.110)$$

This condition simply asserts that the fronts s_l do not vary on the t_0 time scale. Finally, we denote:

$$V(s) \equiv \frac{dU}{ds}(s) = \lambda \operatorname{sech}^2\left(\lambda^{\frac{1}{2}} s\right). \quad (5.111)$$

The following asymptotic expressions, valid for $\pm s \gg \lambda^{-1/2}$, turn out to be useful later on in the analysis:

$$U(s) \sim \pm \lambda^{\frac{1}{2}} \left(1 - 2 \exp \mp 2\lambda^{\frac{1}{2}} s\right), \quad (5.112)$$

$$V(s) \sim 4\lambda \exp \mp 2\lambda^{\frac{1}{2}} s. \quad (5.113)$$

Our strategy now consists to compute the corrections v_l from Eq. (5.9a) and then to impose matching constraints between adjacent transition layers. These conditions will provide the required closed set of equations for the fronts s_l .

5.B.2 Small corrections

Introducing Eq. (5.108) in Eq. (5.5) yields:

$$\begin{aligned} -V(s - s_l(t_1)) \frac{ds_l}{dt_1}(t_1) + \frac{\partial v_l}{\partial t_0}(s - s_l(t_1), t_0, t_1) &= \frac{\partial^2 v_l}{\partial s^2}(s - s_l(t_1), t_0, t_1) \\ + 2v_l(s - s_l(t_1), t_0, t_1) [\lambda - 3U(s - s_l(t_1))^2] &+ (-1)^l \mathcal{A}g'(s, t_0, t_1), \end{aligned} \quad (5.114)$$

where $O(\epsilon^2)$ terms have been neglected. With the help of a global translation in s , Eq. (5.114) can be rewritten as

$$\begin{aligned} \frac{\partial v_l}{\partial t_0}(s, t_0, t_1) &= \frac{\partial^2 v_l}{\partial s^2}(s, t_0, t_1) + 2v_l(s, t_0, t_1) [\lambda - 3U(s)^2] \\ &+ (-1)^l \mathcal{A}g'(s + s_l(t_1), t_0, t_1) + V(s) \frac{ds_l}{dt_1}(t_1). \end{aligned} \quad (5.115)$$

We require that the small correction v_l remain bounded for all t_0 , pointwise in the other two variables. Therefore, the right-hand side of the above equation must average to zero over all t_0 , which yields a solvability condition:

$$\frac{\partial^2 \bar{v}_l}{\partial s^2} + 2\bar{v}_l [\lambda - 3U(s)^2] = -(-1)^l \mathcal{A}\bar{g}(s + s_l, t_1) - V(s) \frac{ds_l}{dt_1}, \quad (5.116)$$

where

$$\bar{v}_l(s, t_1) \equiv \lim_{R \rightarrow \infty} \frac{1}{2R} \int_{-R}^R dt_0 v_l(s, t_0, t_1), \quad (5.117)$$

$$\bar{g}(s, t_1) \equiv \lim_{R \rightarrow \infty} \frac{1}{2R} \int_{-R}^R dt_0 g'(s, t_0, t_1). \quad (5.118)$$

Eq. (5.116) is a linear inhomogeneous ordinary differential equation for \bar{v}_l , in which the time scale t_1 plays the role of a mere parameter. Introducing the new variable w_l as follows:

$$\bar{v}_l(s, t_1) \equiv V(s) \left[A_l(t_1) + \int_0^s ds' V(s')^{-2} w_l(s', t_1) \right], \quad (5.119)$$

where A_l is an arbitrary function of t_1 , Eq. (5.116) reduces to the first order problem:

$$\frac{\partial w_l}{\partial s} = -(-1)^l V(s) \mathcal{A}\bar{g}(s + s_l, t_1) - V(s)^2 \frac{ds_l}{dt_1}, \quad (5.120)$$

in which we have used the relation

$$\frac{d}{ds} \left(\frac{d^2 U}{ds^2}(s) + 2U(s) [\lambda - U(s)^2] \right) = \frac{d^2 V}{ds^2}(s) + 2V(s) [\lambda - 3U(s)^2] = 0. \quad (5.121)$$

The solution of Eq. (5.120) can be written as:

$$w_l(s, t_1) = B_l(t_1) + \frac{1}{2} \left(\int_{-\infty}^s ds' - \int_s^{\infty} ds' \right) \left[-(-1)^l V(s') \mathcal{A}\bar{g}(s' + s_l, t_1) - V(s')^2 \frac{ds_l}{dt_1} \right], \quad (5.122)$$

where B_l is an arbitrary function of t_1 . The peculiar way of writing the integral operator above is chosen so that

$$w_l(\pm\infty, t_1) = B_l \pm C_l, \quad (5.123)$$

where

$$\begin{aligned} C_l &\equiv \frac{1}{2} \int_{-\infty}^{\infty} ds \left[-(-1)^l V(s) \mathcal{A}\bar{g}(s + s_l, t_1) - V(s)^2 \frac{ds_l}{dt_1} \right] \\ &= -\frac{1}{2} (-1)^l \lambda \int_{-\infty}^{\infty} ds \left[\operatorname{sech}^2 \left(\lambda^{\frac{1}{2}} s \right) \right] \mathcal{A}\bar{g}(s + s_l, t_1) - \frac{2}{3} \lambda^{\frac{3}{2}} \frac{ds_l}{dt_1}. \end{aligned} \quad (5.124)$$

In the evaluation of the second term above, we have used the identity

$$\int_{-\infty}^{\infty} ds \operatorname{sech}^4(s) = \frac{4}{3}. \quad (5.125)$$

We now seek an expression of $\bar{v}_l(s, t_1)$ asymptotically valid away from the transition layer. Computing the two limits $\pm s \gg \lambda^{-1/2}$ simultaneously in a single formula, using Eqs. (5.119) and (5.123), and retaining only $O\left(\exp \pm 2\lambda^{\frac{1}{2}} s\right)$ terms, which constitute the dominant contribution, we have

$$\begin{aligned} \bar{v}_l(s, t_1) &\sim V(s) \int_0^s ds' V(s')^{-2} w_l(\pm\infty, t_1) \\ &\sim \frac{1}{16} \lambda^{-\frac{3}{2}} (\pm B_l + C_l) \exp \pm 2\lambda^{\frac{1}{2}} s, \end{aligned} \quad (5.126)$$

where the evaluation of the integral uses the asymptotic expression (5.113).

5.B.3 Matching constraints

Averaging Eq. (5.108) over all t_0 yields, using the asymptotic expressions (5.112) and (5.126):

$$\begin{aligned} &\lim_{R \rightarrow \infty} \frac{1}{2R} \int_{-R}^R dt_0 u(s, t_0, t_1) \\ &= (-1)^l [U(s - s_l) + \epsilon \bar{v}_l(s - s_l, t_1)] + O(\epsilon^2) \\ &\sim (-1)^l \left[\pm \lambda^{\frac{1}{2}} \left(1 - 2 \exp \mp 2\lambda^{\frac{1}{2}} (s - s_l) \right) \right. \\ &\quad \left. + \frac{1}{16} \epsilon \lambda^{-\frac{3}{2}} (\pm B_l + C_l) \exp \pm 2\lambda^{\frac{1}{2}} (s - s_l) \right] + O(\epsilon^2). \end{aligned} \quad (5.127)$$

The domain of validity of this asymptotic expansion is the intersection of the domains of validity of expressions (5.108) and (5.126). That is, it holds in a region between the fronts $s = s_l$ and $s = s_{l\pm 1}$, for corresponding values of the sign pair symbols in Eq. (5.127). We see that the $O(\epsilon)$ contributions to the transition layer at $s = s_l$

grow exponentially fast away from $s = s_l$ and may become very large. By virtue of the matched asymptotic expansion principle, they are expected to match $O(1)$ contributions to the adjacent transition layers at $s = s_{l\pm 1}$ with the same exponential dependence in s . So, we equate the $O(\epsilon)$ term in Eq. (5.127) to the exponential part of the $O(1)$ term with reversed sign pair symbols and $l \pm 1$ being substituted for l :

$$\begin{aligned} \frac{(-1)^l}{16} \epsilon \lambda^{-\frac{3}{2}} (\pm B_l + C_l) \exp \pm 2\lambda^{\frac{1}{2}}(s - s_l) &\sim (-1)^{l\pm 1} \left(\mp \lambda^{\frac{1}{2}} \right) (-2) \exp \pm 2\lambda^{\frac{1}{2}}(s - s_{l\pm 1}) \\ \Leftrightarrow \frac{1}{32} \epsilon \lambda^{-2} (\pm B_l + C_l) &= \mp \exp \pm 2\lambda^{\frac{1}{2}}(s_l - s_{l\pm 1}). \end{aligned} \quad (5.128)$$

Summing this relation over both signs, B_l cancels out, leaving

$$\frac{1}{16} \epsilon \lambda^{-2} C_l = \exp -2\lambda^{\frac{1}{2}}(s_l - s_{l-1}) - \exp -2\lambda^{\frac{1}{2}}(s_{l+1} - s_l). \quad (5.129)$$

This equation involves the fronts s_l and their slow time derivatives $\frac{ds_l}{dt_1}$ through the coefficients C_l , and therefore gives, considering each value of l , the required equations of the motion. It does not involve the ‘‘faster’’ component t_0 of the slow time scale t , so that we may forget about the formal dependence of the forcing term on t_0 and substitute $g(s, t)$ for $\epsilon \bar{g}(s, t_1)$. Eq. (5.129) is then equivalent to the final form (5.28).

5.C Extrema of $\mathcal{G}(z_l)$

This appendix proceeds to the justification of the assertion that the integral $\mathcal{G}(z_l)$ defined in Eq. (5.48) possesses the same extrema as $g(z_l)$ (and none other), and that maxima (resp. minima) of $\mathcal{G}(z_l)$ correspond to maxima (resp. minima) of $g(z_l)$. First, invoking the symmetry properties of g and \mathcal{W} , it is not difficult to establish that

$$\frac{d}{dz_l} \mathcal{G}(z_l) = \int_0^{\frac{1}{2}M^{-1}} dz \left[\frac{d}{dz} \overline{\mathcal{W}}(z, M) \right] [g(z_l - z) - g(z_l + z)], \quad (5.130)$$

where

$$\overline{\mathcal{W}}(z, M) \equiv \sum_{q=-\infty}^{\infty} (-1)^q \mathcal{W}(z - qM^{-1}). \quad (5.131)$$

Now, consider the following identity involving elliptic functions:

$$\operatorname{sn}(z; k) \equiv \frac{\pi}{2k K'(k)} \lim_{N \rightarrow \infty} \sum_{q=-N}^N (-1)^q \tanh \left(\frac{\pi}{2K'(k)} [z - 2qK(k)] \right), \quad (5.132)$$

with the usual notations. This identity holds because both sides of the above equation have the same singularities in the complex plane and the same value at $z = 0$. Differentiating Eq. (5.132) twice with respect to z leads to:

$$\begin{aligned} & -\operatorname{sn}(z; k) [\operatorname{dn}^2(z; k) + k^2 \operatorname{cn}^2(z; k)] \\ & \equiv k^{-1} \left(\frac{\pi}{2K'(k)} \right)^2 \frac{d}{dz} \sum_{q=-\infty}^{\infty} (-1)^q \operatorname{sech}^2 \left(\frac{\pi}{2K'(k)} [z - 2qK(k)] \right). \end{aligned} \quad (5.133)$$

The left-hand side of this equation is negative over the half period starting at $z = 0$. The same must hold for the right-hand side, and thus for $\frac{d}{dz}\overline{\mathcal{W}}(z, M)$, by definition of \mathcal{W} . Therefore, the leftmost factor in the integral in Eq. (5.130) is always negative. Moreover, it is not difficult to establish that, for any fixed value of z_l , the rightmost factor does not change sign over the integration domain. Therefore, the zeros of the left-hand side of Eq. (5.130) are given by the values of z_l such that $g(z_l - z) \equiv g(z_l + z)$ for all z in the integration domain. Such values are exactly the extrema of $g(z_l)$, so that the extrema of $\mathcal{G}(z_l)$ exactly match those of $g(z_l)$. Moreover, the nature of extrema agrees, as determined by how the sign of the right-hand side of Eq. (5.130) varies as a function of z_l .

5.D Number of stable phase-locked modes

We want to compute, for fixed M , the number of stable phase-locked modes, under hypotheses 1–3 in Sec. 5.7. For definiteness, we assume that the modulation $g(z)$ has a positive slope at $z = 0$. The calculations are analogous in the case of a negative slope and lead to the same result.

Consider, for a given integer m in the range $1 \leq m \leq M$, an m -dimensional vector of boolean values,

$$I^{(m)} \equiv (I_0, I_1, \dots, I_{m-1}). \quad (5.134)$$

We shall call such a vector a *partial bitfield*. A partial bitfield will be qualified *stable* if and only if its extensions into M -dimensional vectors of boolean values $I = (I_0, I_1, \dots, I_{m-1}, \dots, I_{M-1})$ form bitfield representations of oscillation patterns that do not contain any unstable front in the open interval $0 < z < mM^{-1}$. With this definition, we see that a phase-locked mode is stable provided its bitfield representation is stable as a partial bitfield (of length $m = M$), and the front at $z = 0$, if any, is stable.

Let $\alpha_{A,B}^{(m)}$ denote the number of stable partial bitfields of length m such that $I_0 = A$ and $I_{m-1} = B$. One has, trivially,

$$\alpha_{A,B}^{(1)} = 1 \quad \text{if } A = B, \quad (5.135a)$$

$$\alpha_{A,B}^{(1)} = 0 \quad \text{if } A \neq B. \quad (5.135b)$$

Furthermore, for odd $m \geq 3$, one has

$$\begin{bmatrix} \alpha_{A,0}^{(m)} \\ \alpha_{A,1}^{(m)} \end{bmatrix} = \begin{bmatrix} 2 & 1 \\ 1 & 1 \end{bmatrix} \begin{bmatrix} \alpha_{A,0}^{(m-2)} \\ \alpha_{A,1}^{(m-2)} \end{bmatrix}, \quad (5.136)$$

where the entries in the square matrix are the numbers of ways of choosing the value of I_{m-2} , knowing the values of I_{m-3} and I_{m-1} from the corresponding entries in the vector columns, in such a way that the fronts at $z = m - 2$ and at $z = m - 1$, if any, are stable. Noting that the two eigenvalues μ_{\pm} of the square matrix can be written as

$$\mu_{\pm} = \left(\frac{1 \pm \sqrt{5}}{2} \right)^2, \quad (5.137)$$

the solution to the recurrence relation (5.136) for $m = M$ with initial condition (5.135) is straightforward to obtain:

$$\alpha_{0,0}^{(M)} = \beta^{(M)}, \quad \alpha_{0,1}^{(M)} = \alpha_{1,0}^{(M)} = \beta^{(M-1)}, \quad \alpha_{1,1}^{(M)} = \beta^{(M-2)}, \quad (5.138)$$

where

$$\beta^{(m)} \equiv \frac{1}{\sqrt{5}} \left[\left(\frac{1 + \sqrt{5}}{2} \right)^m - \left(\frac{1 - \sqrt{5}}{2} \right)^m \right]. \quad (5.139)$$

As mentioned before, a mode is stable provided its bitfield representation is stable as a partial bitfield, and the front at $z = 0$, if any, is stable. By virtue of the antiperiodicity of the mode, the latter condition demands that we do not have simultaneously $I_0 = 1$ and $I_{M-1} = 1$. Therefore, the number of stable modes is given by

$$\begin{aligned} N_M &\equiv \alpha_{0,0}^{(M)} + \alpha_{0,1}^{(M)} + \alpha_{1,0}^{(M)} = \beta^{(M)} + 2\beta^{(M-1)} \\ &= \left(\frac{1 + \sqrt{5}}{2} \right)^M + \left(\frac{1 - \sqrt{5}}{2} \right)^M. \end{aligned} \quad (5.140)$$

The last equality is obtained after a few algebraic simplifications. The second term in its right-hand side is always less than unity in magnitude, which, together with the fact that N_M is an integer number, results in the final expression (5.58).

5.E Stability for nonzero detuning

In this appendix, we solve Eqs. (5.62)–(5.63) for the three modulation waveforms defined in Eqs. (5.61) successively. We obtain closed form expressions of σ as a function of ν . For convenience, we shall denote by n_l and n'_l , respectively, the closest integer to Mz_l , and the closest integer to $Mz_l - \frac{1}{2}$.

5.E.1 Sine waveform: $g = g_1$

Substituting expressions (5.48) and (5.61a), Eqs. (5.62)–(5.63) read:

$$\nu = \gamma(-1)^{l+1} \int_{-\infty}^{\infty} dz \mathcal{W}(z - z_l) \sin(\pi Mz), \quad (5.141)$$

$$\sigma = \gamma(-1)^l \frac{d}{dz_l} \int_{-\infty}^{\infty} dz \mathcal{W}(z - z_l) \sin(\pi Mz). \quad (5.142)$$

Due to the rapid decrease of $\mathcal{W}(z - z_l)$ towards 0 as $z - z_l \rightarrow \pm\infty$, the integrands in the above equations differ significantly from zero only over a finite domain centered on $z = z_l$. By virtue of hypothesis 3 in Sec. 5.7, we may assume that the sine function almost does not vary over such a domain. Therefore, it may be approximated by its

value at $z = z_l$ and taken out of the integrals, which are then carried out. From Eq. (5.30), we have:

$$\int_{-\infty}^{\infty} dz \mathcal{W}(z) = \frac{3}{2} \lambda^{-1},$$

so that Eqs. (5.141)–(5.142) reduce to:

$$\nu = \frac{3}{2} \lambda^{-1} \gamma (-1)^{l+1} \sin(\pi M z_l), \quad (5.143)$$

$$\sigma = \frac{3\pi}{2} M \lambda^{-1} \gamma (-1)^l \cos(\pi M z_l). \quad (5.144)$$

Eq. (5.143) has been used to determine the relationships between the detuning and the front shifts in Fig. 5.10. Eliminating the trigonometric functions between Eqs. (5.143) and (5.144) yields the required expression of σ as a function of ν :

$$\sigma = \frac{3\pi}{2} M \lambda^{-1} \gamma (-1)^{l+n_l} \sqrt{1 - \left(\frac{3}{2} \lambda^{-1} \gamma\right)^{-2} \nu^2}. \quad (5.145)$$

5.E.2 Square waveform: $g = g_2$

Substituting the expressions (5.30), (5.48), and (5.61b), we carry out the integrals in Eqs. (5.62)–(5.63):

$$\nu = \frac{3}{4} \lambda^{-1} \gamma (-1)^{l+1} \sum_{q=-\infty}^{\infty} (-1)^q \left[\tanh\left(\lambda^{\frac{1}{2}}(z - z_l)\right) \right]_{z=qM^{-1}}^{z=(q+1)M^{-1}}, \quad (5.146)$$

$$\sigma = \frac{3}{4} \lambda^{-1} \gamma (-1)^l \frac{d}{dz_l} \sum_{q=-\infty}^{\infty} (-1)^q \left[\tanh\left(\lambda^{\frac{1}{2}}(z - z_l)\right) \right]_{z=qM^{-1}}^{z=(q+1)M^{-1}}. \quad (5.147)$$

By virtue of hypothesis 3, for any other integer Q than the nearest integer to Mz_l , we may approximate the hyperbolic tangent functions in the above expressions as:

$$\tanh\left(\lambda^{\frac{1}{2}}(QM^{-1} - z_l)\right) \simeq \text{sign}(QM^{-1} - z_l). \quad (5.148)$$

Therefore, Eqs. (5.146)–(5.147) reduce to:

$$\nu = \frac{3}{2} \lambda^{-1} \gamma (-1)^{l+n_l} \tanh\left(\lambda^{\frac{1}{2}}(n_l M^{-1} - z_l)\right), \quad (5.149)$$

$$\sigma = \frac{3}{2} \lambda^{-\frac{1}{2}} \gamma (-1)^{l+n_l} \text{sech}^2\left(\lambda^{\frac{1}{2}}(n_l M^{-1} - z_l)\right). \quad (5.150)$$

Eliminating the hyperbolic functions between Eqs. (5.149) and (5.150) yields the required expression of σ as a function of ν :

$$\sigma = \frac{3}{2} \lambda^{-\frac{1}{2}} \gamma (-1)^{l+n_l} \left[1 - \left(\frac{3}{2} \lambda^{-1} \gamma\right)^{-2} \nu^2 \right], \quad |\nu| \leq \frac{3}{2} \lambda^{-1} \gamma. \quad (5.151)$$

5.E.3 Pulsed waveform: $g = g_3$

Substituting the expressions (5.30), (5.48), and (5.61c), we carry out the integrals in Eqs. (5.62)–(5.63):

$$\nu = \frac{3}{4} \lambda^{-\frac{1}{2}} \gamma (-1)^{l+1} \sum_{q=-\infty}^{\infty} (-1)^q \operatorname{sech}^2 \left\{ \lambda^{\frac{1}{2}} \left(\left[q + \frac{1}{2} \right] M^{-1} - z_l \right) \right\}, \quad (5.152)$$

$$\sigma = \frac{3}{4} \lambda^{-\frac{1}{2}} \gamma (-1)^l \frac{d}{dz_l} \sum_{q=-\infty}^{\infty} (-1)^q \operatorname{sech}^2 \left\{ \lambda^{\frac{1}{2}} \left(\left[q + \frac{1}{2} \right] M^{-1} - z_l \right) \right\}. \quad (5.153)$$

By virtue of hypothesis 3, for any other integer q than the nearest integer to $Mz_l - \frac{1}{2}$, the hyperbolic secant functions in the above expressions are vanishingly small. Therefore, Eqs. (5.152)–(5.153) can be approximated as:

$$\nu = \frac{3}{4} \lambda^{-\frac{1}{2}} \gamma (-1)^{l+n'_l+1} \operatorname{sech}^2 \left\{ \lambda^{\frac{1}{2}} \left(\left[n'_l + \frac{1}{2} \right] M^{-1} - z_l \right) \right\}, \quad (5.154)$$

$$\begin{aligned} \sigma &= \frac{3}{2} \gamma (-1)^{l+n'_l} \operatorname{sech}^2 \left\{ \lambda^{\frac{1}{2}} \left(\left[n'_l + \frac{1}{2} \right] M^{-1} - z_l \right) \right\} \\ &\quad \tanh \left\{ \lambda^{\frac{1}{2}} \left(\left[n'_l + \frac{1}{2} \right] M^{-1} - z_l \right) \right\}. \end{aligned} \quad (5.155)$$

Eliminating the hyperbolic functions between Eqs. (5.154) and (5.155) yields the required expression of σ as a function of ν :

$$\begin{aligned} \sigma &= 2 \lambda^{\frac{1}{2}} (-1)^{l+n'_l} |\nu| \sqrt{1 - \left(\frac{3}{4} \lambda^{-\frac{1}{2}} \gamma \right)^{-2} \nu^2 \operatorname{sign} \left(n'_l + \frac{1}{2} - Mz_l \right)} \\ &= 2 \lambda^{\frac{1}{2}} (-1)^{l+n_l} |\nu| \sqrt{1 - \left(\frac{3}{4} \lambda^{-\frac{1}{2}} \gamma \right)^{-2} \nu^2}, \end{aligned} \quad (5.156)$$

where, in the last equality, we have used the relation

$$\operatorname{sign} \left(n'_l + \frac{1}{2} - Mz_l \right) = (-1)^{n_l - n'_l}. \quad (5.157)$$

5.F Stability for nonnegligible front attraction

In this appendix, Eqs. (5.71) and (5.74) are used to determine closed-form relations between σ and M , for both the sine modulation defined in Eq. (5.61a) and the square modulation defined in Eq. (5.61b).

5.F.1 Sine waveform: $g = g_1$

Substituting the expressions (5.29), (5.30), and (5.61a), Eqs. (5.71) and (5.74) can be written as:

$$24\lambda^{\frac{1}{2}} \exp\left(-2\lambda^{\frac{1}{2}}Z\right) = \frac{3}{4}\lambda^{-1}\gamma \operatorname{Im} \left[\int_{-\infty}^{\infty} dy \operatorname{sech}^2(y) \exp\left(i\pi M\lambda^{-\frac{1}{2}}y\right) \exp\left(i\frac{\pi}{2}(1-MZ)\right) \right], \quad (5.158)$$

$$\sigma = 96\lambda \exp\left(-2\lambda^{\frac{1}{2}}Z\right) + \frac{3}{2}\lambda^{-1}\gamma \frac{d}{dZ} \operatorname{Im} \left[\int_{-\infty}^{\infty} dy \operatorname{sech}^2(y) \exp\left(i\pi M\lambda^{-\frac{1}{2}}y\right) \exp\left(i\frac{\pi}{2}(1-MZ)\right) \right], \quad (5.159)$$

where we have performed the integration variable change

$$y = \lambda^{\frac{1}{2}} \left[z - \frac{1}{2}(M^{-1} - Z) \right]. \quad (5.160)$$

Using the formula

$$\int_{-\infty}^{\infty} dy \operatorname{sech}^2(y) \exp(i\omega y) = \frac{\pi\omega}{\sinh\left(\frac{\pi\omega}{2}\right)}, \quad (5.161)$$

The integrals in Eqs. (5.162) and (5.159) can be carried out. This yields:

$$24\lambda^{\frac{1}{2}} \exp -2\lambda^{\frac{1}{2}}Z = \frac{\frac{3}{4}\pi^2 M\lambda^{-\frac{3}{2}}\gamma}{\sinh\left(\frac{\pi^2}{2}M\lambda^{-\frac{1}{2}}\right)} \cos\left(\frac{\pi}{2}MZ\right), \quad (5.162)$$

$$\sigma = \frac{3\pi^2 M\lambda^{-1}\gamma}{\sinh\left(\frac{\pi^2}{2}M\lambda^{-\frac{1}{2}}\right)} \left[\cos\left(\frac{\pi}{2}MZ\right) - \frac{\pi}{4}M\lambda^{-\frac{1}{2}} \sin\left(\frac{\pi}{2}MZ\right) \right], \quad (5.163)$$

where Eq. (5.158) has been substituted into Eq. (5.159). Eq. (5.162) is a closed relation between M and Z that cannot be further simplified, and whose roots must be computed numerically. Eq. (5.163) then gives the corresponding values of σ in explicit form.

5.F.2 Square waveform: $g = g_2$

Substituting the expressions (5.29), (5.30), and (5.61b), we carry out the integrals in Eqs. (5.71) and (5.74):

$$24\lambda^{\frac{1}{2}} \exp -2\lambda^{\frac{1}{2}} Z = \frac{3}{4}\lambda^{-1}\gamma \sum_{q=-\infty}^{\infty} (-1)^q \left[\tanh \left\{ \lambda^{\frac{1}{2}} \left(z - \frac{1}{2} [M^{-1} - Z] \right) \right\} \right]_{z=qM^{-1}}^{z=(q+1)M^{-1}}, \quad (5.164)$$

$$\begin{aligned} \sigma &= 96\lambda \exp -2\lambda^{\frac{1}{2}} Z \\ &+ \frac{3}{2}\lambda^{-1}\gamma \frac{d}{dZ} \sum_{q=-\infty}^{\infty} (-1)^q \left[\tanh \left\{ \lambda^{\frac{1}{2}} \left(z - \frac{1}{2} [M^{-1} - Z] \right) \right\} \right]_{z=qM^{-1}}^{z=(q+1)M^{-1}} \end{aligned} \quad (5.165)$$

In order to further simplify the above equations, we make the assumption that the modulation period is “sufficiently large” with respect the transition layer width, in the following sense:

$$\exp M^{-1}\lambda^{\frac{1}{2}} \gg 1. \quad (5.166)$$

This can be viewed as a weakened form of hypothesis 3 in Sec. 5.7. By virtue of this hypothesis, and under the condition (5.69), for any integer $Q \neq 0$, we may approximate the hyperbolic tangent functions in the above expressions as:

$$\begin{aligned} \tanh \left\{ \lambda^{\frac{1}{2}} (QM^{-1} - \frac{1}{2} [M^{-1} - Z]) \right\} &= \frac{\exp \left\{ \lambda^{\frac{1}{2}} (2QM^{-1} - [M^{-1} - Z]) \right\} - 1}{\exp \left\{ \lambda^{\frac{1}{2}} (2QM^{-1} - [M^{-1} - Z]) \right\} + 1} \\ &\simeq \text{sign}(2QM^{-1} - [M^{-1} - Z]). \end{aligned} \quad (5.167)$$

Therefore, Eqs. (5.164)–(5.165) reduce to:

$$24\lambda^{\frac{1}{2}} \exp \left(-2\lambda^{\frac{1}{2}} Z \right) = \frac{3}{2}\lambda^{-1}\gamma \tanh \left[\frac{1}{2}\lambda^{\frac{1}{2}} (M^{-1} - Z) \right], \quad (5.168)$$

$$\sigma = 96\lambda \exp \left(-2\lambda^{\frac{1}{2}} Z \right) - \frac{3}{2}\lambda^{-\frac{1}{2}}\gamma \text{sech}^2 \left[\frac{1}{2}\lambda^{\frac{1}{2}} (M^{-1} - Z) \right]. \quad (5.169)$$

Performing tedious but straightforward algebraic manipulations, it is possible to eliminate Z between the two above equations, and to obtain an explicit expression of M as a function of σ :

$$M = 2\lambda^{\frac{1}{2}} \left[\ln \left(\frac{16\lambda^{\frac{3}{2}}\gamma^{-1}(\rho - 1)^2}{(\rho - 2)(\rho - 3)^2} \right) \right]^{-1}, \quad 2 < \rho \equiv \sqrt{\frac{2}{3}\lambda^{\frac{1}{2}}\gamma^{-1}\sigma + 5} < 3. \quad (5.170)$$

Remembering the condition (5.27), which is necessary for the equations of the motion (5.28) to be valid, we see from the above equation that $M^{-1}\lambda^{\frac{1}{2}}$ remains the logarithm of a large quantity for all σ , justifying the assumption (5.166) *a posteriori*.

Chapter 6

Perspectives

“The purpose of models is not to fit the data but to sharpen the questions.”

—Samuel Karlin

The four last chapters were devoted to the presentation and the treatment of some problems in nonlinear optics. The main results were summarized at the end of each chapter. We now propose a number of possible extensions to this work.

In Chapter 2, we considered two semiconductor laser problems. The second one was the laser subject to both optical injection and delayed optical feedback. We found a particular type of phase instability characterized by periodic oscillations with a period equal to twice the delay. For the particular parameter values chosen, we found that this mode of oscillation loses stability rather quickly, at a limit point. The relative simplicity of the phase equation (2.81b) and of its discrete map limit (2.114) should allow a more systematic analysis of this oscillatory behavior. In particular, we are interested to find conditions of existence of period-doubling bifurcations and to investigate the possibility of a Feigenbaum cascade to chaos.

In Chapter 4, we provided a simple theoretical description of a particular type of bursting instability characterized by an especially high oscillation frequency in the periods of activity. We took advantage of that high frequency in order to proceed to an analytical treatment of the problem. However, as is readily observed from the experimental data, there exist other types of bursting activities where the fast oscillation frequency is not so high, and which apparently correspond to different periodic sequences of bifurcation crossings. We are interested to see to what extent the two-mode OPO model (4.7) or its degenerate variant (4.10) is able to reproduce these experimentally observed behaviors. A more systematic study of the bifurcation possibilities using a numerical continuation tool is proposed as a possible extension of our work on bursting dynamics in OPOs.

In Chapter 5, we reduced a delay-differential equation modelling an optically bistable device to a partial differential equation, and then to a set of ordinary differential equations. We showed that this approach simplifies considerably the determination of solutions and their stability properties, even in the presence of an external forcing.

However, the validity of our treatment was limited to a neighborhood of the bifurcation to period-2 oscillations. In that domain, higher harmonic oscillation modes in the free-running system were found to be unstable. It is known from numerical studies that these higher harmonic modes acquire stability under some circumstances [58]. A theoretical understanding of the stabilization mechanism is still lacking. We expect that an extension of our method of reduction valid further away from the instability threshold would provide an adequate basis for an analytical investigation of the stabilization phenomenon. Preliminary calculations, not presented in this thesis, suggest that indeed it is possible to reduce the delay-differential equation to a set of ordinary differential equations in an extended domain. We pointed out in Chapter 5 that the discrete map (5.3) obtained by setting $\varepsilon = 0$ in the delay-differential equation (5.1) is not completely valid as an asymptotic limit of the original equation for small ε . Although the discrete map determines the heights of the plateaus in a square-wave-type solution, it does not contain any precise information about the instants at which transitions occur between plateaus. As a consequence, it cannot be used to find out the stability properties of solutions having more than one transition per delay time. A set of ordinary differential equation governing the transition instants may just provide the missing information, as we found in Chapter 5 in the particular case of small-amplitude oscillations.

Bibliography

- [1] N. B. Abraham, P. Mandel, and L. M. Narducci, *Dynamical instabilities and pulsations in lasers*, in Progress in Optics XXV, E. Wolf, Ed., North-Holland (1988) 3–190.
- [2] G. P. Agrawal and N. K. Dutta, *Semiconductor lasers*, 2nd Edition, Van Nostrand Reinhold, New York, 1993.
- [3] T. Aida and P. Davis, *Oscillation modes of laser diode pumped hybrid bistable system with large delay and application to dynamical memory*, IEEE Journal of Quantum Electronics 28 (1992) 686–699.
- [4] T. Aida and P. Davis, *Oscillation mode selection using bifurcation of chaotic mode transitions in a nonlinear ring resonator*, IEEE Transactions on Quantum Electronics 30 (1994) 2986–2997.
- [5] V. Annovazzi-Lodi, A. Sciré, M. Sorel, and S. Donati, *Dynamic behavior and locking of a semiconductor laser subjected to external injection*, IEEE Journal of Quantum Electronics 34 (1998) 2350–2357.
- [6] F. T. Arecchi, G. Giacomelli, A. Lapucci, and R. Meucci, *Two-dimensional representation of a delayed dynamical system*, Physical Review A 45 (1992) 4225–4228.
- [7] J. A. Armstrong, N. Bloembergen, J. Ducuing, and P. S. Pershan, *Interaction between light waves in a nonlinear dielectric*, Physical Review 127 (1962) 1918–1939.
- [8] D. G. Aronson and H. F. Weinberger, *Nonlinear diffusion and population genetics, combustion and nerve propagation*, Proceedings of the Tulane Program in Partial Differential Equations and Related Topics, Lecture Notes in Mathematics 446, Springer, 1975, 5–49.
- [9] S. M. Baer, T. Erneux, and J. Rinzel, *The slow passage through a Hopf bifurcation: delay, memory effects, and resonance*, SIAM Journal on Applied Mathematics 49 (1989) 55–71.
- [10] N. Bloembergen, *Nonlinear Optics*, World Scientific, Singapore, 1996.

- [11] F. J. Bourland, R. Haberman, and W. L. Kath, *Averaging methods for the phase shift of arbitrarily perturbed strongly nonlinear oscillators with an application to capture*, SIAM Journal of Applied Mathematics **51** (1991) 1150–1167.
- [12] P. N. Butcher and D. Cotter, *The elements of nonlinear optics*, Cambridge Studies in Modern Optics **9**, Cambridge University Press, 1990.
- [13] H. J. Carmichael, R. R. Snapp, and W. C. Shieve, *Oscillatory instabilities leading to “optical turbulence” in a bistable ring cavity*, Physical Review A **26** (1982) 3408–3422.
- [14] T. W. Carr, L. Billings, I. B. Schwartz, and I. Triandaf, *Bi-instability and the global role of unstable resonant orbits in a driven laser*, Physica D **147** (2000) 59–82.
- [15] V. N. Chizhevsky, *Multistability in dynamical systems induced by weak periodic perturbations*, Physical Review E **64** (2001) 036223.
- [16] V. N. Chizhevsky, R. Corbalán, and A. N. Pisarchik, *Attractor splitting induced by resonant perturbations*, Physical Review E **56** (1997) 1580–1584.
- [17] S.-N. Chow and J. Mallet-Paret, *Singularly perturbed delay-differential equations, Coupled Nonlinear Oscillators*, Proc. Workshop, Los Alamos 1981, North-Holland Math. Stud. **80** (1983) 7–12.
- [18] P. C. De Jagher, W. A. van der Graaf, and D. Lenstra, *Relaxation-oscillation phenomena in an injection-locked semiconductor laser*, Quantum and Semiclassical Optics **8** (1996) 805–822.
- [19] M. W. Derstine, H. M. Gibbs, F. A. Hopf, and D. L. Kaplan, *Bifurcation gap in a hybrid optically bistable system*, Physical Review A **26** (1982) 3270–3272.
- [20] M. W. Derstine, H. M. Gibbs, F. A. Hopf, and D. L. Kaplan, *Alternate paths to chaos in optical bistability*, Physical Review A **27** (1983) 3200–3208.
- [21] E. J. Doedel, A. R. Champneys, T. F. Fairgrieve, Y. A. Kuznetsov, B. Sandstede, and X. Wang, *AUTO 97: Continuation and bifurcation software for ordinary differential equations*, <http://indy.cs.concordia.ca/auto/>, 1998.
- [22] M. Ebrahimzadeh, R. C. Eckardt, and M. H. Dunn, *Optical parametric devices and processes*, Journal of the Optical Society of America B **16** (1999) 1477–1478.
- [23] S. Eriksson and Å. M. Lindberg, *Periodic oscillation within the chaotic region in a semiconductor laser subjected to external optical injection*, Optics Letters **26** (2001) 142–144.

- [24] S. Eriksson and Å. M. Lindberg, *Observations on the dynamics of semiconductor lasers subjected to external optical injection*, Journal of Optics B: Quantum and Semiclassical Optics **4** (2002) 149–154.
- [25] T. Erneux, A. Gavrielides, and V. Kovanis, *Low pump stability of an optically injected diode laser*, Quantum and Semiclassical Optics **9** (1997) 811–818.
- [26] T. Erneux, V. Kovanis, A. Gavrielides, and P. M. Alsing, *Mechanism for period doubling bifurcation in a semiconductor laser subject to optical injection*, Physical Review A **53** (1996) 4372–4380.
- [27] P. C. Fife, *Stationary patterns for reaction-diffusion equations*, in Nonlinear Diffusion, Research Notes in Mathematics **14**, Pitman, London, 1977, 81–121.
- [28] P. C. Fife, *Mathematical aspects of reacting and diffusing systems*, Lecture Notes in Biomathematics **28**, Springer, 1979.
- [29] P. C. Fife, *Long time behavior of solutions of bistable nonlinear diffusion equations*, Archive for Rational Mechanics and Analysis **70** (1979) 31–46.
- [30] P. C. Fife and J. B. McLeod, *The approach of solutions of nonlinear diffusion equations to travelling front solutions*, Arch. Rat. Mech. Anal. **65** (1977) 335–361.
- [31] I. Fischer, Y. Liu, and P. Davis, *Synchronization of chaotic semiconductor laser dynamics on subnanosecond time scales and its potential for chaos communication*, Physical Review A **62** (2000) 011801(R).
- [32] I. Fischer, G. H. M. van Tartwijk, A. M. Levine, W. Elsässer, E. Göbel, and D. Lenstra, *Fast pulsing and chaotic itinerancy with a drift in the coherence collapse of semiconductor lasers*, Physical Review Letters **76** (1996) 220–223.
- [33] J. Foss, A. Longtin, B. Mensour, and J. Milton, *Multistability and delayed recurrent loops*, Physical Review Letters **76** (1996) 708–711.
- [34] J. Foss, F. Moss, and J. Milton, *Noise, multistability, and delayed recurrent loops*, Physical Review E **55** (1997) 4536–4543.
- [35] P. A. Franken, A. E. Hill, C. W. Peters, and G. Weinreich, *Generation of optical harmonics*, Physical Review Letters **7** (1961) 118–119.
- [36] J. Y. Gao, G. X. Jin, J. W. Sun, X. Z. Guo, Z. R. Zhen, N. B. Abraham, and L. M. Narducci, *The effect of input modulation in a bistable system with delay*, Optics Communications **71** (1989) 224–228.
- [37] J. Y. Gao and L. M. Narducci, *The effect of modulation in a bistable system with delay*, Optics Communications **58** (1986) 360–364.

- [38] J. Y. Gao, L. M. Narducci, L. S. Schulman, M. Squicciarini, and J. M. Yuan, *Route to chaos in a hybrid bistable system with delay*, Physical Review A **28** (1983) 2910–2914.
- [39] A. Gavrielides, T. Erneux, V. Kovanis, P. M. Alsing, and T. B. Simpson, *Subharmonic transition in an optically injected semiconductor laser: theory and experiments*, Quantum and Semiclassical Optics **9** (1997) 575–585.
- [40] A. Gavrielides, V. Kovanis, T. Erneux, and M. Nizette, *Phase locked modulations of optically injected laser diodes*, in Physics and Simulations of Optoelectronic devices VIII, R. Binder, P. Blood, and M. Osínski, Eds., Proceedings of SPIE **3944** (2000) 627–638.
- [41] A. Gavrielides, V. Kovanis, M. Nizette, T. Erneux, and T. B. Simpson, *Period three limit-cycles in injected semiconductor lasers*, Journal of Optics B: Quantum and Semiclassical Optics **4** (2002) 20–26.
- [42] A. Gavrielides, V. Kovanis, P. M. Varangis, T. Erneux and G. Lythe, *Coexisting periodic attractors in injection-locked diode Lasers*, Quantum and Semiclassical Optics **9** (1997) 785–796.
- [43] G. Giacomelli and A. Politi, *Relationship between delayed and spatially extended dynamical systems*, Physical Review Letters **76** (1996) 2686–2689.
- [44] G. Giacomelli and A. Politi, *Multiple scale analysis of delayed dynamical systems*, Physica D **117** (1998) 26–42.
- [45] H. M. Gibbs, *Optical bistability: controlling light with light*, Academic Press, Orlando, 1985.
- [46] H. M. Gibbs, F. A. Hopf, D. L. Kaplan, and R. L. Shoemaker, *Observation of chaos in optical bistability*, Physical Review Letters **46** (1981) 474–477.
- [47] J. A. Giordmaine and R. C. Miller, *Tunable coherent parametric oscillation in LiNbO_3 at optical frequencies*, Physical Review Letters **14** (1965) 973–976.
- [48] A. Goldbeter, *Biochemical Oscillations and Cellular Rhythms*, Cambridge University Press, 1996.
- [49] B. K. Goswami, *Self-similarity in the bifurcation structure involving period tripling, and a suggested generalization to period n -tupling*, Physics Letters A **245** (1998) 97–109.
- [50] C. Grotta-Ragazzo, K. Pakdaman, and C. P. Malta, *Metastability for delayed differential equations*, Physical Review E **60** (1999) 6230–6233.
- [51] W. S. C. Gurney, S. P. Blythe, and R. M. Nisbet, *Nicholson’s blowflies revisited*, Nature **287** (1980) 17–21.

- [52] H. Haken, *Analogy between higher instabilities in fluids and lasers*, Physics Letters A **53** (1975) 77–78.
- [53] S. M. Hammel, C. K. R. T. Jones, J. V. Moloney, *Global dynamical behavior of the optical field in a ring cavity*, Journal of the Optical Society of America B **2** (1985) 552.
- [54] F. A. Hopf, D. L. Kaplan, H. M. Gibbs, and R. L. Shoemaker, *Bifurcations to chaos in optical bistability*, Physical Review A **25** (1982) 2172–2182.
- [55] K. Iga, *Fundamentals of Laser Optics*, Plenum, New York, 1994.
- [56] K. Ikeda, *Multiple-valued stationary state and its instability of the transmitted light by a ring cavity*, Optics Communications **30** (1979) 257–261.
- [57] K. Ikeda, H. Daido, and O. Akimoto, *Optical turbulence: chaotic behavior of transmitted light from a ring cavity*, Physical Review Letters **45** (1980) 709–712.
- [58] K. Ikeda, K. Kondo, and O. Akimoto, *Successive higher-harmonic bifurcations in systems with delayed feedback*, Physical Review Letters **49** (1982) 1467–1470.
- [59] K. Ikeda and K. Matsumoto, *High-dimensional chaotic behavior in systems with time-delayed feedback*, Physica D **29** (1987) 223–235.
- [60] E. Izhikevitch, *Subcritical elliptic bursting of Bautin type*, SIAM Journal of Applied Mathematics **60** (2000) 503–535.
- [61] Journal of the European Optical Society B: Quantum and Semiclassical Optics **9**, 5 (1997) 655–878: Special issue on fundamental nonlinear dynamics of semiconductor lasers.
- [62] W. L. Kath, *Resonance in periodically perturbed Hopf bifurcation*, Studies in Applied Mathematics **65** (1981) 95–112.
- [63] I. V. Koryukin and Paul Mandel, *Two regimes of synchronization in unidirectionally coupled semiconductor lasers*, Physical Review E **65** (2001) 026201.
- [64] V. Kovanis, T. Erneux, and A. Gavrielides, *Largely detuned injection-locked semiconductor lasers*, Optics Communications **159** (1999) 177–183.
- [65] B. Krauskopf, K. Schneider, J. Sieber, S. Wiczorek, and M. Wolfrum, *Excitability and self-pulsations near homoclinic bifurcations in semiconductor laser systems*, Optics Communications **215** (2003) 367–379.
- [66] B. Krauskopf, N. Tollenaar, and D. Lenstra, *Tori and their bifurcations in an optically injected semiconductor laser*, Optics Communications **156** (1998) 158–169.

- [67] B. Krauskopf, W. A. van der Graaf, and D. Lenstra, *Bifurcations of relaxation oscillations in an optically injected diode laser*, Quantum and Semiclassical Optics **9** (1997) 797–809.
- [68] B. Krauskopf, S. Wieczorek, and D. Lenstra, *Different types of chaos in an optically injected semiconductor laser*, Applied Physics Letters **77** (2000) 1611–1613.
- [69] R. Lang and K. Kobayashi, *External optical feedback effects on semiconductor injection laser properties*, IEEE Journal of Quantum Electronics QE–**16** (1980) 347–355.
- [70] W. Ledermann, *Handbook of applicable mathematics IV: Analysis*, Wiley, 1982.
- [71] J. M. Liu and T. B. Simpson, *Four-wave-mixing and optical Modulation in a semiconductor laser*, IEEE Journal of Quantum Electronics **30** (1994) 957.
- [72] Y. Liu, Y. Takiguchi, P. Davis, T. Aida, S. Saito, and J. M. Liu, *Experimental observation of complete chaos synchronization in semiconductor lasers*, Applied Physics Letters **80** (2002) 4306–4308.
- [73] L. A. Lugiato, C. Oldano, C. Fabre, E. Giacobino, R. H. Horowicz, *Bistability, self-pulsing, and chaos in optical parametric oscillators*, Il Nuovo Cimento **10D** (1988) 959–977.
- [74] M. C. Mackey, *Mathematical models of hepatopoietic cell replication and control*, in: The art of mathematical modelling: case studies in ecology, physiology and biofluids, eds. H. G. Othmer, F. R. Adler, M. A. Lewis and J. C. Dallon, Prentice-Hall, New Jersey, 1997, 149–178.
- [75] T. H. Maiman, *Stimulated optical radiation in ruby lasers*, Nature **187** (1960) 493–494.
- [76] J. Mallet-Paret and R. D. Nussbaum, *Global continuation and asymptotic behaviour for periodic solutions of a differential-delay equation*, Annali di Matematica Pura ed Applicata, IV **145** (1986) 33–128.
- [77] P. Mandel, *Theoretical problems in cavity nonlinear optics*, Cambridge Studies in Modern Optics, Cambridge University Press, 1997.
- [78] P. Mandel and T. Erneux, *Laser Lorenz equations with a time-dependent parameter*, Physical Review Letters **53** (1984) 1818–1820.
- [79] C. Masoller and N. B. Abraham, *Stability and dynamical properties of the coexisting attractors of an external-cavity semiconductor laser*, Physical Review A **57** (1998) 1313–1322.

- [80] C. Mayol, M. A. Natiello and M. G. Zimmermann, *Resonance structure in a weakly detuned laser with injected signal*, International Journal of Bifurcation and Chaos **11** (2001) 2587–2605.
- [81] C. Mayol, R. Toral, C. R. Mirasso, S. I. Turovets, and L. Pesquera, *Theory of main resonances in directly modulated diode lasers*, IEEE Journal of Quantum Electronics **38** (2002) 260–269.
- [82] R. Meucci, A. Di Garbo, E. Allaria, and F. T. Arecchi, *Autonomous bursting in a homoclinic system*, Physical Review Letters **88** (2002) 144101.
- [83] Y. Morita and Y. Mimota, *Collision and collapse of layers in a 1D scalar reaction-diffusion equation*, Physica D **140** (2000) 151–170.
- [84] H. Nakatsuka, S. Asaka, H. Itoh, K. Ikeda, and M. Matsuoka, *Observation of bifurcation to chaos in an all-optical bistable system*, Physical Review Letters **50** (1983) 109–112.
- [85] P. Nardone, P. Mandel, and R. Kapral, *Analysis of a delay-differential equation in optical bistability*, Physical Review A **33** (1986) 2465–2471.
- [86] M. Nizette, T. Erneux, A. Gavrielides, and V. Kovanis, *Injection locked semiconductor laser dynamics from large to small detunings*, in Physics and Simulations of Optoelectronic Devices VII, P. Blood, A. Ishibashi, and M. Osinski, Eds., Proc. SPIE **3625** (1999) 679–691.
- [87] M. Nizette, T. Erneux, A. Gavrielides, and V. Kovanis, *Stability and bifurcations of periodically modulated, optically injected laser diodes*, Physical Review E **63** (2001) 026212.
- [88] M. Nizette, T. Erneux, A. Gavrielides, and V. Kovanis, *Averaged equations for injection locked semiconductor lasers*, Physica D **161** (2002) 220–236.
- [89] M. Nizette, T. Erneux, A. Gavrielides, V. Kovanis, and T. B. Simpson, *Bistability of pulsating intensities for double-locked laser diodes*, Physical Review E **65** (2002) 056610.
- [90] G. L. Oppo and A. Politi, *Toda potentials in laser equations*, Zeitschrift für Physik B **59** (1985) 111–115.
- [91] K. Otsuka, *Winner-Takes-All dynamics and antiphase states in modulated multimode lasers*, Physical Review Letters **67** (1991) 1090–1093.
- [92] K. Otsuka and J.-L. Chern, *Dynamical spatial-pattern memory in globally coupled lasers*, Physical Review A **45** (1992) 8288–8291.
- [93] K. Otsuka and K. Ikeda, *Cooperative dynamics and functions in a collective nonlinear optical element system*, Physical Review A **39** (1989) 5209–5229.

- [94] F. Papoff, D. Dangoisse, E. Poite-Hanoteau and P. Glorieux, *Chaotic transients in a CO₂ laser with modulated Parameters: critical slowing down and crisis-induced intermittency*, Optics Communications **67** (1988) 358.
- [95] K. Petermann, *Laser diode modulation and noise*, Kluwer Academic Publishers, Dordrecht, 1991.
- [96] K. Petermann, *External optical feedback phenomena in semiconductor lasers*, IEEE Journal of Selected Topics in Quantum Electronics **1** (1995) 480–489.
- [97] L. M. Pismen, *Vortices in Nonlinear Fields*, International Series of Monographs on Physics, Clarendon Press, Oxford, 1999.
- [98] L. M. Pismen and J. D. Rodriguez, *Mobility of singularities in the dissipative Ginzburg-Landau equation*, Physical Review A **42** (1990) 2471–2474.
- [99] E. S. Polzik, J. Carri, and H. J. Kimble, *Spectroscopy with squeezed light*, Physical Review Letters **68** (1992) 3020–3023.
- [100] C. Richy, K. I. Petsas, E. Giacobino, C. Fabre, and L. Lugiato, *Observation of bistability and delayed bifurcation in a triply resonant optical parametric oscillator*, Journal of the Optical Society of America B **12** (1995) 456–461.
- [101] J. D. Rodriguez, L. M. Pismen, and L. Sirovich, *Motion of interacting defects in the Ginzburg-Landau model*, Physical Review A **44** (1991) 7980–7984.
- [102] S. Rosenblat and D.S. Cohen, *Periodically perturbed bifurcation II Hopf bifurcation*, Studies in Applied Mathematics **64** (1981) 143–175.
- [103] B. E. A. Saleh and M. C. Teich, *Fundamentals of photonics*, Wiley, 1991.
- [104] C. Schwob, P. F. Cohadon, C. Fabre, M. A. M. Marte, H. Ritsch, A. Gatti, L. Lugiato, *Transverse effects and mode couplings in OPOs*, Applied Physics B **66** (1998) 685–699.
- [105] T. B. Simpson, *Phase-locked microwave-frequency modulations in optically-injected laser diodes*, Optics Communications **170** (1999) 93–98.
- [106] T. B. Simpson, *Mapping the nonlinear dynamics of a distributed feedback semiconductor laser subject to external optical injection*, Optics Communications **215** (2003) 135–151.
- [107] T. B. Simpson, J. M. Liu, A. Gavrielides, V. Kovanis, and P. M. Alsing, *Period-doubling cascades and chaos in a semiconductor laser with optical injection*, Physical review A **51** (1995) 4181–4185.
- [108] T. B. Simpson, J. M. Liu, K. F. Huang, and K. Tai, *Nonlinear dynamics induced by external optical injection in semiconductor lasers*, Quantum and Semiclassical Optics **9** (1997) 765–784.

- [109] R. G. Smith, J. E. Geusic, H. J. Levinstein, J. J. Rubin, S. Singh, and L. G. van Utiert, *Continuous optical parametric oscillation in $Ba_2NaNb_5O_{15}$* , Applied Physics Letters **12** (1968) 308–310.
- [110] H. G. Solari and G.-L. Oppo, *Laser with injected signal: perturbation of an invariant circle*, Optics Communications **111** (1994) 173–190.
- [111] D. W. Sukow, V. Kovanis and A. Gavrielides, *Investigation of coupled diode laser dynamics using an electronic circuit analog*, Physics and Simulation of Optoelectronic Devices VII, Proceedings of SPIE **3625** (1999) 778–788.
- [112] P. Suret, *Dynamique temporelle et effets transverses dans les oscillateurs paramétriques optiques continus: observations expérimentales et modélisation*, Ph. D. Thesis, Université de Paris XI, 2000.
- [113] P. Suret, D. Derozier, M. Lefranc, J. Zemmouri, and S. Bielawski, *Self-pulsing instabilities in an optical parametric oscillator: Experimental observation and modeling of the mechanism*, Physical Review A **61** (2000) 021805(R).
- [114] P. Suret, M. Lefranc, D. Derozier, J. Zemmouri, and S. Bielawski, *Periodic mode hopping induced by thermo-optic effects in continuous-wave optical parametric oscillators*, Optics Letters **26** (2001) 1415–1417.
- [115] P. Suret, M. Lefranc, D. Derozier, J. Zemmouri, and S. Bielawski, *Fast oscillations in an optical parametric oscillator*, Optics Communications **200** (2001) 369–379.
- [116] I. Susa, T. Erneux, A. Barsella, C. Lepers, D. Dangoisse, and P. Glorieux, *Synchronization through bursting oscillations for two coupled lasers*, Physical Review A **63** (2000) 013815.
- [117] M. Taki, N. Ouarzazi, H. Ward, and P. Glorieux, *Nonlinear front propagation in optical parametric oscillators*, Journal of the Optical Society of America B **17** (2000) 997–1003.
- [118] Y. Takiguchi, K. Ohyagi, and J. Ohtsubo, *Stability analysis and synchronization in injection-locked semiconductor lasers with optical feedback*, 15th Annual Meeting of the IEEE LEOS, Glasgow (Scotland), 2002.
- [119] Y. Takiguchi, K. Ohyagi, and J. Ohtsubo, *Bandwidth-enhanced chaos synchronization in strongly injection-locked semiconductor lasers with optical feedback*, Optics Letters **28** (2003) 319–321.
- [120] M. Tlidi, P. Mandel, and M. Haelterman, *Spatiotemporal patterns and localized structures in nonlinear optics*, Physical Review E **56** (1997) 6524–6530.
- [121] G. H. M. van Tartwijk and D. Lenstra, *Semiconductor lasers with optical injection and feedback*, Quantum and Semiclassical Optics **7** (1995) 87–143.

- [122] G. D. Van Wiggeren and R. Roy, *Communication with chaotic lasers*, Science **279** (1998) 1198–1200.
- [123] C. O. Weiss and J. Brock, *Evidence for Lorenz-type chaos in a laser*, Physical Review Letters **57** (1986) 2804–2806.
- [124] S. Wieczorek, *The dynamical complexity of optically injected semiconductor lasers*, Ph. D. Thesis, Vrije Universiteit van Amsterdam, 2002.
- [125] S. Wieczorek, B. Krauskopf and D. Lenstra, *A unifying view of bifurcations in a semiconductor laser subject to optical injection*, Optics Communications **172** (1999) 279–295.
- [126] S. Wieczorek, B. Krauskopf, and D. Lenstra, *Mechanisms for multistability in a semiconductor laser with optical injection*, Optics Communications **183** (2000) 215–226.
- [127] S. Wieczorek, B. Krauskopf, and D. Lenstra, *Sudden chaotic transitions in an optically injected semiconductor laser*, Optics Letters **26** (2001) 816–818.
- [128] S. Wieczorek, B. Krauskopf, and D. Lenstra, *Unnested islands of period-doublings in an injected semiconductor laser*, Physical Review E **64** (2001) 056204.
- [129] S. Wieczorek, B. Krauskopf, and D. Lenstra, *Multiplulse excitability in a semiconductor laser with optical injection*, Physical Review Letters **88** (2002) 063901 1–4.
- [130] S. Wieczorek, T. B. Simpson, B. Krauskopf, and D. Lenstra, *Global quantitative predictions of complex laser dynamics*, Physical Review E **65** (2002) 045207(R).
- [131] S. Wieczorek, T. B. Simpson, B. Krauskopf, and D. Lenstra, *Bifurcation transitions in an optically injected diode laser: theory and experiment*, Optics Communications **215** (2003) 125–134.
- [132] L.-A. Wu, H. J. Kimble, J. L. Hall, and H. Wu, *Generation of squeezed states by parametric down conversion*, Physical Review Letters **57** (1986) 2520–2523.
- [133] J. Xin, *Front propagation in heterogeneous media*, SIAM Review **42** (2000) 161–230.
- [134] A. Yariv, *Quantum Electronics*, Wiley, 1989.
- [135] M. G. Zimmermann, M. A. Natiello, and H. G. Solari, *Sil’nikov-saddle-node interaction near a codimension-2 bifurcation: laser with injected signal*, Physica D **109** (1997) 293–314.
- [136] M. G. Zimmermann, M. A. Natiello, and H. G. Solari, *Global bifurcations in a laser with injected signal: beyond Adler’s approximation*, Chaos **11** (2001) 500–513.